

ADVANCED STEEL CONSTRUCTION

An International Journal

Volume 14 Number 3

September 2018

CONTENTS

Technical Papers

Deformation of Steel-Bamboo Composite Beam Considering the Effect of Interfacial Slippage

J.L. Zhang, Y.S. Li, K.T. Tong, J. Guo and P. Wu

Development and Calibration of a Hysteretic Model for CFS Strap Braced Stud Walls

V. Macillo, S. Shakeel, L. Fiorino and R. Landolfo

Panel Zone Modelling of Box Columns: An Analytical and Numerical Approach

F.J. Paghale, H. Saffari and A. Fakhreddini

Effect of Blast-Induced Column Failure Pattern on Collapse Behavior of Steel Frames

G.Q. Li, Y. Zhang, T.C. Yang, J. Jiang, Y. Lu and S.W. Chen

Finite Element Analysis of Demountable Steel-Concrete Composite Beams under Static Loading

V.I. Patel, B. Uly, S.W. Pathirana, S. Wood, M. Singh and B.T. Trang

Investigating the Behavior of Specially Pre-Fabricated Steel Moment Connection under Cyclic Loading

Morteza Kazemi Torbaghan, Mohammad Reza Sohrabi and Hasan Haji Kazemi

Interface Bond Behaviour between Circular Steel Tube and Lightweight Aggregate Concrete

Z.Q. Fu, H.B. Ge, B.H. Ji and J.J. Chen

Fire Resistance of Steel Tubular Columns Infilled with Ultra-High Strength Concrete

X. Lyu, G.P. Shu, J.Y. Richard Liew and Er-F. Du

Experimental Study of Mechanical Behaviour of Angles in Transmission Towers under Freezing Temperature

L.Q. An, W.Q. Jiang, Y.P. Liu, Q. Shi, Y.D. Wang and S.X. Liu

A New Numerical Modelling Approach for Flexible Rockfall Protection Barriers based on Failure Modes

X. Qi, Z.X. Yu, L. Zhao, H. Xu and S.C. Zhao

Axial Residual Capacity of Circular Concrete-Filled Steel Tube Stub Columns Considering Local Buckling

C. Yang, Z.X. Yu, Y.P. Sun, L. Zhao and H. Zhao

Announcements by IJASC:

Announcement for ICASS 2018

Announcement for SDSS 2019

Copyright © 2018 by:

The Hong Kong Institute of Steel Construction

Website: <http://www.hkisc.org>

ISSN 1816-112X

Science Citation Index Expanded, Materials Science Citation Index and ISI Alerting

Cover: The MGM Mansion Roof in Macau, China. Designed by "Second-order Direct Analysis" without effective length.

e-copy of IJASC is free to download at "www.ascjournal.com" in internet and mobile apps.

ADVANCED STEEL CONSTRUCTION

VOL. 14, NO. 3 (2018)

ADVANCED STEEL CONSTRUCTION

an International Journal

ISSN 1816-112X

Volume 14 Number 3

September 2018



Editors-in-Chief

S.L. Chan, The Hong Kong Polytechnic University, Hong Kong

W.F. Chen, University of Hawaii at Manoa, USA

R. Zandonini, Trento University, Italy

ISSN 1816-112X

Science Citation Index Expanded,
Materials Science Citation Index
and ISI Alerting

EDITORS-IN-CHIEF

Asian Pacific, African and organizing Editor

S.L. Chan
*The Hong Kong Polyt. Univ.,
Hong Kong*

American Editor

W.F. Chen
Univ. of Hawaii at Manoa, USA

European Editor

R. Zandonini
Trento Univ., Italy

ASSOCIATE EDITORS

Y.P. Liu
The Hong Kong Polyt. Univ., Hong Kong

S.W. Liu
The Hong Kong Polyt. Univ., Hong Kong

INTERNATIONAL EDITORIAL BOARD

F.G. Albermani
Central Queensland Univ., Australia

I. Burgess
Univ. of Sheffield, UK

F.S.K. Bijlaard
Delft Univ. of Technology, The Netherlands

R. Bjorhovde
The Bjorhovde Group, USA

M.A. Bradford
The Univ. of New South Wales, Australia

D. Camotim
Technical Univ. of Lisbon, Portugal

C.M. Chan
Hong Kong Univ. of Science & Technology, Hong Kong

T.H.T. Chan
Queensland Univ. of Technology, Australia

T.M. Chan
The Hong Kong Polyt. Univ., Hong Kong

S.P. Chiew
Nanyang Technological Univ., Singapore

W.K. Chow
The Hong Kong Polyt. Univ., Hong Kong

G.G. Deierlein
Stanford Univ., California, USA

L. Dezi
Univ. of Ancona, Italy

D. Dubina
The Politehnica Univ. of Timisoara, Romania

R. Greiner
Technical Univ. of Graz, Austria

L. Gardner
Imperial College of Science, Technology and Medicine, UK

Y. Goto
Nagoya Institute of Technology, Japan

L.H. Han
Tsinghua Univ. China

S. Herion
University of Karlsruhe, Germany

G.W.M. Ho
Ove Arup & Partners Hong Kong Ltd., Hong Kong

B.A. Izzuddin
*Imperial College of Science, Technology and
Medicine, UK*

J.P. Jaspart
Univ. of Liege, Belgium

S. A. Jayachandran
IIT Madras, Chennai, India

S.E. Kim
Sejong Univ., South Korea

S. Kitipornchai
The Univ., of Queensland, Australia

D. Lam
Univ. of Bradford, UK

H.F. Lam
City Univ. of Hong Kong, Hong Kong

G.Q. Li
Tongji Univ., China

J.Y.R. Liew
National Univ. of Singapore, Singapore

E.M. Lui
Syracuse Univ., USA

Y.L. Mo
Univ. of Houston, USA

J.P. Muzeau
CUST, Clermont Ferrand, France

D.A. Nethercot
*Imperial College of Science, Technology and
Medicine, UK*

Y.Q. Ni
The Hong Kong Polyt. Univ., Hong Kong

D.J. Oehlers
The Univ. of Adelaide, Australia

J.L. Peng
Yunlin Uni. of Science & Technology, Taiwan

K. Rasmussen
The Univ. of Sydney, Australia

J.M. Rotter
The Univ. of Edinburgh, UK

C. Scawthorn
Scawthorn Porter Associates, USA

P. Schaumann
Univ. of Hannover, Germany

Y.J. Shi
Tsinghua Univ., China

G.P. Shu
Southeast Univ. China

L. Simões da Silva
*Department of Civil Engineering, University of
Coimbra, Portugal*

J.G. Teng
The Hong Kong Polyt. Univ., Hong Kong

G.S. Tong
Zhejiang Univ., China

K.C. Tsai
National Taiwan Univ., Taiwan

C.M. Uang
Univ. of California, USA

B. Uy
University of Western Sydney, Australia

M. Veljkovic
Univ. of Lulea, Sweden

F. Wald
Czech Technical Univ. in Prague, Czech

Y.C. Wang
The Univ. of Manchester, UK

Y.L. Xu
The Hong Kong Polyt. Univ., Hong Kong

D. White
Georgia Institute of Technology, USA

E. Yamaguchi
Kyushu Institute of Technology, Japan

Y.B. Yang
National Taiwan Univ., Taiwan

Y.Y. Yang
China Academy of Building Research, Beijing, China

B. Young
The Univ. of Hong Kong, Hong Kong

X.L. Zhao
Monash Univ., Australia

X.H. Zhou
Chongqing University, China

Z.H. Zhou
The Hong Kong Polyt. Univ., Hong Kong

S.Y. Zhu
The Hong Kong Polyt. Univ., Hong Kong

R.D. Ziemian
Bucknell Univ., USA

General Information

Advanced Steel Construction, an international journal

Aims and scope

The International Journal of Advanced Steel Construction provides a platform for the publication and rapid dissemination of original and up-to-date research and technological developments in steel construction, design and analysis. Scope of research papers published in this journal includes but is not limited to theoretical and experimental research on elements, assemblages, systems, material, design philosophy and codification, standards, fabrication, projects of innovative nature and computer techniques. The journal is specifically tailored to channel the exchange of technological know-how between researchers and practitioners. Contributions from all aspects related to the recent developments of advanced steel construction are welcome.

Instructions to authors

Submission of the manuscript. Authors may submit on-line at www.hkisc.org

Asian Pacific, African and organizing editor : Professor S.L. Chan, Email: ceslchan@polyu.edu.hk
American editor : Professor W.F. Chen, Email: waifah@hawaii.edu
European editor : Professor R. Zandonini, Email: riccardo_zandonini@ing.unitn.it

All manuscripts submitted to the journal are recommended to accompany with a list of four potential reviewers suggested by the author(s). This list should include the complete name, address, telephone and fax numbers, email address, and at least five keywords that identify the expertise of each reviewer. This scheme will improve the process of review.

Style of manuscript

General. Author(s) should provide full postal and email addresses and fax number for correspondence. The manuscript including abstract, keywords, references, figures and tables should be in English with pages numbered and typed with double line spacing on single side of A4 or letter-sized paper. The front page of the article should contain:

- a) a short title (reflecting the content of the paper);
- b) all the name(s) and postal and email addresses of author(s) specifying the author to whom correspondence and proofs should be sent;
- c) an abstract of 100-200 words; and
- d) 5 to 8 keywords.

The paper must contain an introduction and a conclusion. The length of paper should not exceed 25 journal pages (approximately 15,000 words equivalents).

Tables and figures. Tables and figures including photographs should be typed, numbered consecutively in Arabic numerals and with short titles. They should be referred in the text as Figure 1, Table 2, etc. Originally drawn figures and photographs should be provided in a form suitable for photographic reproduction and reduction in the journal.

Mathematical expressions and units. The Systeme Internationale (SI) should be followed whenever possible. The numbers identifying the displayed mathematical expression should be referred to in the text as Eq. 1, Eq. 2.

References. References to published literature should be referred in the text, in the order of citation with Arabic numerals, by the last name(s) of the author(s) (e.g. Zandonini and Zanon [3]) or if more than three authors (e.g. Zandonini et al. [4]). References should be in English with occasional allowance of 1-2 exceptional references in local languages and reflect the current state-of-technology. Journal titles should be abbreviated in the style of the Word List of Scientific Periodicals. References should be cited in the following style [1, 2, 3].

Journal: [1] Chen, W.F. and Kishi, N., "Semi-rigid Steel Beam-to-column Connections, Data Base and Modelling", Journal of Structural Engineering, ASCE, 1989, Vol. 115, No. 1, pp. 105-119.

Book: [2] Chan, S.L. and Chui, P.P.T., "Non-linear Static and Cyclic Analysis of Semi-rigid Steel Frames", Elsevier Science, 2000.

Proceedings: [3] Zandonini, R. and Zanon, P., "Experimental Analysis of Steel Beams with Semi-rigid Joints", Proceedings of International Conference on Advances in Steel Structures, Hong Kong, 1996, Vol. 1, pp. 356-364.

Proofs. Proof will be sent to the corresponding author to correct any typesetting errors. Alternations to the original manuscript at this stage will not be accepted. Proofs should be returned within 48 hours of receipt on-line.

Copyright. Submission of an article to "Advanced Steel Construction" implies that it presents the original and unpublished work, and not under consideration for publication nor published elsewhere. On acceptance of a manuscript submitted, the copyright thereof is transferred to the publisher by the Transfer of Copyright Agreement and upon the acceptance of publication for the papers, the corresponding author must sign the form for Transfer of Copyright.

Permission. Quoting from this journal is granted provided that the customary acknowledgement is given to the source.

Page charge and Reprints. There will be no page charges if the length of paper is within the limit of 25 journal pages. A total of 30 free offprints will be supplied free of charge to the corresponding author. Purchasing orders for additional offprints can be made on order forms which will be sent to the authors. These instructions can be obtained at the Hong Kong Institute of Steel Construction, Journal website: <http://www.hkisc.org>

The International Journal of Advanced Steel Construction is published quarterly by learnt society, The Hong Kong Institute of Steel Construction, c/o Department of Civil & Environmental Engineering, The Hong Kong Polytechnic University, Hung Hom, Kowloon, Hong Kong.

Disclaimer. No responsibility is assumed for any injury and / or damage to persons or property as a matter of products liability, negligence or otherwise, or from any use or operation of any methods, products, instructions or ideas contained in the material herein.

Subscription inquiries and change of address. Address all subscription inquiries and correspondence to Member Records, IJASC. Notify an address change as soon as possible. All communications should include both old and new addresses with zip codes and be accompanied by a mailing label from a recent issue. Allow six weeks for all changes to become effective.

The Hong Kong Institute of Steel Construction

HKISC
c/o Department of Civil and Environmental Engineering,
The Hong Kong Polytechnic University,
Hung Hom, Kowloon, Hong Kong, China.
Tel: 852- 2766 6047 Fax: 852- 2334 6389
Email: ceslchan@polyu.edu.hk Website: <http://www.hkisc.org/>
ISSN 1816-112X

Science Citation Index Expanded, Materials Science Citation Index and ISI Alerting

Copyright © 2018 by:

The Hong Kong Institute of Steel Construction.



ISSN 1816-112X

Science Citation Index Expanded,
Materials Science Citation Index and
ISI Alerting

EDITORS-IN-CHIEF

Asian Pacific, African and organizing Editor

S.L. Chan

*The Hong Kong Polyt. Univ.,
Hong Kong*

Email: ceslchan@polyu.edu.hk

American Editor

W.F. Chen

Univ. of Hawaii at Manoa, USA

Email: waifah@hawaii.edu

European Editor

R. Zandonini

Trento Univ., Italy

Email: riccardo.zandonini@ing.unitn.it

Advanced Steel Construction

an international journal

VOLUME 14 NUMBER 3

SEPTEMBER 2018

Technical Papers

Deformation of Steel-Bamboo Composite Beam Considering the Effect of Interfacial Slippage 324

J.L. Zhang, Y.S. Li, K.T. Tong, J. Guo and P. Wu

Development and Calibration of a Hysteretic Model for CFS Strap Braced Stud Walls 337

V. Macillo, S. Shakeel, L. Fiorino and R. Landolfo

Panel Zone Modelling of Box Columns: An Analytical and Numerical Approach 361

F.J. Paghale, H. Saffari and A. Fakhraddini

Effect of Blast-Induced Column Failure Pattern on Collapse Behavior of Steel Frames 377

G.Q. Li, Y. Zhang, T.C. Yang, J. Jiang, Y. Lu and S.W. Chen

Finite Element Analysis of Demountable Steel-Concrete Composite Beams under Static Loading 392

V.I. Patel, B. Uy, S.W. Pathirana, S. Wood, M. Singh and B.T. Trang

Investigating the Behavior of Specially Pre-Fabricated Steel Moment Connection under Cyclic Loading 412

Morteza Kazemi Torbaghan, Mohammad Reza Sohrabi and Hasan Haji Kazemi

Interface Bond Behaviour between Circular Steel Tube and Lightweight Aggregate Concrete 424

Z.Q. Fu, H.B. Ge, B.H. Ji and J.J. Chen

Fire Resistance of Steel Tubular Columns Infilled with Ultra-High Strength Concrete 438

X. Lyu, G.P. Shu, J.Y. Richard Liew and Er-F. Du

Experimental Study of Mechanical Behaviour of Angles in Transmission Towers under Freezing Temperature 461

L.Q. An, W.Q. Jiang, Y.P. Liu, Q. Shi, Y.D. Wang and S.X. Liu

A New Numerical Modelling Approach for Flexible Rockfall Protection Barriers based on Failure Modes 479

X. Qi, Z.X. Yu, L. Zhao, H. Xu and S.C. Zhao

Axial Residual Capacity of Circular Concrete-Filled Steel Tube Stub Columns Considering Local Buckling 496

C. Yang, Z.X. Yu, Y.P. Sun, L. Zhao and H. Zhao

Announcements by IJASC :

Announcement for ICASS 2018

Announcement for SDSS 2019

DEFORMATION OF STEEL-BAMBOO COMPOSITE BEAM CONSIDERING THE EFFECT OF INTERFACIAL SLIPPAGE

J.L. Zhang ¹, Y.S. Li ^{2,*}, K.T. Tong ³, J. Guo ⁴ and P. Wu ⁵

¹ Ph.D. Candidate, Department of Civil Engineering, Ningbo University, Ningbo, China

² Professor of Civil Engineering, Department of Civil Engineering, Ningbo University, Ningbo, China

³ Ph.D. Candidate, Department of Civil Engineering, Ningbo University, Ningbo, China

⁴ Graduate Student, Department of Civil Engineering, Ningbo University, Ningbo, China

⁵ Graduate Student, Department of Civil Engineering, Ningbo University, Ningbo, China

*(Corresponding author: E-mail: lys0451@163.com)

Received: 23 February 2017; Revised: 28 February 2017; Accepted: 25 June 2017

ABSTRACT: Steel-bamboo composite beams were fabricated with cold-formed thin-walled steel and bamboo plywood bonded by structural adhesive. Six specimens were tested to investigate the effect of the steel-bamboo interfacial slippage on the deformation of the composite beams. Assuming interfacial shear force is proportional to the slippage; differential equations were established to relate deformation with the arbitrary loads, based on the elementary beam theory, and the differential relationship between the interfacial slippage and the strain. The mid-span deflection equations were derived considering the slipping effects of three common load cases. Comparing the theoretical deflections with and without the effect of slippage to the experimental results, the accuracy was improved by 7%. It was found that the interfacial bond stiffness has significant influence on the deformation of the steel-bamboo composite beams. When bond stiffness was up to a value of 700N/mm, it could ensure a reliable composite bonding between the steel and the bamboo plywood. The finite-element software ANSYS was then employed to validate the analytical results. Spring elements COMBIN39 were used to model the interfacial adhesive. The results were in good agreement with those obtained from the experimental and theoretical analyses.

Keywords: Steel-bamboo composite beam, interfacial slippage, static test, theoretical analysis, finite element analysis

DOI: 10.18057/IJASC.2018.14.3.1

1. INTRODUCTION

Bamboo is well-known for its high strength, light weight, great stiffness, and especially for its environmental friendly features [1-2]. Research shows that bamboo improves the natural surrounding environment during its growth, consumes little energy in the manufacturing process, and it is bio-degradable at its end-of-life [3]. Thanks to the development of modern industrial technology, the original bamboo can be manufactured into plywood with fine cross-section and stable mechanical properties after a series of physical and chemical processing. The tensile strength of plywood is 2 times higher than common timbers, as the compressive strength is about 1.5 times [4], so that bamboo can be applied in the construction of modern buildings [5] and bridges [6], with advantages in environmental protection, energy saving and excellent performance in resisting earthquake due to lightweight [7].

Cold-formed thin-wall steel has advantages in material conservation and flexible modeling [8]. Comparing with the normal steel structure, cold-formed steel with the same sectional area has larger radius of gyration and moment of inertia. However, as the ratio of width to thickness increases, global instability and local buckling are more likely to occur in cold-formed steel. Thus, the load bearing capacity is primarily determined by local buckling and instability. If the stability problems could be effectively solved or alleviated, the economic efficiency would be further

improved, and its potential applications would be widened.

In order to better take advantage of the mechanical properties of bamboo and cold-formed steel, the research group at Ningbo University put forward innovative steel-bamboo composite structures, which consist of thin-walled cold-formed steel and bamboo plywood [9]. The steel-bamboo composites can avoid the difficulties of using original bamboo to form sections of hollow shape, I-shape and box shape etc. Meanwhile, the bamboo braces the cold-formed steel sheet, which could effectively reduce its tendency of buckling, so that bamboo and cold-formed steel are well complementary to each other.

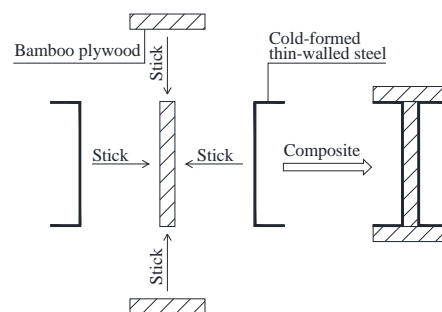
In the steel-bamboo composites, cold-formed steel and bamboo plywood are bonded with structural adhesive, which ensures the two materials work together. Since 2005, the research group has developed different kinds of steel-bamboo composite structural components, such as composite columns [10-11], composite beams [12-13], composite slabs [14-15], composite walls [16-17] and composite joints [18-19]. Lab testing on composite beams shows they exhibit high load bearing capacities and a desirable property of ductility. Thus, the effective control on the deformation of steel-bamboo composite beams is of great importance to ensure the maximum effect when these structures are applied in real construction projects. As the bending moment increases, slippage at the interface would obviously affect the mechanical performances of the composite beam and lead to larger deformation. Therefore, an analysis considering the slipping effect at the interface would better reflect the actual performance of the steel-bamboo composite beams.

The study focuses on the deformation of I-shaped steel-bamboo composite beams considering the slipping effect at the steel bamboo interface. The deformation formula was derived, and one-dimensional non-linear spring element was employed to simulate the steel-bamboo interfacial slippage using ANSYS. Experimental results, theoretical analyses and finite element simulations were compared in this study.

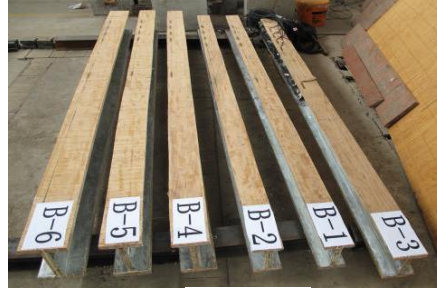
2. EXPERIMENTS OF COMPOSITE BEAMS UNDER STATIC LOADING

2.1 Specimens

Six steel-bamboo composite beams with a typical I-section were prepared for the lab testing and were denoted as B-1~B-6. The shear span ratios of the specimens were all greater than 3 and the failure of these specimens was caused by the bending moment. As shown in Figure 1, the steel-bamboo composite beams were made of three bamboo plywood panels and two thin-walled steel sheets which were first cold formed to the channel shape. The effective lengths of the specimens were all 2300 mm. The variables of the specimens, including the flange width of bamboo panel, and the height of cold-formed thin-walled steel sheet, are listed in Table 1.



(a) cross-section of composite beam



(b) specimens

Figure 1. Bamboo-steel Composite Beams

2.2 Material Testing and Properties

According to GB/T 228-2010, *Metal Material Tensile Testing*, the modulus of elasticity, yield strength and tensile strength of cold-formed thin-walled steel were measured in the lab. The modulus of elasticity and flexural strength of bamboo panel were measured based on GB/T 20241-2006, *Laminated Veneer Lumber*. All the mechanical properties of materials above were listed in Table 1.

2.3 Loading and Tests

All the specimens and tests were carried out in the Civil Engineering laboratory at the Ningbo University, China. The specimen was placed on the universal test machine with four axes and a compressive load was applied to the center of an auxiliary beam through a jack (Figure 2). The loading points and support regions were strengthened using steel plates with the thickness of 5mm to avoid local damages. The loading was force controlled. Each stage of loading was 3kN for B-1~B-3 and 6kN for B-4~B-6. In order to measure the deflection of composite beam under different loadings, the extensometers were deployed at the supports, mid-span and loading point of the composite beam, respectively (Figure 2).

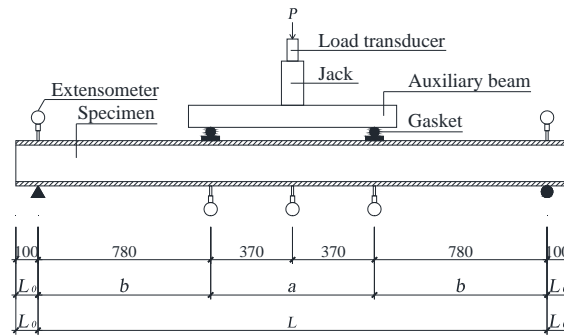


Figure 2. Scheme of Loading Apparatus

2.4 Testing Results and Analysis

The experimental results indicated that the steel-bamboo composite beams had good load bearing capacities and large deformation before failure. According to the steel structures design codes (GB 50017-2003) and the timber design codes (GB 50005-2013) in China, the deformation should be limited to $l/250$ (l is the effective span). The experimental data denoted that the strains of steel and bamboo panel were in elastic state and the load vs mid-span deflection curve presented linear property when the mid-span deflection was less than $l/250$ as shown in Figure 3.

Table1. Parameters of Specimens

Number	Thickness (Bamboo Panel) /mm	Thickness (Steel Sheet) /mm	I-section /mm	Members /mm	MOE (Bamboo Panel) /Mpa	Flexure Strength (Bamboo Panel)/ Mpa	MOE (Steel Sheet) /Mpa	Flexure Strength (Steel Sheet) / Mpa	Tensile Strength (Steel Sheet)/ Mpa	Distance between Symmetric Point Loads a/mm	Shear Span Ratio b/h
B-1	15.0	1.5	30.0×124.0×30.0	79.0×154.0	8500	73	200000	245	340	740	5.06
B-2	17.0	1.5	30.0×124.0×30.0	99.0×158.0	6500	62	200000	245	340	740	4.94
B-3	17.0	2.0	40.0×124.0×40.0	99.0×158.0	6500	62	200000	270	340	740	4.94
B-4	17.0	2.0	40.0×165.0×40.0	99.0×199.0	6500	62	200000	270	340	740	3.92
B-5	19.0	2.0	40.0×165.0×40.0	99.0×203.0	6900	67	200000	270	340	740	3.84
B-6	19.0	2.0	50.0×165.0×50.0	119.0×203.0	6900	67	200000	270	340	740	3.84

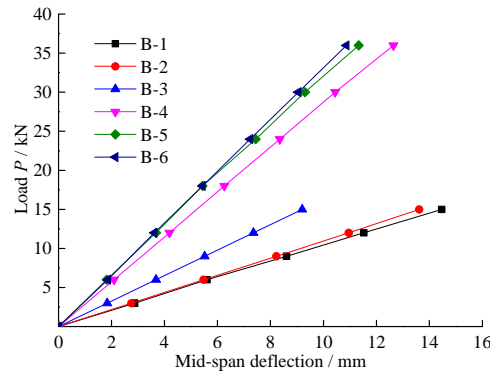


Figure 3. Load vs. Mid-span Deflection Curves of Composite Beam

The steel-bamboo interfacial slippage caused by the shear stress at the bonding interface was observed in the tests. The slippage could also be obtained by analyzing the strain distribution in steel-bamboo interface and the strain differences. The effects of the slippage on the deformation of the steel-bamboo composite beams were summarized as follows: (1) the strain in the section is no longer consistent with the assumption of plane section due to the strain changes at the interface. (2) The mid-span deflection increased due to the reduced stiffness of the composite beam. Therefore, the interfacial slipping effect should be considered in the deformation analysis of the steel-bamboo composite beams.

3. THEORETICAL APPROACH

3.1 Basic Assumptions

In this analysis, the following assumptions were made for the composite beams: (1) the cold-formed thin-walled steel and bamboo plywood are all linear elastic. (2) The relationship between the shear stress at the bonding interface and the slippage is considered, i.e. $Q=k \cdot s$. Here, Q is the shear stress, s is the slippage and k denotes the interfacial bond stiffness as reported in Ref. [20]. The interfacial shear stress equations can be expressed as: $Q_1 = k \cdot s_1$ (compressive region) and $Q_2 = k \cdot s_2$ (tensile region), when the same stiffness k is assumed for the compressive and tensile regions. Q_1 and Q_2 are the shear stresses at the bonding interfaces of the compressive and tensile region, while s_1 and s_2 are the interfacial slippages in the compressive and tensile regions respectively. (3) The strain distributions of cold-formed thin-walled steel and bamboo plywood in the direction of height are both assumed to be linear. (4) No interfacial

slippage is allowed in the web of the steel-bamboo composite beams. (5) The shear deformation and interfacial uplifting force are neglected.

3.2 Differential Equations

Three differential segments of the composite beams are shown in Figure 4, which include the top flange, the web and the bottom flange and are denoted as 1, 2, 3, respectively. According to the equilibrium conditions of the differential segments, the following differential equations can be derived:

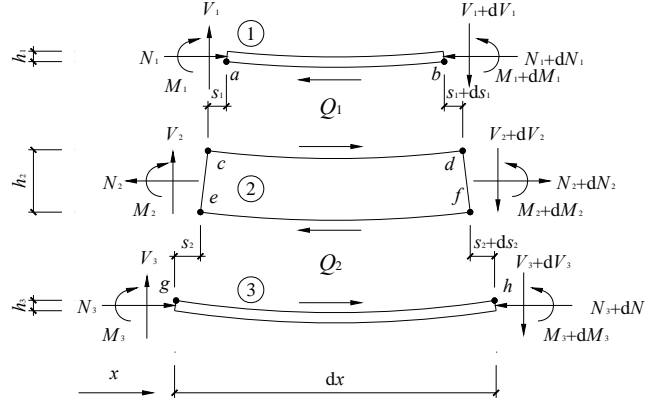


Figure 4. Load State of Micro Element

$$dM_1 - V_1 dx - \frac{1}{2} Q_1 h_1 dx = 0 \quad (1)$$

$$dM_2 - V_2 dx - \frac{1}{2} Q_1 h_2 dx - \frac{1}{2} Q_2 h_2 dx = 0 \quad (2)$$

$$dM_3 - V_3 dx - \frac{1}{2} Q_2 h_3 dx = 0 \quad (3)$$

where M_1 , M_2 and M_3 are the bending moments of the three differential segments respectively. V_1 , V_2 and V_3 are the shear forces of the three differential segments respectively. h_1 , h_2 and h_3 are the section heights of the three differential segments respectively.

Solving from Eqs. 1, 2 and 3.

$$\frac{dM_1}{dx} + \frac{dM_2}{dx} + \frac{dM_3}{dx} - V - Q_1 Z_1 - Q_2 Z_2 = 0 \quad (4)$$

where $Z_1 = (h_1 + h_2)/2$; $Z_2 = (h_2 + h_3)/2$; $V = V_1 + V_2 + V_3$.

Eq. 5 can be obtained based on the general beam theory and assumption of small deformation:

$$\phi = -\frac{d^2 y}{dx^2} = \frac{M_1}{E_1 I_1} = \frac{M_2}{E_2 I_2} = \frac{M_3}{E_3 I_3} \quad (5)$$

where ϕ and y are the curvature, and the distance from the neutral axis of cross section to any point of interest, respectively. E_i and I_j are the modulus of elasticity, and the second moment of area, respectively. The subscript i and j represent the number of the three differential segments ($i, j=1, 2, 3$).

According to the differential relationships between the interfacial slippage and strain differences in the compressive and tensile regions, the following equilibrium equations can be derived as

$$\frac{ds_1}{dx} = \varepsilon_{ab} - \varepsilon_{cd} = \phi \left(\frac{h_1}{2} + \frac{h_2}{2} \right) - \left(\frac{N_1}{E_1 A_1} + \frac{N_2}{E_2 A_2} \right) = \phi Z_1 - \left(\frac{N_1}{E_1 A_1} + \frac{N_2}{E_2 A_2} \right) \quad (6)$$

$$\frac{ds_2}{dx} = \varepsilon_{ef} - \varepsilon_{gh} = \phi \left(\frac{h_2}{2} + \frac{h_3}{2} \right) + \left(\frac{N_3}{E_3 A_3} + \frac{N_2}{E_2 A_2} \right) = \phi Z_2 + \left(\frac{N_3}{E_3 A_3} + \frac{N_2}{E_2 A_2} \right) \quad (7)$$

where N_i and A_i are the axial force and cross-sectional area of the three differential segments respectively.

Solving from Eqs. 4 and 5

$$\frac{d^3 y}{dx^3} + \frac{V}{EI} + \frac{Z_1}{EI} Q_1 + \frac{Z_2}{EI} Q_2 = 0 \quad (8)$$

where $EI = E_1 I_1 + E_2 I_2 + E_3 I_3$. If we take the derivative of Eq. 8 with respect to x , we obtain

$$\frac{d^4 y}{dx^4} + \frac{1}{EI} \cdot \frac{dV}{dx} + \frac{dQ_1}{dx} \cdot \frac{Z_1}{EI} + \frac{dQ_2}{dx} \cdot \frac{Z_2}{EI} = 0 \quad (9)$$

where $\frac{dV}{dx} = -P(x)$.

Substituting Equations $Q_1 = k \cdot s_1$ and $Q_2 = k \cdot s_2$ in Eq. 9 results:

$$\frac{d^4 y}{dx^4} - \frac{1}{EI} P(x) + k \frac{ds_1}{dx} \cdot \frac{Z_1}{EI} + k \frac{ds_2}{dx} \cdot \frac{Z_2}{EI} = 0 \quad (10)$$

Substitution of Eqs. 5 and 6 into Eq. 10 gives the following governing differentiate equation:

$$\frac{d^4 y}{dx^4} - \left(k \frac{Z_1^2}{EI} + k \frac{Z_2^2}{EI} \right) \frac{d^2 y}{dx^2} - \frac{kZ_1}{EI} \cdot \frac{N_1}{E_1 A_1} - \frac{kZ_1}{EI} \cdot \frac{N_2}{E_2 A_2} + \frac{kZ_2}{EI} \cdot \frac{N_2}{E_2 A_2} + \frac{kZ_2}{EI} \cdot \frac{N_3}{E_3 A_3} = \frac{P(x)}{EI} \quad (11)$$

In this study, the same top and bottom flange of the composite beam is considered, i.e.

$$Z_1 = Z_2 = Z \quad (12)$$

Based on the section equilibrium of the composite beam, the governing differential equation is given as below:

$$-EIy'' = M - N_1 Z + N_3 Z \quad (13)$$

where M is the bending moment in the section of the composite beam.

Substitution of Eqs. 12 and 13 into Eq. 11 gives:

$$\frac{d^4 y}{dx^4} - \alpha^2 \frac{d^2 y}{dx^2} = y_0(x) \quad (14)$$

$$\text{where } \alpha^2 = k \left(\frac{2Z^2}{EI} + \frac{1}{A_0 E_0} \right), \quad y_0(x) = \frac{1}{EI} \left(P(x) + \frac{kM}{A_0 E_0} \right).$$

3.3 Solution of the Mid-span Deflection

The mid-span deflection of a composite beam subjected to two symmetric point loads are derived in this study. Setting the origin of coordinate at the mid-span of the composite beam, the bending moment of the beam can be expressed as:

In the pure bending zone:

$$M = P \left(\frac{L}{2} - \frac{a}{2} \right) \quad x \in \left[-\frac{a}{2}, \frac{a}{2} \right]$$

In the shear and bending zone:

$$M = P \left(\frac{L}{2} - x \right) \quad x \in \left[\frac{a}{2}, \frac{L}{2} \right],$$

$$M = P \left(\frac{L}{2} + x \right) \quad x \in \left[-\frac{L}{2}, -\frac{a}{2} \right]$$

where L , a , P , and M denote the span length, the distance between two point loads (Figure 2), the magnitude of the point load, and the bending moment in the cross section, respectively.

Because of the symmetry, only half of the beam in $[0, L/2]$ is considered. The deflection equations need to be determined by applying suitable boundary conditions:

$$y_{x=L/2} = 0; \quad y_{x=0}'' = 0; \quad y_{x=L/2}'' = 0$$

Solving Eq. 14 according the boundary conditions gives the deflection equations:

In the pure bending zone:

$$y_{pb} = \frac{P}{48EI} (2L^3 + a^3 - 3La^2) - \frac{P}{2EI\alpha^2} (L - a) - \frac{P(e^{\alpha L} - e^{\alpha a})}{EI\alpha^3 (e^{\alpha L} + e^{\alpha a})} + \frac{P}{4EI} x^2 (a - L)$$

In the shear and bending zone:

$$y_{sb} = \frac{P}{48EI} (2L^3 - 3La^2 - \frac{24}{\alpha^2} L + \frac{48 + 6a^2\alpha^2}{3\alpha^3} (L - a) + \frac{48(e^{\alpha L - \alpha x} - e^{\alpha x})}{\alpha^3 (e^{\frac{1}{2}\alpha a} + e^{\alpha L - \frac{1}{2}\alpha a})} + \frac{P}{12EI} x^3 (2x - 3L)$$

The mid-span deflection is given by:

$$y_{m,s} = \frac{P}{48EI} (2L^3 + a^3 - 3La^2) - \frac{P}{2EI\alpha^2} (L - a) - \frac{P(e^{\alpha L} - e^{\alpha a})}{EI\alpha^3 (e^{\alpha L} + e^{\alpha a})} \quad (15)$$

The last two items in Eq. 15 are the additional deflections caused by the slipping effect. The expression for mid-span deflection in a composite beam subjected to a central point load and uniformly distributed load can be determined based on the method discussed above.

The composite beam is subjected to a central point load:

$$y_{m,c} = \frac{P}{EI} \left[\frac{L^3}{48} - \frac{L}{4\alpha^2} + \frac{e^{\alpha L} - 1}{2\alpha^3(e^{\alpha L} + 1)} \right] \quad (16)$$

The composite beam is subjected to a uniform load:

$$y_{m,u} = \frac{q}{EI} \left[\frac{5L^4}{384} - \frac{L^2}{8\alpha^2} + \frac{(e^{\frac{1}{2}\alpha L} - 1)^2}{\alpha^4} \right] \quad (17)$$

3.4 Test Verification

3.4.1 Comparison of Mid-span Deflection

To verify the analytical model, the theoretical calculation results are compared with the experimental data. The load vs. mid-span deflection curves of the composite beams are shown in Figure 5. It can be seen that the theoretical solutions show a good agreement with the experimental data. Table 2 compares the mid-span deflections from the experiments and the theoretical calculation in the serviceability limit state. It is found that the calculations from the analytic model are in good agreement with the corresponding measurements and the average errors are less than 10% except B-6. The theoretical values of B-1~B-5 are lower than the experimental data due to the shear deformation and the weight of auxiliary beam, etc. The error of B-6 is larger and this is mainly triggered by the following factors: (1) the bonding at the interface between steel and bamboo may not be uniform. (2) there may be vertical disturbances at the extensometers during loading process.

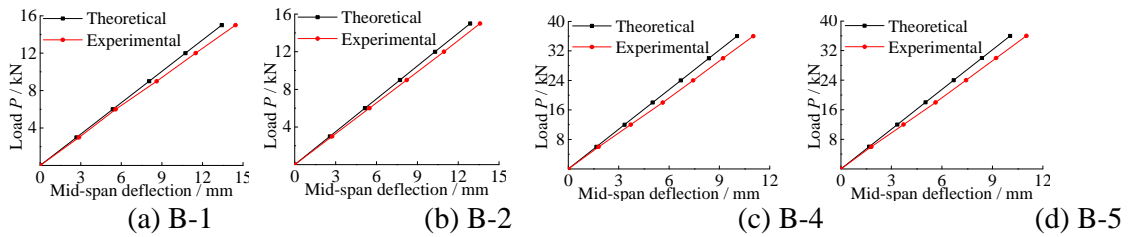


Figure 5. Load vs. Mid-span Deflection Curves of Composite Beam

3.4.2 Effect of the slippage

In order to explore the effect of the steel-bamboo interfacial slippage on the deformation of composite beam, the mid-span deflection has been predicted without considering the slipping effect using the following equation [21]:

$$y_m = P(L - a) \frac{2L^2 + 2La - a^2}{48E_s I_{SB}} \quad (18)$$

where y_m , E_s and I_{SB} denote the mid-span deflection without considering the slipping effect, the modulus of elasticity of cold-formed thin-walled steel, and the second moment of area respectively. The theoretical calculations are compared with experimental results in Table 2.

Table 2. Mid-span Deflection Results by Calculation

Number	Loading /kN	Experiments y_1 /mm	Predictions $y_{m,s}$ /mm	Predictions y_m /mm	Error δ_1 /%	Error δ_2 /%
B-1	12	11.49	10.74	9.51	6.53	17.23
B-2	12	10.95	10.30	9.23	5.94	15.71
B-3	15	9.19	8.33	7.66	9.36	16.65
B-4	30	9.21	8.38	7.90	8.79	13.10
B-5	30	9.30	8.40	7.92	9.68	14.84
B-6	36	10.78	8.85	8.36	17.90	22.45

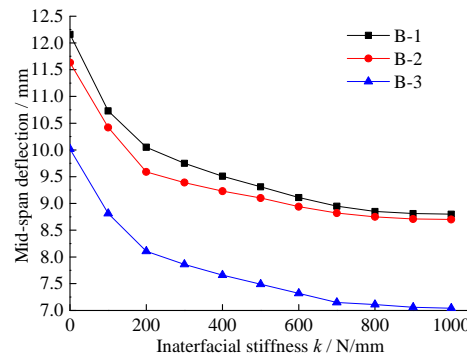
Note: The value of $y_{m,s}$ is calculated by Eq. 15 and y_m is calculated by Eq. 18. The values of error δ can be obtained by the following equations.

$$\delta_1 = \left| \frac{y_1 - y_m}{y_1} \right| \times \% \quad \delta_2 = \left| \frac{y_1 - y_{m,s}}{y_1} \right| \times \%$$

It can be seen that the average error δ_2 without considering the slipping effect is 15.5% and the calculation accuracy of Eq. 15 is about 4.4% ~ 10.7% higher than that of Eq. 18. The ratio between additional deflection due to the interface slippage and the global deflection significantly increases with the increased load. The superiority of the analytical model considering the slipping effect becomes more apparent.

3.4.3 Effect of the bond stiffness

Eq. 15 can be expressed in terms of the load P , the bending stiffness EI and the interface bond stiffness k and so on, i.e. $y=f(P, EI, k, \dots)$. The mid-span deflection vs. interface stiffness curves of the composite beams B-1~ B-3 are illustrated in Figure 6. It is revealed that the interface bond stiffness ($0 \leq k \leq 700$ N/mm) has significant influences on the mid-span deflection. When $k=0$, the ratio between the additional deflection and the global deflection is around 25%. When $k > 700$ N/mm, the sensitivity of mid-span deflection to the interface bond stiffness is low. Therefore, the additional deflection caused by the slipping effect cannot be neglected for the interface bond stiffness k of the steel-bamboo composite beam, which is typically around 425 N/mm measured in the lab testing. The interface bond stiffness of the composite beam must meet certain requirements to ensure sufficient structural integrity.

Figure 6. Mid-span Deflection vs. Interface Stiffness k Curves

4. FINITE ELEMENT NUMERICAL SIMULATION

4.1 Modeling

In this section, a finite element model using ANSYS 11.0 was established to predict the mid-span deflection of the steel-bamboo composite beam. In the model, the shell element (SHELL63), the solid element (SOLID45) and the one-dimensional nonlinear spring element (COMBIN39) were adopted to simulate the cold-formed thin-walled steel, the bamboo panel and the steel-bamboo interfacial slippage, receptively. The properties of the component materials used in the numerical analysis are listed in Table 1 and the spring stiffness can be calculated according to Ref. [20].

4.2 Numerical Simulations

The establishment and solution of the finite element model of steel-bamboo composite beam are summarized as follows:

- (1) By choosing appropriate element types and material properties, and setting corresponding real constants and key options, finite element models of cold-formed thin-walled steel and bamboo plywood were established respectively, as well as the meshes, shown in Figure 7 (a) and (b).
- (2) To minimize the discrepancies between the numerical results and the actual situations, gaskets with infinite stiffness were employed at the loading points and the bearings, to avoid the stress concentrations.
- (3) Spring elements were generated and particular nodes were coupled, shown in Figure 7 (c). Under the loading, slippages at the composite beam's web were relatively small, which was neglected, thus node coupling were applied in three dimensions (longitudinal, transverse and normal) on steel and bamboo elements of the web. Vertical lift was not found at the flange in the serviceability limit state, and it can be considered that the stiffness of the flange in the vertical direction is infinite. Nodes at the contact interface between flange and web were coupled in tangential and normal directions and spring element were generated in the vertical direction.
- (4) Symmetric point loads were applied and numerical solutions were obtained, deformation is presented in Figure 7 (d).

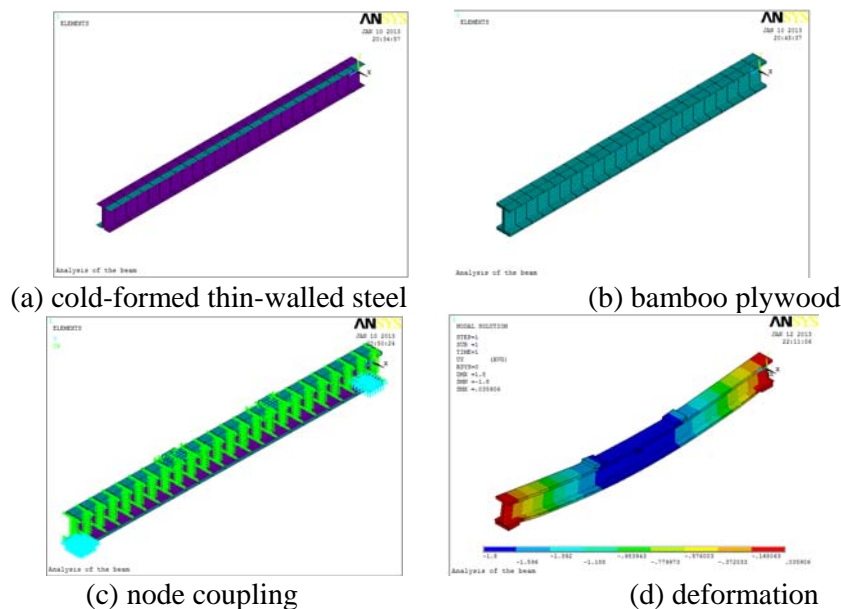


Figure 7. Finite Element Model

4.3 Numerical Results

Using the finite element method, the mid-span deflections of the composite beams are determined in ANSYS. The solutions are compared with experimental results in Table 3. It is revealed that the differences δ_3 between the numerical and the lab testing values are small except B-6, which might be caused by the human errors during the production process and the testing process. The efficiency and feasibility of the analytical method and the finite element model are verified.

Table3. Mid-Span Deflection Results by FEM Simulation

Number	Loading/ kN	Experiments y_1/mm	Predictions $y_{m,s}/\text{mm}$	FEM y_2/mm	Ratio y_1/y_2	Error $\delta_3/\%$
B-1	12	11.49	10.74	10.65	1.08	7.31
B-2	12	10.95	10.30	10.42	1.06	4.84
B-3	15	9.19	8.33	8.48	1.08	7.73
B-4	30	9.21	8.38	8.81	1.05	4.34
B-5	30	9.30	8.40	8.47	1.10	8.92
B-5	36	10.78	8.85	9.28	1.16	13.91

Note: The values of error δ_3 can be obtained by the following equations.

$$\delta_3 = \left| \frac{y_1 - y_2}{y_1} \right| \times \%$$

CONCLUSIONS

The mid-span deflection of the steel-bamboo composite beam has been studied based on the steel-bamboo interfacial slipping effect. The following conclusions are drawn from a detailed analysis:

- (1) Based on the shear slipping relationship $Q = k \cdot s$, and the equilibrium condition, the deformation equations of the slipping effect of the steel-bamboo composite beam under three common loading effects are established, which can be used as theoretical reference to the actual engineering applications.
- (2) The theoretical results considering the slipping effect agree well with the experiment data and the average error is around 8.1%. This demonstrates that the analytical method to derive the mid-span deflection of the steel-bamboo composite beam is reasonable.
- (3) The average error between the theoretical values without considering the interface slipping effect and the experimental results is 15.5%, and the calculation accuracy is effectively improved considering the slipping effect.
- (4) The interface bond stiffness has significant influence on the deformation of the steel-bamboo composite beam. Therefore, the interface adhesive should have enough stiffness to ensure the structural integrity of the steel-bamboo composite beams.
- (5) The nonlinear one-dimensional spring element COMBIN39 and the relevant element generation technologies can be used to model the bamboo-steel interface and the deformation of steel-bamboo composite beam well in ANSYS.

ACKNOWLEDGEMENTS

The authors gratefully acknowledge the financial support provided by National Key R&D Program of China [grant numbers 2017YFC502], the National Natural Science Foundation of China (NSFC) [grant numbers 51678310 & 51378265], Ningbo Natural Science Foundation [grant numbers 2017A610305], and K.C. Wong Magna Fund at the Ningbo University. Special thanks are given to Dr. Rui Liu, Assistant Professor of Structures in the College of Architecture and Environmental Design, Kent State University, for his time to revise the English of the manuscript. Acknowledgment is also extended to the technical support of Civil Engineering Laboratory of Ningbo University.

REFERENCES

- [1] Wang, K., Li, Q. and Gao, X., "Utilization Status and Development of Bamboo Resources", *Journal of Bamboo Research*, 2000, Vol. 19, No. 4, pp. 72-75.
- [2] Jain, S., Kumar, R. and Jindal, U., "Mechanical Behavior of Bamboo and Bamboo C Composite", *Journal of Materials Science*, 1992, Vol. 27, No. 17, pp. 4598-4604.
- [3] Xiao, Y., Yang, R., Shan, B., et al., "Experimental Research on Mechanical Properties of Glubam", *Journal of Building Structures*, 2012, Vol. 33, No. 11, pp. 150-157.
- [4] Zhang, X.E.J., Li, Y., et al., "Experimental Research on Compression and Flexural Mechanical Performance of Recombinant Bamboo", *Industrial Construction*, 2016, Vol. 46, No. 1, pp. 7-12.
- [5] Xiao, Y., Chen, G., Shan, B., et al., "Research and Applicant of Lightweight Glue-laminated Bamboo Frame Structure", *Journal of Building Structures*, 2010, Vol. 31, No. 6, pp. 195-203.
- [6] Xiao, Y., Zhou, Q. and Shan, B., "Design and Construction of Modern Bamboo Bridges", *Journal of Bridge Engineering*, 2010, Vol. 15, No. 5, pp. 553-541.
- [7] Lv, Q., Wei, Y., Zhang, Q., et al., "Key Technologies of the New Anti-seismic Model Living Room with Bamboo Engineering Materials", *Special Structures*, 2008, Vol. 25, No. 4, pp. 6-10.
- [8] Al-Mosawi, S. and Saka, M.P., "Optimum Shape Design of Cold-formed Thin-walled Steel Sections", *Advances in Engineering Software*, 2000, Vol. 31, No. 11, pp. 851-862.
- [9] Li, Y. and Zhang, J., "State of the Art of Steel-bamboo Composite Components and Structural System", *Industrial Construction*, 2016, Vol. 46, No. 1, pp. 1-6.
- [10] Jiang, T., Li, Y., Shan, W., et al., "Seismic Behavior of Thin-waled C Steel-bamboo Plywood Composite Column", *Journal of Northeast Forestry University*, 2011, Vol. 39, No. 12, pp. 82-85.
- [11] Liu, T., Li, Y., Xu, K., et al., "Research on Mechanical Performance of Steel-bamboo Composite Box Short Column", *Industrial Construction*, 2016, Vol. 46, No. 1, pp. 25-29.
- [12] Li, Y., Shen, H., Shan, W. et al., "Experimental Study on Shear Behavior of I-shaped Section Bamboo-steel Composite Beams", *Journal of Building Structures*, 2011, Vol. 32, No. 7, pp. 80-86.
- [13] Li, Y., Shan, W., Shen, H., et al., "Bending Resistance of I-section Bamboo-steel Composite Beams Utilizing Adhesive Bonding", *Thin-walled Structures*, 2015, Vol. 89, pp. 17-24.
- [14] Li, Y., Shan, W., Huang, Z. et al., "Experimental Study on Mechanical Behavior of Profiled Steel Sheet-bamboo Plywood Composite Slabs", *Journal of Building Structures*, 2008, Vol. 29, No. 1, pp. 96-102.
- [15] Li, Y., Shen, H., Shan, W., et al., "Flexural Behavior of Lightweight Bamboo-steel Composite Slabs", *Thin-walled Structures*, 2012, Vol. 53, pp. 83-90.

- [16] Li, Y., Guo, J., Jiang, T., et al., "Experimental Study on Seismic Behavior of Cold-formed Thin-walled C. Steel-bamboo Plywood Composite Walls", *Journal of Shenyang Jianzhu University (Natural Science)*, 2013, Vol. 29, No. 6, pp. 969-976.
- [17] Zhang, J., Li, Y., Zhai, J., et al., "Experimental Study on Heat Transfer Behavior of Cold-formed Thin-walled Steel-bamboo Plywood Composite Walls", *Industrial Construction*, 2016, Vol. 46, No. 1, pp. 13-19.
- [18] Li, Y., Jiang, T., Shan, W., et al., "Quasi-static Test on Steel-bamboo Composite Beam-column Exterior Joints", *Engineering Mechanics*, 2013, Vol. 30, No. 4, pp. 241-248.
- [19] Li, Y., He, J., Zhang, J., et al., "Seismic Response Analysis of Bamboo-steel Composite Frame Structure based on Performance of Beam-column Joints", *Journal of Architecture and Civil Engineering*, 2016, Vol. 33, No. 5, pp. 22-28.
- [20] Xie, Q., "Research on Bond Property of Steel-bamboo Interface under Static Loads", MD Thesis, Faculty of Architectural, Civil Engineering and Environment, Ningbo University, Ningbo, China, 2012.
- [21] Shen, H., Li, Y., Zhang, W., et al., "Experimental Study on Flexural Behavior of Cold-formed Thin-wall Steel-bamboo Composite Beams", *Journal of Building Structures*, 2009, Vol. 30, No. S2, pp. 171-175.

DEVELOPMENT AND CALIBRATION OF A HYSTERETIC MODEL FOR CFS STRAP BRACED STUD WALLS

V. Macillo, S. Shakeel, L. Fiorino * and R. Landolfo

*Research fellow, Department of Structures for Engineering and Architecture,
University of Naples "Federico II", Naples, Italy*

*Research fellow, Department of Structures for Engineering and Architecture,
University of Naples "Federico II", Naples, Italy*

**Assistant professor, Department of Structures for Engineering and Architecture,
University of Naples "Federico II", Naples, Italy*

*Full Professor, Department of Structures for Engineering and Architecture,
University of Naples "Federico II", Naples, Italy*

**(Corresponding author: E-mail: lfiorino@unina.it)*

Received: 10 June 2016; Revised: 26 June 2016; Accepted: 13 July 2017

ABSTRACT: Cold-formed steel (CFS) members in buildings are in use for decades, but their earthquake performance remained unexplored, until recently. Eurocodes, which provide common approach for the design of buildings in Europe still lack the information on seismic design of CFS structures. However, for the last few years, University of Naples "Federico II" CFS research group is dedicated in investigating their seismic performance. One of the focus areas is characterizing seismic behaviour of CFS strap braced stud walls. This paper presents a generalized approach adopted in simulating hysteretic behaviour of these walls under cyclic load in OpenSees software. Numerical models are developed and calibrated on the basis of available experimental results.

Keywords: Cold-formed steel, Strap braced stud walls, Hysteretic behaviour, OpenSees, Non-linear model, backbone curve

DOI: 10.18057/IJASC.2018.14.3.2

1. INTRODUCTION

In recent years, there has been rapid increase in use of cold formed steel (CFS) for low-rise buildings in North America, Europe and Oceania. Their ability to guarantee good structural response under an earthquake has brought them in spotlight for many researchers. CFS is a common term used for products made by rolling or pressing steel at relatively low temperatures (cold working). CFS products, characterized by high structural performance, light weightiness and rapid construction presents a good alternative to traditional construction materials. There are mainly three construction techniques for CFS structures used nowadays; stick built, penalized and modular constructions. In case of stick built construction, the structure is assembled on site using the modest number of members (e.g. studs, joists and tracks) and sheathing panels. Panelized constructions are made of two-dimensional prefabricated block elements (wall and floor sub-frames with roof trusses). Modular structures use pre-engineered units with all frame elements and finishes assembled in workshop and added in horizontal or vertical direction on site.

To resist the horizontal loads, namely earthquake and wind loads, two different energy dissipative systems are used in CFS constructions, all-steel and sheathed-braced. In case of all-steel solutions, lateral resistance is usually provided by thin steel straps acting as braces in an X configuration. While for sheathing-braced solutions, steel sheets or wood based panels generally provide the lateral bracing effect to withstand horizontal loads. Currently, North American Standard AISI S400 [1] is the key reference document for seismic design of these systems. However, in recent years,

extensive research [2, 3, 4, 5, 6, 7] has been carried out at University of Naples “Federico II” in order to better understand seismic performance of these CFS lateral force resisting systems and to incorporate guidelines for their seismic design in European and Italian Standards.

Iuorio et al. [7] tested three configurations (twelve tests) of CFS strap braced stud walls designed according to elastic (non-dissipative) and dissipative design approaches. Walls lateral response was investigated by carrying out tests under monotonic and cyclic loading. Additionally, they performed several tests on steel materials, elementary connections and joints between strap and gusset plate in order to study the component influence on global wall behaviour.

Macillo et al. [6] validated capacity design procedure for CFS strap braced stud walls according to European Standards. Moreover, seismic peculiarities of CFS strap braced stud walls were studied in contrast with seismic provisions for traditionally braced steel structures in European Standard EN 1998-1 [8]. Fiorino et al. [9] validated the design criteria of CFS strap braced stud wall against the provision in North American Standard AISI S213 [10] and seismic provisions for traditionally braced steel structures in European Standard EN 1998-1 [8]. Besides, they also evaluated behaviour factor at the component level based on tests performed by Iuorio et al. [7]. However, for more accurate estimation of behaviour factor, non-linear dynamic analysis and shake table test of 3D structures are needed.

In this perspective, the present paper provides the outcomes of numerical modelling of CFS strap braced stud wall in OpenSees software [11]. In particular, the calibration of pinched hysteretic material known as *pinching4* [12] used to predict behaviour of CFS strap braced stud walls under dynamic loading is explained. The paper is organized as follows: Section 2 provides recent research in modelling of CFS shear walls and details about the theoretical design procedure for seismic design of CFS strap braced stud wall; Section 3 summarizes the design of walls modelled in this study, provides the description of numerical models developed for them and the calibration of *pinching4 material*; Section 4 checks the reliability of developed numerical models against the test results; Sections 5 explores the adequacy of the calibrated models by using theoretical procedure for the definition of wall response; and section 6 checks their ability to simulate brittle failure modes.

2. BACKGROUND

2.1 Previous Research on Numerical Modelling of CFS Shear Walls

In the past, several researchers developed numerical models of CFS shear walls for both all steel and sheathing braced solutions. These models ranged from simple analytical to very complex finite element representations. This section summarizes the main intent behind the development of these models and their main features.

Pastor and Rodríguez-Ferran [13] presented a differential model of hysteretic behaviour for CFS strap braced walls, which can capture the slackness due to buckling of braces as well as strength and stiffness degradation. However, their model assumes that wall is able to maintain its load carrying capacity under excessive lateral displacements without ever reaching to failure.

Kim et al. [14] developed the analytical models for CFS strap braced stud walls in DRAIN-2DX [15] program. In their model, they used beam column element with plastic hinges lumped at both end for the studs. Addition of plastic hinges at the end of studs was due to the fact that they had fixed connections in earlier tested specimen of walls [16] and it accounted for additional bending stiffness of studs. For straps, they used inelastic truss bar elements. However, original hysteretic

model of this element in DRAIN-2DX [15] did not capture severe pinched behaviour of CFS strap braced stud walls, therefore they added a gap property to truss element to capture the complete behaviour.

Comeau et al. [17] evaluated the seismic performance factors for CFS strap braced stud walls using Incremental Dynamic Analysis (IDA) based on FEMA P695 [18] methodology. Bilinear spring elements with strain hardening and slackness characteristics were used to model hysteretic response on walls in Ruaumoko [19] software. Mirzaei et al. [20] developed an elastic analytical model with fixed connections except for the end of braces, in order to study the effect of wall aspect ratio on the moment generated in chord studs due to frame action.

In addition to above mentioned analytical models, several finite element models were also developed. Gad et al. [21] developed FE models in ANSYS [22] for Plasterboard lined CFS frame without bracing in order to study effect of presence of different boundary conditions and aspect ratio on ultimate capacity of wall using nonlinear static analysis. Later on, they combined these models with models of braced frame developed by Barton [23]. In the combined model, straps were modelled as series of three nonlinear springs: strap-frame connection, solid strap and strap tensioner unit system.

Zeynalian and Ronagh [24] developed finite element models of CFS strap braced stud walls with additional brackets at corner of walls. A nonlinear static analysis was conducted in ANSYS [22] with varying the length of brackets for each model in order to optimize their seismic response.

Shamim et al [25-26] performed several shake table tests on CFS shear walls braced with wood based panels and steel sheets in order to check their behaviour under an earthquake and to propose seismic design provisions for North American standards. They developed non-linear model of walls in OpenSees [11], which were calibrated based on their experimental results. Then, these non-linear model of walls were used in 3d Incremental Dynamic Analysis (IDA) of archetype buildings to evaluate the seismic performance factors according to FEMA P695 [18]. In sheathed braced walls, sheeting material is responsible for energy dissipation. Shamim et al. modelled sheets by equivalent diagonals as truss elements (braces). *Pinching4 material* [12] was used to represent the non-linear behaviour of walls. Additionally, they used *Zero length springs* to model tension anchors at wall corners. For wall frame profiles, they used *Elastic beam column elements*. P-delta effects were modelled using an additional frame in direction of seismic loads using *rigid Truss* and *Beam column elements* having *Co-rotational coordinate transformation*.

In USA, major research of modelling of CFS sheathed braced shear walls, ranging from hysteretic characterization of single walls to complete 3D model development, is carried under CFS NEES project. Leng et al. [27] modelled a complete double storey CFS building and performed non-linear Incremental Dynamic Analysis (IDA) using OpenSees [11]. Equivalent energy elastic plastic (EEEP) and *Pinching4 material* models were fitted to the tested data by Liu et al. [28]. It was shown that the EEEP models are only appropriate for static pushover analysis and *Pinching4 material* [12] models are capable of reasonably capturing the full hysteretic response, including degradation and were recommended for use in non-linear time history analysis.

Kechidi et al. [29] presented an accurate model to represent pinched hysteretic behaviour of wood and steel sheathed shear walls. Developed model were implemented in OpenSees [11] as user defined uniaxial material instead of *Pinching4 material*. Their models had both strength and stiffness degradation capabilities with curvature in loading and unloading branches. They used a pair of rigid truss element in X configuration with an equivalent non-linear *Zero Length element* in the middle having user-defined material to represent the wall behaviour in OpenSees.

To sum up, numerical models presented in Pastor and Rodríguez-Ferran [13], Kim et al. [14] and Comeau et al. [17] lacked the ability to capture brittle failure modes for CFS strap braced stud walls. Available models developed for CFS strap braced stud walls did not represent all wall structural components, except models presented in Kim et al. [14]. In addition, finite element models presented in Gad et al. [21] and Zeynalian and Ronagh [24] only represented the static behaviour of CFS strap braced stud walls and cannot be used in analysis of complete buildings due their complexity. In this context, there is a need to develop a numerical model which can capture brittle and ductile failure modes, properly represents the contribution of all components to lateral force resistance under dynamic and cyclic loads and is computationally efficient to be used in models of complete 3D buildings.

2.2 Procedure for Predicting the Wall Response

CFS strap braced stud wall (Figure 1) is an all steel solution to resist horizontal loads in CFS structures. The lateral system consists of concentric X bracings, made of very slender steel straps placed on both sides of walls, which are considered active only in tension. Any lateral load applied on walls is absorbed by straps in tension transmitting significant axial compression force on studs located at the ends of the wall.

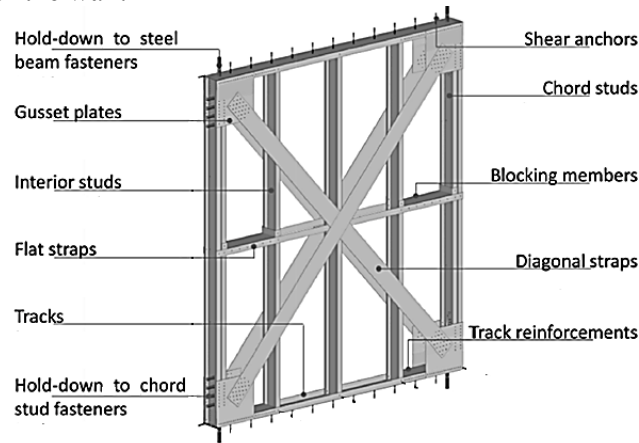


Figure 1. Typical CFS Strap Braced Stud Wall

CFS walls are made of series of studs (columns) usually placed 600mm apart fitted on horizontal tracks. External studs (chord studs) can either be back to back lipped C-channel or box cross section, in order to avoid buckling due to compression force transmitted by straps. Track members are usually made of un-lipped U cross sections. Gusset plates are usually provided at corner of walls in order to attach straps with the wall frame, generally with self-drilling screws. Flat straps can be attached at the mid height of the wall in order to reduce the buckling length of studs. Local buckling of tracks can be avoided by placing channel section profiles to form a box shape. Hold-down devices and shear anchors are used to connect the wall to foundation or to other floors. Three main structural components of the wall: diagonal in tension (d_d), tension anchors (d_a) and diagonal to frame connections (d_c) contribute to total top displacement (d) of the wall, when it is subjected to a lateral load. Hence, the total lateral displacement is calculated according to Eq. 1

$$d = d_d + d_a + d_c \quad (1)$$

The lateral resistance of the wall subjected to in plane loading can be evaluated by taking into account strength associated with each wall component [6]. Table 1 provides the procedure for the evaluation of design strength of each wall component. For each wall component, one or more

failure mechanism can be identified and then strength associated with the weakest failure mode define the design lateral strength of the wall. Therefore, the lateral design strength of the wall (H_c) can be computed according to Eq. 2 :

$$H_c = \min(H_{c,c}, H_{c,d}, H_{c,g}, H_{c,s}, H_{c,t}, H_{c,a}) \quad (2)$$

For seismic design, current trends propose to design the seismic resisting system according to capacity design criteria, which direct to the failure mechanism that maximizes the walls ductility. In case of CFS strap braced stud walls, the most ductile failure mechanism is the yielding of steel straps in tension. Therefore, the net section rupture of straps connections as well as the failure of studs, tracks and anchors should be avoided through an appropriate over strength.

Table 1. Design Wall Strength Associated to each Wall Component

Strength of the wall component	Failure modes	Design Formula
$H_{c,c}$ - wall strength associated to the diagonal to strap connection	Bearing failure in the strap of a screw $-F_{b,Rd}$ Shear failure of a screw $-F_{v,Rd}$	$n_d \cdot n_s \cdot \min(F_{b,Rd}, F_{v,Rd}) \cos\theta$
$H_{c,d}$ -wall strength associated to the yielding of the diagonal strap	Yielding of a steel the strap- $N_{pl,Rd}$ Net section failure of a strap- $N_{u,Rd}$	$n_d \cdot \min(N_{pl,Rd}, N_{u,Rd}) \cos\theta$
$H_{c,g}$ - wall strength associated to the net section failure of the gusset plate	Net section failure of a gusset plate- $F_{n,Rd}$	$n_d \cdot F_{n,Rd} \cos\theta$
$H_{c,s}$ - wall strength associated to the buckling of the studs	Buckling of a chord stud- $N_{s,Rd}$	$\frac{N_{s,Rd} - N_{Ed,G}}{h} L$
$H_{c,t}$ - wall strength associated to the buckling of the track	Buckling of a track- $N_{t,Rd}$	$N_{t,Rd}$
$H_{c,a}$ - wall strength associated to the tension and shear anchors	Strength of a tension anchor- $N_{a,Rd}$ Strength of a shear anchor- $V_{a,Rd}$	$\min\left(\frac{N_{a,Rd} + N_{Ed,G}}{h} L; n_a V_{a,Rd}\right)$
n_d is the total number of straps in tension; n_s is the total number of screws in a strap-to-frame connection; $N_{Ed,G}$ is the axial force due to gravity loads; θ is the angle of strap with respect to horizontal; L is the length of the wall; h is the height of the wall		

3. Numerical Model Development

3.1 Design of Walls

In this study, two walls configurations are selected in order to calibrate the proposed model. These walls are designed following the dissipative design approach summarized in section 2.2 and described in detail by Macillo et al. [6]. The selected walls correspond to light (WLD) and heavy (WHD) dissipative capacity walls tested by Iuorio et al. [7]. Therefore, for the sake of simplicity, numerical model of walls presented in this study are also named as WLD and WHD. The cyclic test results are used for calibrating the numerical models for the walls. In particular, two identical set of experiments (C1 and C2) are available for both WLD and WHD wall configurations.

Table 2 summarizes the general design characteristics of both wall configurations, while Table 3 gives the design and nominal values of lateral wall strength associated to each wall component.

Table 2. Design of CFS Strap Braced Stud Walls

	WLD	WHD
Width x Height	2400x2700 mm	2400x2700 mm
Chords studs	Back to back channel section (S350) C150x50x20x1.5 mm ^a	Back to back channel section (S350) C150x50x20x3 mm ^a
Straps	70x2mm ^b (S235)	140x2mm ^b (S235)
Diagonal to frame connection	No.15 4.8 x 16 mm screws ^c	No.25 6.3 40 mm screws ^d
Design wall strength	42 kN	85 kN
Theoretical wall strength^e	56kN	112kN
Tension anchors	M24 class 8.8 bolt rods	M24 class 8.8 bolt rods
Shear anchors	M8 class 8.8 bolts spaced at 300 mm on center	M8 class 8.8 bolts spaced at 300 mm on center
Hold down to chord stud fastener	4 M16 class 8.8 bolts	4 M16 class 8.8 bolts
Theoretical wall stiffness	4.37 kN/mm	7.52 kN/mm

a. C-section: outside-to-outside web depth x outside-to-outside flange size x outside-to-outside lip size x thickness.

b. Width x thickness.

c. Nominal diameter x length, modified truss head self-drilling screws.

d. Nominal diameter x length, hexagonal flat washer head self-drilling screws.

e. Theoretical wall strengths predicted on the basis of average experimental strength of materials.

3.2 Model Description

2D models with 3 degrees of freedoms, i.e. vertical and horizontal translation and rotation in plane are developed in OpenSees [11] for both selected walls. Figure 2 shows generic OpenSees model developed for CFS strap braced stud walls.

Chord Studs are modelled using *truss elements* with a *Uniaxial elastic material*, having modulus of elasticity of 210 GPa. The *OpenSees MinMax material* is used in conjunction with *uniaxial elastic material* in order to simulate the chord stud failure due to tension or global buckling. *OpenSees MinMax material* is always used in conjunction with another material, which define its stress-strain behaviour, and it enforces the threshold values of strain, beyond which strength and stiffness of element are set to zero. In the specific case, threshold values which govern the occurrence of failure of studs in tension ($\epsilon_{t,Rk}$) and compression ($\epsilon_{b,Rk}$) are calculated using Eqs. 3 and 4.

$$\epsilon_{t,Rk} = \frac{N_{t,Rk}}{A \cdot E} \quad (3)$$

$$\epsilon_{b,Rk} = \frac{N_{b,Rk}}{A \cdot E} \quad (4)$$

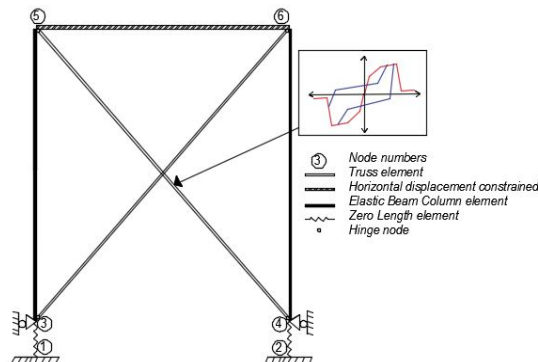


Figure 2. OpenSees Model for CFS Strap Braced Stud Wall

where, $N_{t,Rk}$ and $N_{b,Rk}$ are nominal resistances corresponding to the tensile and buckling failure of chord studs, respectively, E is the Young's modulus of steel and A is gross cross section area. $N_{t,Rk}$ and $N_{b,Rk}$ are obtained according to prescriptions given in EN 1993-1-1 [30] and EN 1993-1-3 [31]. Straps are modelled with *Truss elements* using *Pinching4 material*. Information about the calibration of strap's *pinching4 material* is provided in section 3.3. Stiffness contribution through hold down anchors to foundation is integrated by using *Zerolength elements* of unit area at bottom of stud's end. *ElasticMultiLinear material* with a stiffness of 30 kN/mm in tension, defined on the basis of experimental results of Iuorio et al. [7] and a very high stiffness (10,000 kN/mm) in compression is used for *Zerolength elements*. In OpenSees definition of *ElasticMultiLinear material*, the nonlinear stress-strain relationship is given by a multi-linear curve that is defined by a set of points. The material behaviour is nonlinear but elastic without any energy dissipation. *MinMax material* is used in conjunction with *ElasticMultiLinear material* in order to take into account tensile failure of anchors. Tensile strain in *MinMax material* for anchors is set to not exceed the nominal tensile strain $\epsilon_{a,Rk}$ of anchors preventing any tensile rupture in them while there is no strain limit in compression. Nominal tensile strain in anchors $\epsilon_{a,Rk}$ is calculated using Eq. 5 :

$$\epsilon_{a,Rk} = \frac{N_{a,Rk}}{k_a} \quad (5)$$

where $N_{a,Rk}$ is the nominal tensile resistance of anchors and k_a is the stiffness of tension anchor equal to 30kN/mm. Rigid diaphragm effect is incorporated by constraining the horizontal displacements at the wall top, using *EqualDOF* command between nodes 5 and 6. P- Δ effects are neglected in OpenSees model because there were no gravity loads present in the test [7].

In order to check consistency of the developed model against test results [9], non-linear quasi static analysis using cyclic load is performed. Same cyclic protocol as used in the reference tests [7] is imposed at top of walls. In experimental activity, CUREE ordinary ground motions reversed cyclic load developed by Krawinkler et al. [21] for wood walls and modified by Velchev et al. [22] for CFS strap braced walls was used. The loading protocol consists of initiation, primary and trailing cycles (Figure 3). First six cycles of the protocol are initiation cycles, which serve to check loading equipment, measuring devices and force deformation response at small amplitudes. After execution of initiations cycles, there are series of primary and trailing cycles. Primary cycles have bigger amplitude than all of the preceding cycles and is followed by small amplitude cycles, which are called as trailing cycles. All trailing cycles have amplitude equal to 75% of the amplitude of the preceding primary cycle. In this paper, primary cycles before the cycle number 32 are identified as minor primary cycles, while after 32 they are recognized as major primary cycles.

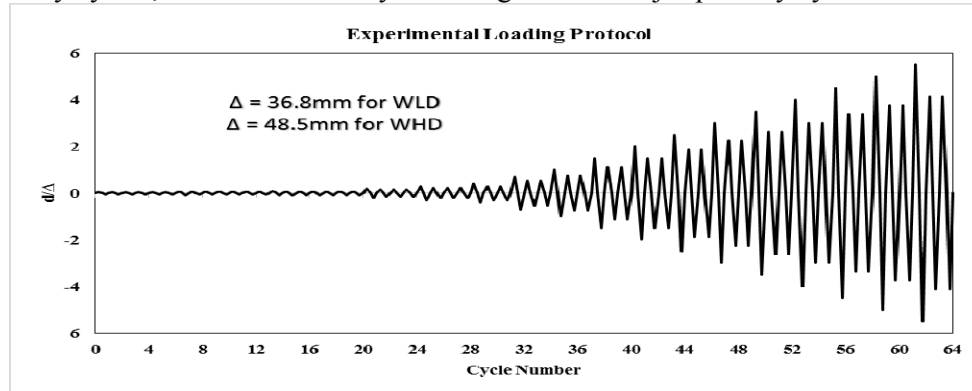


Figure 3. Experimental Cyclic Loading Protocol [6]

3.3 Hysteretic Characterization

Pinching4 material [12] is used to represent pinched hysteretic response of straps. *Pinching4 material* is a uniaxial material that can represent pinched load deformation response with the ability to exhibit degradation under cyclic loading. OpenSees [11] definition of *Pinching4 material* requires a set of 39 parameters to be defined in order to represent the non-linear hysteretic behaviour. It includes 16 parameters for the definition of the backbone curve ($ePf1$, $ePd1$, $ePf2$, $ePd2$, $ePf3$, $ePd3$, $ePf4$, $ePd4$, $eNf1$, $eNd1$, $eNf2$, $eNd2$, $eNf3$, $eNd3$, $eNf4$, $eNd4$), 6 parameters for defining the cyclic behaviour ($rDispP$, $rDispN$, $rForceP$, $rForceN$, $uForceP$ and $uForceN$), 5 parameters for governing the strength degradation ($gF1$, $gF2$, $gF3$, $gF4$, $gFLim$), 5 parameters for controlling the unloading stiffness degradation ($gK1$, $gK2$, $gK3$, $gK4$, $gKLim$), 5 parameters for controlling the reloading stiffness degradation ($gD1$, $gD2$, $gD3$, $gD4$, $gDLim$) and 2 parameters for limiting the maximum degradation in each cycle (gE , $dmgType$). The key parameters used in this study to define *Pinching4 material* are illustrated in Figure 4. These parameters are selected based on available experimental results [7]. Out of the 39 parameters required for definition of *Pinching4 material*, only 22 parameters are calibrated to represent the wall behaviour in this study. The calibration process of these parameters is explained in following passages. The rest of 17 parameters representing the strength and stiffness degradation in hysteretic behaviour are taken as 0, because this type of degradation behaviour was not observed during the experiment and is not significant for the investigated system.

In particular, the material law is defined by a 4-points multi-linear backbone envelope in both positive and negative directions, which is calibrated on the basis of experimental results. In Figure 4, points ($ePd1$, $ePf1$) to ($ePd4$, $ePf4$) and ($eNd1$, $eNf1$) to ($eNd4$, $eNf4$) represent the positive and negative branch of the backbone envelope curve in terms of stress and strain, respectively. This 4-points backbone curve is adjusted to capture entire envelope of hysteretic behaviour. First and second point of the backbone curve lies within elastic limit, third point represents the wall strength and fourth point is used to capture the post peak behaviour. Theoretically, there should be no energy dissipation until wall is in linear state, but experimental results showed non-linear behaviour from start. In order to catch this type of behaviour, the first point of the backbone curve is positioned at 50% strength of the second point where the second point corresponds to the elastic limit. The third point is the maximum strength achieved in experimental results. Experimental results also showed a vertical drop of strength after the peak. This decreasing of strength may lead to convergence problems in numerical analysis. Therefore, last branch of the backbone curve is aligned with little positive slope downwards using fourth point on backbone.

Eqs. 6 to 8 are used to transform force and displacement from experimental results into stress and strain of *Pinching4 material* used in the numerical model.

$$f = \frac{F}{\cos(\theta)} \quad (6)$$

$$\delta = \Delta \cos(\theta) \quad (7)$$

$$strain = \frac{\delta}{l} = \frac{\Delta \cos(\theta)}{l} \quad (8)$$

where, F is the force applied during the test, Δ is the top wall displacement recorded during the test, f is the stress in a strap of unit area, δ is the axial deformation in the strap, l is the length of the strap and θ is the angle of the diagonal strap respect to bottom track.

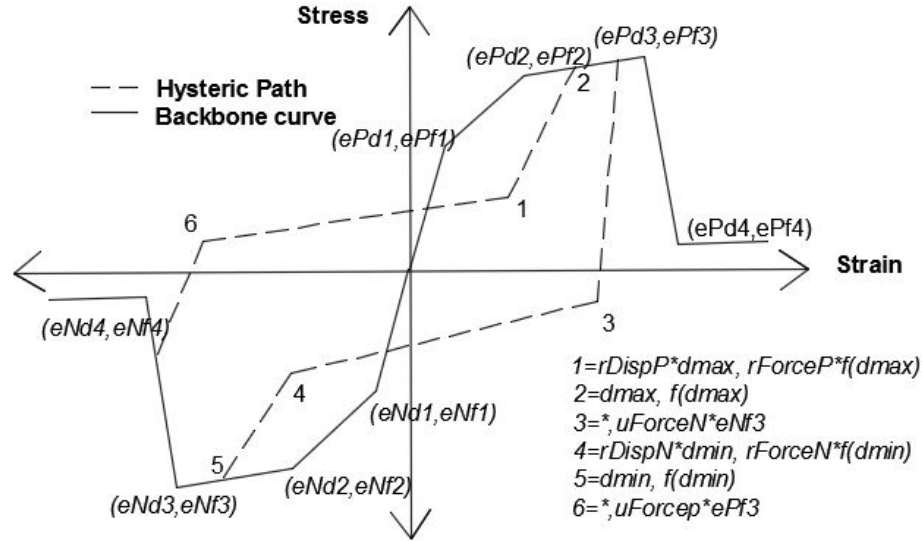


Figure 4. OpenSees Definition of Pinching4 Material

Unloading and reloading paths are controlled by series of force and displacement ratios, which include positive and negative $uForce$, $rDisp$ and $rForce$ parameters. As regards positive branches, $uForceP$ defines the ratio between the strength developed upon unloading and maximum strength of the positive backbone curve. $rDispP$ and $rForceP$ mark the strength and displacement at which reloading occurs. In particular, $rForceP$ is the ratio between the strength of reloading point and strength at maximum positive displacement of preceding cycles. $rDispP$ is the ratio between the displacement of the reloading point and maximum positive displacement of preceding cycles. Obviously, same definitions apply for negative branches ($uForceN$, $rDispN$, $rForceN$).

For proposed models, symmetric values of all parameters are used for both negative and positive branches of hysteric path. In particular, $uForce$, $rDisp$ and $rForce$ are selected and calibrated in a way to achieve good match with respect to experimental results, in terms of force vs. displacement relationship and dissipated energy. Since in experimental results unloading branch nearly approaches zero for all cycles, therefore $uForce$ is taken equal to 0. The reloading points on experimental curves are characterized by very low values of force, therefore $rForce$ is set equal to 0.01 ($rForce$ needs to be more than 0). Conversely, $rDisp$ is calibrated by varying the values in the range from 0.60 to 0.90 and selecting the value that minimizes, for each test, the square error in terms of dissipated energy. The obtained values for $rDisp$ are 0.80 and 0.70 for WLD and WHD wall configurations, respectively. Table 4 summarizes the properties of *Pinching4 material* used for WLD and WHD wall configurations. As stated earlier that two identical sets of experimental results C1 and C2 are available for both WLD and WHD wall configurations from the cyclic tests performed by Iuorio et al. [7], therefore a numerical model is developed for each set.

4. COMPARISON BETWEEN NUMERICAL MODELS AND EXPERIMENTAL RESULTS

Numerical results are compared with experimental ones both in terms of force vs. displacement response curves and energy dissipation. Numerical forces and displacements of walls are measured by a set of recorders in OpenSees and post processed with MATLAB subroutine to plot different parameters.

Figures 5 and 6 illustrate force vs displacement response curves of both numerical models and experimental results along with the comparison of typical small and large amplitude cycles for WLD-C1 and WLD-C2 walls. It can be seen that numerical models are able to capture experimental hysteretic response in terms of overall shape and location of peaks. Adjustment of the first point of the backbone curve in mid of second point allowed the numerical models to capture the non-linear response observed from beginning of experimental response.

Figure 7 and 8 illustrate force vs displacement response curves of both numerical models and experimental results along with the comparison of typical small and large amplitude cycles for the WHD-C1 and WHD-C2 walls. Also, in this case numerical models are able to capture experimental hysteretic response in terms of overall shape and location of peaks with minute differences. It has to be noticed that, in the test of WHD-C2 wall the net section failure occurred in one straps at cycle no. 40. This unpredicted phenomenon resulted in strength reduction of about 45% in negative phase of cyclic load for displacement more than 75 mm. Obviously, this brittle rupture cannot be accounted for by the numerical model.

Quantitative comparison of the energy dissipation of numerical and experimental results is made using Eqs. 6 to 9.

$$CE_{e,j} = \sum_{i=1}^j E_{e,i}, [i, j \leq n] \quad (9)$$

$$CE_{n,j} = \sum_{i=1}^j E_{n,i}, [i, j \leq n] \quad (10)$$

$$\Delta_{E,i} = \frac{E_{n,i} - E_{e,i}}{E_{e,i}} \times 100, [i \leq n] \quad (11)$$

$$\Delta_{CE,j} = \frac{CE_{n,j} - CE_{e,j}}{CE_{e,j}} \times 100, [j \leq n] \quad (12)$$

Where $CE_{e,j}$ and $CE_{n,j}$ represent the cumulative energy dissipated for j^{th} cycle of the loading protocol obtained accounting for numerical and experimental results, respectively; $E_{n,i}$ and $E_{e,i}$ represent the energy dissipated in i^{th} cycle of numerical and experimental results, respectively; $\Delta_{E,i}$ is the percentage difference of the energy dissipation for i^{th} cycle of loading protocol between numerical and experimental results; $\Delta_{CE,j}$ is the percentage difference of the cumulative energy for the j^{th} cycle of loading protocol between numerical and experimental results; n is the last cycle of the loading protocol.

Figures 9 and 10 show the comparison in terms of cumulative and cycle by cycle energy dissipation between the numerical and experimental results for the WLD-C1 and WLD-C2 walls, respectively. In case of trailing cycles of the loading protocol, the numerical model captures the energy dissipation quite well. For major primary cycles, the average of the absolute values of $\Delta_{E,i}$ is quite small and results 7.0% and 3.8% for WLD-C1 and WLD-C2 walls, respectively. A similar result is observed in terms of cumulative energy, with the average of the absolute values of the $\Delta_{CE,j}$ calculated for cycles from 32 to n equal to 8.9 % and 7.6% for WLD-C1 and WLD-C2 walls, respectively; whereas the error $\Delta_{CE,n}$ (at the n^{th} cycle) is about 2% for both walls.

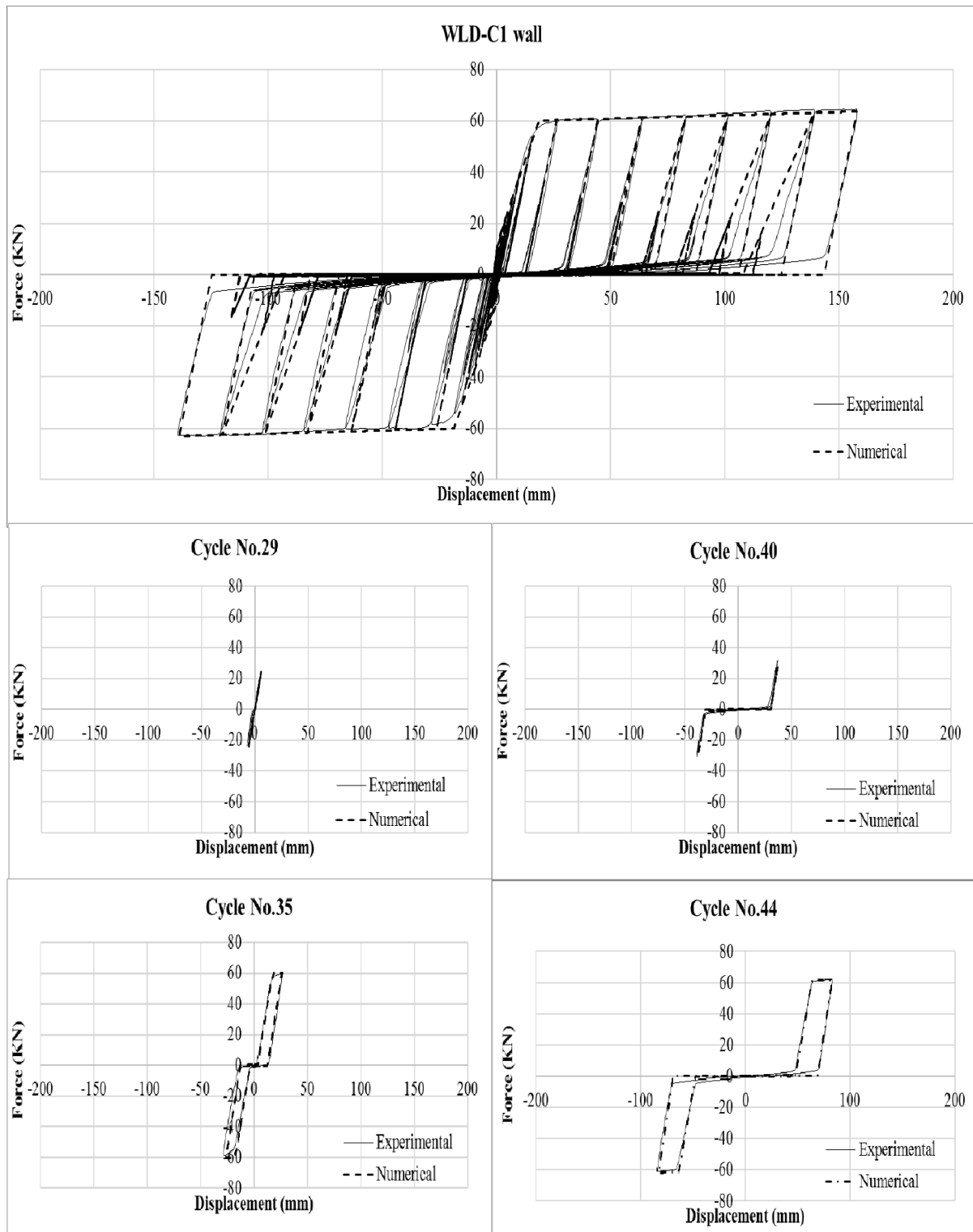


Figure 5. Comparison of Cyclic Force vs Displacement Diagrams of Numerical Models and Experimental Results for the WLD-C1 Wall

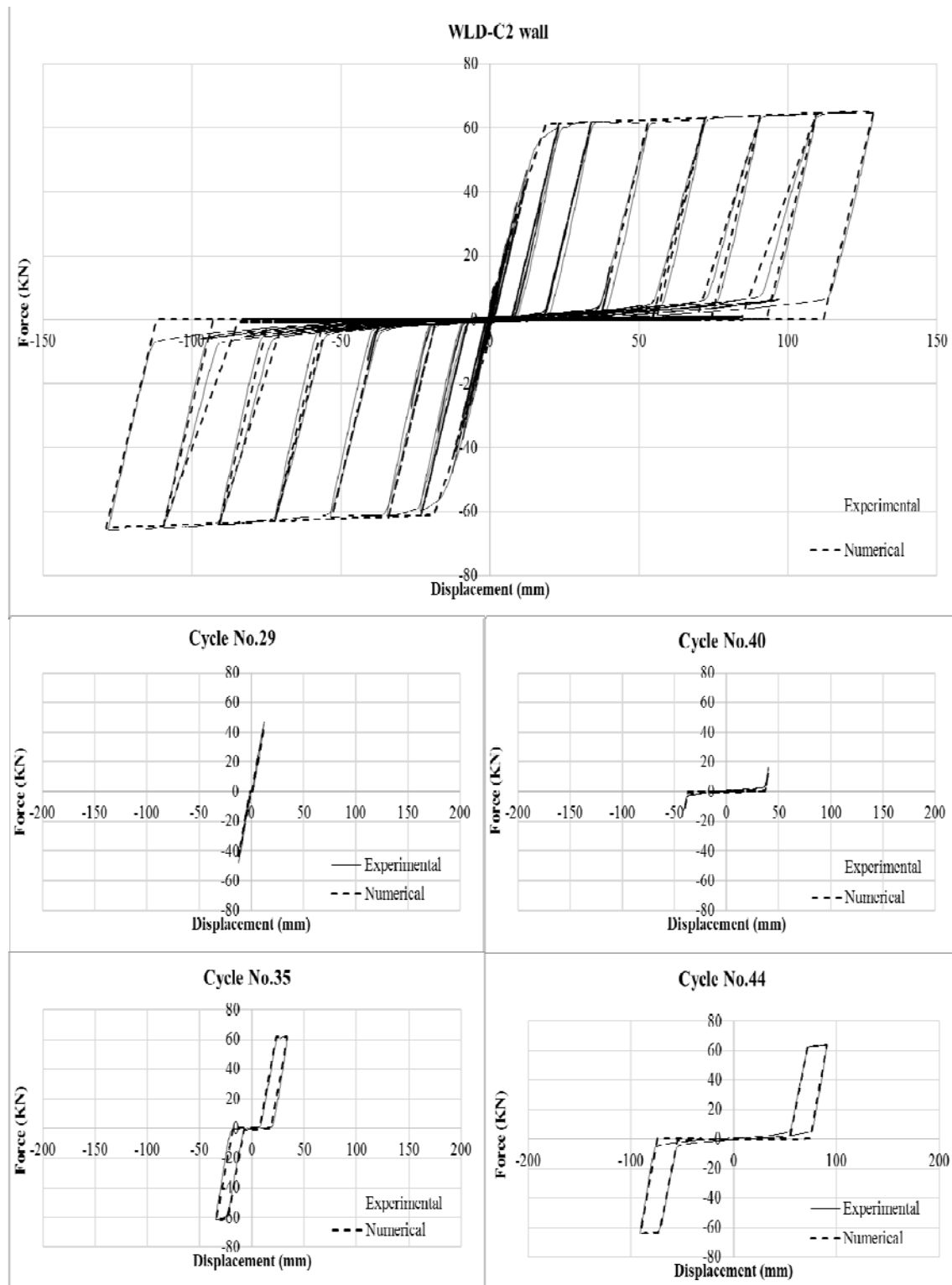


Figure 6. Comparison of Cyclic Force vs Displacement Diagrams of Numerical Models and Experimental Results of WLD-C2 for Wall

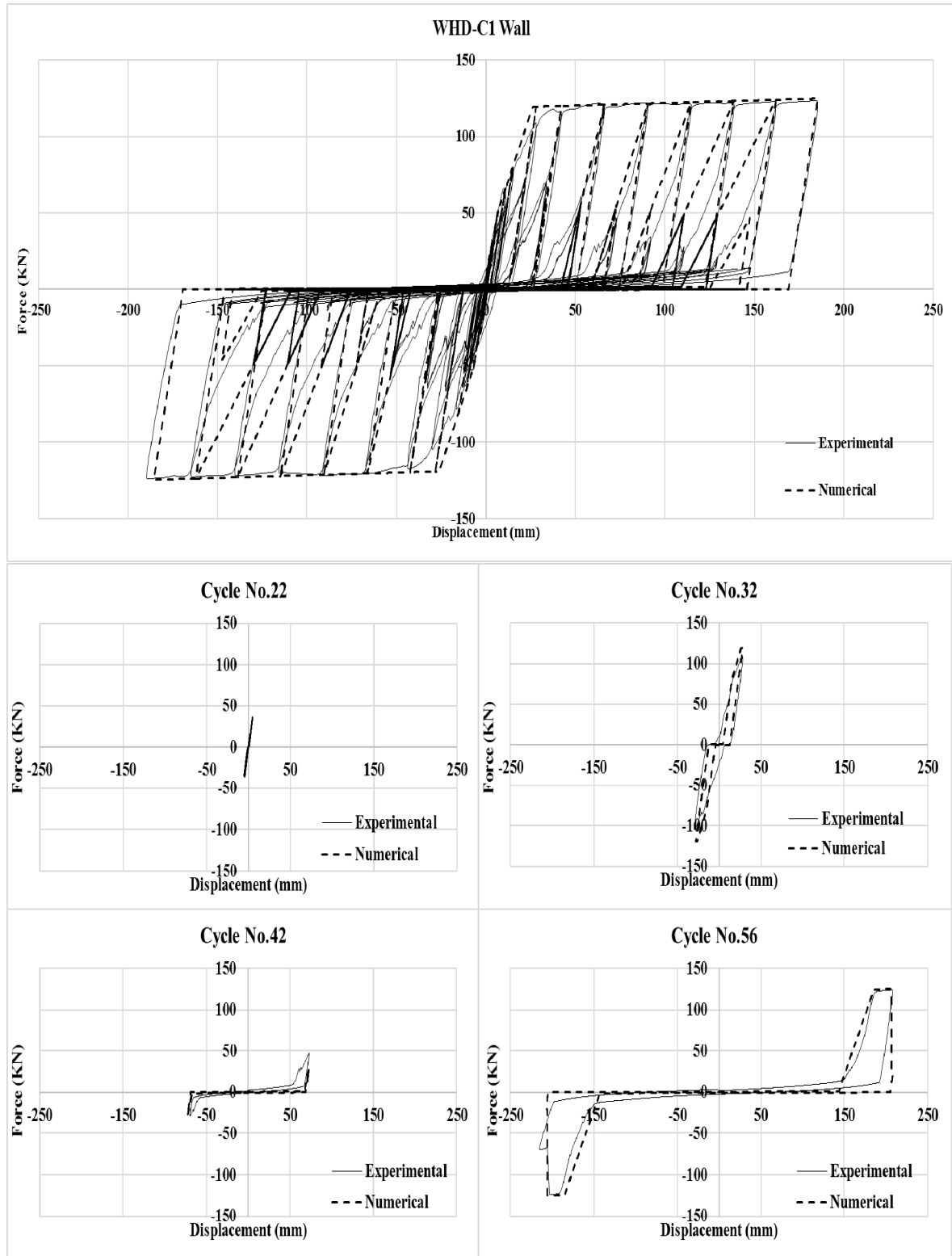


Figure 7. Comparison of Cyclic Force vs Displacement Diagrams of Numerical Models and Experimental Results for WHD-C1 Wall

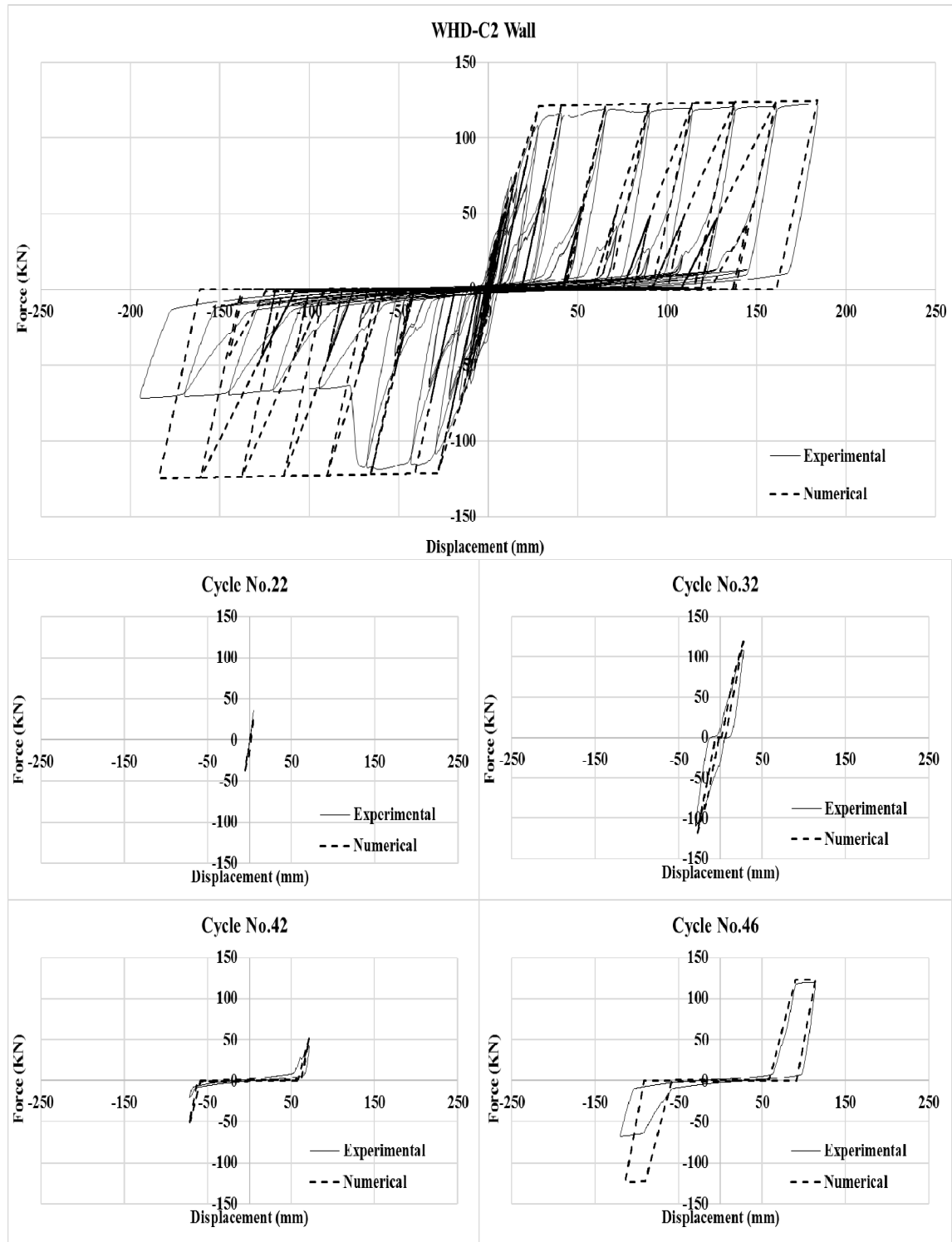


Figure 8. Comparison of Cyclic Force vs Displacement Diagrams of Numerical Models and Experimental Results for WHD-C2 Wall

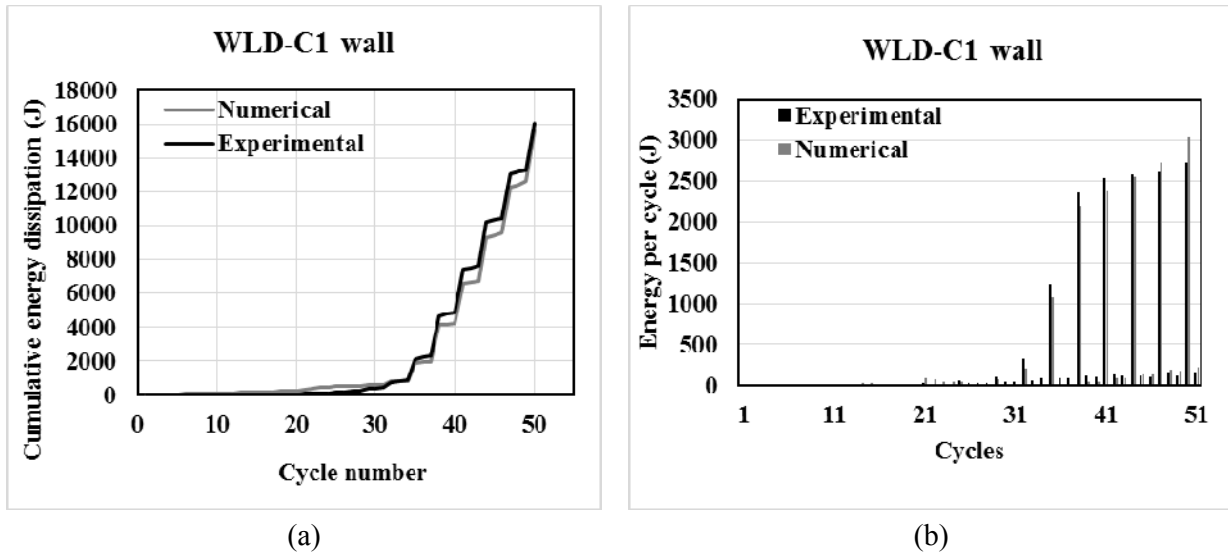


Figure 9. Comparison of a) Cumulative Energy Dissipation of Experimental and Numerical Results for the WLD-C1 Wall b) Cycle by Cycle Energy Dissipation of Experimental and Numerical Results for the WLD-C1 Wall

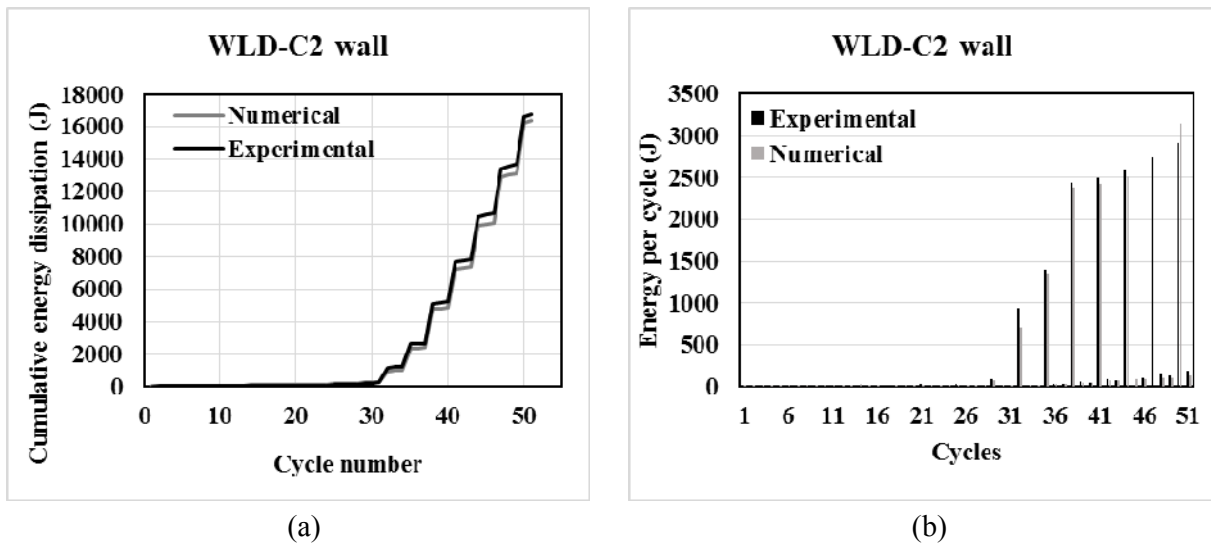


Figure 10. Comparison of a) Cumulative Energy Dissipation of Experimental and Numerical Results for the WLD-C2 Wall b) Cycle by Cycle Energy Dissipation of Experimental and Numerical Results for the WLD-C2 Wall

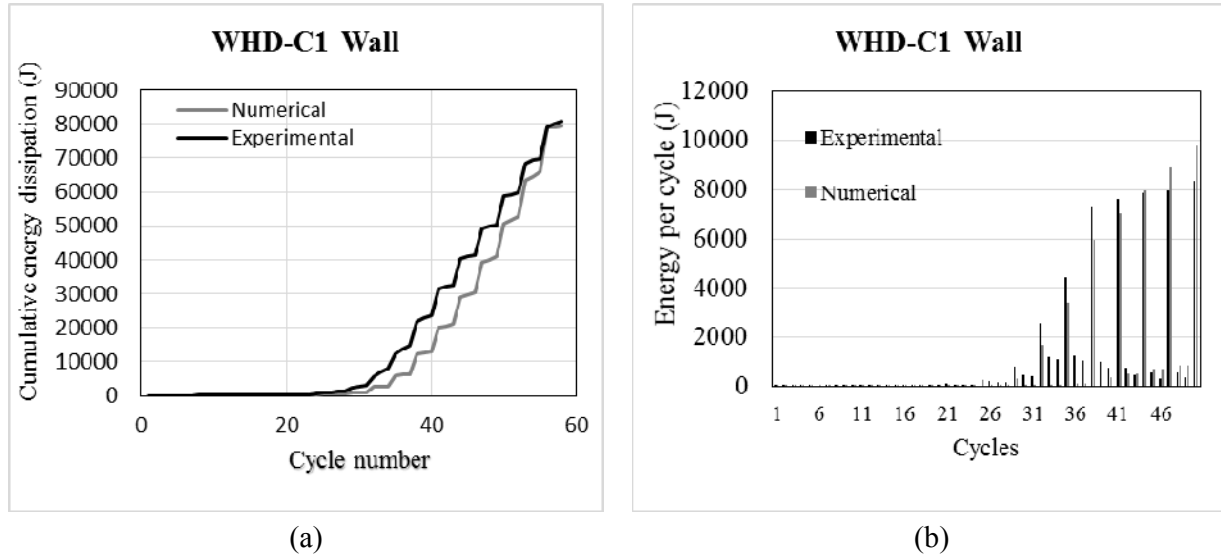


Figure 11. Comparison of a) Cumulative Energy Dissipation of Experimental and Numerical Results for the WHD-C1 Wall b) Cycle by Cycle Energy Dissipation of Experimental and Numerical Results for the WHD-C1 Wall

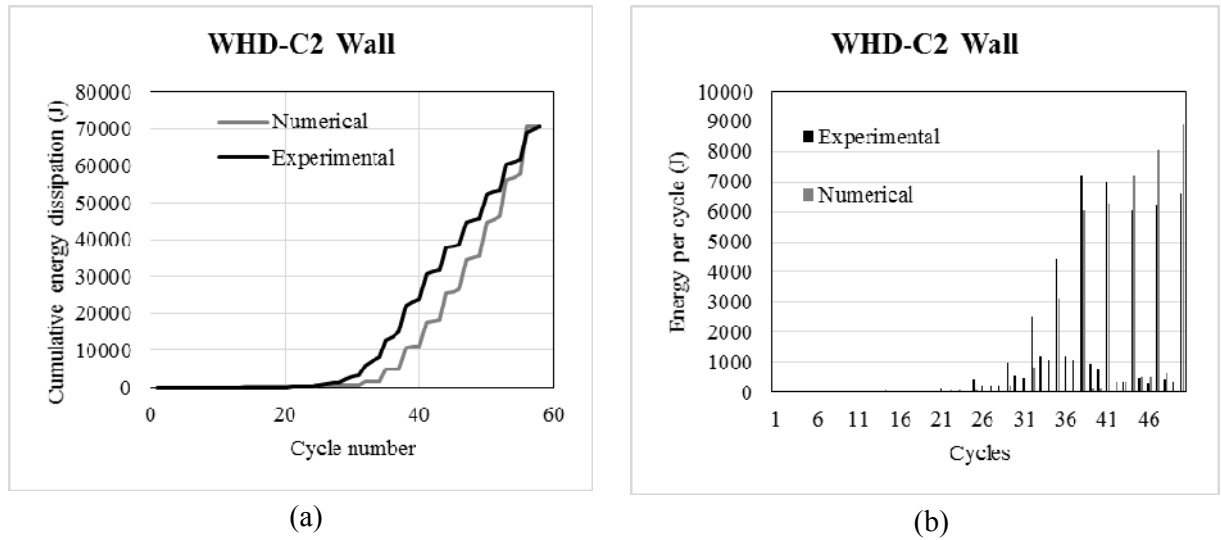


Figure 12. Comparison of a) Cumulative Energy Dissipation of Experimental and Numerical Results for the WHD-C2 Wall b) Cycle by Cycle Energy Dissipation of Experimental and Numerical Results for the WHD-C2 Wall

As far as WHD-C1 and WHD-C2 walls are concerned, the comparison between cumulative and cycle by cycle energy dissipation for the numerical model and experimental results is shown in Figures 11 and 12, respectively. Energy dissipation in trailing cycles between 31 and 42 is underestimated by the numerical model. For these cycles, experiment results depicted an increase in the area of hysteretic loops, which is not properly captured by the numerical model. This difference can be seen in the plot of the cycle 42 in Figure 7. On the contrary, for trailing cycles after the 42nd, the experimental dissipated energy decreases, whereas the numerical one increases. The comparison of the dissipated energy in major primary cycles shows higher differences respect to the WLD configuration. Indeed, the average of the absolute values of $\Delta E_{e,i}$ is 13.2% and 23.2 for WHD-C1 and WHD-C2 walls, respectively. In terms of cumulative energy, the average of the

absolute values of $\Delta_{CE,j}$ calculated for cycles from 32 to n is 29.2 % and 34.6% for WHD-C1 and WHD-C2 walls, respectively. A small difference is observed for $\Delta_{CE,n}$ at the n^{th} cycle, which is less than 2% for both walls. Overall, it can be noted that energy dissipated in numerical models is in a quite good agreement with the experimental results.

5. HYSTERETIC MODEL BASED ON THEORETICAL PREDICTION OF THE BACKBONE RESPONSE CURVE

In this section, a comparison between the numerical models calibrated using a theoretical approach and experimental results is presented. Motivation behind this comparison is to check the possibility to use a theoretical prediction procedure for backbone curve of the *pinching4* material for walls, which would not have any experimental results available.

Table 3. Nominal and Design Values of Wall Lateral Strength Associated with each Wall Component

Strength Associated with each component	WLD		WHD	
	Nominal Resistance (KN)	Design Resistance (KN)	Characteristic Resistance (KN)	Design Resistance (KN)
Hc,d^a	42.84	42.84	85.68	85.68
Hc,c^b	92.59	74.07	183.50	146.80
Hc,g^c	137.67	110.13	216.61	173.29
Hc,s^d	137.53	137.53	346.81	346.81
Hc,d^e	110.50	110.50	323.98	323.98
Hc,a^f	87.21	69.77	140.54	112.44
Hc^g	42.84	42.84	85.68	85.68

- a. wall strength associated to the yielding of steel straps.
- b. wall strength associated to the diagonal to strap connection
- c. wall strength associated to the net failure of strap connections
- d. wall strength associated to the buckling of studs
- e. wall strength associated to the buckling of tracks
- f. wall strength associated to the tension and shear anchors
- g. minimum wall strength

The theoretical backbone curve of the wall is based on the prediction of only three structural response parameters: (1) wall strength; (2) wall stiffness; and (3) ultimate displacement. Therefore, an elastic perfectly plastic backbone (without hardening) curve having a limited plastic branch is adopted for the theoretical approach. Wall strength and stiffness are evaluated according to the procedure described in [5], by using experimental mechanical properties of materials and components obtained in [7]. Values of theoretical wall strength and stiffness for WLD and WHD wall configurations are given in Table 3.

Figure 13 illustrates the comparison between theoretical and experimental backbone curves for WLD and WHD wall configurations. In particular, the first point of the theoretical backbone curve is positioned at the middle of the elastic branch defined by the theoretical predicted stiffness, whereas the second point is positioned at the end of elastic branch, defined by the theoretical predicted wall strength. The third point is defined by the theoretical predicted wall strength and a displacement corresponding to the 5% of the inter-story drift ratio. Finally, the fourth point defines the vertical drop of strength after the displacement corresponding to the 5% inter-story drift ratio.

The parameters governing cyclic behaviour ($uForce$, $rForce$ and $rDisp$) are set equal to those give in Table 4, obtained by the calibration of the model on the basis of the experiment results. Based on theoretical backbone curves, numerical models of two walls are analysed again, and their performance is checked in terms of force-displacement response curves and cumulative energy dissipation. Numerical results based on theoretical backbone curve predictions is then been compared with available experimental results.

Table 4. Pinching04 Material properties for tested walls

Wall ID	WLD-C1	WLD-C2	WHD-C1	WHD-C2
Parameters for backbone curve				
ePf1 (N/mm²)	45150	45150	75250	90301
ePf2 (N/mm²)	89548	90301	177591	180601
ePf3 (N/mm²)	97826	99331	186621	186621
ePf4 (N/mm²)	7525	7525	30100	7525
ePd1 (mm/mm)	0.00092	0.00110	0.00074	0.00147
ePd2 (mm/mm)	0.00276	0.00276	0.00368	0.00405
ePd3 (mm/mm)	0.02851	0.02538	0.03679	0.03623
ePd4 (mm/mm)	0.02869	0.02557	0.03697	0.03642
Parameters for cyclic behavior				
uForce	0.00	0.00	0.00	0.00
rDisp	0.80	0.80	0.70	0.70
rForce	0.01	0.01	0.01	0.01

From Figure 14, it can be noticed that numerical models obtained on the basis theoretical backbone curves are able to represent the cyclic behaviour of walls with good accuracy. Test results showed more strength as compared numerical model based on theoretical backbone curves. This difference can be attributed to the strain hardening of the material. In fact, experimental tests on WLD and WHD wall configurations showed a strength hardening of 8.5% and 4.0%, respectively, which is not accounted for by the theoretical backbone curve. Therefore, the absence of strength hardening in backbone curves results in the underestimation of strength and energy dissipation.

Figure 15 illustrates the comparison of cumulative energy dissipation for WLD and WHD wall configurations. Numerical models based on the theoretical backbone curves of both wall generally underestimates the energy dissipation with respect to the experimental results. In particular, for WLD walls, the average of the absolute values of $\Delta E_{e,i}$ considering major primary cycles is 17.0% and 24.3% for WLD-C1 and WLD-C2 walls, respectively. Similar values are obtained for the mean of the absolute values of the cumulative energy error $\Delta_{CE,j}$ (from 32 to n), which are equal to 21.6 % and 14.3% for WLD-C1 and WLD-C2, respectively. The value of $\Delta_{CE,n}$ at the n^{th} cycle ranges between 12% and 15%.

For the WHD wall configurations the comparison in terms of dissipated energy showed higher differences with respect to the WLD wall configurations. The average of the absolute values of $\Delta E_{e,i}$ is 21.6 % and 14.3% for WHD-C1 and WHD-C2 walls, respectively. In terms of cumulative energy, the average of the absolute values of $\Delta_{CE,j}$ calculated for cycles from 32 to n is 28.5 % and 31.8% for WHD-C1 and WHD-C2 walls, respectively. The value of $\Delta_{CE,\Delta}$ at the n^{th} cycle is equal to 18.5% and 28.2 for WHD-C1 and WHD-C2 walls, respectively. The largest differences in terms of cumulative dissipated energy observed in the comparison with WHD-C2 wall are related to brittle rupture during the test, which cannot be accounted in OpenSees. Overall, the adoption of a theoretical predicted backbone curve seems to be reasonable for use in numerical models, at least for preliminary assessment of the hysteretic response.

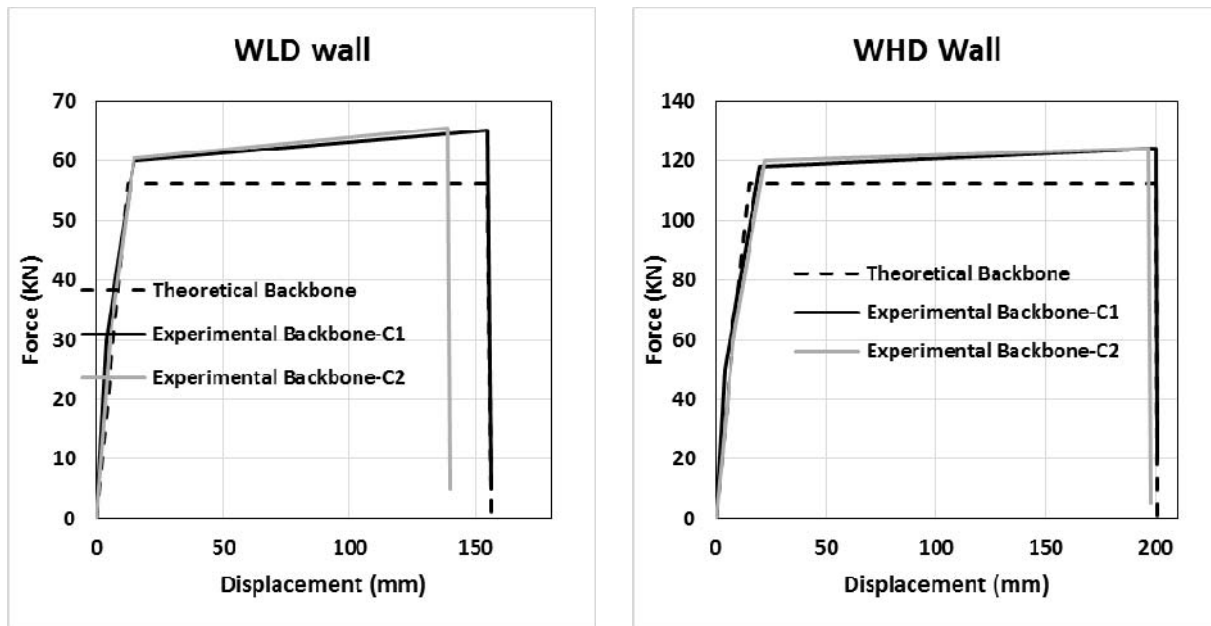


Figure 13. Comparison of Theoretical and Experimental Backbone Curve of WLD and WHD Wall Configurations

6. BRITTLE FAILURE MODES IN NUMERICAL MODEL

In order to show the ability of numerical models to capture brittle failure modes such as the tensile failure of tension anchors or buckling of chord studs, additional nonlinear cyclic analyses of walls with weak studs and anchors are performed. In fact, the walls modelled in this study are designed based on the capacity design approach, which ensures the ductile behaviour of system through proper over strength, it is not possible to observe any brittle failure modes in these walls. However, it is very important to ensure that the numerical models presented in this study are capable of simulating possible brittle failure modes for walls, which are not designed following the capacity design rules. In this context, two additional non-linear quasi static analyses are performed on WHD-C1 wall configuration with weak tension anchors and chord studs. Rest of the model parameters are same as that of experimentally calibrated WHD-C1 wall.

Anchors with 15% reduced tensile resistance $N_{a,Rk}$ corresponding to a wall strength $H_{c,a}$ of 140.5kN are used in a model with weak tension anchors. This resulted in tension anchor failing after the yielding of straps but prior to wall reaching its full ductility capacity. Failure is observed at a top wall displacement of 65mm in comparison with 200mm for wall designed based on capacity design rules. Figure 16 shows force vs displacement response curve of weak tension anchor model against the model designed based on capacity design rules.

Chord Studs with a 65% reduced buckling resistance $N_{b,Rk}$ corresponding to a wall strength of $H_{c,s}$ of 113.4kN are used in a weak stud model. This lead to buckling of chord studs after the yielding of straps and before the wall is able to reach its full ductility capacity. Failure occurred at a top wall displacement of 85mm in comparison with 200mm of wall designed following capacity design rules. Figure 17 shows the comparison of force vs displacement response curves of weak chord stud model against the model designed based on capacity design rules.

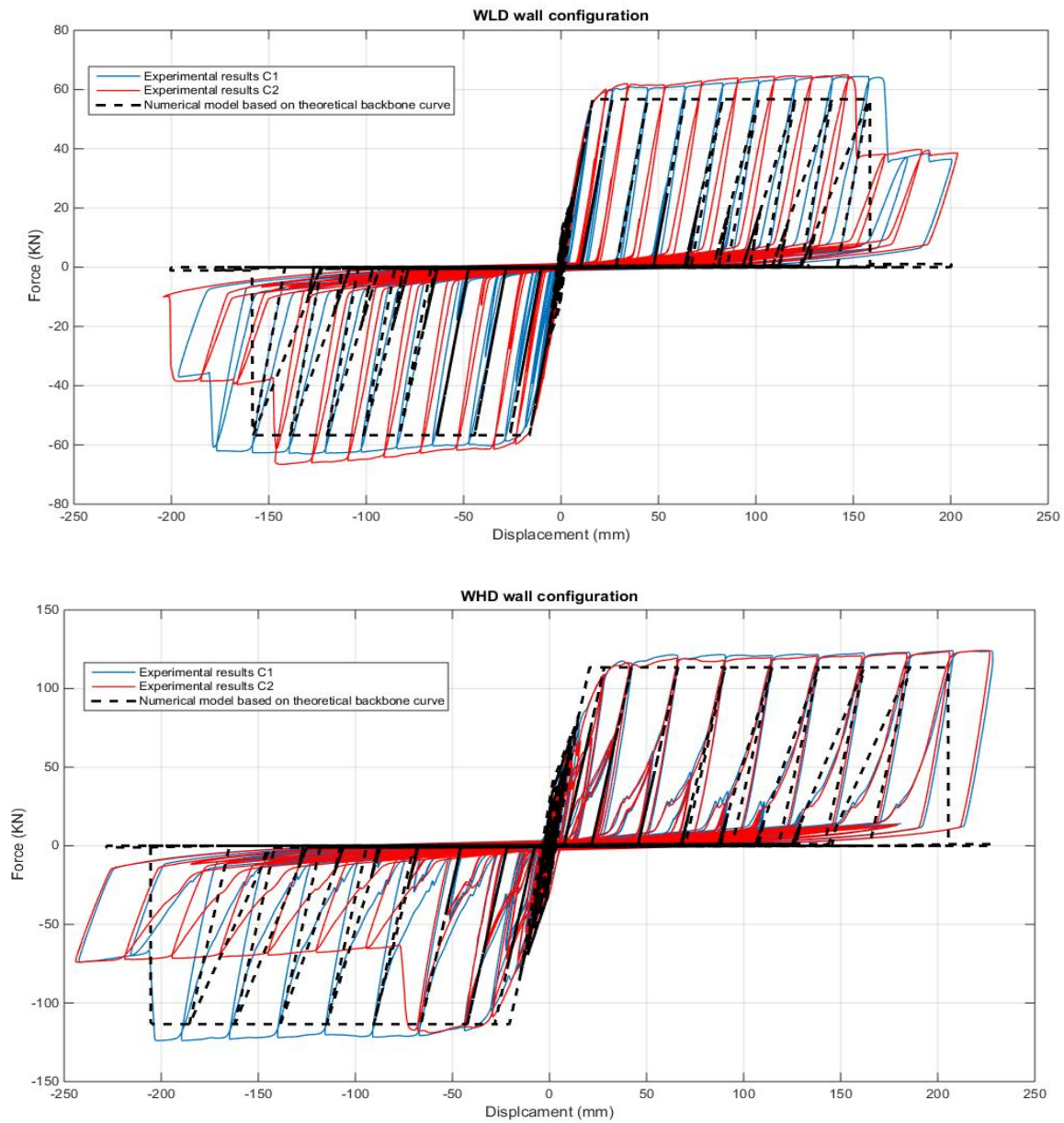


Figure 14. Comparison of Force vs. Displacement for WLD and WHD Walls

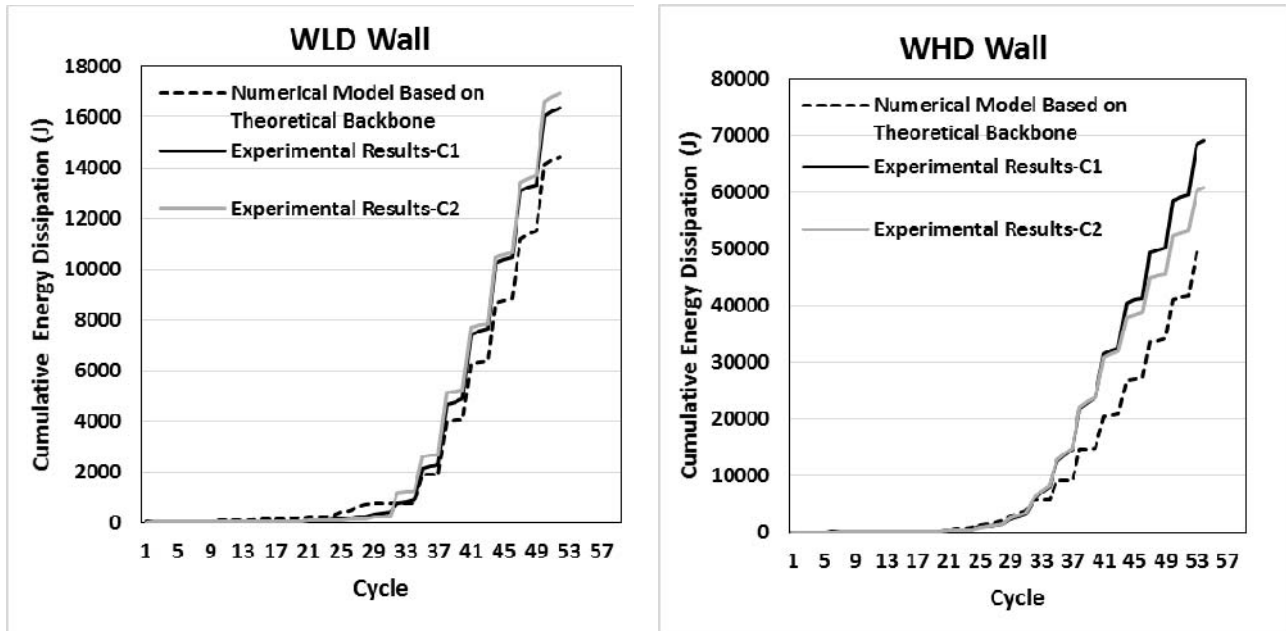


Figure 35. Comparison of Cumulative Energy Dissipation of WLD and WHD Walls

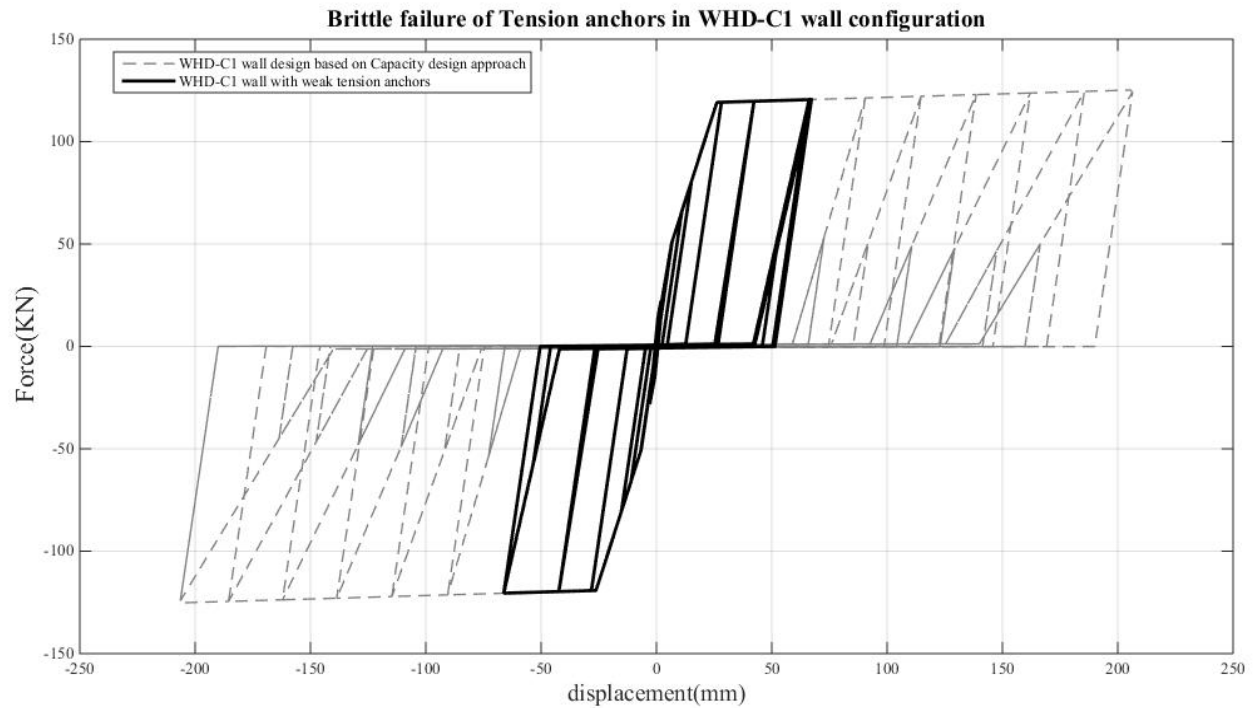


Figure 46. Force vs Displacement Response of Model with Weak Tension Anchors

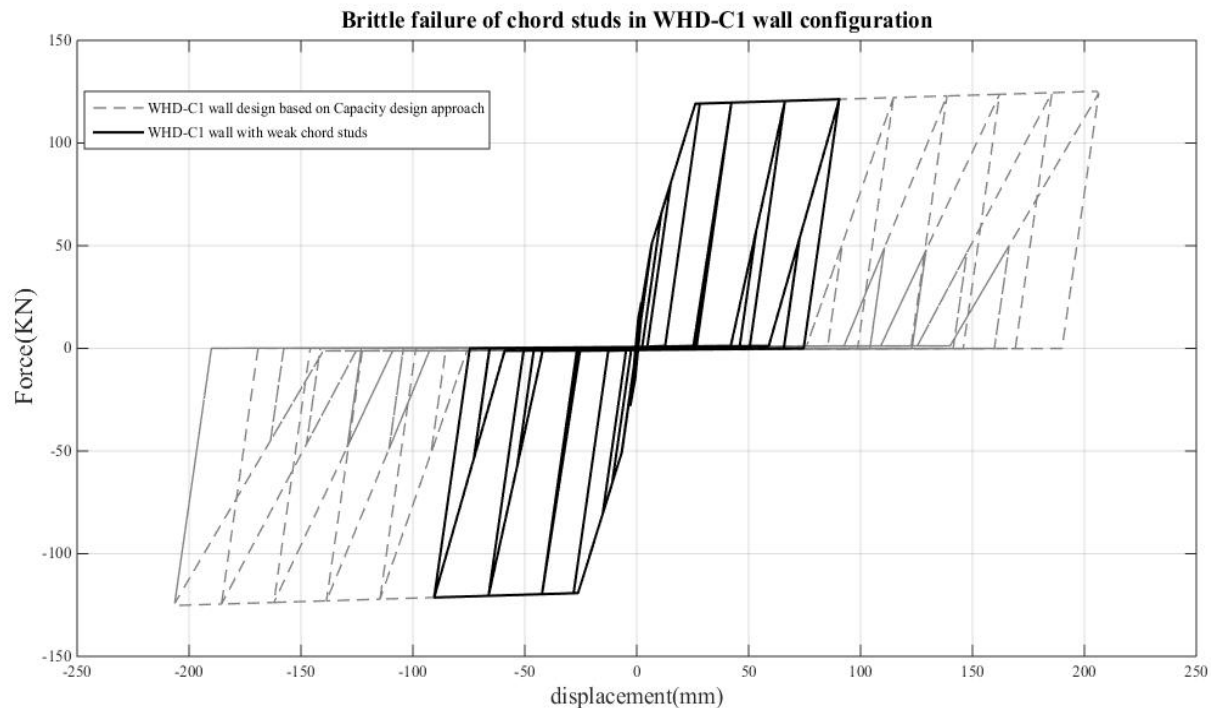


Figure 57. Force vs Displacement Response of Model with Weak Chord Studs

7. CONCLUSIONS AND FURTHER DEVELOPMENTS

In this paper development and calibration of numerical non-linear models in OpenSees using *Pinching4* material for CFS strap braced stud walls is explained. Models are calibrated based on available experimental results. The developed model accurately captures the hysteretic behaviour of CFS strap braced stud walls. A good agreement in terms of hysteretic force-displacement response curves and energy dissipation is observed between numerical models and test results. Moreover, capability of numerical models based on the theoretical prediction of backbone curves to simulate hysteretic behaviour of CFS strap braced stud walls is explored, in order to provide evidence of their adequacy for walls, which do not have any experimental results available. Finally, the proposed numerical model shows the ability to capture also brittle failure mechanisms due to the collapse of chord studs and tension anchors, which represent possible behaviour in the case of inadequate design approach. In future, these models will be utilized to perform non-linear analysis on 3D buildings in order to evaluate the behaviour factor according to FEMA P695.

ACKNOWLEDGEMENTS

The authors acknowledge *Italian Department of Civil Protection within RELUIS DPC 2014-2016* research project. This work has also been developed as thesis of European Erasmus Mundus master program on Sustainable Constructions under natural and catastrophic events (SUSCOS). Authors would also like to acknowledge European Commission (EACEA) for providing financial support.

REFERENCES

- [1] AISI-S400-15, "North American Standard for Seismic Design of Cold formed Steel Structural Systems," American Iron and Steel Institute (AISI), 2015.
- [2] Fiorino, L., Iuorio, O., and Landolfo, R., "Seismic Analysis of Sheathing-braced Cold-formed Steel Structures", *Engineering Structures*, 2011, Vol. 34, pp. 538–547.
- [3] Fiorino, L., Iuorio, O., Macillo, V. and Landolfo, R., "Performance-based Design of Sheathed cfs Buildings in Seismic Area", *Thin-Walled Structures*, 2012, Vol. 61, pp. 248–257.
- [4] Iuorio, O., Fiorino, L. and Landolfo, R., "Designing cfs Structures: The New School bfs in Naples", *Thin-Walled Structures*, 2014, Vol. 78, pp. 37–47.
- [5] Iuorio, O., Fiorino, L. and Landolfo, R., "Testing cfs Structures: The New School bfs in Naples", *Thin-Walled Structures*, 2014, Vol. 84, pp. 275–288.
- [6] Macillo, V., Iuorio, O., Terracciano, M.T., Fiorino, L. and Landolfo, R., "Seismic Response of cfs Strap-braced Stud Walls : Theoretical Study", *Thin Walled Structures*, 2014, Vol. 85, pp. 301–312.
- [7] Iuorio, O., Macillo, V., Terracciano, M.T., Pali, T., et al., "Seismic Response of cfs Strap-braced Stud Walls: Experimental Investigation", *Thin-Walled Structures*, 2014, Vol. 85, pp. 466–480.
- [8] CEN, "EN 1998-1 Eurocode 8: Design of Structures for Earthquake Resistance-Part 1: General Rules, Seismic Actions and Rules for Buildings", European Committee for Standardization, Brussels, 2004.
- [9] Fiorino, L., Iuorio, O., Macillo, V., Terracciano, M.T., et al., "Seismic Design Method for cfs Diagonal Strap-braced Stud Walls: Experimental Validation", *Journal of Structural Engineering*, 2015, No. 4015154.
- [10] AISI-S213-07, "North American Standard for Cold-Formed Steel 2007 Edition with Supplement No.1", Vol. 9, American Iron and Steel Institute (AISI), Washington, DC 2010.
- [11] Mazzoni, S., McKenna, F., Scott, M.H., and Fenves, G.L., "Open System for Earthquake Engineering (OpenSees)" n.d.
- [12] Lowes, L.N., Mitra, N. and Altoontash, A., "A Beam-column Joint Model for Simulating the Earthquake Response of Reinforced Concrete Frames a Beam-column Joint Model for Simulating the Earthquake Response of Reinforced Concrete Frames," Berkeley 2004.
- [13] Pastor, N. and Rodríguez-Ferran, A., "Hysteretic Modelling of x-braced Shear Walls", *Thin-Walled Structures*, 2005, Vol. 43, pp. 1567–1588.
- [14] Kim, T., Wilcoski, J. and Foutch, D.A., "Analysis of Measured and Calculated Response of a Cold-formed Steel Shear Panel", *Journal of Earthquake Engineering*, 2007, Vol. 11, pp. 67–85.
- [15] Rakesh Allahabadi, G.H.P., "Drain-2dx", 1988.
- [16] Kim, T.-W., Wilcoski, J., Foutch, D.A. and Lee, M.S., "Shaketable Tests of a Cold-formed Steel Shear Panel", *Engineering Structures*, 2006, Vol. 28, pp. 1462–1470.
- [17] Comeau, G., Velchev, K. and Rogers, C.A., "Development of Seismic Force Modification Factors for Cold-formed Steel Strap Braced Walls", *Canadian Journal of Civil Engineering*, 2010, pp. 236–249.
- [18] Federal Emergency Management Agency (FEMA), "Quantification of Building Seismic Performance Factors", Washington, DC, USA 2009.
- [19] Carr, A.J., "Ruaumoko", 2000.
- [20] Mirzaei, A., Sangree, R.H., Velchev, K., Comeau, G., et al., "Seismic Capacity-based Design of Narrow Strap-braced Cold-formed Steel Walls", *Journal of Constructional Steel Research* 2015, Vol. 115, pp. 81–91.
- [21] Gad, E.F., Chandler, A.M., Duffield, C.F. and St, G., "Lateral Behavior of Plasterboard -clad Residential Steel Frames", *Journal of Structural Engineering*, 1999, pp. 125.

- [22] Swanson Analysis Systems Inc. (SASI), “Ansys” 1994.
- [23] Barton, A.D., “Performance of Steel Framed Domestic Structures Subjected to Earthquake Loads”, Faculty of Engineering, Civil and Environmental Engineering, University of Melbourne, 1997.
- [24] Zeynalian, M. and Ronagh, H.R., “Thin-walled Structures a Bumerical Study on Seismic Performance of Strap-braced Cold-formed Steel Shear Walls”, *Thin Walled Structures*, 2012, Vol. 60, pp. 229–238.
- [25] Shamim, I. and Rogers, C. a., “Steel Sheathed/cfs Framed Shear Walls under Dynamic Loading: Numerical Modelling and Calibration”, *Thin-Walled Structures*, 2013, Vol. 71, pp. 57–71.
- [26] Shamim, I. and Rogers, C.A., “Numerical Evaluation: aisi s400 Steel-sheathed cfs Framed Shear Wall Seismic Design Method”, *Thin-Walled Structures*, 2015, Vol. 95, pp. 48–59.
- [27] Leng, J., Schafer, B.W. and Buonopane, S.G., in: *Struct. Stab. Res. Counc. Annu. Stab. Conf.* 2013, SSRC 2013, 2013, pp. 426–442.
- [28] Liu, P., Peterman, K., Yu, C. and Schafer, B., in: 2012.
- [29] Kechidi, S. and Bourahla, N., “Deteriorating Hysteresis Model for Cold-formed Steel Shear Wall Panel based on its Physical and Mechanical Characteristics”, *Thin-Walled Structures*, 2016, Vol. 98, No. 421–430.
- [30] CEN, “EN1993-1-1 Eurocode 3 : Design of Steel Structures -Part 1-1: General Rules and Rules for Buildings”, European Committee for Standardization, Brussels 2005.
- [31] CEN, “En 1993-1-3 Eurocode 3: Design of Steel Structures-part 1-3: General Rules-supplementary Rules for Cold-formed Members and Sheetting”, 2006, Vol. 3.
- [32] Krawinkler, H., Francisco, P., Ibarra, L., Ayoub, A. and Medina, R., “CUREE Publication No. W-02 Development of a Testing Protocol for Woodframe Structures,” 2001.
- [33] Velchev, K., Comeau, G., Balh, N. and Rogers, C.A., “Evaluation of the aisi s213 Seismic Design Procedures through Testing of Strap Braced Cold-formed Steel Walls”, *Thin-Walled Structures*, 2010, Vol. 48, pp. 846–856.

PANEL ZONE MODELLING OF BOX COLUMNS: AN ANALYTICAL AND NUMERICAL APPROACH

F.J. Paghale, H. Saffari* and A. Fakhraddini

Department of Civil Engineering, Shahid Bahonar University of Kerman, P.O. Box 76175-133, Kerman, Iran

**(Corresponding author: E-mail: hsaffari@uk.ac.ir)*

Received: 14 February 2016; Revised: 28 March 2017; Accepted: 15 July 2017

ABSTRACT: Panel zone is a region of the column which is bounded by the column flanges and continuity plates and plays a vital role in determining stiffness and capacity of the frame. Despite the extensive researches conducted on the panel zone behavior, there are different viewpoints on how panel zones function. Since box columns are used widely in the moment-resisting frames, presentation of a mathematical model for the panel zone behavior for these columns seems essential. This study attempts to present some relations in order to determine the shear capacity, the linear stiffness and non-linear stiffness of the panel zones in the box columns. For this purpose, a comprehensive parametric study is conducted, using the ABAQUS software; accordingly, a mathematical model is introduced. Then, the results of the mathematical model are compared with the results of other sources, and the accuracy of the obtained results of the model is proved.

Keywords: Mathematical model, panel zone, box column, moment-resisting frame, steel structures

DOI: 10.18057/IJASC.2018.14.3.3

1. INTRODUCTION

Moment resisting frames (MRFs) are one of the frequently used lateral load resisting systems that resist lateral forces through the flexural and shear strength of the beams and columns. One of the most important components of the MRFs is their connections; furthermore, the most prominent component of a flexural rigid connection is how to transfer the moment between the beam and the column. A rectangular zone of the column web, which is surrounded between the continuity plates and the column flanges has a significant role in the connection behavior; this zone is called the panel zone (see Figure. 1).

In lateral loadings like seismic conditions, the connection of the beam to the column in MRFs is extensively subjected to asymmetric moments, leading to shearing deformations in the column panel zones. The panel zone plays a vital role in general stiffness and capacity of the frame. In addition, the panel zone could have a significant effect on the distribution of plasticity and energy dissipation of the structure.

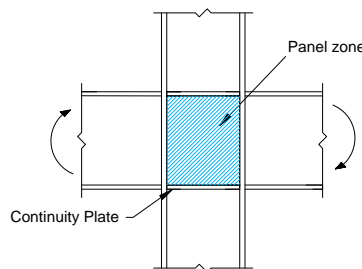


Figure 1. Geometry of a Panel Zone

2. A REVIEW ON MATHEMATICAL PANEL ZONE MODELS FOR H-SHAPED COLUMN

Previous studies show that the panel zone has ductile and stable behavior. In other words, when a MRF is subjected to lateral loads, huge shear forces are created in the panel zone and the resulted deflection can play an important role in the response of frame to both the elastic and inelastic cases.

Considering the aforementioned issues related to the panel zone, many researchers have been addressed to the study of the seismic behavior of the panel zone in the early 1970's; also for many years, the codes and instructions were presented with different equations related to the panel zone behavior. Most of the conducted researches have focused on the panel zone behavior of the I-shaped columns. Krawinkler *et al.* [1], Bertero *et al.* [2], and then Popov and Takhirov [3] showed that the panel zone has a high resistance even after yielding. High ductility, the stable hysteresis loops and the high cyclic work-hardening are some of the observations and findings of those researchers. The studies conducted after the 1994 Northridge earthquake showed that the panel zone's over-distortion could cause brittle fractures in welded of flange connections to column flange [4-9]. These studies led to determining new design criteria for the panel zone, which could consider a more real panel zone behavior and performance in response to the MRFs. The main problem was the suitable performance of the structures under the service and seismic loads. For this purpose, the presentation of a design, in which more contribution of the structure components to absorb energy is considered, seems essential because in case the structure remains in elastic range under seismic loads, it leads to high expenditure and the structure becomes uneconomical. On the other hand, to consider the inelastic behavior of the structure necessitates a full understanding of the performance and extensive studies in the subject. For this reason, the studies have focused on the better understanding of the inelastic behavior of the connections of the MRFs. To understand the effects of various loadings, different types of loadings were simulated in the experiments, whereby the gravity loads and the seismic cyclic loads were applied on the samples, and the effects of the axial loads on the performance of connections were considered in few cases. Based on the obtained results, the researchers suggested that the panel zone should be considered as an energy contributor while considering the yield mechanism that would be simultaneous to the beam mechanism [10].

As described before, the panel zone performance is important in the MRFs. Due to the high moment of the inertia of box sections in both directions, as well as the high torsional resistance, the box columns are vastly used in the MRFs. Therefore presenting a suitable design to describe the panel zone behavior in those columns seems essential. However, since most of the studies were conducted on the I-columns which they didn't had thick flanges. It is predicted that the existing relationships are not accurate enough to describe the panel zone behavior in the box columns. In this study, using the finite elements parametrically, the panel zone behavior in the box columns is studied. Based on the results, the mathematical models are proposed to be applied on the linear and non-linear behavior of the panel zone.

3. PANEL ZONE SHEAR STRENGTH CAPACITY IN THE AISC

In recent seismic criteria of the AISC Code of Standard Practice that is based on LRFD design, the design resistance of the panel zone is categorized based on the axial forces applied on the column as follows [11,12]:

a) When the effect of panel zone deformation on frame stability is not considered in the analysis:

i) for $P_r \leq 0.4 P_c$

$$R_n = 0.6 F_y d_c t_{cw} \quad (1)$$

ii) for $P_r > 0.4 P_c$

$$R_n = 0.6 F_y d_c t_{cw} \left(1.4 - \frac{P_r}{P_c} \right) \quad (2)$$

b) When frame stability, including plastic panel-zone deformation, is considered in the analysis:

i) for $P_r \leq 0.75 P_c$

$$R_n = 0.6 F_y d_c t_{cw} \left(1 + \frac{3b_{cf} t_{cf}^2}{d_b d_c t_{cw}} \right) \quad (3)$$

ii) for $P_r > 0.75 P_c$

$$R_n = 0.6 F_y d_c t_{cw} \left(1 + \frac{3b_{cf} t_{cf}^2}{d_b d_c t_{cw}} \right) \left(1.9 - \frac{1.2P_r}{P_c} \right) \quad (4)$$

In the above formulae, F_y is the yield stress of the column, d_c is the depth of the column section, and t_w is the web thickness of the column. In addition, b_{cf} is the flange width of the column, t_{cf} is the flange thickness of the column, and d_b is the beam depth. Moreover, P_r is the factored axial force of the column and P_c is the axial yield resistance of the column.

4. FINITE ELEMENT MODELS OF BOX COLUMN PANEL ZONE

To reach a suitable mathematical model, first an extensive parametric study regarding the effective factors on the behavior of panel zone is conducted out by ABAQUS [24] software. These parameters are: column flange thickness (t_{cf}), column web thickness (t_{cw}), beam flange thickness (t_{bf}) and axial force. All parametric studies were done for BSAC group, which represent a wide range of connections of different beam overall depths (from 450 to 912 mm). Details of these specimens are presented in Table 1. B-SAC specimens comprised of a built-up box-shape column and a wide flange I-shape beam. The connection details of these specimens are exactly the same as SAC specimens presented in [13], (i.e., all specimens have post-Northridge connection detail) except that the box shape columns have been used instead of I-shape columns. Box columns have the same flanges and webs used in SAC specimens presented in [13].

Table 1. BSAC Samples Specifications

Specimen	Type	Section/size(mm)	Yield stress (MPa)
BSAC3	Beam	W24×68	306
	column	Box (d=368, b=373, $t_f=24$, $t_w=7.4$)	318
BSAC5	Beam	W30×99	306
	column	Box (d=386, b=399, $t_f=33$, $t_w=11$)	318
BSAC7	Beam	W 36×150	306
	column	Box (d=417, b=406, $t_f=48$, $t_w=15$)	318

To consider the column web thickness effect in the reached model acquired by the software, the webs thickness sections have been multiplied by the coefficients of 1 and 0.75 in the Table 1. To consider the column flange effects, the thickness of the column flange have been multiplied by the coefficients of 0.5, 0.75, 1, and 1.25; and to consider the beam flange effects, the beam flange thicknesses have been considered to be 0.85, 1, 1.5, and 2 times the introduced sections in the Table 1. In addition, to consider the effect of the axial force, the axial force have been considered 0.0, 0.2, 0.5, 0.6, 0.75, 0.8, and 0.9 times of the yield axial force of the column. Therefore, the number of the built samples equaled 672 samples, that is $(3 \text{ samples}) \times (2 \text{ column web thicknesses}) \times (4 \text{ column flange thicknesses}) \times (4 \text{ beam flange thicknesses}) \times (7 \text{ axial force ratios})$. In Table 2, the connection details of the SAC samples are shown. Moreover, the details of the SAC7 sample are fully shown in Figure 2.

The ABAQUS software was used for modelling and Quadrilateral four-node shell elements (the S4R element) are used for constructing three-dimensional models of subassemblies. Shell element has been taken into account successfully by several researchers [7]. To reduce the computational efforts, dense meshes have been used in the panel zone region while the other regions have coarse meshes. Column flanges plate are modelled in 5 layers of elements. The free end of beam moves vertically under displacement control analysis. (see Figure 3)

Table 2. Connection Details of the SAC Samples [7]

specimen	Shear tab	No. of A325 SC Bolts (mm)	Continuity Plate (mm)	Weld type and size (mm)	
				Beam flange	Shear tab
SAC3	457X127X9.50	6Φ22	355X335X16	CJP, root opening = 9 mm, Angle = 30° and E70TG-	Fillet 8mm E70T-7
SAC5	610X127X12.70	8Φ25	375X345X19		Fillet 8mm E70T-8
SAC7	762X127X15.88	10Φ25	350X330X25		Fillet 8mm E70T-7

The considered analysis is non-linear static and it is introduced in the form of the General Static in the ABAQUS. Loading is considered as a monotonic displacement at the end of the beam and it is regarded 178 millimeters. The maximum imperfection value is considered with a factor of 1% of the beam flange thickness from first buckling mode [14-17] and distribution of geometric imperfections matched the first eigenvector of the loaded connection configuration. The supports of column ends are considered hinged (as in experiments). In all samples, the length of the beam is considered to be 3400 mm and the length of the column is considered to be 3650 mm. Two lines of nodes at each end of the column were restrained against translation only (i.e., a pinned connection) to approximately replicate the support conditions used for the laboratory tests [13]. The behavior of materials is considered using the Von Mises yield criterion and the materials non-linearity was considered according to the reference [13], along with the young modulus of 200000 MPa and the Poisson ratio of 0.3. Stress-strain diagram of steel is considered bilinear [13] as seen in Figure 4.

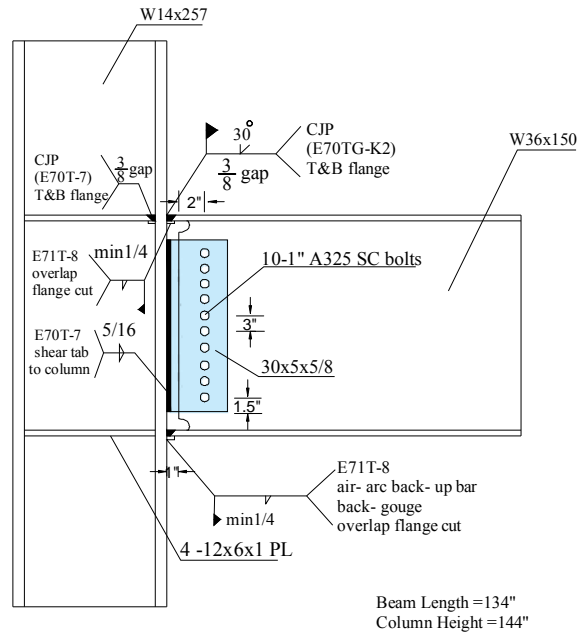


Figure 2. Details of the SAC7 Sample [13]

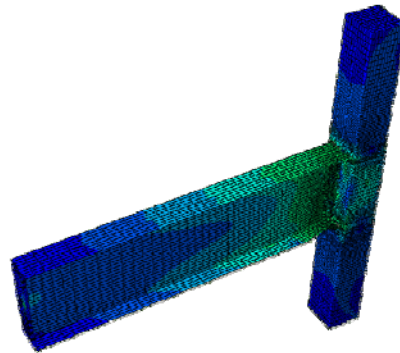


Figure 3. Finite Element Modeling

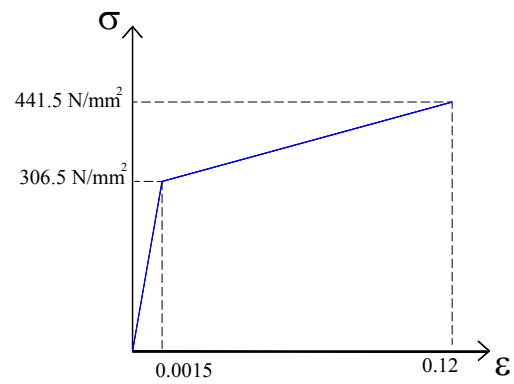


Figure 4. Stress-strain Diagram of Steel [13]

4.1 Shear Computing Method

To calculate the panel zone shear (V_{pz}) in the conducted modeling, the proposed relationship derived from the reference [18] have been used. In addition, to calculate the panel zone strain (γ), the proposed relationship derived from the reference [19] have been used.

$$V_{pz} = \frac{PL}{h_t} \left(1 - \frac{h_t}{H}\right) \quad (5)$$

$$\gamma = \frac{\Delta^+ - \Delta^-}{2} \frac{\sqrt{d_{pz}^2 + b_{pz}^2}}{d_{pz} b_{pz}} \quad (6)$$

In the above relationships, P is the applied force to the end of the beam, L is the distance between the applied force and the column face, h_t is the distance between the centers of the flanges of the beam, H is the height of the column, Δ^- and Δ^+ are the diagonal displacements of the panel zone, and d_{pz} and b_{pz} are the vertical and horizontal dimension of the panel zone, respectively (see Figure 6).

5. VERIFICATION STUDY

As validation is essential in numerical studies, specimen SP7 [13], is modeled by the ABAQUS software and compared with experimental results, before the main study in this research is being carried out. As seen from Figure 10, results of the SP7 specimen modeling in ABAQUS software are in a good agreement with the experimental results.

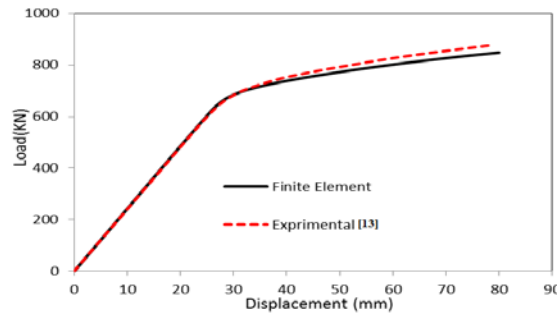


Figure 5. Comparing Experimental Results and Finite Element Results for SP7 Sample.

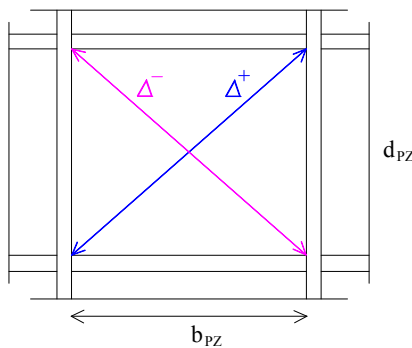


Figure 6. Geometry of Panel Zone to Determine Panel Zone Distortion [20]

6. PROPOSED MATHEMATICAL MODEL

6.1 Initial Stiffness of the Panel Zone

As shown in Figure 7, the panel zone behavior is modeled as a column which its supports have been shown in Figure 8.

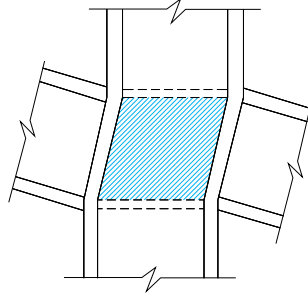


Figure 7. PZ Deformation caused by Applied Forces

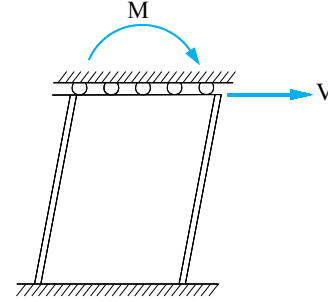


Figure 8. The Proposed Model of a PZ

To determine the initial stiffness of the panel zone, at first, a unit load is applied at the end of the panel zone in the horizontal direction and the correspondent displacement is obtained. Then, since the inverse of the obtained displacement is actually the stiffness, the panel zone initial stiffness is found by inverting the displacement. Therefore, first, the horizontal unit load is applied at the end of the panel zone, then the corresponding displacement (Δ) is obtained as follows;

$$\Delta = \frac{d_b^3}{12EI} + \frac{d_b}{\eta GA} \quad (7)$$

In the above relationship, d_b is the vertical distance between continuity plates of the panel zone, E is the elasticity modulus, I is the moment of inertia of column, η is the shape factor, G is the shear modulus and A is the sectional area of the column. By inverting the above relationship, the panel zone stiffness (k_e) have been obtained as follows;

$$K_{e0} = \frac{1}{\frac{d_b^3}{12EI} + \frac{d_b}{\eta GA}} \quad (8)$$

Since the shear-distortion relationship is often used in researches, the Eq. 8 multiplied by d_b ; consequently, the stiffness of the linear district of the panel zone, is resulted as follows;

$$K_e = \frac{1}{\frac{d_b^2}{12EI} + \frac{1}{\eta GA}} \quad (9)$$

Considering $E=2.6G$, estimating the moment of inertia by the relationship $I=A_{cf}d_c^2/2$ (that is ignored from the effect of the web in the moment of inertia), and by placing them into the Eq. 9 the Eq. 10 is obtained as follows:

$$K_e = \frac{\eta GA}{1 + 0.064\eta \frac{A}{A_{cf}} \left(\frac{d_b}{d_c} \right)^2} \quad (10)$$

In the Eq. 10, if it is supposed that $A=A_w$, where A_w is the sum of the areas of the two webs of the column, and assuming that $\eta=1$, the Eq. 11 is obtained:

$$K_e = \frac{GA_w}{1 + 0.064 \frac{A_w}{A_{cf}} \left(\frac{d_b}{d_c} \right)^2} \quad (11)$$

Thus, the stiffness of the elastic range is obtained. The relationship between the yield shear strain of γ_y and the yield shear force of V_y is stated as follows:

$$K_e \gamma_y = V_y \quad (12)$$

6.2. Shear Force of the Panel Zone

After obtaining the initial stiffness of the panel zone, the shear force of the panel zone will be studied. There are several theories regarding the panel zones of the I-columns. These theories compare the shear force of the panel zone with the yield shear force obtained from the finite elements models of the box columns. In Figure 9, the considered shear area in some models is shown.

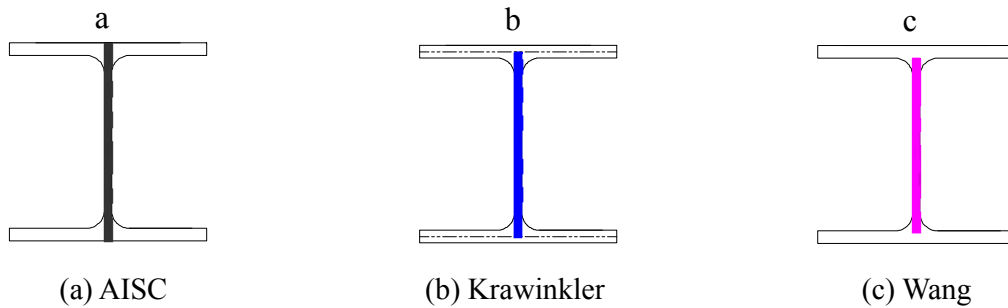


Figure 9. The Considered Shear Area

Figure 9(a) shows the shear area considered by the AISC Code of Standard Practice [6] that is equal to $(d_c t_{cw})$. Figure 9(b) demonstrates the considered area in the reference [1] that is equal to $(d_c - t_{cf}) t_{cw}$; and Figure 9(c) illustrates the considered shear area by the reference [21] whose value equals $(d_c - 2t_{cf}) t_{cw}$. In the above relationships, t_{cw} is the web thickness of the column; and the rest of the parameters previously defined.

In addition to the differences existing among the three presented models while selecting the shear area, there are also differences in selecting the shear yield stress of τ_y in the relationship of $V_y = A_v \tau_y$ (where A_v is the considered shear area in each model in Figure 9). Both references [1] and [21] have presented the yield shear stress according to the von Mises criterion in accordance with the Eq. 13.

$$\tau_y = \frac{F_y}{\sqrt{3}} \left(\sqrt{1 - \left(\frac{P}{P_y} \right)^2} \right) \quad (13)$$

While the amount of the yield shear stress in the AISC Code of Standard Practice is in accordance with Eq. 14.

$$\tau_y = \begin{cases} 0.6F_y & \text{for } \frac{P}{P_y} \leq 0.75 \\ 0.6F_y \left(1.9 - 1.2 \frac{P}{P_y} \right) & \text{for } \frac{P}{P_y} > 0.75 \end{cases} \quad (14)$$

In these relationships, F_y is the yield stress of the column materials, P is the axial force of the column, and P_y is the axial yield resistance of the column that is equal to $F_y A_g$ where the A_g is the gross area of the column.

From comparing the results of 672 box column panel zone models which are explained in the next sections and the previously presented models, it is derived that the amount of the yield shear force corresponds with the model presented by Krawinkler with an acceptable error percentage up to the loadings of $P_y \leq 0.5$. Nevertheless, in higher loadings, this model underestimates the yield shear force; therefore, this model has been modified in the higher axial loading amounts. In Figure 10, the considered shear area for the box column in present study is shown.

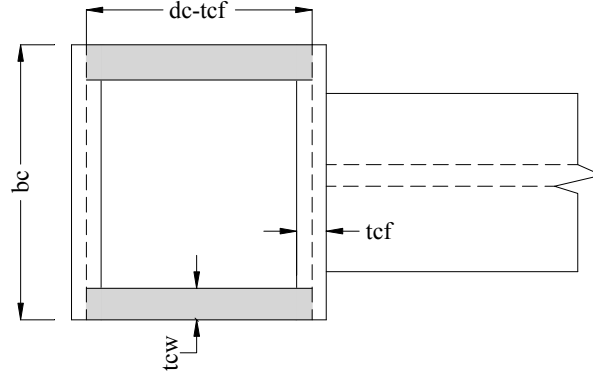


Figure 10. The Considered Shear Area for the Box Column

After analyzing the results obtained from the finite elements parametrical study, it is concluded that in case the yield shear stress is considered to be $\tau_y = \alpha F_y / \sqrt{3}$, and the decreasing coefficient of α is regarded by the Eq. 15, the finite elements of parametrical results will suitably correspond with the mathematical model.

$$\alpha = \begin{cases} \sqrt{1 - \left(\frac{P}{P_y} \right)^2} & \text{for } \frac{P}{P_y} \leq 0.5 \\ 0.1066 - 0.4 \frac{P}{P_y} & \text{for } \frac{P}{P_y} > 0.5 \end{cases} \quad (15)$$

Therefore, using the shear area adopted by Krawinkler and the Eq. 15, the yield shear force have been calculated as follows:

$$V_y = \frac{\alpha F_y}{\sqrt{3}} (d_c - t_{cf}) 2t_{cw} \quad (16)$$

As demonstrated in the Eqs. 3 and 4, the amount of the decreasing coefficient in the AISC Code of Standard Practice is as follows:

$$\alpha_A = \begin{cases} 1 & \text{for } \frac{P}{P_y} \leq 0.75 \\ 1.9 - 1.2 \frac{P}{P_y} & \text{for } \frac{P}{P_y} > 0.75 \end{cases} \quad (17)$$

In the above relationship, α_A is considered to be the decreasing coefficient of the AISC Code of Standard Practice. Moreover, the amount of the decreasing coefficient in the von Mises theory is as follows:

$$\alpha_v = \sqrt{1 - \left(\frac{P}{P_y} \right)^2} \quad (18)$$

In the above relationship, α_v is the considered decreasing coefficient according to the von Mises relationship. In Figure 11, the comparison between the adopted decreasing coefficient in the proposed relationship, the AISC Code and the Von Mises relationship is presented.

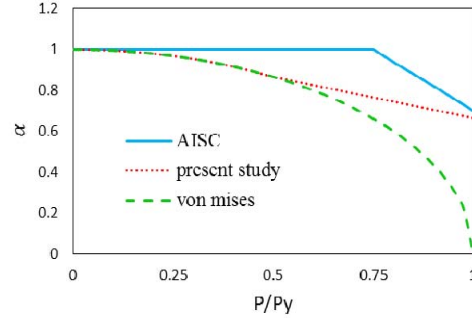


Figure 11. The Comparison between the Adopted Decreasing Coefficient in the Proposed Formula with the AISC and the Von Mises Formula

6.3 Yield Shear Strain of the Panel Zone

After the calculation of the yield shear force of the panel zone and the initial stiffness, the only remaining unknown, i.e. γ_y , is calculable, using the Eq. 12.

Replacing the Eq. 12 by the Eqs. 11 and 16, the yield shear strain of the panel can be derived zone as follows:

$$\gamma_y = \frac{F_y \alpha (d_c - t_{cf})}{G d_c} \left(0.577 + 0.037 \left(\frac{A_w}{A_{cf}} \right) \left(\frac{d_b}{d_c} \right)^2 \right) \quad (19)$$

Taking into consideration that most box column designs consider the web and the flange thicknesses to be equal, and the box column is in square-shape with equal dimensions, the amount of the A_{cf} equals 2 in Eq. 19, and the equation is simplified as follows:

$$\gamma_y = \frac{F_y \alpha (d_c - t_{cf})}{G d_c} \left(0.577 + 0.074 \left(\frac{d_b}{d_c} \right)^2 \right) \quad (20)$$

6.4 Inelastic Region of the Panel Zone

The surrounding elements of the panel zone continuity plates and column flanges help to increase the shear resistance of the panel. It should be mentioned that this only occurs when the continuity plates exist. In case the plastic moment of the column flange is $M_{y,cf}$, the moment equals to [22]:

$$M_{y,cf} = F_{y,cf} \frac{b_{cf} t_{cf}^2}{4} \alpha_v \quad (21)$$

Consequently, the shear force increment of the panel zone in the non-linear district, with the elastic district of ΔV_{PZ} , will be obtained as in [22].

$$\Delta V_{PZ} = \frac{4M_{y,cf}}{h_t} = \frac{F_{y,cf} b_{cf} t_{cf}^2}{h_t} \alpha_v \quad (22)$$

In the above relationships, b_{cf} is the flange width of the column, and $F_{y,cf}$ is the yield stress of the web materials of the column; the rest of the parameters are defined as before. In Figure 12, the details of the shear force increment caused by the boundary elements contribution are shown. It should be noted that the final capacity of the panel zone, according to the suggestions of Krawinkler [20] and Lin *et al.*[23], is considered to be four times the yield shear strain ($\gamma = 4\gamma_y$) because of the contribution of the shear force boundary elements related to the shear strain.

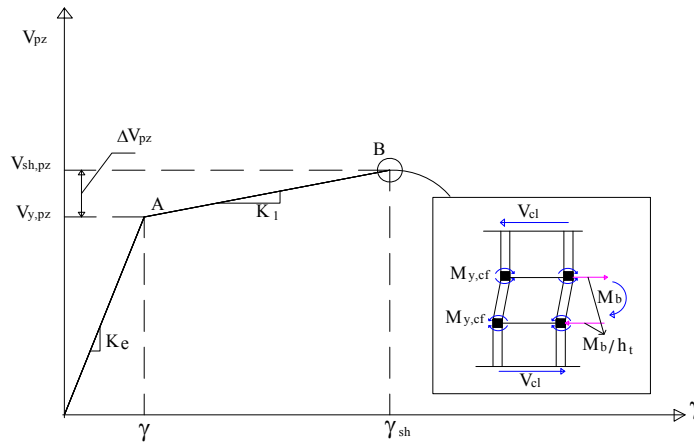


Figure 12. Shear Resistance Increment of the PZ Resulted from the Boundary Elements Contribution

According to the presented relationships in the AISC Code of Standard Practice, the amount of increment in the shear force in the district after the elastic district is considered to be as follows:

$$\Delta V_{PZ} = \frac{1.8F_y b_{cf} t_{cf}^2}{d_b} \alpha_A \quad (23)$$

Studying the results of the finite elements parametrical studies shows that the coefficient for applying the shear resistance increment caused by the boundaries elements is 1.5; consequently, the shear force increment of the district after the elastic district is obtained as follows:

$$\Delta V_{PZ} = \frac{1.5F_y b_{cf} t_{cf}^2}{h_t} \alpha \quad (24)$$

Thus, the final shear capacity of the panel zone , $V_{sh,PZ}$, results as follows:

$$V_{sh,PZ} = V_{y,PZ} + \Delta V_{PZ} \quad (25)$$

Placing the Eqs. 16 and 24 into the Eq. 25, we obtain the result in Eq. 26.

$$V_{sh,PZ} = \frac{F_y \alpha}{\sqrt{3}} (d_c - t_{cf}) 2t_{cw} + \frac{1.5f_y b_{cf} t_{cf}^2 \alpha}{h_t} \quad (26)$$

To calculate the stiffness of the panel zone in the non-elastic district next to the elastic district, supposing that the final shear capacity of the panel zone occurs in $\gamma = 4\gamma_y$, the stiffness of the non-elastic district of the K_{sh} panel zone is obtained as follows:

$$K_{sh} = \frac{\Delta V_{PZ}}{3\gamma_y} \quad (27)$$

Placing the Eqs. 19 and 24 into the Eq. 27, we obtain:

$$K_{sh} = \frac{b_{cf} t_{cf}^2 G d_c}{h_t (d_c - t_{cf}) \left(1.154 + 0.074 \left(\frac{A_w}{A_{cf}} \right) \left(\frac{d_b}{d_c} \right)^2 \right)} \quad (28)$$

Again, considering that the box columns with square shape and equal thicknesses of flange and web, the equation can be simplify Eq. 29 as follows:

$$K_{sh} = \frac{b_{cf} t_{cf}^2 G d_c}{h_t (d_c - t_{cf}) \left(1.154 + 0.148 \left(\frac{d_b}{d_c} \right)^2 \right)} \quad (29)$$

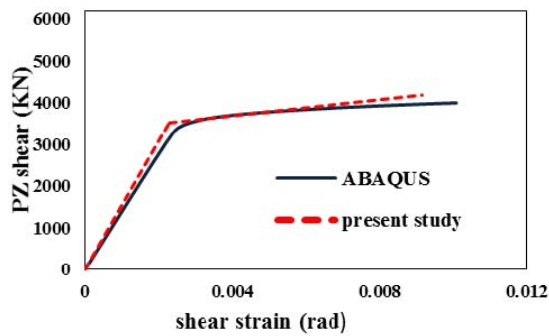
7. COMPARING THE ACCURACY OF DIFFERENT METHODS

To illustrate the accuracy of the presented relationships in this article, they have been compared with the finite elements results (see Figures 13(a)-(f)). In Table 3, the specifications of these samples are shown: t_f is the thickness of the flange section, t_w is the thickness of the web, d is the depth of the section and b_f is the flange width of the section.

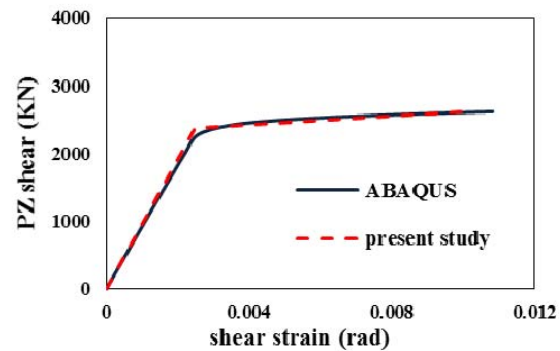
Table3. Specifications of the Samples 1, 2 and 3

Sample	Section	t_f (mm)	t_w (mm)	d (mm)	b_f (mm)
1	Column	60	30	428	406
	Beam	47.7	16	935.7	305
2	Column	33	21	386	399
	Beam	34	13	762	266.7
3	Column	11	11	356	373
	beam	30	10.5	617	228

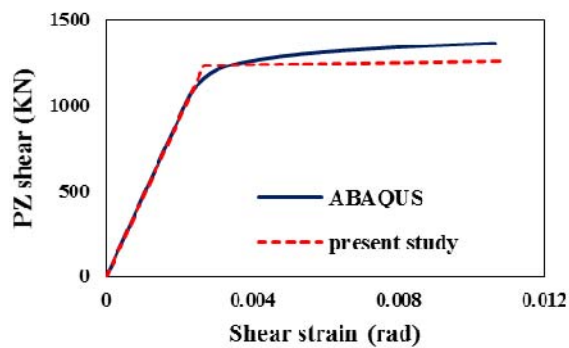
Figures 13(a) and 13(b) are related to the columns with thick and medium flange thicknesses respectively, along with the axial force ratio of 0.5. As it can be seen in the two figures, there is a suitable correspondence between the finite elements results and the present study.



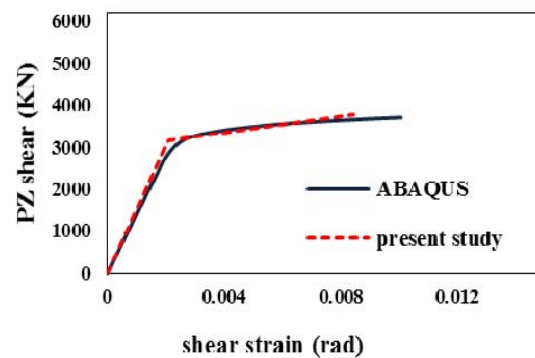
(a) Sample No.1



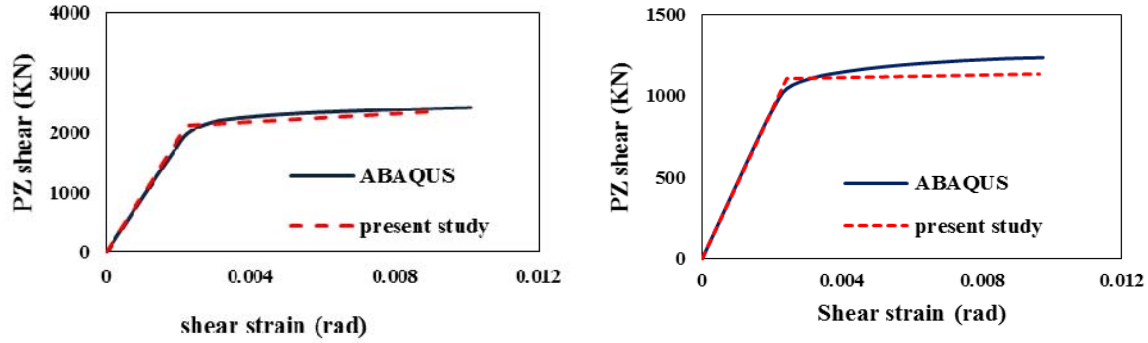
(b) Sample No.2



(c) Sample No.3



(d) Sample No.1



(e) Sample No.2

(f) Sample No.6

Figure 13. Comparison of the Presented Relationships and ABAQUS

Figure 13(c) is related to a column with a thin flange thickness and the axial force ratio of 0.5. As demonstrated in the figure, the presented results in this article are slightly lower (in the non-linear district) than the finite elements results, but the amount of the difference is negligible. Figure. 15(d) is related to a column with thick flange thickness and the axial ratio of 0.75. As illustrated in this figure, there is a suitable correspondence among the presented relationships and the finite elements results.

Figures 13(e) and 13(f), in a row, are related to columns with medium and thin flange thicknesses respectively, and the axial force ratio of 0.75. It is obvious that there is a suitable correspondence between the presented results and the finite elements results in Figure 13(e). However, in Figure. 13(f), the results of the presented relationships of this study are slightly lower than the finite elements results, but this difference is negligible.

The comparisons of the proposed with the results of finite element show that the average error for yield shear resistance of the panel zone is 2.19% and maximum error is 8%, For the final shear resistance of the panel zone the average error is 3.4% and maximum error is 9%. It show that the proposed relations has a good agreement with the result of finite element models.

8. SUMMARY AND CONCLUSIONS

The present relationships of the panel zone have been obtained from the analytical and experimental results of the I-shape columns in the panel zone. Yet, in most of these experiments, the columns with thick flange thicknesses and the vast existence of the axial force present on the columns are not considered. With regard to the importance of the box columns in the MRFs in seismic areas, we have concluded that the presentation of a mathematical model for the panel zones of the box columns that would estimate the behavior of these panel zones with higher accuracy seems essential. In this study, to reach a suitable mathematical model for extensive parametrical studies in relation to the effective parameters on the performance of the panel zone, we have implemented the ABAQUS software. The parameters include the flange thickness of the column, the web thickness of the column, and the flange thickness of the beam. Then, the mathematical relationships for the behavior of the panel zones in box columns are presented. The comparison of the presented relationships and the obtained results from the modeling shows a suitable correspondence between the relationships and the finite elements results. However, it should be mentioned that this correspondence is at the non-linear district of the shear force diagram; and the shear strain in columns with medium and thick flange thicknesses is more than the columns with

thin flange thicknesses. Of course, considering that the error in the columns with thin flange thickness is negligible, it is concluded the presented model gives acceptable results for different types of flange thicknesses of the columns.

REFERENCES

- [1] Krawinkler, H., Bertero, V.V. and Popov, E.P., "Inelastic Behavior of Steel Beam-to-column Subassemblages", EERC Rep. No. 71-7, University of California, Berkeley, CA, USA, 1971.
- [2] Bertero, V.V., Krawinkler, H. and Popov, E.P., "Further Studies on Seismic Behavior of Steel Beam-to-column Subassemblages", EERC Rep. No. 73-27, University of California, Berkeley, CA, USA, 1973.
- [3] Popov, E.P. and Takhirov, S., "Experimental Study of Large Seismic Steel Beam -to- ColumnC onnections", PEER-2001/01, Pacific Earthquake Engineering Research Center, University of California, Berkeley, 2001.
- [4] Mahin, S.A., Hamburger, R.O. and Malley, J.O., "An Integrated Program toI mprove the Performance of Welded Steel Frame Buildings", Proc. of 11th WCEE, World Conf. Earthquake Engineering. Acapulco, Mexico : Elsevier Science Ltd, 1996, Paper N 1114.
- [5] Kunnath, S.K. and Malley, J.O., "Advances in Seismic Design and Evaluation of Steel Moment Frames": Recent Findings from FEMA/SAC Phase II Project, J Struct Eng ASCE, 2002, Vol. 128, No. 4, pp. 415-9.
- [6] Malley, J.O., SAC Steel Project: Summary of Phase-1 Testing Investigation Results", Eng Struct, 1998, Vol. 20, No. 4, pp. 300-9.
- [7] El-Tawil, S., Mikesell, T., Vidarsson, E. and Kunnath, S.K., "Strength and Ductility of FR Welded-bolted Connections", Report No. SAC/BD-98/01, SAC Joint Venture, 1998.
- [8] El-Tawil, S., Vidarsson, E., Mikesell, T. and Kunnath, S.K., "Inelastic Behavior and Design of Steel Panel Zones", J. Struct. Eng. ASCE, 1999, Vol. 125, No. 12, pp. 183-193.
- [9] Ricles, J.M., Fisher J.W., Le-WuLu and Kaufmann, E.J., "Development of Improved Welded Moment Connections for Earthquake-resistant Design", Journal of Constructional Steel Research, 2002, Vol. 58, pp. 565-604.
- [10] Davila-Arbona, F.J., "Panel Zone Behavior in Steel Moment Resisting Frames", Master Dissertation, European School for Advanced Studies in Reduction of Seismic, Rose School, 2007.
- [11] AISC (American Institute of Steel Construction), "Specification for Structural Steel Buildings", AISC 360-10, Chicago, IL, 2010.
- [12] AISC (American Institute of Steel Construction), "Seismic Provisions for Structural Steel Buildings", AISC 341-10, Chicago, IL, 2010.
- [13] Lee, K.H., Stojadinovic, B., Goel, S.C., Margarin, A.G., Choi, J., Wongkaew, A., Reyher, B.P. and Lee, D.Y., "Parametric Tests on Unreinforced Connections", SAC Background Document, SAC/BD-00/01, SAC Joint Venture, Richmond, CA, USA, 2000.
- [14] Saffari, H., Hedayat, A.A and Nejad, M.P., "Post-Northridge Connections with Slit Dampers to Enhance Strength and Ductility", Journal of Constructional Steel Research, 2013, Vol. 80, pp. 138 -152.
- [15] Saffari, H., Hedayat, A.A. and Goharizi, N. S., "Suggesting Double-web I-shape Columns for Omitting Continuity Plates in a Box Column", Steel and Composite Structures, 2013, Vol. 15, No. 6, pp. 585-603.
- [16] Hedayat, A.A., Saffari, H. and Mousavi, M., "Behavior of Steel Reduced Beam Web (RBW) Connections with Arch-shape Cut", Journal of Advances in Structural Engineering, 2013, Vol. 16, No. 10, pp.1644-1662.

- [17] Mansouri, I. and Saffari, H., “A New Steel Panel Zone Model Including Axial Force for Thin to Thick Column Flanges”, *Steel and Composite Structures*, 2014, Vol. 16 No. 4, pp. 417-436.
- [18] Kim, K.D. and Engelhardt, M.D., “Monotonic and Cyclic Loading Models for Panel Zones in Steel Moment Frames”, *Journal of Constructional Steel Research*, 2002, Vol. 58, No. 5-8, pp. 605-635.
- [19] Ricles, J.M., Zhang, X., Lu, L.W. and Fisher, J.W., “Development of Seismic Guidelines for Deep-column Steel Moment Connections”, 2004, ATLSS Report No. 04-13.
- [20] Krawinkler, H., “Shear in Beam-column Joints in Seismic Design of Steel Frames”, *Engineering Journal*, AISC, 1978, Vol. 5, No. 3, pp. 82–91
- [21] Wang, S.J., “Seismic Response of Steel Building Frames with Inelastic Joint Deformation”, Lehigh University, 1988.
- [22] Brandonisio, G., De Luca, A. and Mele, E., “Shear Strength of Panel Zone in Beam-to-column Connections”, *Journal of Constructional Steel Research*, 2012, Vol.71, pp. 129-142.
- [23] Lin, K.C., Tsai, H.C., Kong, S.L. and Hsieh, S. H., “Effect of Panel Zone Deformations on Cyclic Performance of Welded Moment Connections”, XII WCEE, New Zealand, Doc. No. 1252, 2000.
- [24] SIMULIA. ABAQUS, Analysis and Theory Manuals. Providence (RI, USA): SIMULIA, the Dassault Systèmes, Realistic Simulation, 2013.

EFFECT OF BLAST-INDUCED COLUMN FAILURE PATTERN ON COLLAPSE BEHAVIOR OF STEEL FRAMES

G.Q. Li^{1,2}, Y. Zhang^{2,3}, T.C. Yang⁴, J. Jiang^{2,*}, Y. Lu⁵ and S.W. Chen^{1,2}

¹ State Key Laboratory for Disaster Reduction in Civil Engineering, Shanghai 200092, China;

² College of Civil Engineering, Tongji University, Shanghai 200092, China;

³ Department of Building Engineering, Logistics University of PAPF, Tianjin 300309, China

⁴ School of Civil Engineering and Architecture, University of Jinan, Jinan 250022, China;

⁵ School of Engineering, the University of Edinburgh, Edinburgh EH9 3JF, United Kingdom

*(Corresponding author: E-mail: jiangjian_0131@163.com)

Received: 11 April 2017; Revised: 11 June 2017; Accepted: 22 July 2017

ABSTRACT: This paper proposes two reduced-order modeling approaches (Equivalent spring model and Single degree of freedom model) to simplify the traditional dynamic analysis of a whole structure by two steps: (1) local damage analysis of columns under blast on a member level, and (2) global analysis with an equivalent spring model considering the failure process of damaged columns. This avoids the global structural analysis in Step 1 and also avoids the simulation of blast loads in Step 2. The failure time and residual load-bearing capacity of damaged columns under blast are considered and their effect on the global collapse resistance is studied. The results show that they have significant effect on the collapse resistance. The longer the failure time, the larger the residual resistance, the smaller the structural displacement, and the greater the collapse resistance. It is found that the dynamic behavior of structures is sensitive to the ratio of column failure time to the structural vibration period t_0/T . The larger the t_0/T , the smaller the dynamic amplification effect. It is suggested to consider a smaller dynamic amplification factor rather than 2 for $t_0/T > 0.3$. For the selection of analysis methods for blast-induced collapse of structures, it is recommended to adopt the alternate path method for $t_0/T < 0.2$, and static analyses for $t_0/T > 3$. While for $0.2 < t_0/T < 3$, dynamic analyses considering the effect of failure time and residual resistance of damaged columns should be conducted.

Keywords: Progressive collapse, steel framed structure, blast, equivalent spring method, single degree of freedom model, failure time, residual load-bearing capacity

DOI: 10.18057/IJASC.2018.14.3.4

1. INTRODUCTION

Since the collapse of the World Trade Centre Towers under terrorist attack on September 11, 2001, there have been considerable interests in understanding the mechanism of blast-induced progressive collapse of tall buildings. The term “progressive collapse” is defined as “the spread of an initial local failure eventually resulting in the collapse of an entire structure or a disproportionately large part of it” [1]. It is generally recognized that increasing robustness is the key to reduce the chance of progressive collapse of structures. However, specific methodologies and design guides for robustness of steel framed structures are lacking. This situation is inconsistent with the fact that steel structures have increasingly become the predominant structural form for high-rise building construction, where explosion and impact are the major forms of abnormal loads and the consequence of collapse is immense.

Since the loss of a column in a structure may trigger its progressive collapse, resistance of columns against blast loads are given growing attentions. Song et al. [2] and Izzuddin et al. [3] presented a developed method for integrated adaptive nonlinear analysis of steel frames subject to fire and explosion loading. Parametric studies were conducted on column and frame configurations subjected to blast. Liew and Chen [4,5] studied the behavior of steel columns under various blast loads and boundary conditions. Yu and Liew [6,7] investigated the behavior of steel framed structures subjected

to combined blast and fire loads. The methods for determining the blast load and finite element techniques were reviewed, and numerical analysis of a five-storey building under blast and fire conditions were carried out. The results showed that the blast-damaged structures possessed little fire resistance. Magallanes et al. [8] carried out a series of full-scale blast tests on steel wide-flange columns. The results showed that severe local column deformations that essentially “open up” the section were observed though global deformation was small. Turcic et al. [9] investigated the cause and influencing factors of the collapse of a long-span steel roof structure. Yu et al. [10] studied the influence of levels of structural idealization (assembled beam model, grillage model and frame model) on the progressive collapse of steel framed structures. The results showed that the dynamic response of floors had a significant effect on the structural robustness. Grillage models with a simplified assembly procedure was proposed and its performance was verified. Demonceau and Jaspart [11] experimentally simulated the column loss process in a composite structure. The development and effect of membrane forces on the behavior of beam-to-column connections were discussed. Wu et al. [12] studied the dynamic response and residual axial capacity of reinforced concrete columns subjected to blast loads. The influence of material strength, column detailing and blast loads on the residual axial capacity was investigated. Nethercot et al. [13] proposed quantitative measures to improve the robustness of steel and composite buildings, based on a number of parametric studies. Wang et al. [14] conducted finite element analysis of progressive collapse of transmission tower system. The mass of the elements was retained after their removal due to loss of strength. It was found that the ultimate strain and strain rate of material had significant effect on the collapse modes.

The assessment of collapse performance of structures and measures for mitigating progressive collapse can be found in various design codes [1, 15-17]. ASCE 7 [1] proposes two general approaches for reducing the possibility of progressive collapse: Direct Design and Indirect Design. The former includes the Alternate Path method which requires that a structure be capable of bridging over a missing structural element in the event of a localized damage, and the Specific Local Resistance method which requires a building to provide sufficient strength to resist a specific load. For the Indirect Design approach, the structural resistance of the progressive collapse is considered implicitly through the provision of minimum levels of strength, continuity and ductility, such as catenary action of the floor slab, redundant structural systems, etc. The Tie Force approach is usually applied which prescribes a tensile force capacity to the connections between principal elements of the structure with the intention of allowing the structure to transfer load from the damaged portion of the structure to the undamaged part. Furthermore, in Eurocode EN 1991-1-7 [16], high-rise buildings would be classified as Class 3 and a systematic risk assessment approach is necessary [18].

The alternate path method assumes that the column is removed immediately regardless of the magnitude and duration of blast loads. In practice, although the duration of explosion on structural members is very short (in a unit of millisecond), the duration of dynamic response of a member under explosion to failure may be longer depending on material properties and geometry dimensions. It is unreasonable to neglect the failure process of members in all cases. Furthermore, the damaged components may have some residual load-bearing capacity. The presence of the failure time and residual capacity of the damaged members may affect the resistance of the whole structure against progressive collapse. The proposed approach in this paper is to contribute to the resolution of these two issues.

This paper investigated the effect of the failure process of columns subjected to explosion on the collapse of steel framed structures. The traditional dynamic analysis of a whole structure was simplified by using equivalent spring model and single degree of freedom (SDOF) model. The development of these two models was first presented. The methods to determine the failure time and residual load-bearing capacity of the column under blast were proposed. The performance of these two models were verified against results from analysis of a whole frame. Parametric studies were

carried out to investigate the influence of the failure time and residual capacity of damaged columns on the collapse resistance of structures. Finally, recommendations were proposed for the selection of dynamic amplification factors and analysis methods for the progressive collapse of steel framed structures.

2. WHOLE FRAME MODEL

To study the collapse behavior of structures under explosion, a 2D steel frame was modeled in finite element software LS-DYNA, as shown in Figure 1. The frame had six bays of 4.5m and twelve storey of 3m. All connections are assumed rigid in this study, which is the common practice for steel frame buildings in seismic zones. All the steel beams and columns were taken as I-type members of I400×200×8×10mm and H500×500×12×15mm, respectively. The four numbers represent the height of the section, the width of the flange, thickness of the web and flange, respectively. A uniformly distributed load of q was imposed on all the beams, and a lateral blast load p was applied on the middle column of the ground floor. The three-dimensional Hughes Liu beam element was used to model the steel columns and beams. This element had an integrated cross-section and the command *INTEGRATION_BEAM was used to define an I-shape section. The arrangement of the integration points was achieved by an integration refinement parameter k . A value of $k=2$ was taken in this study where 7 and 6 integration points were arranged for the flange and web, respectively. The Plastic Kinematic model was used for the stress-strain curve of steel, and the Cowper-Symonds model was used to consider the effect of strain rate. The elastic, bulk and shear modulus of steel were taken as 2.06×10^5 MPa, 1.49×10^5 MPa and 8.11×10^4 MPa, respectively. The yielding stress was 310 MPa. The hardening constant, T hardening exponent (β), strain rate constant (C) and strain rate exponent (P) were taken as 31MPa, 1, 40 and 5, respectively. The numerical modeling in LS-DYNA had been extensively validated and verified against experimental and analytical results, respectively, as presented in the references [19-22].

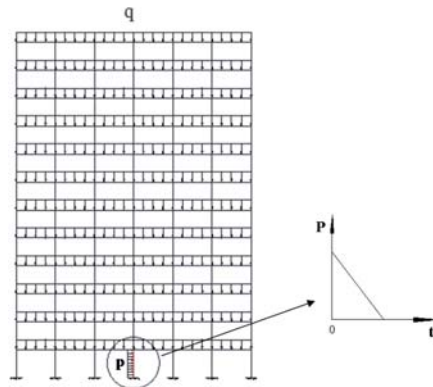


Figure 1. A 2D Steel Frame subjected to Blast Loads on a Ground Floor Column

Four cases of blast loads were considered in this study, as listed in Table 1. The overpressures of the blast loads were taken as 160MPa, 84MPa, 57MPa and 30MPa, respectively. The equivalent linearly distributed load on the column were calculated by multiply the overpressure by the width of the column flange (0.5m in this case). It was assumed that the blast loads reduced linearly to zero in a duration of 0.8ms, 1.2ms, 1ms and 1ms, respectively (Figure 1). Figure 2 shows the variation of the axial forces and mid-span displacement of the columns subjected to the first three blast loads. Due to a large blast load imposed in a short duration (Case 1), the blast load caused large lateral displacement of the column (Figure 2b), leading to decreasing compressive axial forces in it which even turned over to tensile forces as the frame did not response to this transient loading (Figure 2a). As running time increased, the response of the frame caught up with that of the column, and the column was

subjected to compression again until its buckling. For the column subjected to a much smaller blast load (Case 3), the column did not fail after the blast but maintained a certain residual load-bearing capacity (Figure 2a). For the loading Case 2, the blast load caused large mid-span lateral displacements of the column (about 200mm), compared to that of about 30mm for Case 3. The large lateral mid-span displacement for Case 2 lead to the failure of the column, i.e. no residual load-bearing capacity.

Table 1. List of Loading Cases adopted in this Study

Case No.	Blast pressure (MPa)	Specific impulse (kPa·s)	p (10^3 kN/m)	Time duration (ms)	q (kN/m)
1	160	128	80	0.8	100
2	84	101	42	1.2	100
3	57	57	29	1	100
4	30	30	15	1	75

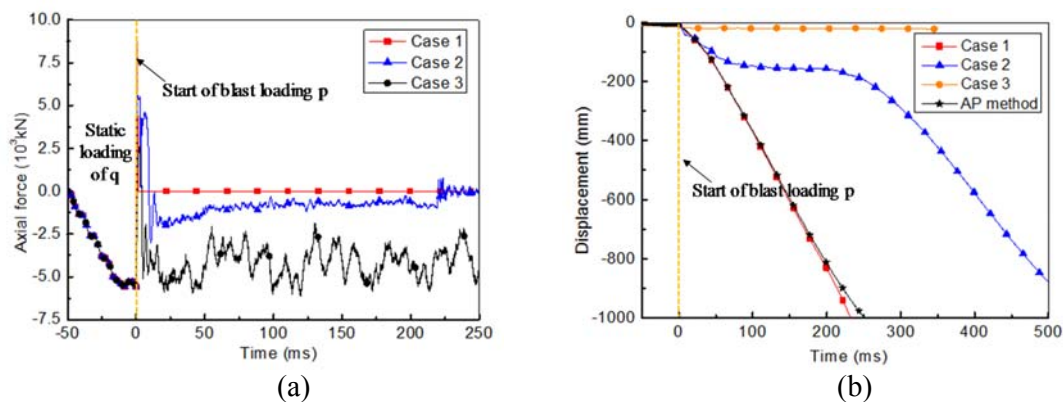


Figure 2. Variation of Responses in the Column subjected to Blast Loads: (a) Axial Forces; (b) Mid-span Lateral Displacement

As shown in Figure 2b, the column mid-span displacement for Case 1 agreed well with those from Alternate Path (AP) method, while those for the other cases were quite different. In the alternate path method, a column is assumed to be removed immediately regardless of the magnitude and duration of blast loads. The vertical load q is then amplified to some extent to consider the dynamic effect of the column removal. This method is applicable for unforeseeable explosion or impact loading conditions and is generally recognized to be conservative. In contrast, for an identified blast load imposed on the column, the axial force in the column may decrease from its initial value N_0 to N' as show in Figure 3. After the explosion, the frame will continue to deform under the vertical loads and thus the damaged column reaches its residual load-bearing capacity N_r [12, 22, 23].

In this case, the response of the column to failure (t_0) during the explosion may be too long to be neglected depending on its material properties and geometry dimensions. Furthermore, there will exist some residual load-bearing capacity in the column after the explosion. The presence of the failure time and residual capacity of the damaged column will affect the resistance of the whole structure against progressive collapse. In this study the failure time t_0 of the column under explosion was defined as the occurrence of the maximum lateral displacement at mid-span of the column.

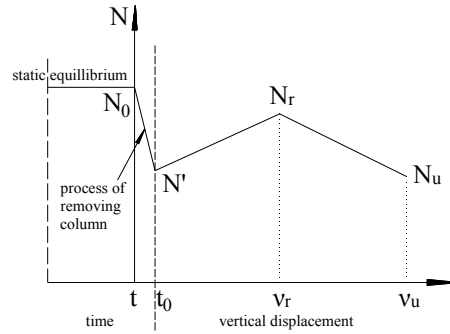


Figure 3. Variation of Axial Forces in a Column subjected to Blast Loads

Simplified models (Equivalent spring model and SDOF model) were proposed and presented in the following sections, to further investigate the effect of these two factors and also to simplify the analysis procedure of progressive collapse of structures.

3. EQUIVALENT SPRING MODEL

As an alternative to dynamic analysis of the whole structure, an equivalent spring method was proposed in this paper to simplify the analysis procedure, as illustrated in Figure 4. The development of the equivalent spring model is explained as follows: (1) Separate the column subjected to blast loads from the frame, and determine its failure time and residual load-bearing capacity on a member level, either analytically or numerically. This process will be demonstrated in more detail later; (2) Replace the damaged column by a spring model and apply a concentrated load on it, as shown in Figure 4a. The load has the same magnitude of the initial axial force in the column but opposite direction, i.e. the whole frame is still in equilibrium; (3) Change the magnitude of the load imposed on the spring according to Figure 4b until the rebalance or collapse of the frame.

As shown in Figure 4b, it is assumed that the axial force in the damaged column reduces linearly from its initial value N_0 to its residual load-bearing capacity N_r . After that, the axial resistance of the column is assumed to be constant (i.e. N_r) until the rebalance or collapse of the frame. Note that the variation of axial forces in the damaged column in Figure 4b was used in this study, to simplify the process shown in Figure 3. The proposed equivalent spring method took into account the dynamic effect of the column removal in terms of the column failure time t_0 and the residual bearing capacity in terms of N_r .

The proposed method divides the conventional complex analysis of steel frames against collapse into two independent steps: (1) Analysis of the local damage under explosion in a member-based level, i.e. analysis of the whole frame is avoided; (2) Analysis of the global behavior of the frame by considering the failure process of the damaged column, i.e. simulation of the blast load is avoided.



Figure 4. Schematic of Equivalent Spring Model: (a) Replacement of the Column with a Spring and Initial Axial Force in the Column; (b) Variation of the Axial Force during and after the Explosion

4. SDOF MODEL

To further simplify the mechanism and assessment procedure of progressive collapse of steel frames, a single degree of freedom (SDOF) model was established, as shown in Figure 5. The middle column on the ground floor of the frame subjected to blast loads was replaced by a force N_0 with the same magnitude as the initial axial compression force in the column but in the opposite direction. Taking into account the restraint from surrounding bays, the frame above the damaged bay was simplified into a substructure with fixed end boundary conditions. The substructure was then reduced to a SDOF system with a mass of weight m representing the whole substructure and a spring of stiffness k equivalent to the vertical stiffness of the frame above the damaged column. When subjected to explosion, the column may experience large deformation. Thus, the axial displacement of the column reached its maximum value and its residual axial force reduced to N_r . The failure process of the column under explosion can be characterized by the variation of the axial force in the column. There were mainly three models (A, B, C) for simulating the variation of axial forces in columns. The Model A represents the immediate removal of columns assumed in the alternate path method. The Models B and C consider the failure process of the column. It was assumed that the axial force in the column decreased linearly during the failure time t_0 . The initial force in the column decreases to zero in the model B while a residual axial force N_r exists in the column after the blast loading for Model C.

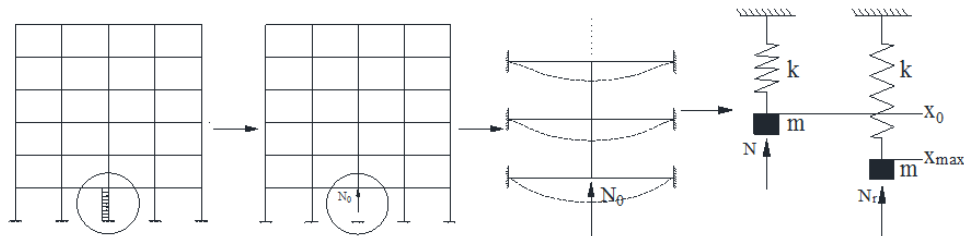


Figure 5. Schematic of SDOF model

In the SDOF model, the maximum displacement of the mass subjected to a blast load as in the Model A can be obtained simply through energy balance method. However, in the Models B and C, it is somewhat difficult to derive the analytical solution of the maximum response of the mass.

(1) In the model A, the maximum displacement x_{max} of the mass is given as:

$$x_{max} = 2 \cdot x_s = 2 \cdot \frac{N_0}{k} \quad (1)$$

where x_s is the static displacement of the mass in equilibrium under the force N_0 ; k is the stiffness of the spring.

From Equation 1, it can be seen that the maximum displacement x_{max} of the mass based on the alternate path method (Model A) is two times the corresponding static displacement x_s . The consideration of the residual capacity N_r may result in a reduction in the displacement of the mass which is beneficial for mitigating progressive collapse of structures.

(2) The model C is considered to be the most practical case since it considers both the failure process and residual resistance of the column under explosion. When the deformation of the column follows the model C, the displacement of the mass in the proposed SDOF system can be given as:

$$u = \begin{cases} \left(\frac{N_0 - N_r}{k} \right) \left[\left(\frac{t}{t_0} \right) - \left(\frac{1}{\omega \cdot t_0} \right) \sin \omega t \right] & (0 \leq t \leq t_0) \\ \left(\frac{N_0 - N_r}{k} \right) \left\{ 1 + \left(\frac{1}{\omega \cdot t_0} \right) [\sin \omega(t - t_0) - \sin \omega t] \right\} & (t > t_0) \end{cases} \quad (2)$$

where t_0 is the failure time of the column under explosion; ω is the natural frequency of the SDOF system; t is the time.

By defining R as the dynamic amplification factor, Equation 2 can be transformed to:

$$u = \begin{cases} \left(\frac{N_0 - N_r}{k} \right) R_1 & (0 \leq t \leq t_0) \\ \left(\frac{N_0 - N_r}{k} \right) R_2 & (t > t_0) \end{cases} \quad (3)$$

The displacement of the mass is expressed as the product of the static displacement (in the bracket) and dynamic amplification factor R_i . The parameter R depends on the frequency of the system and loading duration. The static displacement of the mass is given as:

$$u_s = \frac{N_0 - N_r}{k} = \frac{N_0}{k} - \frac{N_r}{k} \quad (4)$$

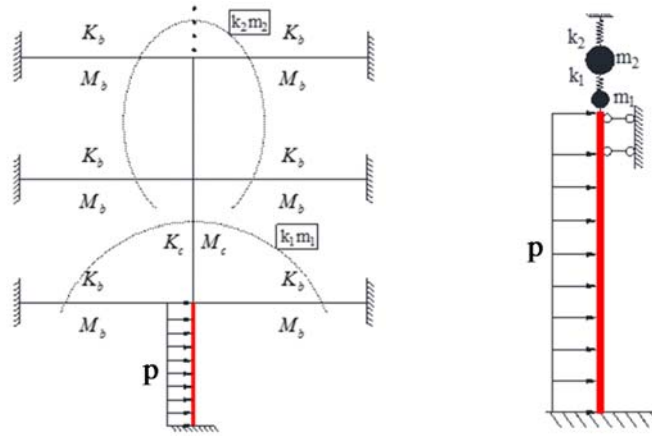
According to Equation 4, the residual resistance N_r affects the static displacement directly. The greater the residual resistance, the smaller the displacement of the structure. The displacement is reduced by $(N_r/k)R$ due to the presence of the residual resistance of the damaged column compared with the alternate path method. Therefore, the residual resistance in the column under blast actions has beneficial effects on arresting progressive collapse of structures.

As shown in Equation 2 and Figure 5, the axial displacement at the top of the column subjected to blast was affected by four key parameters (k , m , t_0 , N_r). The determination of these four parameters will be presented in the following sections. The details of the deduction can refer to the reference [21].

4.1 Determination of k and m

The axial displacement at the top of the ground column under blast is restrained by the frame above the column. The contribution of each storey to the restraining effect was not uniform along the height of the frame but reduced gradually from the second storey to the top of the frame. To consider the non-uniform distribution of vertical restraint, the frame above the column under blast was divided into two portions: the second storey just above the damaged column, and the frame from the third storey to the top, as shown in Figure 6. The spring stiffness and equivalent lumped mass of these two portions were defined as k_1 , m_1 and k_2 , m_2 , respectively.

To further simplified this two-spring model to a single-spring model, the spring stiffness and mass of the model in Figure 5 can be calculated as $m = m_1 \cdot \phi_1^2 + m_2 \cdot \phi_2^2$, $k = k_1 \cdot (1 - \phi_2)^2 + k_2 \cdot \phi_2^2$ where the parameters ϕ_1 , ϕ_2 are the displacement of the mass m_1 and m_2 .

Figure 6. Schematic of Determination of k and m

4.2 Determination of Failure Time t_0

The time to failure t_0 of a column under blast actions is defined as the occurrence of the maximum lateral displacement at its mid-span, as shown in Figure 4b. It was found that the failure time of an individual column with two ends fixed was similar to that resulting from the analysis on the whole frame [21]. This indicates that the boundary conditions of the column have little effect on its lateral displacement. To this end, the failure time of a column fixed at its two ends was studied in this section. The failure time of a clamped column depends on such factors as the magnitude and duration of the blast action, the ultimate plastic moment of the column section, the vibration period of the column, etc. It is difficult to obtain the analytical solution of the failure time due to the large plastic deformation of steel columns under explosion. The clamped-clamped column can be simplified to a SDOF model. Under this condition, the failure time of the column can be solved simply based on the characteristics of SDOF system.

For the SDOF system, the blast load was assumed to be reduced linearly from p_0 to zero during a period of t_d . The spring had an ideal elastic-plastic load-force curve. In the elastic and plastic phase, the motion equations of the SDOF model were expressed by Equation 5 and 6, respectively, as

$$m\ddot{u} + ku = P(t) \quad (5)$$

$$m\ddot{u} + R = P(t) \quad (6)$$

where m is the weight of the mass; k is the stiffness of the spring; R is the residual resistance of the spring; $P(t)$ is the overpressure of the blast load at time t .

In the elastic state of the SDOF model, when $t < t_d$, the displacement response of the mass can be written as:

$$u(t) = \left(\frac{p_0}{k}\right) \left[1 - \left(\frac{t}{t_d}\right) - \cos \omega_n t + \left(\frac{1}{\omega_n t_d}\right) \sin \omega_n t\right] \quad (7)$$

when $t > t_d$, the displacement response of the mass is expressed as:

$$u(t) = \left(\frac{p_0}{k}\right) \left(\frac{1}{\omega_n t_d}\right) [\sin \omega_n t (1 - \cos \omega_n t_d) - \cos \omega_n t (\omega_n t_d - \sin \omega_n t_d)] \quad (8)$$

While in the plastic state, the displacement response is given as:

$$u_{2(t)} = \frac{1}{m} \left[\iint_{t'} P_{(t)} dt dt - \frac{R(t-t')^2}{2} \right] + \dot{u}_{1(t')}(t - t') + u_{1(t')} \quad (9)$$

where t' is the start time of the plastic state.

The determination of the dynamic response of the SDOF system above is still very complex because it needs to deal with the conversion process from elastic to plastic for ideal elasto-plastic resistance model. A simplification on it can resort to the numerical solution.

Given the relevant parameters of SDOF for the clamped-clamped column, the failure time of the column can be calculated easily using the exiting SDOF program.

Numerical analyses were conducted on the frame model (Figure 1) with the same geometry and loads as Case 4 in Table 1. Comparison of the mid-span lateral displacement of the damaged column between the frame model and SDOF model is shown in Figure 7. The parameters for the equivalent SDOF model were taken as $K=2.31 \times 10^6 \text{ kN/m}$, $M=202 \text{ kg}$, $P=28.8 \times 10^6 \text{ kN}$, $R=7.82 \times 10^6 \text{ kN}$. The maximum displacement and failure time of the column in the SDOF model agreed well with those from the frame model.

Given the material properties and geometry dimensions of the column under explosion, parameters for the equivalent SDOF model can be calculated and thus the failure time of the column can be determined based on the peak value and duration of blast loads. Figure 8 shows the relationship of the occurrence time of the system maximum displacement and the ratio of the column failure time to the system period for two peak blast loads of $P=28.8 \times 10^6 \text{ kN}$ and $P=18.0 \times 10^6 \text{ kN}$, respectively. The occurrence of the maximum system displacement was delayed as t_d/T increased.

The failure time of the column under blast actions can be determined based on the SDOF system with ideal elasto-plastic material. However, a numerical method should be taken to solve the equation. To further simplify the calculation, a rigid-plastic model was used for the stiffness of the spring in the SDOF, thus the motion equation of SDOF can be expressed as:

$$m\ddot{u} = P_{(t)} - R \quad (10)$$

Substitution of the expression of $p_{(t)}$ into Equation 10 and through integration yields:

$$m\dot{u}_{(t)} = p_0 \left(t - \frac{t^2}{2t_d} \right) - Rt \quad (11)$$

According to $\dot{u}_{(t)} = 0$, the occurrence time t_{\max} of the maximum displacement of the column, i.e. t_0 can be derived as:

$$t_0 = t_{\max} = 2t_d \left(1 - \frac{R}{p_0} \right) \quad (12)$$

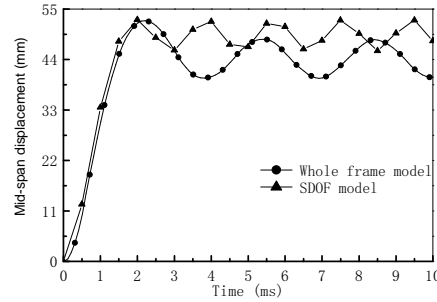


Figure 7. Comparison of the Lateral Displacement of the Column between Whole Steel Frame Model and Simplified SDOF System

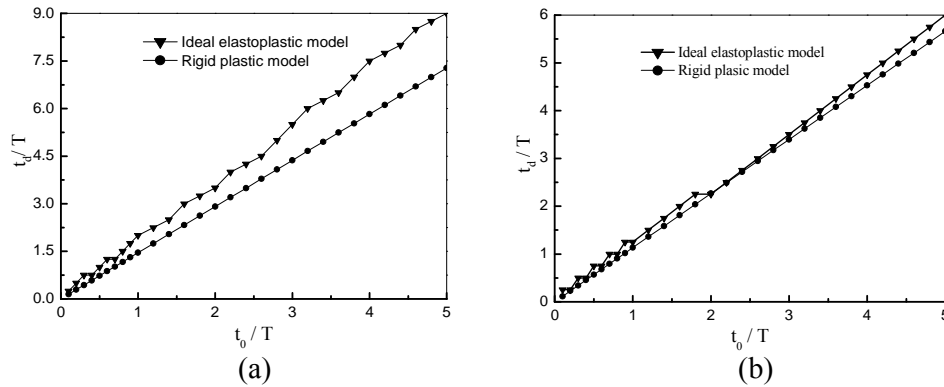


Figure 8. Variation of Occurrence Time of the Maximum Displacement Versus t_d/T for: (a) $P=28.8 \times 10^6 \text{ kN}$; (b) $P=18.0 \times 10^6 \text{ kN}$

The column failure time of the frame using rigid-plastic resistance model were compared with elastoplastic model in Figure 8 where reasonable agreement was obtained. Therefore, the rigid-plastic resistance model (Equation 12) can be used to reasonably predict the failure time of columns under explosion to facilitate the calculation.

4.3 Determination of Residual Capacity N_r

Figure 9 illustrates the three steps to numerically determine the residual load-bearing capacity of columns. Firstly, the static equilibrium state is achieved for initial static loads. Secondly, based on the deformation and stress distribution of columns in the static equilibrium, the response of the column under blast loads is then solved. Finally, the residual load-bearing capacity N_r is obtained by displacement control method, i.e. gradually increase the vertical displacement of the top of the column until failure. The residual load-bearing capacity of the column depends on its initial static load, blast load and boundary conditions. Figure 10 shows the variation of axial forces in the column with the axial displacement of the column top for the Case 4 in Table 1.

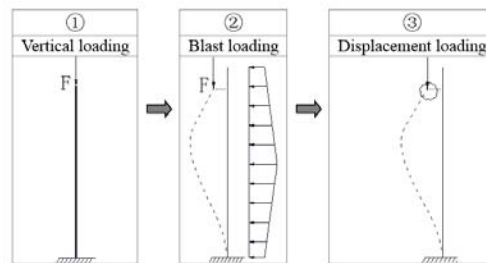


Figure 9. The Solution Process of the Residual Bearing Capacity of Columns using LS-DYNA

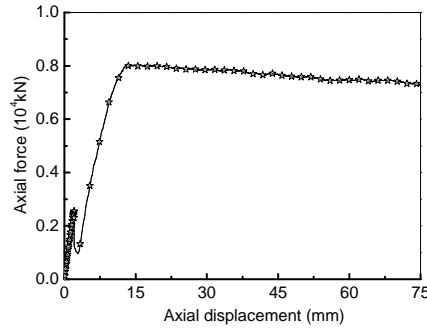


Figure 10. Variation of Axial Forces in the Damaged Column with Axial Displacement (Case 4 in Table 1)

5. VERIFICATION OF SIMPLIFIED MODELS AND PARAMETRIC STUDY

5.1 Verification of Equivalent Spring Model

The performance of the proposed spring models in Sections 3 and 4 was verified in this section by comparing with the results from whole frame model (Figure 1) and alternate path. The Case 3 and Case 4 in Table 1 were selected and the results are shown in Figure 11. The resistance of structures against progressive collapse was measured in terms of the axial displacement at the top of the column under explosion. The spring stiffness and mass in the SDOF model were calculated as $k=1.15 \times 10^5 \text{ kN/m}$ and $m=45.5 \times 10^3 \text{ kg}$, respectively. This led to a fundamental period of $T=125 \text{ ms}$. According to Figure 10, the failure time and residual load-bearing capacity of the column were determined as $t_0=40 \text{ ms}$ and $N_r=3500 \text{ kN}$ for Case 3, and $t_0=60 \text{ ms}$ and $N_r=8000 \text{ kN}$ for Case 4. Figure 11 shows that due to the small static load and blast load, there was still some residual load-bearing capacity left in the column and no collapse of the frame occurred. The alternate path method overestimated the response of structures due to dynamic effects. The results from the whole frame model and proposed equivalent spring method were in a reasonable agreement.

The proposed equivalent spring method were used to study the influence of the failure time t_0 and residual bearing capacity N_r of the column under explosion on the axial displacement of the frame in Figure 1 as follows.

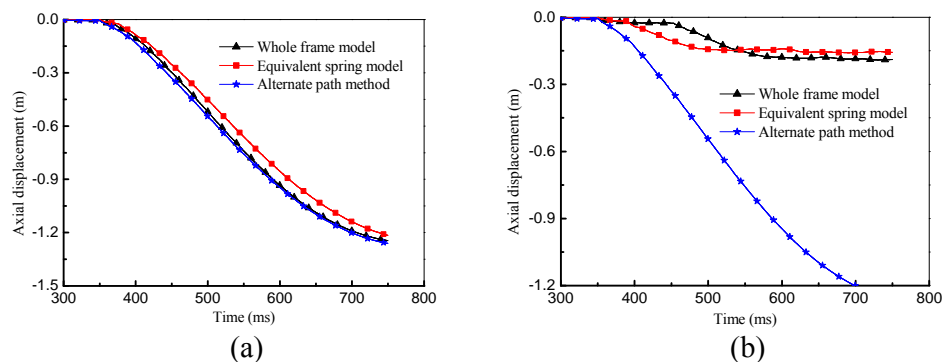


Figure 11. Comparison of Axial Displacement of the Columns Predicted from Different Modeling Approaches: (a) Loading Case 3 in Table 1; (b) Loading Case 4 in Table 1

5.2 Influence of Failure Time t_0

The residual load-bearing capacity model ($N_r=8000\text{kN}$) of the column under explosion in Figure 4b was used in this case. Five cases of failure duration of the column were adopted (0ms, 12ms, 60ms, 120ms, infinity). Comparison of the axial displacement at the top of the column for the five failure cases is shown in Figure 12. The longer the failure time of the column, the smaller the displacement of the structure. When the failure time was infinite, the displacement is equivalent to the static response. Obvious dynamic effects were observed for an immediate removal (0ms). The response for a removal of 12ms almost coincided with the immediate removal. This indicates that only if the failure time is within certain range such as 60ms, it is necessary to consider the effect of the failure time of columns.

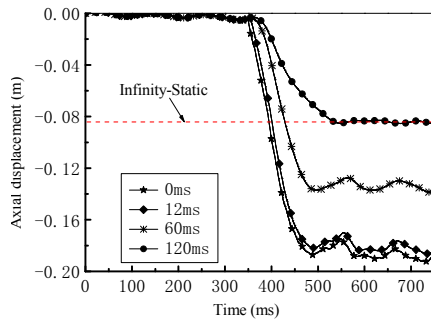


Figure 12. Comparison of Axial Displacements of Columns for Different Failure Times

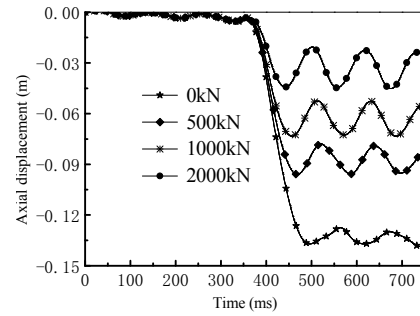


Figure 13. Comparison of Axial Displacements of Columns for Different Residual Load-bearing Capacity

5.3 Influence of Residual Load-bearing Capacity N_r

The effect of the residual bearing capacity N_r of the damaged column on the progressive collapse of structures was studied herein. The same failure time of 60ms was taken. Four conditions of residual load-bearing capacity N_r of the column were considered (0kN, 500 kN, 1000 kN, 2000 kN).

Figure 13 shows the variation of the axial displacement of the column for the four residual capacity cases. It showed that the larger the residual bearing capacity of the column, the smaller the displacement of the structure given the same failure time. Therefore, the existence of the residual bearing capacity can enhance the resistance of structures against progressive collapse. Therefore, it is of importance to consider the residual bearing capacity of the damaged column under explosion in the assessment of progressive collapse of structures.

6. APPLICATION OF SDOF MODEL IN THE DESIGN

According to Equation 2, the variation of the dynamic amplification factor against time was plotted in Figure 14. Two cases with different ratios of the failure time t_0 to the system period T of 0.2 and 1.5 were compared. The results showed that when $t_0 < T$ (e.g. $t_0 = 0.2 T$), the occurrence of the maximum response of the system greatly lagged behind the failure of the column. This can be attributed to the fact that the failure process of the column was so short that there was no time for the frame to react and thus the displacement at the early stage of loading was small. In this case, the loading played a role in the form of impulse which was then transferred into the initial velocity of the mass. In contrast, when $t_0 > T$ (e.g. $t_0 = 1.5 T$), the displacement response of the frame reached its peak earlier than that for $t_0 < T$, and the whole frame fluctuated about the center axis of the pseudo-static deflection curve.

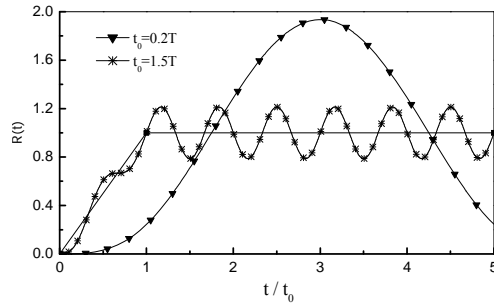


Figure 14. Variation of Dynamic Amplification Factors with the Ratio t/t_0

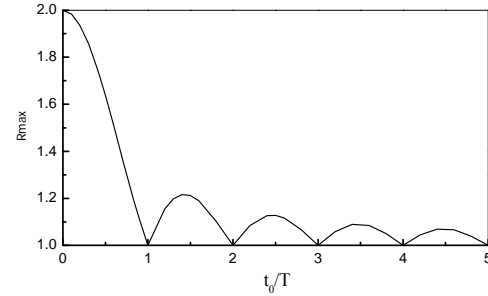


Figure 15. Variation of Dynamic Amplification Factors with the Ratio t_0/T

Figure 15 shows the variation of dynamic amplification factors against the ratios of the failure duration t_0 to the system period T . The maximum dynamic amplification factor was 2 corresponding to the immediate column removal. It decreased with the increase of the ratio. For the ratios ($\tau = t_0/T$) of 0.1, 0.2 and 0.3, the dynamic amplification factors were 1.98, 1.94 and 1.86 respectively. For ratios greater than 3, the amplification factor is smaller than 1.1. To simplify the analysis of collapse of structures, it is suggested that the effect of the failure duration of the column on the dynamic response of structures can be neglected for $\tau < 0.2$, i.e. alternate path method can be used. While for $\tau > 3$, the failure process of the structure is equivalent to static and thus its dynamic effect can be neglected, i.e. static analysis can be used. For $0.2 < \tau < 3$, the effect of failure process of the column under blast should be considered.

In a word, the failure process of the column under explosion should be considered in the assessment of progressive collapse of structures for $0.2 < t_0/T < 3$, while the alternate path method is available for $t_0/T < 0.2$ and static analysis for $t_0/T > 3$.

7. CONCLUSIONS

This paper proposed an equivalent spring model and SDOF model to simplify the analysis of progressive collapse of steel framed structures. The development and verification of these two models were presented. The influence of the failure time and residual load-bearing capacity of the column subjected to blast on the progressive collapse of structures was studied. The following conclusions can be drawn:

(1) The results from analysis of a whole frame under blast showed that the collapse resistance of the frame depended on the magnitude and duration of blast loads, which in turn affected the failure time and load-bearing capacity of the column subjected to blast. For a smaller blast load imposed in a relatively longer duration, there was some residual resistance in the damaged column which may enhance the resistance of the frame against blast-induced progressive collapse.

(2) The traditional dynamic analysis of progressive collapse of whole structures can be simplified by using an equivalent spring model. This includes two independent steps: (1) determine the failure process (failure time and residual load-bearing capacity) of the column under blast based on a member-level model; (2) replace the damaged column with an equivalent spring model considering the column failure process, and analyze the behavior of the remaining structure. The advantage of this simplification is to avoid the global structural analysis in Step 1 and also avoid the simulation of blast loads in Step 2.

(3) A SDOF model was proposed to further simplify the analysis, and to analytically determine the failure time and residual load-bearing capacity of columns under blast. A rigid-plastic model was used instead of ideal elasto-plastic model to determine the failure time of columns.

(4) The failure time and residual resistance of the damaged column had significant effect on the collapse resistance of structures. The longer the failure time of the column, the larger the residual resistance, the smaller the displacement of the structure, and the greater its collapse resistance.

(5) It was found that the dynamic behavior of structures was sensitive to the ratio of column failure time to the structural vibration period t_0/T . The larger the t_0/T , the smaller the dynamic amplification effect. It was too conservative to use a dynamic amplification factor of 2 regardless of the failure process of the damaged column, since the factor reduced to 1.86 for $t_0/T=0.3$, and for $t_0/T>3$, the factor was smaller than 1.1.

(6) For the selection of analysis methods for the blast-induced progressive collapse of structures, it was suggested that alternate path method be used for $t_0/T<0.2$, and static analyses can be used for $t_0/T>3$. For $0.2<t_0/T<3$, the effect of failure time and residual resistance of damaged columns should be considered.

ACKNOWLEDGMENTS

The work presented in this paper was supported by the National Natural Science Foundation of China with grant 51120185001, 51408418, and 51508412. This work was also supported by Natural Science Foundation of Tianjin 16JCQNJC07000.

REFERENCES

- [1] ASCE 7. American Society of Civil Engineers Standard 7 Minimum Design Loads for Buildings and Other Structures, American Society of Civil Engineers, 2010.
- [2] Song, L., Izzuddin, B.A. and Elnashai, A.S., "Integrated Adaptive Environment for Fire and Explosion Analysis of Steel Frames - Part I: Analytical Models", *Journal of Constructional Steel Research*, 2000, Vol. 53, No. 1, pp. 63-85.
- [3] Izzuddin, B.A., Song, L. and Elnashai, A.S., "Integrated Adaptive Environment for Fire and Explosion Analysis of Steel Frames - Part II: Verification and Application", *Journal of Constructional Steel Research*, 2000, Vol. 53, No. 1, pp. 87-111.
- [4] Liew, J.Y.R. and Chen, H., "Explosion and Fire Analysis of Steel Frames using Fiber Element Approach", *Journal of Structural Engineering*, 2004, Vol. 130, No. 7, pp. 991-1000.
- [5] Chen, H. and Liew, J.Y.R., "Explosion and Fire Analysis of Steel Frames using Mixed Element Approach", *Journal of Engineering Mechanics*, 2005, Vol. 131, No. 6, pp. 606-616.
- [6] Yu, H.X. and Liew, J.Y.R., "Steel Framed Structures Subjected to the Combined Effects of Blast and Fire - Part 1: State-of-the-art Review", *Advanced Steel Construction*, 2005, Vol. 1, No. 1, pp. 67-84.
- [7] Yu, H.X. and Liew, J.Y.R., "Steel Framed Structures subjected to the Combined Effects of Blast and Fire - Part 2: Case Study", *Advanced Steel Construction*, 2005, Vol. 1, No. 1, pp. 85-104.
- [8] Magallanes, J.M., Martinez, R. and Koenig, J.W. "Experimental Results of the AISC Full-scale Column Blast Test", Report. Karagozian & Case, 2006.
- [9] Turcic, F., Luketina, I. and Plisic, M., "Collapse and Rehabilitation of Steel Tanks Roof Structures", *Advanced Steel Construction*, 2007, Vol. 3, No. 4, pp. 723-736.

- [10] Yu, H., Izzuddin, B.A. and Zha X.X., "Progressive Collapse of Steel-framed Buildings: Influence of Modelling Approach", *Advanced Steel Construction*, 2010, Vol. 6, No. 4, pp. 932-948.
- [11] Demonceau, J.F. and Jaspart, J.P. "Experimental Test Simulating a Column Loss in a Composite Frame", *Advanced Steel Construction*, 2020, Vol. 6, No. 3, pp. 891-913.
- [12] Wu, K., Li, B. and Tsai, K., "Residual Axial Compression Capacity of Localized Blast-damaged RC Columns", *International Journal of Impact Engineering*, 2011, Vol. 38, No. 1, pp. 29-40.
- [13] Nethercot, D.A., Stylianidis, P., Izzuddin, B.A. and Elghazouli, A.Y. "Enhancing the Robustness of Steel and Composite Buildings", *Advanced Steel Construction*, 2011, Vol. 7, No. 1, pp. 64-85.
- [14] Wang, W.M., Li, H.N. and Tian, L., "Progressive Collapse Analysis of Transmission Tower-line System under Earthquake", *Advanced Steel Construction*, 2013, Vol. 9, No. 2, pp. 161-172.
- [15] Design of Buildings to Resist Progressive Collapse, Unified Facilities Criteria (UFC) 4-023-03, US Department of Defense (DoD), 2013.
- [16] Eurocode 1: Actions on Structures - Part 1-7: General Actions -Accidental Actions, 2010.
- [17] Progressive Collapse Analysis and Design Guidelines for New Federal Office Buildings and Major Modernization Projects, US General Services Administration (GSA), 2005.
- [18] Manual for the Systematic Risk Assessment of High-risk Structures against Disproportionate Collapse. The Institute of Structural Engineers, UK, 2013.
- [19] Li, G.Q., Sun, J.Y. and Wang, K.Q. "Research on a Simplified Frame Column Model to Resist Blast Load", *Journal of Vibration and Shock*, 2007, Vol. 26, No. 1, pp. 8-11.
- [20] Sun, J.Y., "Study on the Behavior of Steel Reinforced Concrete Columns under Blast and Impact Loads", PhD thesis, Tongji University, Shanghai, China, 2006.
- [21] Yang, T.C., "The Failure Mechanism of Steel Column under Blast Loading and its Effect on Progressive Collapse of Steel Frame", PhD Thesis, Tongji University, Shanghai, China, 2013.
- [22] Qu, H.Y., "Research on the Characteristics of Concrete-filled Steel Tubular Column Subjected to Blast Loading", PhD Thesis, Tongji University, Shanghai, China, 2011.
- [23] Pilchard, S.J. and Perry, S.H., "The Impact Behavior of Sleeved Concrete Cylinders", *The Structural Engineer*, 2000, Vol. 178, No. 17, pp. 34-42.

FINITE ELEMENT ANALYSIS OF DEMOUNTABLE STEEL-CONCRETE COMPOSITE BEAMS UNDER STATIC LOADING

V.I. Patel^{1,2*}, B. Uy^{2,3}, S.W. Pathirana², S. Wood², M. Singh² and B. T. Trang²

¹ *School of Engineering and Mathematical Sciences, La Trobe University,
Bendigo, VIC 3552, Australia*

² *Centre for Infrastructure Engineering and Safety, School of Civil and Environmental Engineering,
The University of New South Wales, NSW 2232, Australia*

³ *School of Civil Engineering, The University of Sydney, Sydney, NSW 2006, Australia*

**(Corresponding author: E-mail: v.patel@latrobe.edu.au)*

Received: 29 August 2016; Revised: 23 June 2017; Accepted: 20 August 2017

ABSTRACT: This paper investigates the innovative beam-slab connectors to enable steel-concrete framed structures to be made demountable. A computational simulation for determining the fundamental performance of the demountable composite beams with hollow core concrete slabs, profiled steel deck and bolted shear connectors is developed using the computational code ABAQUS. This numerical model was employed to compare the strength, stiffness and ductility of conventional composite beams utilising welded shear connectors with that of demountable steel-concrete beams utilising blind bolts. The bolted shear connectors not only overcome problems that prevent rehabilitation of existing composite beams with headed studs but also allow for the demountability in the composite beams. The adequacy of the developed computational models is evaluated by verifying the computational results against the corresponding experimental performance. The verification demonstrates that the computational simulations agree with the test performance. The numerical prediction indicated that the shear capacity of blind bolts used in demountable composite metal decking slabs is higher than that of welded connectors utilised in the conventional steel-concrete composite beams. It is found that the composite beams with bolted connectors can be made demountable up to a load of about 50% of the ultimate load which is greater than typical service loads. The strength of shear connectors obtained from the finite element models and experiments were compared with the predicted strength using Eurocode 4 and AS2327.1-2003. It appears that Eurocode 4 and AS2327.1-2003 provide the conservative solutions for the design of shear connector strengths.

Keywords: Demountable composite beams, bolted connectors, finite element analysis, profile slabs, solid slabs, blind bolts

DOI: 10.18057/IJASC.2018.14.3.5

1. INTRODUCTION

The global carbon emission promotes the sustainable concept of reusing the structural members. This can be achieved through changes in the constructional methods including structures to be made demountable. The steel-concrete composite beams provide the construction economy in steel-concrete framed structures owing to the combine contribution achieved from the steel beam and concrete slabs. A current construction method uses headed studs to develop the steel-concrete combine contribution. The headed studs are permanently welded over a metal deck on the steel beams before casting the concrete slabs. This constructional practice does not allow the steel-concrete composite beams to be made demountable. Therefore, structural steels used in steel-concrete composite beams need to be recycled before reusing them. However, the recycling of structural steels consumes approximately the same energy when compare with the energy consumption for manufacturing the steels from scratch.

This paper employs blind bolts in composite beams which allow these beams to be made demountable. The reusing of structural steels instead of recycling them has a great potential to provide cost effective systems and environmental benefits for constructions. The bolted shear connectors in preference to headed studs can be utilized to make composite beams demountable. Their use facilitates the deconstruction of structural elements in composite buildings. Performances of demountable steel-concrete beams with blind bolts, profiled steel decks and hollowcore planks have not been addressed previously. Therefore, this investigation presents the stiffness, strength and ductility of the demountable composite beams. Figure 1 illustrates the proposed demountable steel-concrete composite beams. The steel beams have predrilled holes on the flanges of their steel beams. The blind bolts are connected with the steel flange passing through pre-drilled holes. Oversized holes for tolerances used in the current construction practice are utilized to achieve demountability. The bolts can be removed as the head is situated on the exterior of the steel beam flange. The bolt arrangement is shown in Figure 2.

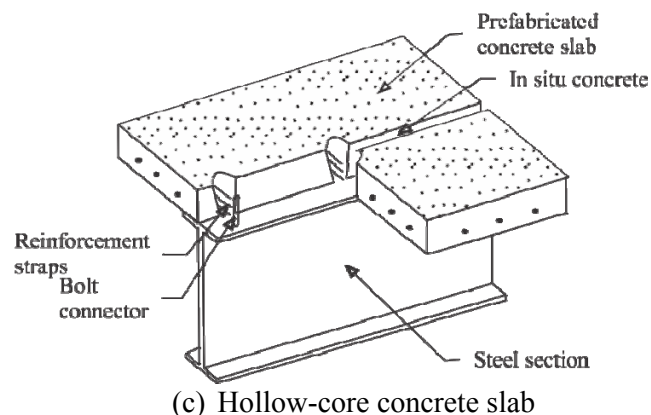
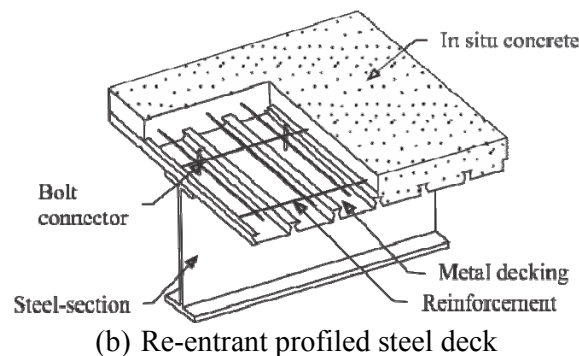
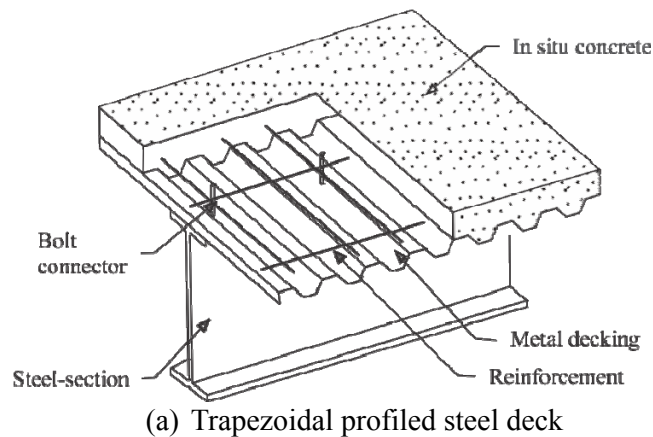


Figure 1. Demountable Steel-concrete Composite Beams with Bolted Connectors

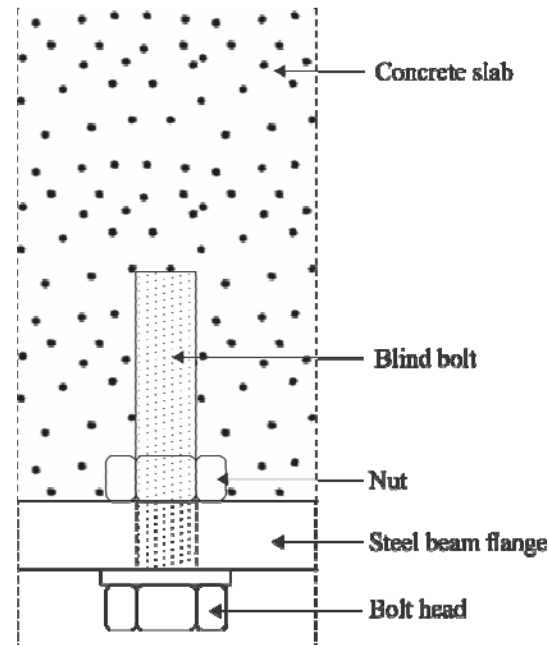


Figure 2. Bolt Arrangement in Demountable Composite Beams

Many research studies have been carried out in recent years to evaluate the shear connector behaviour for demountable construction. Lam et al. [1-2] conducted the study on the composite behavior of precast concrete slabs on steel beams. The results indicated that the stud shear capacity is affected by stud shear tensile strength, gap width, reinforcement ratio and concrete strength. Ellobody and Young [3] conducted the finite element analysis of steel-concrete beams with profiled sheeting. They reported that Eurocode 4 [4] provides the conservative solution for predicting the shear strength of composite beams. Four push-out tests on the prefabricated concrete slabs with high strength bolts and headed studs subjected to static loading were performed by Pavlović et al. [5] to evaluate the bolted shear connector performance. Test results indicated that the bolted shear connectors achieved approximately 95% of the shear strength of the welded shear studs under static shear force. However, the stiffness of the bolted connectors was 50% lesser than the stiffness of the headed studs. Previous experimental research into the demountable solid slabs and composite slabs with bolted shear connectors was conducted by Dai et al. [6], Rehman et al. [7] and Moynihan and Allwood [8]. They concluded that the steel-concrete beams were failed by concrete crushing and connector fracture. The shear resistance was achieved about 84% of the headed studs at the slip of 6 mm. Further tests on full scale beams by Mirza and Uy [9] and Pathirana et al. [10-11] illustrated that the steel-concrete composite beams could be loaded to very high service loads and the blind bolts could still be removed. The experimental studies conducted by Loh et al. [12], Wang et al. [13] and Mirza and Uy [14] illustrated the benefits of using blind bolts connections to concrete-filled steel tubular columns. These types of joints can be made demountable as illustrated by Liu et al. [15] and Ataei et al. [16]. The numerical research on the computational analysis of the demountable composite beams utilizing profiled steel decks and blind bolts was performed by Ban et al. [17] and Uy et al. [18] who concluded that the structural connections can be demounted at approximately 50% of the ultimate load.

The composite beam exhibits not only the axial compression or tension but also the hogging or sagging bending moments. Vasdravellis et al. [19-22] studied the behaviour of composite beams under the effects of sagging-hogging bending moments and axial compression-tension. The results indicated that ultimate moment capacity of a composite beam is considerably decreased when the compression or tension load applies in the composite section. It is also noted that the local buckling

of the steel beam for these combined loading conditions is found to be more pronounced which reduces the ductility of composite section. It is suggested that the use of longitudinal stiffeners in the web of the steel beams at the internal support regions of continuous beam reduces the web buckling and increase the rotational capacity of the composite section. A simple design equation is proposed for determining the interaction of axial compression and bending moments of the composite beams.

Further research on the demountable connections for the composite metal decking beams is needed. In addition, the hollowcore planks on steel beams are also a very popular method of construction and demountable connection to these structural forms needs to be evaluated. The broad purpose of this paper is to promote the reuse of structural members by utilizing innovative beam-slab connectors that allow demountability in composite steel-concrete beams with hollow core concrete slab and steel decks. The Dassault Systemes SIMULA Abaqus program was utilized for the simulation of demountable composite beams. Two profiled steel decks, trapezoidal and re-entrant profiled steel deck were considered in the computational analysis. High strength blind bolts were used in the analysis of the demountable composite beams. The demountable composite metal decking beams were simulated by taking into account for the geometric and material nonlinearities. The finite element computational method was utilized to simulate the headed shear stud strength, bolted connector capacity, load-slip characteristics and modes of failure. The effects of concrete compressive strengths, slab types, shear connector types and metal decking thickness on the performance of the steel-concrete metal decking slabs were investigated. The developed computational models were utilized to examine the influences of these material and geometric variables on the strength, stiffness and ductility of the demountable composite beams. Finally, international standards were employed to predict the shear strength of connectors.

2. COMPUTATIONAL ANALYSIS – FINITE ELEMENT METHOD

2.1 Basic Concept

A three-dimensional half model of the steel-concrete beams was constructed for the nonlinear inelastic analysis using the ABAQUS finite element code [23]. Three models were developed for composite beams with blind bolts as depicted in Figure 3. The corresponding finite element model was also constructed for composite steel-concrete beam with headed studs. This computational model was assessed by verifying the predicted behaviour with test performance presented by Uy and Bradford [24] and Mirza et al. [25]. The finite element analysis was conducted using ABAQUS/Implicit static general procedure. Material stress-strain characteristics, surface-to-surface interactions, constraints and boundary conditions were defined to accurately simulate the experimental performance.

2.2 Geometry, Finite Element Types and Mesh Size

The steel-concrete composite beams with metal decking slab and hollow core concrete slab are shown in Figure 3. The geometric and material properties for steel beams, bolts and concrete are considered based on the current limits set in the various Australian Standards [26-29]. The composite metal decking beams were symmetrical in the longitudinal direction so only half 3-D model was constructed to minimize the computational time. The steel beams, blind bolts, headed studs and concrete slabs were discretized using the eight-node linear hexahedral solid elements with reduced integration and hourglass control (C3D8R). The finite elements with reduced-integration were selected because they reduced the analysis time. These finite elements were employed with a fine mesh to maintain the accuracy of the simulation. A sensitivity study was

conducted to evaluate the reasonable mesh size. The reinforcing bars were meshed with two-node linear three-dimensional truss elements (T3D3). The typical geometries and element types used in modelling of the composite metal decking beams are illustrated in Figure 4.

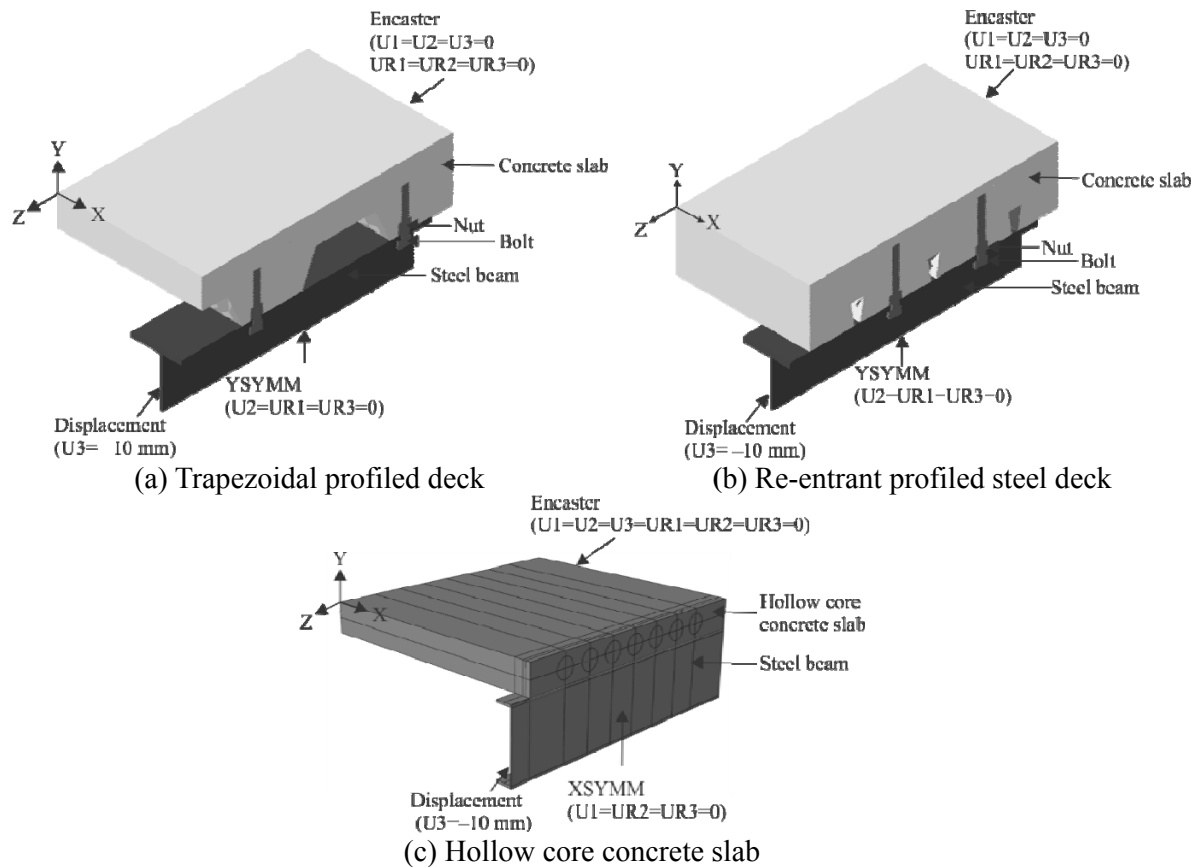


Figure 3. Finite Element Models for Demountable Composite Beams

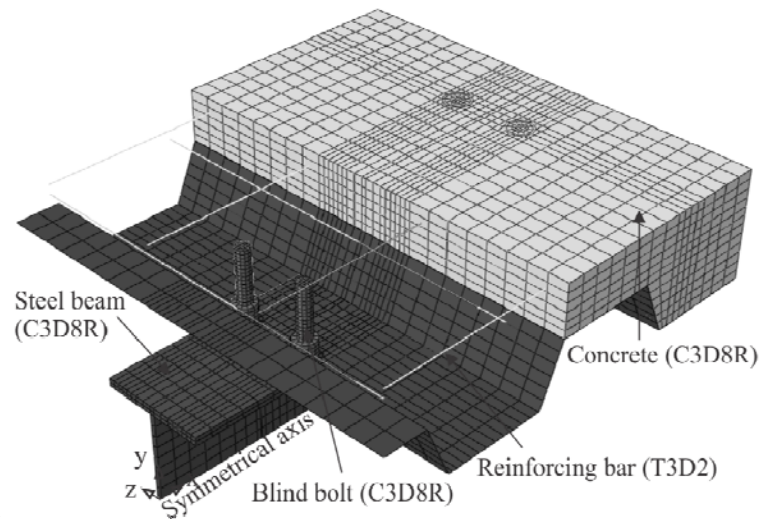


Figure 4. Finite Element Models with Geometries, Mesh Size and Element Types

2.3 Surface-To-Surface Interaction, Boundary Conditions and Load

Appropriate constraints were used to define the interaction between beam and bolt, decking and bolt, concrete and bolt, decking and concrete, decking and beam and bolts and nuts. The surface-to-surface contact with finite sliding was employed. The penetration between the contacted components was restricted by using 'Hard Contact' in the normal direction. The tangential characteristic of the contact was simulated by selecting the penalty friction formulation. The surface-to-surface interactions of the composite metal decking beam components are listed in Table 1. As shown in Figure 5(a), the surface-to-surface interaction was applied to the steel beam and bolt surfaces. The steel flange surfaces were taken as a master surface and the bolt shank surfaces were selected as a slave surface. It can be seen from Figure 5(b) that the contact between the decking and bolt was analyzed using the interaction algorithm. The decking and bolt surface is selected as a master and slave surface, respectively. The contact interaction was also used at the concrete-to-bolt (Figure 5c), decking-to-concrete (Figure 5d) and decking-to-beam (Figure 5e) interfaces. It was found from the push-out experiment that the nut surface did not separate from the bolt surface [11]. Therefore, the bolt and nut were created as a single part as shown in Figure 5(f). In addition, reinforcing rebar is located inside the concrete slab as depicted in Figure 4. The embedded element method was employed to model the rebar in the concrete slab. The embedded element method is utilized to specify an element which lie embedded in a host elements. The response of the host elements is used to constrain the translational degrees of freedom of the embedded nodes. In this analysis, the concrete slab is defined as host regions and the reinforcement is considered as embedded region. It is assumed that the perfect bond exists between the reinforcement and concrete [19].

Table 1. Surface-to-surface Interaction of Composite Beam Components

Name	Surface selection		Contact type	Interaction property	
	Master surface	Slave surface		Tangential behaviour: Friction coefficient	Normal behaviour
Bolt-steel beam	Steel beam	Bolt	Interaction	0.3	Hard contact
Bolt-steel deck	Steel deck	Bolt	Interaction	0.3	Hard contact
Concrete slab-bolt	Concrete slab	Bolt	Interaction	0.3	Hard contact
Steel deck-concrete slab	Steel deck	Concrete slab	Interaction	0.3	Hard contact
Steel beam-steel deck	Steel deck	Steel beam	Interaction	0.6	Hard contact
Concrete slab-reinforcement	-	-	Embedded	-	-

The symmetric boundary conditions were defined at the middle of the beam web. The symmetrical axis for the demountable composite metal decking beams is depicted in Figure 4. The surface along the middle of steel beam were restrained from translating in the Y direction and rotating about X and Y directions for applying the symmetrical conditions. The base of the concrete slab was fixed in all directions. This is to ensure that the concrete slab does not move, and only the steel beam is translated.

The simulation of the composite metal decking beams is generally conducted by using the static analysis procedure. A uniform displacement on the upper end of the beam was applied to model the loading used in the tests. A uniform displacement load of -10 mm was applied. The nonlinear inelastic analysis of demountable composite beams requires multiple steps. The surface-to-surface interactions were established in the first step of analysis for the contact formulation which may cause the convergence problems in the consecutive steps. The bolted shear connectors were pre-tensioned to loads of 20 kN in the second step. The deflection control method utilising the static general procedure is used in the nonlinear analysis to determine the slip and load in the third step. It

should be noted that the analysis of composite beams generally faces the convergence problems. The initial increment in the analysis step was adjusted to overcome the convergence problems.

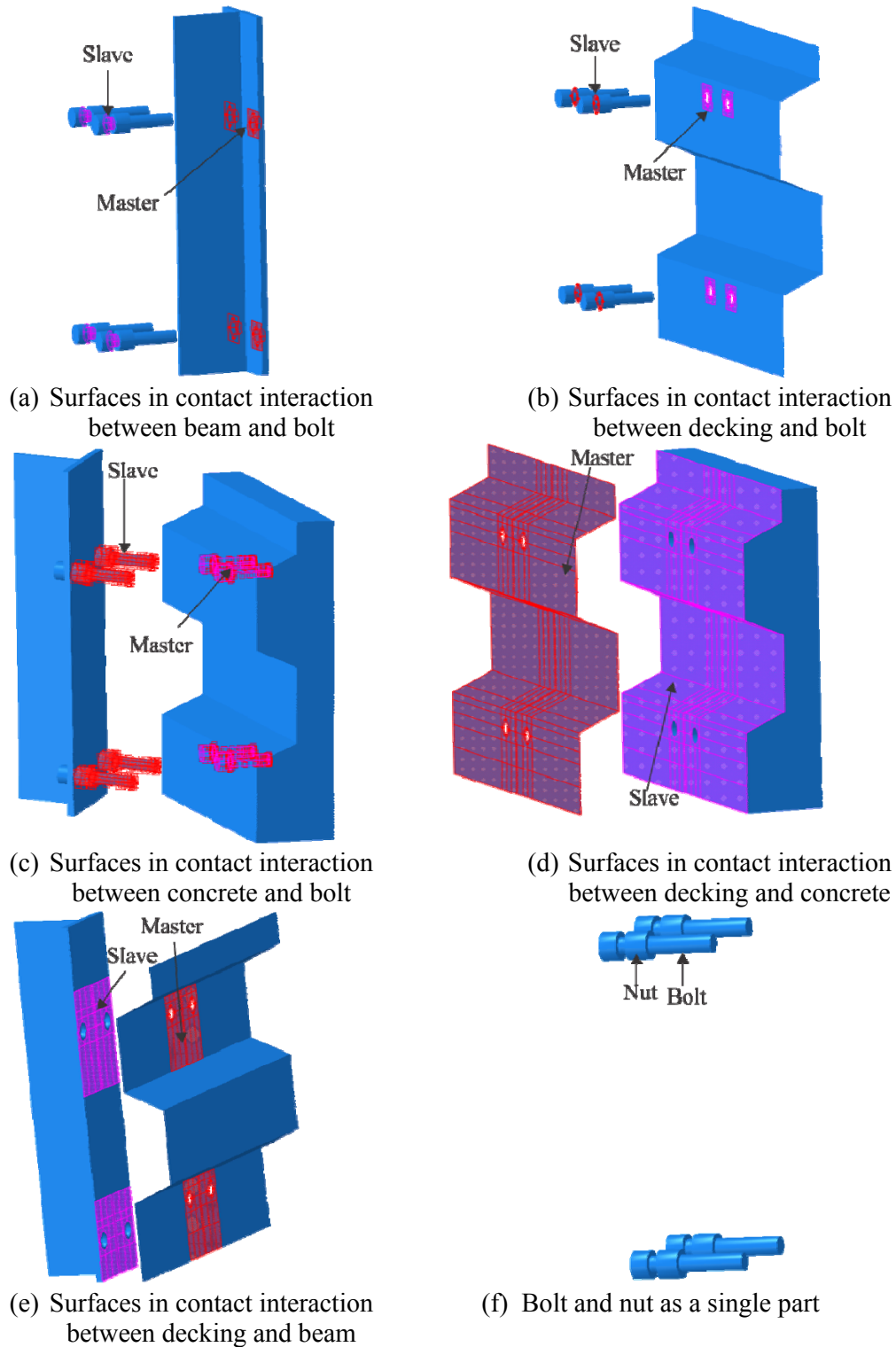


Figure 5. Interaction and Constrain Surfaces

2.4 Material Constitutive Models

2.4.1 Material characteristics of structural steels

The structural steel has the same material characteristics in compression and tension. The steel has the elastic linear relationship up to the yield stress which is followed by strain hardening before failure. Figure 6(a) depicts the two-stage linear material characteristics of steel subjected to compression, in which ϵ_{sy} denotes for steel yield strain, ϵ_{su} is steel ultimate strain, f_{sy} is the yield strength and f_{su} represents the steel ultimate strength. The stress-strain curves shown in Figure 6(a) are employed in the computational simulation for simulating the material behaviour of the steel beam, reinforcing bar, headed connectors and bolts.

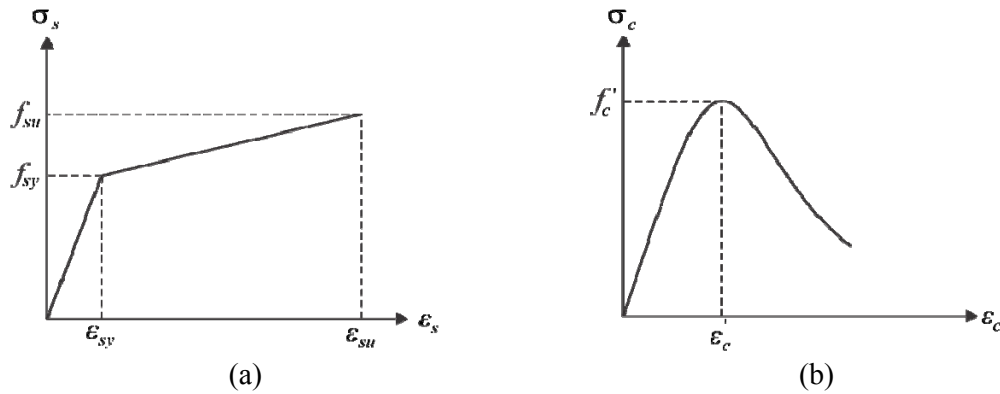


Figure 6. Material Constitutive Models:

(a) Strucutral Steel for Profiled Deck, Bolts, Steel Beam and Studs and (b) Concrete

2.4.2 Stress-strain characteristic for concrete

A compressive and tensile plasticity damage model was utilised to analyse the constitutive performance of concrete. This damage is defined with the concrete compression hardening and concrete tension stiffening options in Abaqus. The plasticity parameters suggested by Pathirana [10] are employed in the computational simulation for defining the plasticity parameters. The behaviour of concrete was simulated with the elastic-plastic approach with strain softening. The stress-strain response for concrete is depicted in Figure 6(b). The concrete stress is calculated based on the equations given by Carreira and Chu [30] as

$$\sigma_c = \frac{\left(\frac{\epsilon_c}{\epsilon'_c}\right) \lambda f'_c}{\left(\frac{\epsilon_c}{\epsilon'_c}\right)^\gamma - 1 + \lambda} \quad (1)$$

in which ϵ_c denotes the compressive concrete strain, σ_c represents the concrete stress in compression, f'_c is cylinder concrete compressive strength, ϵ'_c denotes the strain corresponding to f'_c and γ is expressed by

$$\gamma = 1.55 + \left| \frac{f'_c}{32.4} \right|^3 \quad (2)$$

in which f'_c is in MPa and the strain ϵ'_c is taken as 0.002.

For concrete under tension, the stress of concrete is direct proportion to the concrete strain before concrete cracking which is taken as $0.1f'_c$. After attaining concrete cracking, the concrete stress is defined by fracture energy (G_F) which is given by Bažant and Becq-Giraudon [31]

$$G_F = \left(0.0469d_{\max}^2 - 0.5d_{\max} + 26\right) \left(\frac{f'_c}{10}\right) \quad (3)$$

where d_{\max} stands for the maximum coarse aggregate size in mm and it is taken as 20 mm.

2.4.3 Failure criteria

The failure of the composite beams in the finite element analysis was identified by using the specific failure criteria corresponding to the ultimate strength of the various section components. The failure of the composite beam in the analysis was identified by concrete crushing, shear connection failure and buckling of steel beams. The concrete crushing was defined when the principal compressive strain at a point reached the crushing strain, equal to 0.004. Shear connection failure was defined when the recorded slip at a shear connector reached a value of 6 mm. Buckling of steel beams and decking can explicitly captured in Abaqus so it was identified from the deformed shape of the model [19].

3. VERIFICATION

The evaluation of the developed finite element models are examined by the verifications between the computational and corresponding test results. The shear connector capacities and load-slip curves of the composite metal decking beams are included in the evaluation of the finite element model. The shear connector capacities for composite metal decking beams obtained from the simulation were compared with test data in Table 2. The shear connector capacities obtained from the computational simulation agree with tested specimens. The mean shear connector capacity determined using the finite element simulation is 1.07 times the test data. The standard deviation of P_{FEA}/P_{Test} is 0.09 while its coefficient of variation is 0.08.

Table 2. Comparison of Shear Connector Capacities for Tested Specimens

Test	P_{Test} (kN)	P_{FEA} (kN)	P_{EC4} (kN)	$P_{AS2327.1}$ (kN)	P_{FEA}/P_{Test}	P_{EC4}/P_{Test}	$P_{AS2327.1}/P_{Test}$
Profiled slab	72	79.3	66	68	1.10	0.92	0.95
Solid slab	86.3	98.8	88.8	88	1.14	1.03	1.02
Hollow-core	105.8	103.0	100.5	103	0.97	0.95	0.97
Mean					1.07	1.03	0.98
Standard deviation (SD)					0.09	0.06	0.04
Coefficient of variation (CoV)					0.08	0.06	0.04

The load-slip curves for composite beams predicted by the computational simulation are verified by the test data provided by Uy and Bradford [24] and Mirza et al. [25]. Figure 7(a) depicts the load-slip curves for the steel-concrete composite beams determined from the finite element simulation and obtained from the experiments performed by Uy and Bradford [24] for composite beam with hollow core concrete slab. The load-slip curves determined from the finite element simulation reasonably agree with the test data. The linear elastic stiffness of the load-slip curves determined from the finite element simulation is a little lower than that of the test data. However,

the computational load-slip response agrees with the test data near the peak load level. The finite element simulation was employed to determine the load-slip curves of the steel-concrete composite beams investigated by Mirza et al. [25]. Figure 7(b) illustrates the evaluation of tested and numerical load-slip responses for the steel-concrete composite trapezoidal metal decking slabs. The figure demonstrates that the finite element simulations predict well the load-slip response for the experimented composite beam up to the peak load level. The computed linear elastic stiffness of the steel-concrete composite beams matches with the test data. However, the tested load-slip response differs from the simulated one after attaining the ultimate load. This is due to the fact that the microcracks observed in the concrete resulting in the load reduction [32], while the finite element analysis does not consider the microcracks in modelling of concrete element. To further examine the evaluation of the nonlinear analysis, the computational model developed was utilised to predict the load-slip curves for the steel-concrete composite beams with re-entrant profiled steel deck tested by Mirza et al. [25]. The computational and experimental load-slip curves for composite beam with re-entrant profiled steel deck are given in Figure 7(c). It can be observed from the figure that both tested and simulated curves closely match up to the load level about 400 kN and after that the tested value deviates from the simulated one. This is because the microcracks observed in the concrete resulting does not consider in modelling of concrete element.

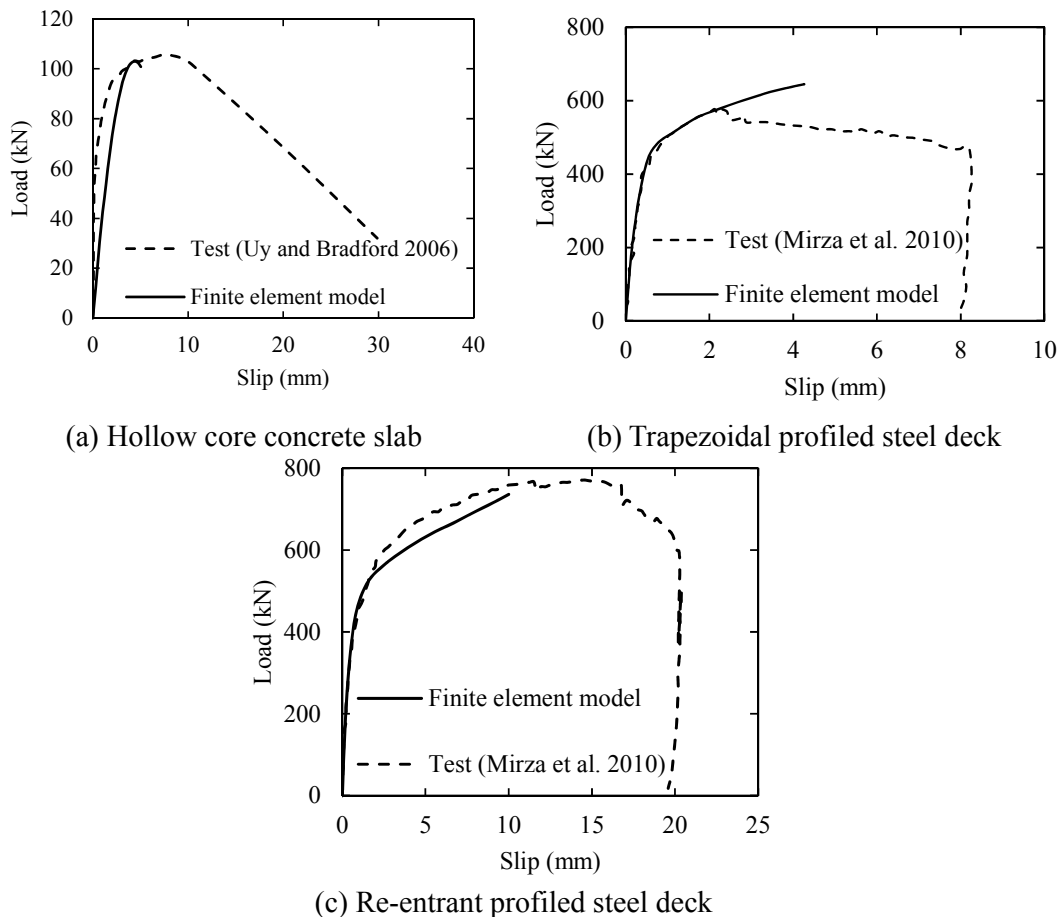


Figure 7. Comparison of Numerical and Experimental Load-slip Curves for Composite Beams

4. RESULTS AND DISCUSSION

Figure 8(a) shows a typical failure mode of concrete in composite beam. It can be seen from the figure that the bolt rotates and the inclination of the embedded nut pushes the concrete. This results in a prying out force which is responsible for concrete pull out of high strength bolt. Consequently, the failure mode is concrete failure as the removal of the bolt begins before the yielding of the shank. The excessive deflection in the concrete slab indicates the concrete slab crushing. The steel beam rupture is also observed from the excessive strain within the cross-section. It can also be seen from Figure 8(a) that the metal deck tends to separate from the concrete slab. It means that the concrete slab is delaminated from the steel deck, which results in the concrete slab tends to move up and slide over the steel deck.

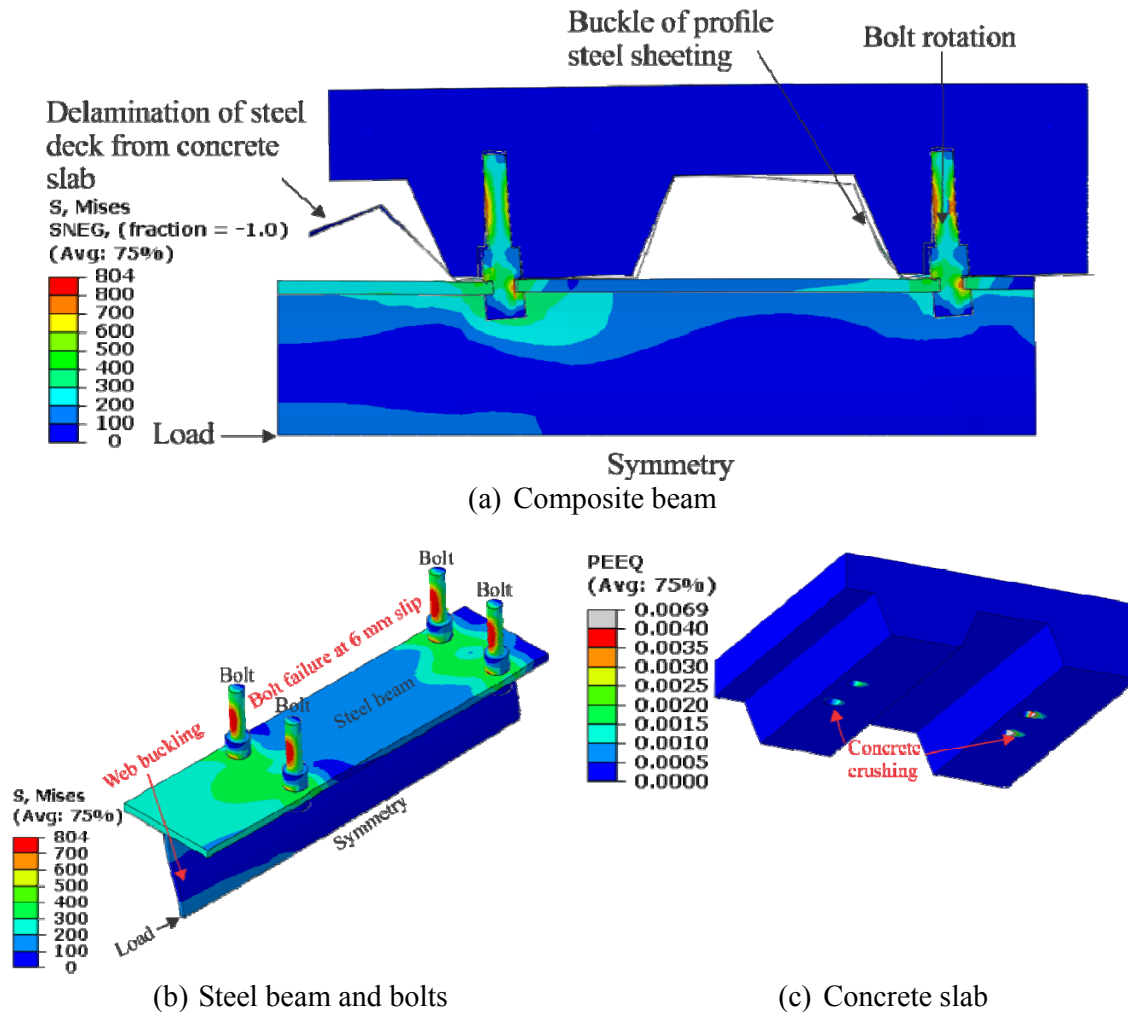
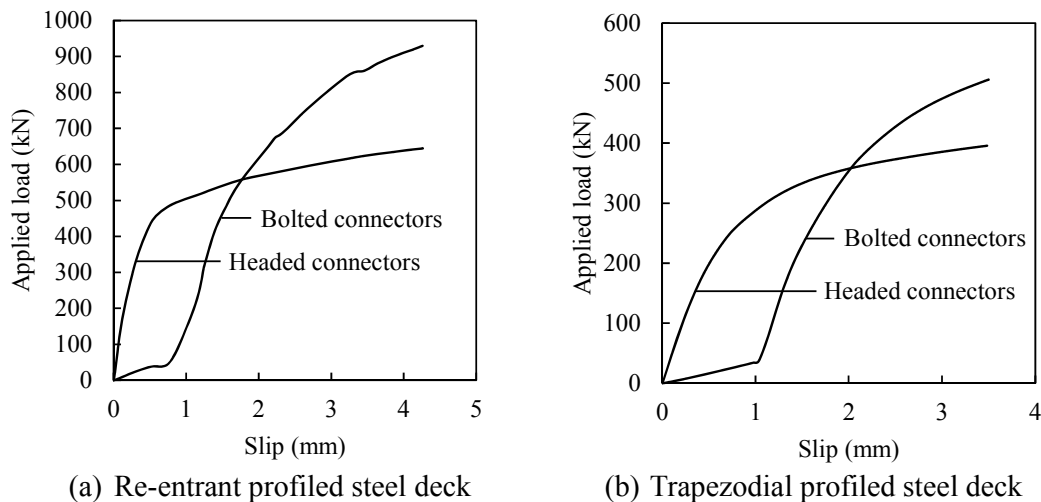


Figure 8. Failure Mode of Demountable Composite Beams with Blind Bolts

The failure mode which are observed experimentally for composite beams with bolted connectors was compared with that obtained from the finite element model. Figure 8(a) depicts the stress contour at failure of composite beams predicted from the finite element model. The failure mode of composite beam with bolted connectors was a combination of shear failure of the bolted connectors (Figure 8b) and concrete crushing failure (Figure 8c) [11]. The shear connector failure is defined at the slip of 6 mm as shown in Figure 8(b). The bolted connector failure results in the slab uplifting and separating from the steel beam as shown in Figure 8(a). The deformed shape of steel beam in Figure 8(b) illustrates the web buckling failure of steel beam under axial compression. It should be

noted that the failure criteria for the concrete slab are found in the regions in front of the bolted connectors at the concrete compressive strain of 0.004 shown in Figure 8(c). The concrete crushing failure in front of bolted connectors was explained in details experimentally by Pathirana et al. [11] for the study of push-out tests with bolted connectors.

The comparison of load-deflection curves for headed stud and high strength bolts is shown in Figure 9. It can be seen from the figure that the behavior of the headed stud and bolted connectors differs substantially. The high strength bolt exhibits lower stiffness at serviceability loads compare with welded studs. Initially, the bolt experiences a slip of 1 mm at low loads, which is due to the clearance space surrounding the shank of the bolt. The high strength bolt was modelled to sit on the steel flange, however in practice after fastening the bolt would experience some tensile forces which would result in a higher initial stiffness until full bearing in the hole is achieved. Once closure in the bolt-to-hole clearance has been achieved the stiffness of the bolt connection increases linearly up to load level 210 kN. The bolt experiences nonlinear stiffness compared to the stud as shown in Figure 9.



(a) Re-entrant profiled steel deck (b) Trapezoidal profiled steel deck
Figure 9. Influences of Type of Connectors on the Applied Load-slip Responses of Demountable Composite Metal Decking Slabs

The demountability of metal decking beams is characterized by the elasticity of the bolted connectors and steel beams. This elasticity under increasing loads is maintained without undergoing the plastic deformation. The demountability of composite beams greatly depends on the elastic deformation of steel components because it cannot be achieved with large plastic deformation. The zero equivalent plastic strain (PEEQ) can be utilized to determine the plastic deformation in the composite beams. The numerical results indicate that the composite beams can be demounted for the load, where the PEEQ is observed to be zero, which is about 50% of the ultimate load and greater than typical service loads which are usually less than 40% of the ultimate load.

5. PARAMETRIC STUDY

The structural behaviour of demountable steel-concrete metal decking slabs is characterised by determining the slip between the composite slabs and steel beam. The slip may be described as the longitudinal displacement between the composite metal decking slabs and steel beams [33]. The behaviour of demountable composite metal decking beams depends on concrete compressive strengths, profiled steel deck thickness and shear connector positions. A small range of geometric and material parameters are covered in the experimental test program so the numerical models are

utilised to examine the influences of the various geometric and material changes that would be reasonably be expected in Australian construction. Therefore, the geometric properties are varied consistently with the range of steel cross-section sizes which are typically available in Australia. Bolt sizes and strength are also varied with respect to those commonly available in Australian construction. Concrete and steel material properties are varied based on the current limits set in the various Australian Standards for Concrete, Steel and Composite Structures [26-29]. In this parametric study, each bolt has provided with a 1 mm of clearance in the oversized holes. Therefore, the initial 1 mm of slip occurs before the bolt contact with the side of the hole. The size of the bolted connectors, concrete slab, reinforcement and geometry of the metal decks are all kept constant in the parametric analysis.

5.1 Influence of Concrete Slab Strength

The elastic modulus of the concrete relies on its compressive strengths. The elastic modulus of concrete increases with an increase in the compressive strength. Therefore, elastic stiffness of the composite metal decking slabs is influenced by the concrete slab strengths. The influences of concrete slab strengths on the load-slip curves of the demountable composite metal decking slabs were studied. The normal strength concrete with compressive strengths of 27 and 32 MPa provided in Australian Standard AS 3600-2009 (Clause 3.1) [29] was used in the computational simulations. The load-slip responses for the demountable composite metal decking slabs with different concrete slab strengths are illustrated in Figure 10. Increased concrete slab strengths tend to increase the ultimate strength of the demountable composite metal decking slabs. An increased concrete compressive strength from 25 MPa to 32 MPa increases the ultimate capacity by 20% for steel-concrete composite beam with trapezoidal profile steel deck while it increases the ultimate strength by 2.6% for steel-concrete composite beam with re-entrant profiled steel deck. The elastic linear stiffness of the steel-concrete composite beams with profiled steel decks increases with an increase in the concrete slab strength.

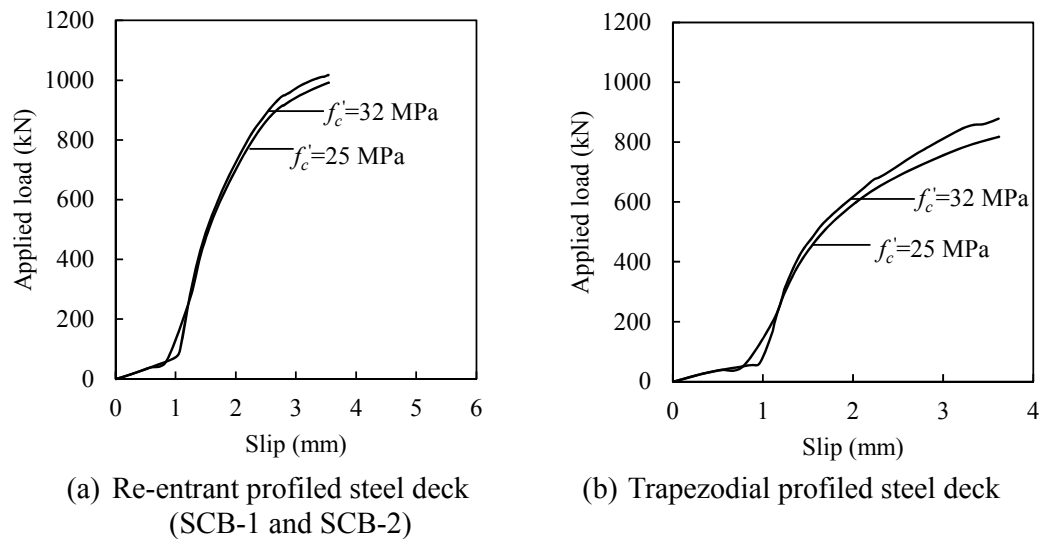


Figure 10. Influences of Concrete Slab Strengths on the Applied Load-slip Responses of Demountable Composite Metal Decking Slabs

For re-entrant metal decking, the elastic linear stiffness of the demountable composite metal decking with concrete slab strengths of 25 MPa and 32 MPa is determined as 529 kN/mm and 1109 kN/mm, respectively. For trapezoidal metal decking, the initial stiffness of the demountable composite metal decking with concrete slab strengths of 25 MPa and 32 MPa is calculated as 439 kN/mm and 503 kN/mm, respectively.

5.2 Influence of Profiled Slab and Solid Slab

The trapezoidal profiled metal decking are increasingly utilised in steel-concrete framed structures because they allow large spans without propping and plywood formwork. The structural element of the steel-concrete composite beams with trapezoidal profiled steel decking can easily be separated for subsequent reuse. This makes the composite metal decking slabs demountable at the end of its service life. The stiffness, strength and ductility of the profiled slabs and solid slabs was studied experimentally and numerically by Mirza et al. [9, 25]. The finite element model was utilised to examine the effects of profiled slab and solid slab on the load-slip curves for composite beams. Figure 11 illustrates the effects of profiled slab and solid slab on the load-slip curves for composite beams. The figure shows that the initial stiffness for the profiled slabs and solid slabs are almost same up to the loading level of 400 kN. It can be seen from the figure that after attending the loading level of 400 kN, the profiled slab is stiffer than the solid slabs. This is due to the metal decks contribute in achieving the higher stiffness in profile slabs when compared with solid slabs. It should be noted that the ductility of the solid slabs is higher than that of the profiled slabs. This is because the solid slab failed in stud fracture while the profile slab failed by concrete crushing. Furthermore, the ultimate strength of the solid slabs is higher than that of the profiled slabs.

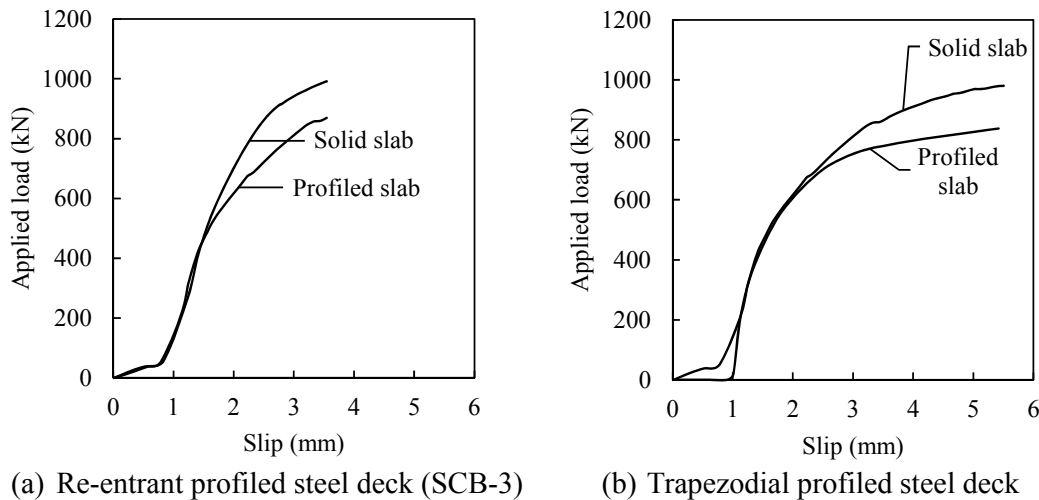


Figure 11. Influences of Slab Types on the Applied Load-slip Responses of Demountable Composite Metal Decking Slabs

5.3 Effects of Shear Connector Type (Headed vs Bolted)

Test results indicated that blind bolts can be utilised in the composite metal decking beams more efficiently than headed stud connectors [10]. Blind bolt connectors are connected through the steel beam and profiled decks into the composite slabs. These bolts can be removed as the bolt head is situated on the steel beam web, which allows for ease of dismantling. The finite element model is utilised to evaluate the influence of using oversized holes for demountability on composite beams. Figure 9 depicts the effects of bolted shear connectors and headed studs on the load-slip curves for composite beams with steel decks. It can be observed from the figure that the use of bolted shear connectors tends to increase the ultimate strengths of composite beams. This is attributed to the fact that the yield strength of bolted shear connectors is higher than that of headed studs. It can also be seen from the figure that the initial 1 mm slip is noted with the use of bolted shear connectors. This is due to the oversized hole arrangements that are initially provided to achieve demountability in composite beams. The stiffness of blind bolts is much lower than that of welded shear stud connectors.

5.4 Effects of Profiled Metal Decking Thickness

The finite element model was employed to study the effects of profiled steel deck thickness on the behaviour of demountable steel-concrete composite beams. The thickness of the profiled steel deck was 0.5 mm and 1.0 mm. The effects of the sheeting thickness on the behaviour of centrally placed studs with the 1 mm rounded gap between the stud and steel beams. Figure 12 shows the load-slip curves for demountable steel-concrete composite beams with different profiled steel deck thicknesses. It can be observed that the profiled steel deck thickness does not have a significant effect on the initial stiffness of steel-concrete composite beams. An increase in the profiled steel deck thickness increases the ultimate strength of demountable composite beams. It is suggested that the behaviour of demountable structures depends on the concrete and shear connector interactions.

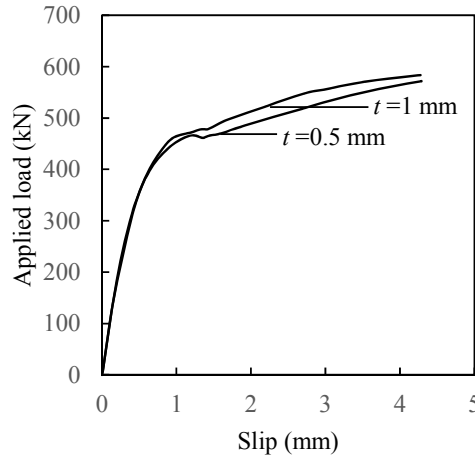


Figure 12. Influences of Profiled Thickness on the Applied Load-slip Reponses of Demountable Composite Metal Decking Slabs

6. DESIGN CONSIDERATIONS

For the design of shear connectors in composite beams, the engineers are generally interested in finding the strength which each stud transfers under shear. The design equations for the shear resistance of headed studs were given in various international standards [4, 28]. The Australian Standard, AS2327.1-2003 (Clause 8.3.2.1) [28], provides the design rules for the shear connectors, which are expresses by

$$f_{vs} = \begin{cases} 0.63d_{bs}^2 f_{uc} & \text{Shear stud fails by fracture of the weld collar} \\ 0.31d_{bs}^2 \sqrt{f'_{cj} E_c} & \text{Concrete cone failure surrounding the stud} \end{cases} \quad (4)$$

in which d_{bs} represents the shank diameter of stud, f_{uc} denotes the ultimate strength of the stud material, f'_{cj} is the concrete characteristic cylinder strength, E_c is the elastic modulus of concrete which is expressed as:

$$E_c = \rho_c^{1.5} 0.043 \sqrt{f'_{cj}} \quad (5)$$

in which ρ_c is taken as 2100 kg/m³ based on the design guideline given in Australian Standard AS3600-2009 [29].

The Eurocode 4-Clause 6.6.3.1 [4] equation for the same failure modes is given by

$$P_{Rd} = \begin{cases} 0.8f_u(\pi d^2/4)/\gamma_v & \text{Shear stud fails by fracture of the weld collar} \\ 0.29\alpha d^2 \sqrt{f_{ck} E_{cm}} / \gamma_v & \text{Concrete cone failure surrounding the stud} \end{cases} \quad (6)$$

in which d is the shank diameter which is varied between 16 mm and 25 mm, f_u is the ultimate strength of the study material which is not greater than 500 MPa, f_{ck} is the concrete characteristic cylinder strength, h is the overall height of stud, γ_v is a partial safety factor, taken as 1.25 for the ultimate limit state and α is expressed by

$$\alpha = \begin{cases} 0.2h/d + 0.2 & \text{for } 3 \leq h/d \leq 4 \\ 1 & \text{for } h/d > 4 \end{cases} \quad (7)$$

In Eq. 6, E_{cm} is the average concrete elastic modulus which is determined as

$$E_{cm} = 22000 \left(\frac{f_{ck} + 8}{10} \right)^{1/3} \quad (8)$$

Lam et al. [1] and Lam and Uy [34] reported that the shear strength of an automatically welded stud with a normal weld collar in a hollow-core slab is determined by

$$P_{RD} = 0.8f_u(\pi d^2/4)/\gamma_v \quad (8)$$

or

$$P_{RD} = 0.29\alpha\beta\epsilon d^2 \sqrt{\omega f_{cp} E_{cp}} / \gamma_v \quad (9)$$

It is should be noted that P_{RD} is taken as the smaller of Eq. 7 and 8, in which d is the shank diameter, f_u is the ultimate tensile strength of stud material, β is the reduction factor which considers the gap width g (mm) and it is given by $0.5(g/70 + 1) \leq 1.0$, and $g \geq 30$ mm, ϵ is the reduction factor which considers the diameter ϕ of transverse high tensile tie steel (grade 460) and is determined by $0.5(\phi/20 + 1) \leq 1.0$, and $\phi \geq 8$ mm, ω denotes a transverse joint factor which is given by $0.5(w/600 + 1)$, f_{cp} represents the average concrete cylinder strength of the insitu and precast concrete and E_{cp} illustrates the average elastic modulus of the insitu and precast concrete.

The partial safety factor (γ_v) is considered as 1.25 for the ultimate limit state. The existing Australian Standard, AS2327.1-2003 [28], formula given in Eq. 4 can be modified by considering the safety factor which account in Eqs. 7 and 8. Therefore, the equations for the shear strength used in Australian construction to account for the strength reductions in hollow core slab is given as

$$f_{vs} = \begin{cases} 0.63d_{bs}^2 f_{uc} & \text{Shear stud fails by fracture of the weld collar} \\ 0.31d_{bs}^2 \beta \epsilon \sqrt{\omega f_{cj}' E_c} & \text{Concrete cone failure surrounding the stud} \end{cases} \quad (10)$$

The shear strengths of connectors obtained from the experiments reported by Uy and Bradford [24] and Mirza et al. [25] are compared with the current design rule given in the AS 2327.1-2003 [28] for solid and composite slabs. The AS2327.1-2003 [28] equation for shear strengths of connectors is given as

$$f_{vs} = 0.63d_{bs}^2 f_{uc} \quad (11)$$

in which d_{bs} represents the shank diameter of headed studs.

The shear strength of bolted connectors for composite beams predicted by the finite element models and design codes are compared in Table 3. Eurocode 4 [4] and AS2327.1-2003 [28] reasonably predicts the shear strength of bolted connectors. The mean ratio of shear connector strength determined utilising the finite element model and Eurocode 4 [28] and is 1.05 with a standard deviation of 0.05 and a coefficient of variation of 0.04. The mean ratio of shear connector capacities predicted using the finite element model and AS2327.1-2003 [28] is 1.07. The standard deviation of $P_{AS2327.1}/P_{Test}$ is 0.05 and its coefficient of variation is 0.05.

Table 3. Comparison of Shear Strengths obtained from
FE Model and Design Standards for Re-entrant Profiled Steel Deck

Specimens	d_{bs} (mm)	f_c' (MPa)	P_{FEA} (kN)	P_{EC4} (kN)	$P_{AS2327.1}$ (kN)	P_{EC4}/P_{FEA}	$P_{AS2327.1}/P_{FEA}$
SCB-1	19	20	69	66	67	0.95	0.97
SCB-2	19	25	78	82	83	1.05	1.07
SCB-3	19	32	101	99	100	0.98	0.99
Mean						1.05	1.07
Standard deviation (SD)						0.05	0.05
Coefficient of variation (CoV)						0.05	0.05

7. CONCLUSIONS

The reuse of structural steels by using the beam-slab connectors which allow demountability has been promoted in this paper. A finite element model for simulating the behaviour of bolted shear connectors in a demountable composite beam with hollow core concrete slabs, profiled steel decks and bolted shear connectors has been developed. The bolted connectors between the steel beams and metal decking slabs allow the composite beams to be made demountable. The finite element model takes into account for the effects of nonlinear geometric and material characteristics. The finite element model can accurately predict the load-slip responses of composite beams with profiled steel deck. This paper has provided numerical results on the behaviour of demountable composite beams with various parameters including the effects of concrete compressive strengths, bolted shear connectors, welded studs, solid slabs and composite slabs. The plastic deformation in the steel-concrete composite beams was characterized using the equivalent plastic strain (PEEQ). It was found that the composite beams can be dismantled until the steel beam and bolted connectors maintain its elastic deformation without any plastic damage. The composite beams can be demounted up to about 50% of the ultimate load and this is greater than typical service loads which are usually less than 40% of the ultimate load. Eurocode 4 [4] and AS2327.1-2003 [28] give the

reasonable prediction for the shear capacity of composite beams. The concept of reusing structural steels presented in this paper has the potential to provide significant savings and environmental benefits for construction.

ACKNOWLEDGMENTS

The research presented in this study is funded by the Australian Research Council (ARC) under its Discovery Scheme (Project No: DP140102134). The research funding is gratefully acknowledged.

REFERENCES

- [1] Lam, D., Elliott, K.S. and Nethercot, D.A., "Push-off Tests on Shear Studs with Hollow-cored Floor Slabs", *The Structural Engineer*, 1998, Vol. 76, No. 9, pp.167-174.
- [2] Lam, D., Elliott, K.S. and Nethercot, D.A., "Parametric Study on Composite Steel Beams with Precast Concrete Hollow Core Floor Slabs", *Journal of Constructional Steel Research*, 2000, Vol. 54, No. 2, pp. 283-304.
- [3] Ellobody, E. and Young, B., "Performance of Shear Connection in Composite Beams with Profiled Steel Sheeting", *Journal of Constructional Steel Research*, 2006, Vol. 62, No. 7, pp. 682-694.
- [4] Eurocode 4. Design of Composite Steel and Concrete Structures–Part 1.1, General Rules and Rules for Buildings, London, UK: British Standards Institution; 2004. BS EN 1994-1-1.
- [5] Pavlović, M., Marković, Z., Veljković, M. and Buđevac, D., "Bolted Shear Connectors vs. Headed Studs Behaviour in Push-out Tests", *Journal of Constructional Steel Research*, 2013, Vol. 88, pp. 134-149.
- [6] Dai, X.H., Lam, D. and Saveri, E., "Effect of Concrete Strength and Stud Collar Size to Shear Capacity of Demountable Shear Connectors", *Journal of Structural Engineering*, ASCE, 2015, Vol. 141, No. 11, 04015025.
- [7] Rahman, N., Lam, D., Dai, X. and Ashour, A.F., "Experimental Study on Demountable Shear Connectors in Composite Slabs with Profile Decking", *Journal of Constructional Steel Research*, 2016, Vol. 122, pp. 178-189.
- [8] Moynihan, M.C. and Allwood, J.M., "Viability and Performance of Demountable Composite Connectors", *Journal of Constructional Steel Research*, 2014, Vol. 99, pp. 47-56.
- [9] Mirza, O. and Uy, B., "Effects of Strain Regimes on the Behaviour of Headed Stud Shear Connectors for Composite Steel-concrete Beams", *Advanced Steel Construction*, 2010, Vol. 6, No. 1, pp. 635-661.
- [10] Pathirana, S.W., Uy, B., Mirza, O. and Zhu, X., "Flexural Behaviour of Composite Steel-concrete Beams Utilising Blind Bolt Shear Connectors", *Engineering Structures*, 2016, Vol. 114, pp. 181-194.
- [11] Pathirana, S.W., Uy, B., Mirza, O. and Zhu, X., "Bolted and Welded Connectors for the Rehabilitation of Composite Beams", *Journal of Constructional Steel Research*, 2016, Vol. 125, pp. 61-73.
- [12] Loh, H.Y., Uy, B. and Bradford, M.A., "The Effects of Partial Shear Connection in Composite Flush End Plate Joints Part I – Experimental Study", *Journal of Constructional Steel Research*, 2006, Vol. 62, No. 4, pp. 378-390.
- [13] Wang, J.F., Han, L.H. and Uy, B., "Behaviour of Flush End Plate Joints to Concrete-filled Steel Tubular Columns", *Journal of Constructional Steel Research*, 2009, Vol. 65, No. 4, pp. 925-939.

- [14] Mirza, O. and Uy, B., "Behaviour of Composite Beam-column Flush End-plate Connections subjected to Low-probability, High-consequence Loading", *Engineering Structures*, 2011, Vol. 33, No. 2, pp. 647-662.
- [15] Liu, X., Bradford, M.A. and Lee, M.S.S., "Behavior of High-strength Friction-grip Bolted Shear Connectors in Sustainable Composite Beams", *Journal of Structural Engineering*, 2015, Vol. 114, No. 6, 04014149.
- [16] Ataei, A., Bradford, M.A., Liu, X., "Experimental Study of Flush End Plate Beam-to-column Composite Joints with Precast Slabs and Deconstructable Bolted Shear Connectors", *Structures*, 2016, Vol. 7, pp. 43-58.
- [17] Ban, H., Uy, B., Pathirana, S. W., Henderson, I., Mirza, O. and Zhu, X., "Time-dependent Behaviour of Composite Beams with Blind Bolts under Sustained Loads", *Journal of Constructional Steel Research*, 2015, Vol. 112, pp. 196-207.
- [18] Uy, B., Patel, V., Li, D. and Aslani, F., "Behaviour and Design of Connections for Demountable Steel and Composite Structures", *Structures*, 2017, Vol. 9, pp. 1-12.
- [19] Vasdravellis, G., Uy, B., Tan, E.L., Kirkland, B., "The Effects of Axial Tension on the Hogging-moment Regions of Composite Beams", *Journal of Constructional Steel Research*, 2012, Vol. 68, pp. 20-33.
- [20] Vasdravellis, G., Uy, B., Tan, E.L., Kirkland, B., "The Effects of Axial Tension on the Sagging-moment Regions of Composite Beams", *Journal of Constructional Steel Research*, 2012, Vol. 72, pp. 240-253.
- [21] Vasdravellis, G., Uy, B., Tan, E.L., Kirkland, B., "Behaviour and Design of Composite Beams Subjected to Negative Bending and Compression", *Journal of Constructional Steel Research*, 2012, Vol. 79, pp. 34-47.
- [22] Vasdravellis, G., Uy, B., Tan, E.L., Kirkland, B., "Behaviour and Design of Composite Beams subjected to Sagging Bending and Axial Compression", *Journal of Constructional Steel Research*, 2015, Vol. 110, pp. 29-39.
- [23] ABAQUS User's Manual, Version 6.12-1, Hibbit, Karlsson and Sorensen, Inc., Pawtucket, R.I., 2012.
- [24] Uy, B. and Bradford, M., "Composite action of Structural Steel Beams and Precast Concrete Slabs for the Flexural Strength Limit State", *Australian Journal of Structural Engineering*, 2006, Vol. 7, No. 2, pp. 1-10.
- [25] Mirza, O., Uy, B. and Ha, L., "Time-dependent Analysis of Composite Steel-concrete Beams with Innovative Deep Trapezoidal Decks", *Steel and Composite Structures-Proceedings of the 4th International Conference*, 2010.
- [26] Standard Australia, Australian Standard AS 3600-2009 Concrete Structures, 2009, Australia
- [27] Standard Australia, Australian Standard, Steel Structures, AS4100-1998 (incorporating Amendment 1-2012), 1998, Australia.
- [28] Standard Australia, AS/NZS 2327 Composite Structures Part 1: Simply supported Beams, Sydney, 2003.
- [29] AS 3600-2009. Concrete Structures, Sydney, New South Wales, Australia: Standard Australia; 2009.
- [30] Carreira, D. J. and Chu, K. H., "Stress-strain Relationship for Plain Concrete in Compression", *ACI Journal*, 1985, Vol. 82, No. 6, pp. 797-804.
- [31] Bažant, Z. P. and Becq-Giraudon, E., "Statistical Prediction of Fracture Parameters of Concrete and Implications for Choice of Testing Standard", *Cement and Concrete Research*, 2002, Vol. 32, No. 4, pp. 529-556.
- [32] Mirza, O. and Uy, B., "Numerical Modelling of Short and Long Term Behaviour of Headed Stud Shear Connector in Composite Steel-concrete Beams", *Incorporating Sustainable Practice in Mechanics of Structures and Materials*, CRC press, 2010, pp. 91-96.

- [33] Kwon, G., Engelhardt, M.D. and Klingner, R.E., "Behavior of Post-installed Shear Connectors under Static and Fatigue Loading", *Journal of Constructional Steel Research*, 2010, Vol. 66, No. 4, pp. 532-541.
- [34] Lam, D. and Uy, B., "Recent Research and Development in Composite Steel Beams with Precast Hollow Core Slabs", *Steel Construction-Journal of the Australian Institute of Steel Construction*, 2003, Vol. 37, No. 2, pp. 1-13.

INVESTIGATING THE BEHAVIOR OF SPECIALLY PRE-FABRICATED STEEL MOMENT CONNECTION UNDER CYCLIC LOADING

Morteza Kazemi Torbaghan ¹, Mohammad Reza Sohrabi ^{2,*} and Hasan Haji Kazemi ³

¹ Department of Civil Engineering, University of Sistan and Baluchestan, Zahedan, Iran

² Associate Professor, Department of Civil Engineering, University of Sistan and Baluchestan, Zahedan, Iran

³ Professor, Department of Civil Engineering, Ferdowsi University, Mashhad, Iran

*(Corresponding author: E-mail: sohrabi@hamoon.usb.ac.ir)

Received: 10 June 2016; Revised: 9 July 2017; Accepted: 16 September 2017

ABSTRACT: The connections of pre-fabricated steel structures have become a major issue in recent decades due to the need for rapid constructions. In the past years, several studies have been conducted with the aim of developing simple and efficient connections. Here, a new modularized pre-fabricated steel moment connection is proposed, which is composed of a short column with a pyramid head for a fast and easy assembling. In this paper, the behavior of this connection is investigated through using several cross-section shapes and plates with different thickness. The obtained force-displacement and moment-rotation curves of the connection under cyclic loads indicate that a 20 percent increase in the thickness of the beam and column connection plates raises the yielding moment, yielding rotation and the maximum rotation capacity of the connection by 21, 19 and 13 percent respectively. The results also suggest that the proposed model has a higher capacity as well as reliable performance comparing to other moment connections.

Keywords: Special steel moment connection, pre-fabricated structures, force-displacement curve, cyclic loads, moment-displacement curve

DOI: 10.18057/IJASC.2018.14.3.6

1. INTRODUCTION

Since the traditional construction methods are not efficient for today's requirements, the use of modern materials and techniques is essential. Compared to traditional methods, modularized pre-fabricated structures offer several benefits such as low costs and fast construction and implementation procedures. The components of the connection in the modularized pre-fabricated steel structural are composed of beam and column connection plates and a short column. In this form, the floor slabs can be constructed completely in factory and then carried to the site and placed on the columns. The implementation of the pre-fabricated floor slabs is difficult, particularly on the upper floors. Therefore, a new method for faster and easier floor assembly has been developed in which a pyramidal section is provided on the connection plate of the lower-floor column in a way that during the floor slabs implementation, the pyramidal section is placed into the short column. Figure 1 indicates the components of the proposed moment connection and the implementation process using the pyramidal section.

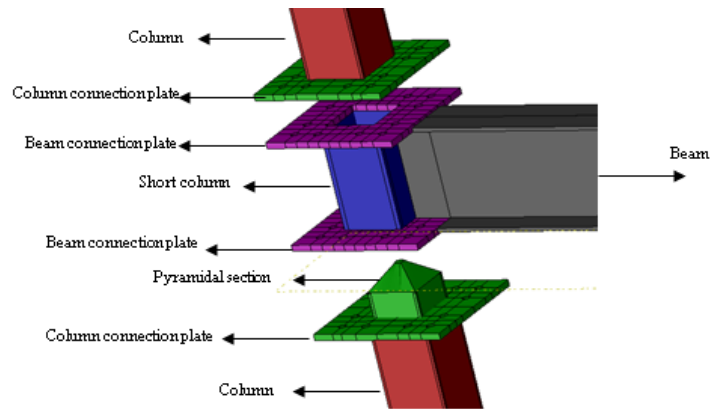


Figure 1. Components of the Proposed Connection and Implementation Process

In this study, the force-displacement curves obtained by applying cyclic loads were used for evaluating the capacity and ductility of the connections. Additionally, the effect of using stiffener and pyramidal section as well as changing the thickness of beam and column connection plates on the behavior of the connection under cyclic loads was investigated. For this purpose, a 3D finite element model was developed in ABAQUS and the results were verified using experimental data.

Despite the fact that pre-fabricated assemblies are a challenging area for research, a few studies have been conducted on the moment connection of these structures thus far. Generally, the main focus has usually been on the beam to column connection components since it is one of the main parts of the structure (Liu et al. [1]). The studies have been mostly conducted using finite element method as well as experimental tests in which different properties of various moment connection types with innovative configuration have been assessed. Since the proposed pre-fabricated steel moment connection has never been studied before, in this paper the most related literatures were reviewed to present a more comprehensive view of this connection.

The behavior of moment connections has been investigated by many scholars using different methods. Ghassemieh et al. [2] studied the seismic behavior of extended endplate moment connections. In their research, a test setup was modeled and the connections were analyzed using ANSYS and the model was validated by comparing the results with experimental data. Then, the effect of changing the dimension of the connection components on the overall seismic performance of the connection was investigated. Popov and Tsai [3] also evaluated the cyclic behavior of extended endplate moment connection and suggested that the methods which used the results of monotonic loading for the design of connections in seismic regions may need to be revised. Maggi et al. [4] used ANSYS for modeling moment connections and compared the FEM outcomes with experimental results obtained from monotonic loading. By using ABAQUS, Alhendi and Celikag [5] improved the moment-rotation curves of reverse channel connection by changing its geometrical shape. Kulkarni and Gaurang [6] also studied the reduced beam section steel moment connections (RBS) fabricated from Indian sections and analyzed them under cyclic loads. Their findings showed that the RBS connections have an acceptable capacity under this type of loading. Gerami et al. [7] studied the effect of bolts arrangement in extended endplate and T-stub connection under cyclic loads using ABAQUS. In their study, 14 specimens of these connections were modeled by changing the horizontal and vertical arrangement of the bolts. The behavior of bolted T-stub connections with welded plates was also experimentally investigated by Coelho et al. [8]. Brunesi et al. [9] evaluated the performance of partially-restrained bolted beam-to-column connections under cyclic loads and proposed an alternative and conservative method for a quick rotational stiffness estimation of these PR bolted top-and-seat angle connections. Arul Jayachandran et al. [10] studied the behavior of semi-rigid endplate connections by experimentally

and numerically evaluating the moment-rotation behavior of semi-rigid bolted endplate connections. All the specimens were modeled using ABAQUS. Brunesi et al. [11] evaluated the seismic performance of MRFs with partially-restrained bolted beam-to-column connections through FE analyses. Pucinotti [12] predicted the cyclic moment-rotation behavior of top-and-seat and web angle connection using a mechanical model. The results of their analyses showed that the simple mechanical model yields the results that are reasonably consistent with the experimental data and are more accurate than the results of the Eurocode3.

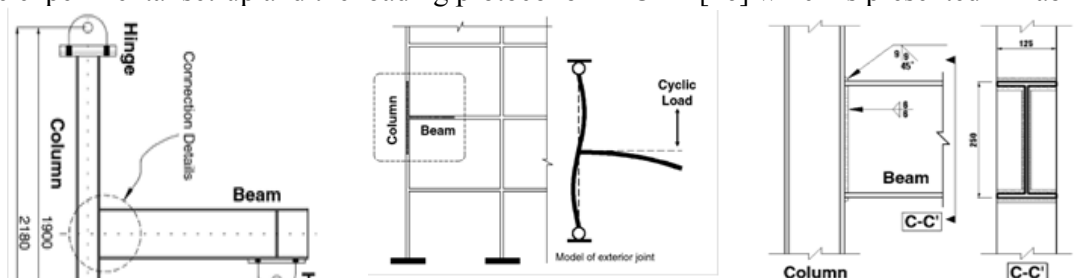
Among these studies, the most relevant works have been performed by Liu et al. [1, 13, 14] on the pre-fabricated steel moment connections. In 2015, Liu et al. [13] studied the seismic behavior of welded joints in modularized pre-fabricated steel structures. The model was analyzed under monotonic and cyclic load using finite element method. In another study from these authors (Liu et al [1]), the bolted-welded beam to column joint for the modularized pre-fabricated steel structures was studied. The properties of the connection behavior including static performance, hysteretic performance, skeleton curves, ductile performance, energy dissipation capacity and rotation capacity were assessed using both finite element and experimental methods. The effect of the thickness of the components as well as the welding capacity was also investigated. In order to fulfil all aspects of their studies, simplified formulas were developed to measure the load-bearing capacity of the connection. Liu et al. [14] furthered their works by studying the pre-fabricated bolted connections for multi-rise and high-rise structures. For this purpose, finite element and experimental analyses were performed and the results were compared to develop the finite element modeling. This was established to determine the mechanical properties of the connection which were difficult to be studied through experimental tests.

All these studies indicated the capability of finite element software packages like ABAQUS to yield valid results comparing to experimental tests. In this study, finite element method was employed and the results were then compared with the experimental data to investigate the different properties of the proposed moment connection.

2. MODELING

In order to validate the finite element models, the numerical results were first compared with the experimental results of the Specimen from Yang and Kim research [15]. Figure 2 represents the selected moment frame, dimensions, the section of beam and columns, and the model of the exterior joint.

The entire components used in this research including columns, beams, connection plates, stiffeners and boxes were made of SS400 steel. The bolts were also A490. The mechanical properties of all materials were taken from the experimental specimens mentioned in Table 1. (Yang and Kim [15]). Modulus of elasticity and the Poisson's ratio for all sections were 200 Gpa and 0.3 respectively. Loads were included by applying the corresponding displacement at the end of the beam according to the experimental set-up and the loading protocol of ATC-24 [16] which is presented in Table 2.



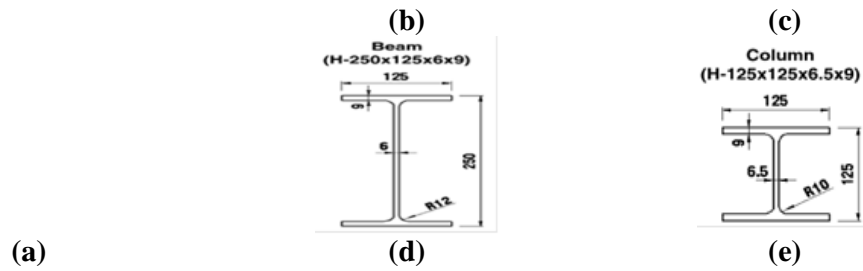


Figure 2. Model Feature and Configuration, a: Test set-up, b: Model of the Exterior Joint, c: Beam to Column Connection Type, d: Beam Section, e: Column Section

Table 1. Material Properties of Numerical and Experimental Specimens (Yang and Kim [15])

Material	Application	Strain	Stress (MPa)
SS400	Beam, column, plate, box	0.00178	332
		0.0196	332
		0.2134	450

Table 2. Values of Displacements Applied to the End of the Beam (ATC-24 [16])

Step no.	1	2	3	...	6	...	9	10	...	13	14	...	18
Displacement (mm)	±3	±6	±9	...	±18	...	±30	±35	...	±50	±60	...	±100
Drift (rad. %)	.324	.649	.973	...	1.95	...	3.24	3.78	...	5.41	6.49	...	10.81

The force-displacement curves are presented for the experimental and numerical specimens in Figure 3. It can be seen that there is a good agreement between experimental and numerical results.

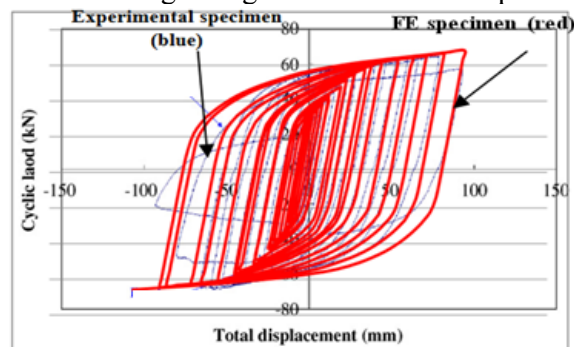


Figure 3. Force-displacement Curves for Experimental and FE Specimens

3. CONNECTION

All properties of the connection including steel property, beam section, beam and column length, loading and support conditions were similar to the experimental sample except that the column was a box-section type. Such a profile was selected to ease the assembling procedure since the section of the short column was also box-shaped. Other dimensions of connection can be seen in Table 3 and Figure 4. For FE modeling, shell and solid elements were used for sections and bolts respectively. All the connecting assemblies were modeled using S4R while C3D8R which refers to continuum three dimensional 8-noded brick element with reduced order integration was used for modeling the bolts. The latter has three degrees of freedom at each node and translations in the nodal x, y, & z direction (Jayachandran et al. [10]). For applying structure mesh technique, sections were created separately and then tied together. The holes were standard and loading was performed in two steps. In the first step, according to the types and sizes of the bolts, pre-tension force equal to 107 kN was applied to all bolts (Salmon et al. [17]) and in the second step the displacement was applied to the end of the beam. The type of contact between bolts and connection plates was “penalty” with a friction coefficient of 0.5 (Salmon et al. [17]). The names and properties of the specimens were presented in Table 4.

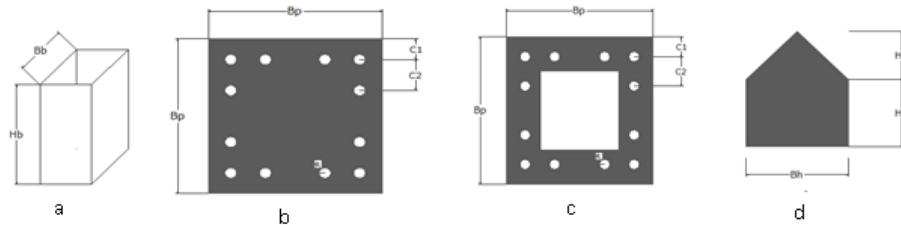


Figure 4. Dimension of the Connection Component,
a: Short Column, b: Column Connection Plat,
c: Beam Connection Plate, d: Pyramidal Section

Table 3. Geometry and Dimensions of the Connection Component
(parameters was shown in Figure 4)

Element	Section size (mm)
Column	13.53×13.53× 5.85 □
Column connection plate	Bp=300, C1=30, C2=40, R=9, t=variable
Beam connection plate	Bp=300, C1=30, C2=40, R=9, t=variable
Box	Bb=150, Hb=232,t=10
pyramidal section	Bh=148, H ₁ =100, H ₂ =100
Bolt	D=16

Table 4. Properties of Specimens

Specimens	Properties			
	Column section	Thickness of connection plates (mm)	Pyramidal section	Stiffener
Numerical	I shape	-	-	-
Ct12	Box	12	-	-
Ct15	Box	15	-	-
Ct18	Box	18	-	-
Ct15P	Box	15	available	-
Ct15S	Box	15	-	available
Ct15I	I shape	15	-	-

In Ct12 specimen, when the amount of the applied force reached up to 55.03 kN ($P_y=55.03\text{kN}$), the first section that yielded was the parts of the column connection plates. As the force increased, the yielding area expanded and other sections began to yield as well. When force was 95.45 kN, the stress in column and beam connection plates reached its maximum capacity and the plates could not bear more forces. As a result, the thickness of the connection plates in this specimen was not suitable. Figure 5 represents Von Mises stress distribution in a connection when force was 95.45 kN and Figure 6 represents the force-displacement curve at the end of the beam.

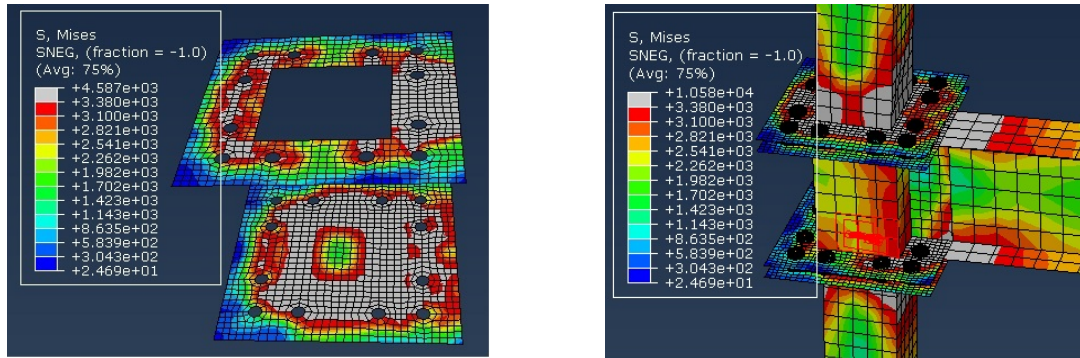
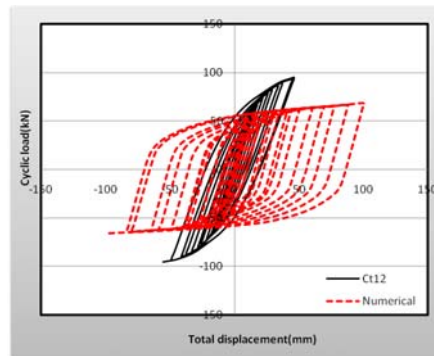
Figure 5. Contour Plot for Von Mises Stress Distribution in Ct12 (unit: kg/cm^2)

Figure 6. Force-displacement Curves for Ct12 and Numerical Specimens

Figure 6 implies that the load bearing capacity of Ct12 was more than the numerical model (the verified model) while it could not bear 100 mm displacement due to the failure of the beam and column connection plates.

In Ct15, when the amount of the applied force reached up to 71.62 kN ($P_y=71.62\text{kN}$), the first sections that yielded were some parts of the column connection plates. As the force increased, other

sections began to yield as well. In the last step (displacement was 100 mm, force was 114.25kN), the large areas of the connection plates, columns and beam yielded without any failure. Figure 7 represents the force-displacement curve at the end of the beam.

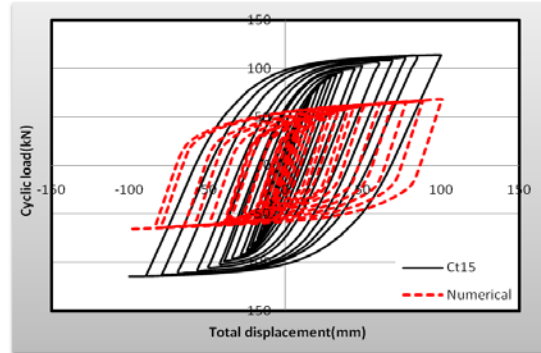


Figure 7. Force-displacement Curves for Ct15 and Numerical Specimens

Figure 7 indicates that P_{100} (the amount of force multiplied by the 100 mm displacement at the end of the beam) was 114.25 and 65.92 kN for Ct15 and the numerical specimen respectively. Figures 8 to 12 show the Von Mises stress distribution and force-displacement curves for other specimens and table 5 shows the values of P_y , P_{100} and $P_{failure}$ for all of the specimens.

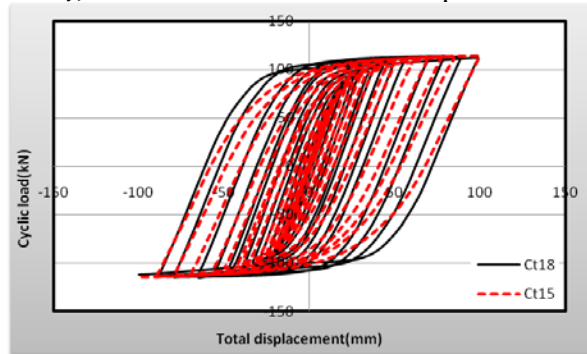


Figure 8. Force-displacement Curves for Ct18 and Ct15

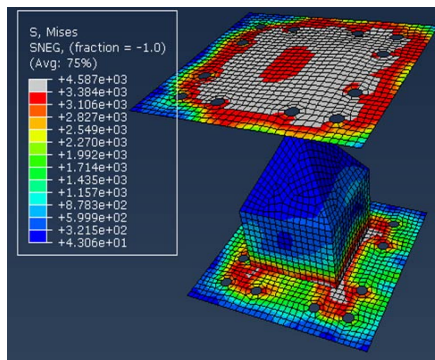


Figure 9. Contour Plot for Von Mises Stress Distribution in Ct15P (unit: kg/cm²)

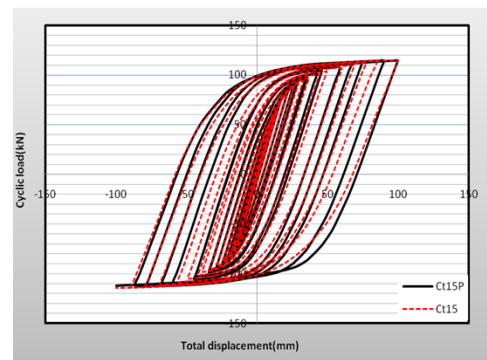


Figure 10. Force-displacement Curves for Ct15 and Ct15P

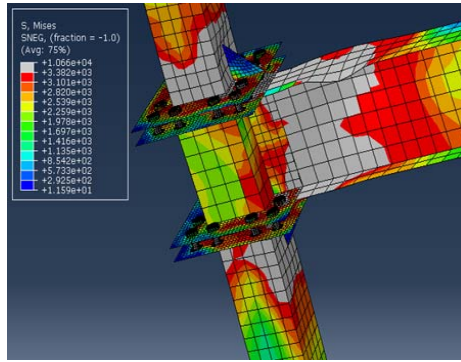


Figure 11. Contour Plot for Von Mises Stress Distribution in Ct15S (unit: kg/cm²)

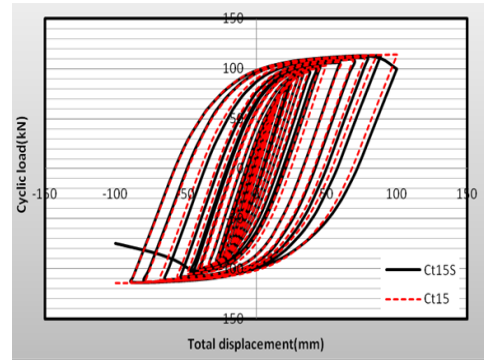


Figure 12. Force-displacement Curve for Ct15 and Ct15S

In Ct15I, when the applied force reached up to 57.86 kN, the first section that yielded was the parts of column connection plates. As the applied force became 104.69 kN (displacement is 90 mm), some parts of the column connection plates failed and the connection reached its ultimate capacity. Figure 13 shows Von Mises stress distribution in the connection when displacement was 90 mm and Figure 14 shows the force-displacement curve at the end of beam.

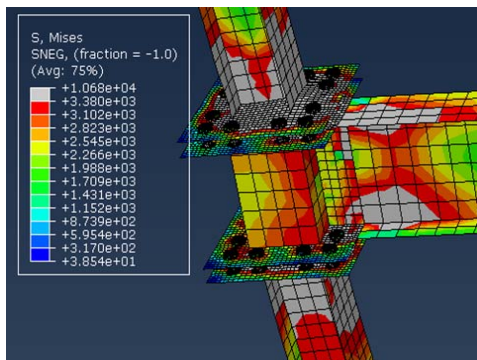


Figure 13. Contour Plot for Von Mises Stress Distribution in Ct15I Specimen (unit: kg/cm²)

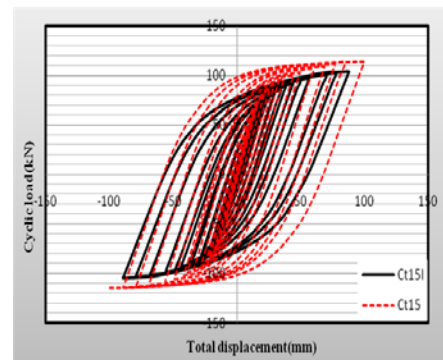


Figure 14. Force-displacement Curve for Ct15I and Ct15 Specimens

Table 5. Values of P_y , P_{100} and P_{failur}

specimens	P_y (kN)	P_{100} (kN)	P_{failur} (kN)
Ct12	55.03	-	95.45
Ct15	71.62	114.25	No failure
Ct18	86.24	111.64	No failure
Ct15P	71.62	111.9	No failure
Ct15S	71.39	99.7	No failure
Ct15I	57.86	-	104.69

4. EXPERIMENTAL AND NUMERICAL SKELETON CURVES

In this section, experimental skeleton curves for the three connection types (Yang and Kim [15]) are presented and then compared with the curves of pre-fabricated steel pyramidal special connections. The detail of the DWA and TSD joints is given in Figure 15.

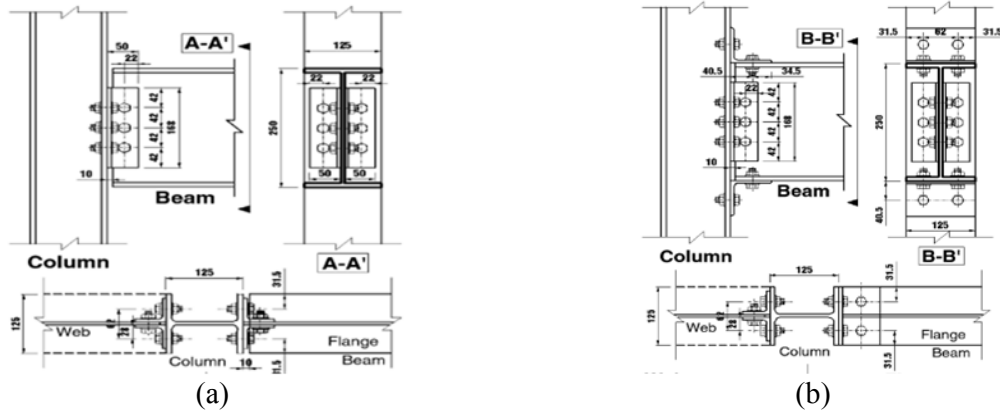


Figure 15. Details and Dimensions of Connections. a: DWA, b: TSD (Yang and Kim [15])

For a progressive sequence of compression and tension, the line joining the peak points in the load–displacement curve of each loading sequence forms the skeleton curve. In many cases, the skeleton curve coincides with the monotonic loading curve (Popov and Takhirov [18], SAC Joint Venture [19]). Figures 16 and 17 represent the skeleton curves of experimental and numerical specimens respectively.

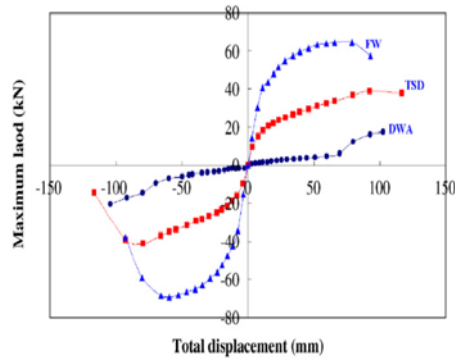


Figure 16. Skeleton Curves of Load – Displacement of Experimental Specimens (Yang and Kim [15])

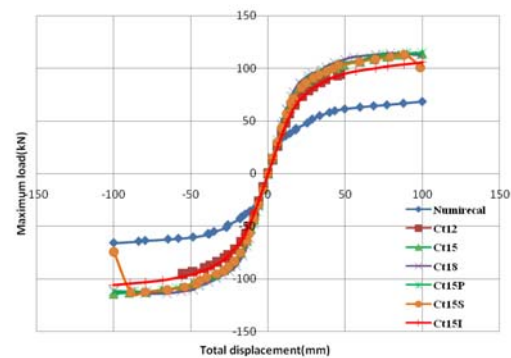


Figure 17. Skeleton Curves of Load – Displacement of Numerical Specimens

According to the Figures 5 to 17, pre-fabricated steel connections had a high capacity under cyclic loads such that most specimens could bear 100 mm displacement (10.81% drift) at the end of the beam without a decrease under the applied force. Since these connections were composed of many components, the moment redistribution occurred which postponed the failure mechanism and increased the load bearing capacity of the connection.

5. MOMENT- ROTATION BEHAVIOR

In this section, the flexural and rotational behavior of the connections was evaluated for all of the specimens. Figure 18 demonstrates the calculation of rotational capacity (θ_z) under the applied force to the end of the beam. The results were presented in Table 6 in which M_y and R_y represent the yielding moment and yielding rotation while M_{max} and R_{max} are the maximum moment and rotation of the specimens respectively.

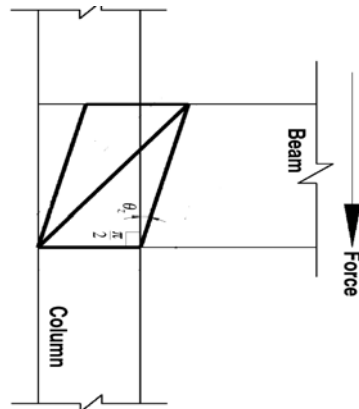


Figure 18. Calculation of Connection Rotation Capacity (Yang and Kim [15])

Table 6. Moment- Rotation Behavior of the Connections

Specimens	M_y (kN.m)	R_y (Rad.)	M_{max} (kN.m)	R_{max} (Rad.)	Percentage of increment/ decrement compared to the FW specimen(M_y)	Percentage of increment/ decrement compared to the FW specimen(M_{max})	Percentage of increment/ decrement compared to the FW specimen(R_y)	Percentage of increment/ decrement compared to the FW specimen(R_{max})
Ct12	50.9	0.01053	88.28	0.0474	+28.86	+41.25	+229.1	+110.7
Ct15	66.25	0.01266	107.63	0.0795	+67.72	+72.2	+295.65	+253.3
Ct18	79.77	0.0151	103.26	0.0898	+101.9	+65.22	+371.9	+299.1
Ct15H	65.99	0.01196	103.5	0.0896	+67.06	+65.6	+273.7	+298.2
Ct15S	66.03	0.01258	104.89	0.06	+67.16	+65	+293.1	+166.7
Ct15I	53.52	0.01201	96.83	0.0702	+35.5	+54.9	+275.3	+212
FW[15]	39.5	0.0032	62.5	0.0225	-	-	-	-
DWA[15]	1.1	0.0027	17.7	0.1073	-97.21	-71.7	-15.6	+376.9
TSD[15]	15.3	0.0069	36.6	0.0856	-61.27	-41.44	+115.6	+280.4

According to Table 6, by increasing the thickness of the connection plates; M_y , R_{max} and R_y were increased. The maximum rotation capacity was increased by using pyramidal section while it was reduced through applying the stiffener. The Table 6 also shows that all pre-fabricated connections had a high capacity such that in all specimens, M_y and M_{max} were higher and R_y and R_{max} were lower than FW moment and rotation capacity respectively. Based on this, the pre-fabricated demonstrated a high rotational capacity as well as adequate ductility.

6. CONCLUSION

In this paper, the effects of the thickness of the beam, column, connection plates and the stiffeners as well as the pyramidal section on the force-displacement curve of the pre-fabricated steel moment connection under cyclic loads were investigated. For this purpose, the connection was modeled and analyzed using ABAQUS and the model was compared and validated with several experimental specimens. The main results of this study can be summarized as follows:

1. In this connection, the beam and column connection plates are the first sections that yield which implies that the thickness of these plates has a negligible effect on the maximum moment capacity (M_{max}) while increases the yielding moment capacity (M_y) of the connection. Based on the experimental results, M_y of Ct12, Ct15 and Ct18 is 50.9 kN.m, 66.25 kN.m and 79.77 kN.m respectively. In addition, increasing the thickness of the plates from 12 mm to 15 mm and 18 mm raises M_y by 30.2 percent and 56.72 percent respectively. It also increases R_y of Ct12 from 0.01053 radian to 0.01266 and 0.0151 radian and R_{max} of Ct12 from 0.0474 radian to 0.0795 and 0.0898 radian for Ct15 and

- Ct18 respectively, which means that R_y grows to 20.23 and 43.4 percent while R_{max} is increased by 67.72 and 89.45 percent respectively.
2. Adding a pyramidal section to the column assembly simplifies the implementation procedure, particularly in upper stories and increases R_{max} by 12.7 percent and decreases M_{max} by 3.84 percent since it acts as a support. It also decreases the stress at the plate connected to the pyramidal section.
 3. Using the stiffener increases the stiffness of the connection and causes torsion in the beam after creating a plastic hinge resulting in a 24.53 and 2.55 percent decrease in R_{max} and in M_{max} respectively.
 4. Since an I-shaped column in comparison with a box-shaped column cannot align with the short column, the connection plates yield earlier and the connection capacity diminishes such that R_{max} and M_{max} decrease by 11.7 and 10.03 percent respectively.
 5. According to the findings of this study, pre-fabricate steel connections represent a high capacity and acceptable performance under cyclic loads. R_y , R_{max} , M_y and M_{max} were obtained 0.01266 rad., 0.0795 rad., 66.25 kN.m, 107.63 kN.m for Ct15 while 0.0032 rad., 0.0225 rad., 39.5 kN.m and 62.5 kN.m for FW respectively. Based on these results, the mentioned parameters of Ct15 are 295.65, 253.3, 67.72 and 72.2 percent which are higher than FW.

REFERENCES

- [1] Liu, X., Pu, S., Zhang, A., Xu, A., Ni, Z., Sun, Y. and Ma, L., "Static and Seismic Experiment For Bolted-Welded Joint In Modularized Prefabricated Steel Structure", *Journal Of Constructional Steel Research*, 2015, Vol. 115, pp. 417-433.
- [2] Ghassemieh, M., Jalalpour, M. and Gholampour, A., "Numerical Evaluation of the Extended Endplate Moment Connection Subjected to Cyclic Loading", *Current Advances in Civil Engineering*, 2014, Vol. 2, No. 1, pp. 35-43.
- [3] Popov, E. and Tsai, K.C., "Performance of Large Seismic Moment Connections under Cyclic Loads", *AISC Engineering Journal*, 1989, Vol. 26, No. 2, pp. 51-60.
- [4] Maggi, Y. I., Gonçalves, R. M., Leon, R. T. and Ribeiro, L. F. L., "Parametric Analysis of Steel bolted Endplate Connections Using Finite Element Modeling", *Journal of Constructional Steel Research*, 2005, Vol. 61, No. 5, pp. 689-708.
- [5] AlHendi, H. and Celikag, M., "Parametric Study on Moment-rotation Characteristics of Reverse Channel Connections to Tubular Columns", *Journal of Constructional Steel Research*, 2015, Vol. 104, pp. 261-273.
- [6] Kulkarni Swati, A. and Gaurang, V., "Study of Steel Moment Connection with and without Reduced Beam Section", *Case Studies in Structural Engineering*, 2014, Vol. 1, pp. 26-31.
- [7] Gerami, M., Saberi, H., Saberi, V. and Saedi Daryan, A., "Cyclic Behavior of Bolted Connections with Different Arrangement of Bolts", *Journal of Constructional Steel Research*, 2011, Vol. 67, No. 4, pp. 690-705.
- [8] Coelho, M. Girao., Bijlaard Frans, S.K. Gresnigt, N. and Simoes da Silva, L., "Experimental Assessment of the Behavior of Bolted T-stub Connections Made up of Welded Plates", *Journal of Constructional Steel Research*, 2004, Vol. 60, No. 2, pp. 269-311.
- [9] Brunesi, E., Nascimbene, R. and Rassati, G.A., "Response of Partially-restrained Beam-to-column Connection under Cyclic Loads", *Journal of Constructional Steel Research*, 2014, Vol. 97, pp. 24-38.
- [10] Arul Jayachandran, S., Marimuthu, V., Prabha, P., Seetharaman, S. and Pandian, N., "Investigation on the Behavior of Semi-rigid Endplate Connections", *Advanced Steel Construction*, 2009, Vol. 5, No. 4, pp. 432-451.

- [11] Brunesi, E., Nascimbene, R. and Rassati, G. A., “Seismic Response of MRFs with Partially-restrained Bolted Beam-to-column Connection through FE Analyses”, *Journal of Constructional Steel Research*, 2015, Vol. 107, pp. 37–49.
- [12] Pucinotti, R., “Prediction of Cyclic Moment-rotation Behavior for Top and Seat & Web Angle Connections by Mechanical Model”, *Advanced Steel Construction*, 2007, Vol. 115, No. 1, pp. 530-552.
- [13] Liu, X., Xu, A., Zhang, A., Ni, Z., Wang, H. and Wu, L., “Static and Seismic Experiment for Welded Joints in Modularized Prefabricated Steel Structure”, *Journal of Constructional Steel Research*, 2015, Vol. 112, pp. 183-195.
- [14] Liu, X., Pu, S., Zhang, A. and Zhan, X., “Performance Analysis and Design of Bolted Connections in Modularized Prefabricated Steel Structures”, *Journal Of Constructional Steel Research*, 2017, Vol. 133, pp. 360-373.
- [15] Min Yang, C. and Moon Kim, Y., “Cyclic Behavior of Bolted and Welded Beam-to-Column Joints”, *Journal of Mechanical Sciences*, 2007, Vol. 49, pp. 635-649.
- [16] ATC-24, “Guidelines of Cyclic Seismic Testing on Components for Steel Structures”, Redwood City, California, Applied Technology Council, 1992.
- [17] Salmon, C. G. and Johnson, J. E. and Malhas, F. A., “Steel Structure Design and Behavior”. 5rd ed., New York, Prentice Hall, 2008.
- [18] Popov, EP. and Takhirov, SM., “Bolted Large Seismic Steel Beam-to-column Connections Part 1: Experimental Study”, *Engineering Structures*, 2002, Vol. 24, No. 12, pp. 1523–1534.
- [19] SAC Joint Venture, “Protocol for Fabrication, Inspection, Testing, and Documentation of Beam-column Connection Tests and Other Experimental Specimens”, Report No. SAC/BD-97/02, 1997.

INTERFACE BOND BEHAVIOUR BETWEEN CIRCULAR STEEL TUBE AND LIGHTWEIGHT AGGREGATE CONCRETE

Z.Q. Fu¹, H.B. Ge^{2,*}, B.H. Ji¹ and J.J. Chen¹

¹ School of Civil and Transportation Engineering, Hohai University, Nanjing 210098, China

² Department of Civil Engineering, Meijo University, Nagoya 468-8502, Japan

*(Corresponding author: E-mail: gehanbin@meijo-u.ac.jp)

Received: 19 December 2016; Revised: 22 July 2017; Accepted: 19 November 2017

ABSTRACT: To ascertain the nature of the interface bond behaviour of lightweight aggregate concrete-filled steel tubes (LACFSTs), 27 specimens were tested by push-out loading and four of them were subjected to repeated push-out loading. Influence factors such as lightweight aggregate concrete strength, concrete vibration and curing method, steel surface conditions, slenderness ratio, and diameter-to-thickness ratio were considered. The bond slip process and strength were analysed and a formula was proposed to calculate the bond strength of the LACFSTs. The results show that the bond-slip curve can take one of two forms: one with an obvious peak, the other without, and each one manifests three different trends after reaching ultimate load. According to the test results, the bond strength is independent of the lightweight aggregate concrete strength. Higher diameter-to-thickness ratios cause a reduction in the bond strength. A good quality of concrete vibration and curing can improve the bond strength. The bond strength after the first of the repeated push-out tests is the largest. In the same push-out direction, the bond strength decreases as the push-out time increases, and the load-slip curves are similar among all samples tested. The comparisons between test results and calculations show that the proposed formula has a good accuracy.

Keywords: Lightweight aggregate concrete, concrete-filled steel tube, push-out test, bond strength, bond-slip

DOI: 10.18057/IJASC.2018.14.3.7

1. INTRODUCTION

Concrete filled steel tube (CFST) fully utilizes the tensile- compressive properties of steel and compressive strength of concrete, and has a wide range of applications in various types of structures [1-2]. Research has also been carried out into the design and construction of steel tube concrete structures [3-4]. The demands of different applications, section shapes, and categories of in-filled concrete contribute to various types of CFST including: square CFST, circular CFST, high-strength concrete filled steel tubes, recycled concrete filled steel tubes, and so on. According to the stress acting on the section, CFST can be classified into partially-filled steel tubes, confined concrete-filled steel tubes, and normal CFST, depending on whether the stress acts only on the steel tube, coral concrete or the combined section as a whole [5-7]. Lightweight aggregate concrete-filled steel tube (LACFST) is one type studied here. Previous studies show that the behaviour of LACFSTs is excellent and can replace normal CFSTs [7-9]. Due to their lighter weight, it can expect a more significant advantage in application [10].

As a type of composite structures, the bond strength directly affects whether the two materials can work together or not [11]. Due to the lack of accurate constitutive relationships, many studies assume that there is no slip between the steel tube and the concrete under load. To describe the bond behaviour, the interface bond slip of CFSTs was studied [12-13]. Early studies mostly involved normal CFST. In recent years with the application of research into various kinds of new composite structures, such as recycled aggregate CFSTs, high-strength CFSTs, *etc.*, the corresponding bond slip behaviour was also studied. Some of the studies examined the change of interface bond behaviour of CFSTs after fire or fatigue load action [14-15]. At present, there are

two main methods used to test the interface bond slip in a CFST. Push-off tests, with the load acting on the whole section, can be used to simulate the actual change in a structure while only the ultimate bond strength can be tested by this method [16]. The Push out test is adopted by most studies because it can measure the bond strength in the whole loading process [17-18]. Tao *et al.* [13] prepared a total of 24 specimens to consider influence of various parameters, including the section shape, steel type, concrete type, concrete age and interface type. The results showed that the bond strength declined dramatically with increasing of tube size and the concrete age. Pre-stressing concrete was adopted by Chen *et al.* [17] and 20 specimens were fabricated to study the influences of the pre-stress on the bond strength of steel-concrete interface. The bond strength of CFST with pre-stressing concrete was approximately 1.2~3.3 times than that with normal concrete. A new stiffening system was proposed by Chen *et al.* [19] to improve the bond strength at the steel-concrete interface and the degree of improvement increased with decreasing tab stiffener spacing. Tests carried out by researchers [20-26] mainly focused on the section shape, steel grade, concrete strength, number of specimens, *etc.*, and the bond strength concluded from the tests above ranges from 0.03 to 3.29, showing a distinct discreteness.

So far, it is still not possible to provide reliable equations to predict the bond strength in CFST columns because of the numerous influencing parameters and uncertainties. For simplification purposes, existing design codes only specify constant design bond strengths for CFST columns based on previous test data. In Europe standard [27] and American standard [28], the specified design bond strength is 0.4 MPa for both circular and rectangular CFST columns. In contrast, the specified bond strength values in Japan standard [29] are 0.225 MPa and 0.15 MPa for circular and rectangular CFST columns, respectively. In China standard [30], the bond strength ranges from 0.40~0.60 considering different concrete grades. To study the mechanical properties of lightweight concrete filled steel tubes, an experimental study of bond slip was carried out considering different factors influencing the bond strength.

2. EXPERIMENTAL PROGRAM

2.1 Material and Specimens

The coarse aggregate used in this lightweight aggregate concrete is ceramsite. The bulk density is 814 kg/m³, the cylindrical compressive strength is 8.5 MPa, and the water absorption is 6% at one hour. Ordinary Portland cement was used in the concrete. The fine aggregate is a kind of medium sand with a fineness modulus of 2.6 and a bulk density of 2600 kg/m³. Slag powder and JM-B water reducer were used to improve the concrete mechanical properties. Three strength types of lightweight aggregate concretes (LAC) numbered: CL1, CL2, and CL3, were considered. According to the relevant Chinese standards, compression tests were carried out on a number of standard cubes ([150 × 150 × 150] mm³) to determine the concrete grade and prisms ([150 × 150 × 300] mm³) and determine the compressive strength (f_{ck}) and elastic modulus (E_c) of the unconfined concrete. The concrete mix proportions and mechanical properties are given in Table 1.

Table 1. Mixture Ratio and Mechanical Properties of Lightweight Aggregate Concrete

Number	Mass in per cubic meter of concrete/ kg						f_{ck} (MPa)	E_c (MPa)
	Cement	Ceramsite	Sand	Slag	Water	Water reducer		
CL1	460	670	650	—	203.5	—	28.71	19.50×10 ³
CL2	387	645	643	43	150	3.8	30.71	23.84×10 ³
CL3	450	650	650	50	125	6.8	37.38	24.83×10 ³

Straight welded steel tube Q235 was used in the test. A group of three standard specimens was tested to determine the tensile strength of the steel and the section thickness of each steel tube fitted the standard specimen dimensions. The test method followed the Chinese Standard for “GB/T228-2002 Metallic materials-Tensile testing at ambient temperature” [31]. The steel specimen is shown in Figure 1. The yield strengths (f_y) of the steel with thicknesses of 2.5 mm and 4.0 mm were 305.6 MPa and 274.7 MPa, respectively, and test results are shown in Figure 2.

A 50 mm length at the upper end of each steel tube was left empty. After pouring the LAC, a 50 mm diameter vibrator was used to compact the concrete, except in one group of specimens which were manually vibrated. Some 10 days of curing later, the bottom of the column was smoothed with fresh cement paste. The details of the test specimens are shown in Table 2, where group A was designed for comparison of different lightweight aggregate concrete strengths, group B for comparison of different curing techniques, group C for comparison of different pouring techniques, group D for comparison of different surface conditions, group E for comparison of different slenderness ratios, and group F for comparison of different diameter to thickness ratios.

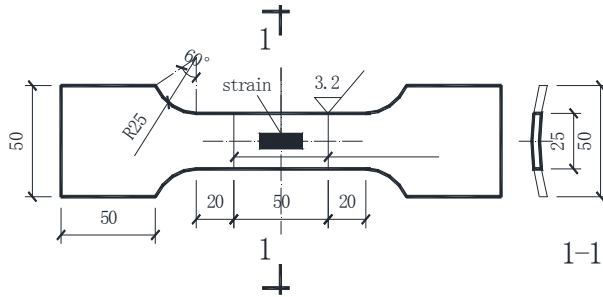


Figure 1. Steel Tensile Specimen (Unit:mm)

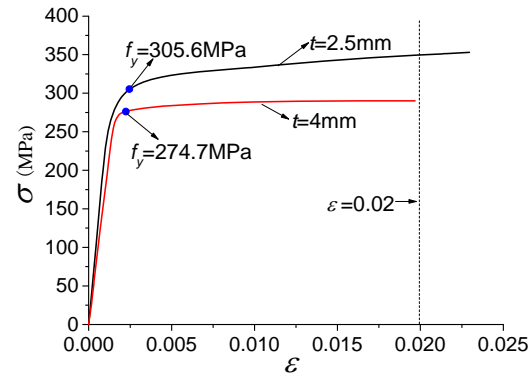


Figure 2. Stress-Strain Curve of Steel

2.2 Test Instruments and Procedure

Figure 3 shows the loading and measurement system. The load was applied by hydraulic jack with a maximum load range of 3000 kN and measured by a pressure sensor with maximum range equivalent to 500 kN. To measure the relative displacement of the steel tube and the core concrete, two displacement transducers were arranged at the bottom end of the steel tube column on magnetic meter bases. Throughout the test, the data were continuously collected by a data acquisition system which was composed of TS3890 dynamic strain gauges, gauge readers, and a personal computer.

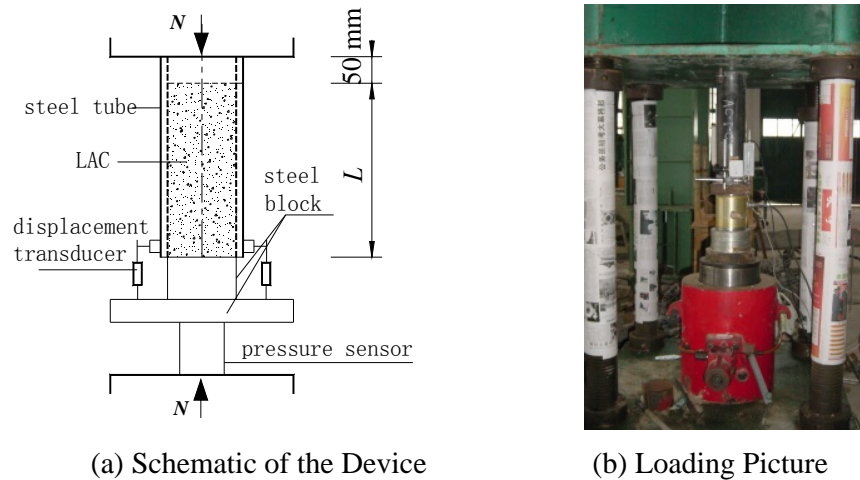


Figure 3. Loading and Measurement System

Before testing, a pre-load of 1 kN to 2 kN was applied to ensure that all component of the loading and measurement system were brought into close contact. Then this seating load was removed and the test started. The specimens were loaded at rate of 1/20 of the predicted ultimate load at the beginning. Each load was maintained for about 2-3 minutes to enable development of the full associated deformation. When obvious non-linear sliding between the steel tube and concrete was observed, the samples were loaded slowly and continuously. The test was stopped when the concrete underwent an apparent slip displacement. Four specimens were selected for reloading in the opposite direction and this procedure was repeated for a total of four load cycles.

3. DISCUSSIONS OF INITIAL PUSH-OUT TESTS RESULTS

3.1 Testing process and slip curves

At the beginning of the test, the displacement increased slowly and minimal slip occurred. On approaching the failure load, brittle acoustic emissions from the concrete could be heard. The displacement increased with the load increasing and the acoustic emissions from the concrete also increased in frequency and intensity. After the maximum value of load was conducted, the load plateaued for a period of time while the displacement still increased. Then, the load began to decrease as the displacement still increased. The displacement reached the maximum when the core concrete was pushed out. For the failure specimens, concrete showed obvious slippage with crushing at one end. Figure 4 shows the failed specimens after a push-out test. No local buckling appeared on the steel tube, which indicated that the steel tube restrained concrete effectively.

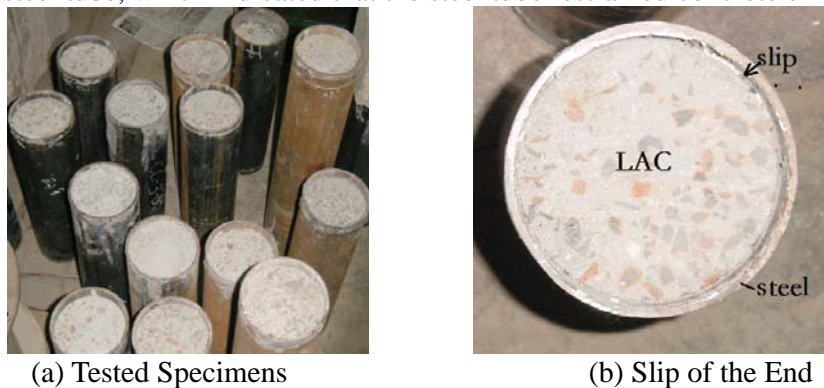


Figure 4. Specimens after Testing

Table 2. Dimensions and Results of Tested Specimens.

Specimen	Tube size (mm) $D \times t \times L$	Slenderness ratio $4L/D$	Diameter to thickness ratio D/t	Concrete strength f_{ck} (MPa)	Ultimate load (kN)	Bond strength (MPa)	Average strength (MPa)	Concrete vibration	Curing	Surface
A-1-a	114×4×350	12.28	28.5	28.71	169.5	1.45				
A-1-b	114×4×350	12.28	28.5	28.71	162.9	1.40	1.42	Vibrator	Natural	Smooth
A-1-c	114×4×350	12.28	28.5	28.71	163.5	1.40				
A-2-a	114×4×350	12.28	28.5	30.71	181.6	1.56				
A-2-b	114×4×350	12.28	28.5	30.71	181.8	1.56	1.52	Vibrator	Natural	Smooth
A-2-c	114×4×350	12.28	28.5	30.71	167.2	1.43				
A-3-a	114×4×350	12.28	28.5	37.38	161.7	1.39				
A-3-b	114×4×350	12.28	28.5	37.38	165.3	1.42	1.39	Vibrator	Natural	Smooth
A-3-c	114×4×350	12.28	28.5	37.38	158.4	1.36				
B-4-a	114×4×350	12.28	28.5	28.71	145.8	1.25				
B-4-b	114×4×350	12.28	28.5	28.71	150.1	1.29	1.26	Vibrator	Sealed curing	Smooth
B-4-c	114×4×350	12.28	28.5	28.71	145.2	1.25				
C-5-a	114×4×350	12.28	28.5	28.71	148.0	1.27				
C-5-b	114×4×350	12.28	28.5	28.71	153.9	1.32	1.28	Manual	Natural	Smooth
C-5-c	114×4×350	12.28	28.5	28.71	147.1	1.26				
D-6-a	114×4×350	12.28	28.5	28.71	291.7	2.50				
D-6-b	114×4×350	12.28	28.5	28.71	273.4	2.35	2.45	Vibrator	Natural	Rough
D-6-c	114×4×350	12.28	28.5	28.71	289.8	2.49				
E-7-a	114×4×490	17.19	28.5	28.71	318.4	1.95				
E-7-b	114×4×490	17.19	28.5	28.71	370.4	2.27	2.09	Vibrator	Natural	Rough
E-7-c	114×4×490	17.19	28.5	28.71	336.1	2.06				
E-8-a	114×4×780	27.37	28.5	28.71	380.2	1.46				
E-8-b	114×4×780	27.34	28.5	28.71	362.0	1.39	1.46	Vibrator	Natural	Rough
E-8-c	114×4×780	27.37	28.5	28.71	400.4	1.54				
F-9-a	114×2.5×350	12.28	45.6	28.71	184.5	1.53				
F-9-b	114×2.5×350	12.28	45.6	28.71	174.2	1.45	1.48	Vibrator	Natural	Rough
F-9-c	114×2.5×350	12.28	45.6	28.71	177.7	1.47				

Notes: (1) D is the external diameter, t is the thickness, and L is the length of the tube.

(2) f_{ck} is the axial compressive strength of the lightweight aggregate concrete.

(3) The bond strength τ is given by $\tau = N_u/(\pi L d)$, where N_u is the ultimate load and d is the inner diameter of the tube.

The load-slip curves from initial push-out tests are shown in Figure 5. The corresponding ultimate load and bonding strength are shown in Table 2. The relative slip of concrete increased linearly and slowly with a sharply increasing load at the beginning of test. When the load approached its ultimate value, the slip grew rapidly, indicating that the bond between the lightweight aggregate concrete and the steel tube began to be damaged. After the ultimate load was reached, the slip increased quickly and showed different load-displacement trends.

3.2 Bond Slip Process

Figure 5 shows several different types $S-N$ curves. In order to find the load-slipage rule, the bond slip process and the slip mechanism were analyzed.

For the LACFSTs, the bonding force is similar to that of normal CFSTs, and includes the following components: the chemical cementing force at the interface between the cement and the steel pipe, the mechanical interaction force between the concrete and the rough surface of the steel, and the friction at the surface. The chemical cementing force is very small and determined by the concrete properties. The mechanical interaction force generates mainly due to the shearing resistance of the concrete, which depends on the roughness of the steel surface and the shear strength of the concrete. The friction is proportional to the friction coefficient and the pressure on the contact surface. The

friction coefficient depends on the roughness of the interface between the steel tube and the concrete, and the pressure refers to the restriction imposed by the steel tube on the concrete.

The axial load only acts on the concrete section in the push-out test. Therefore, the longitudinal force is transmitted from the concrete to the steel tube because of the bonding between concrete and steel. Meanwhile, the steel tube is subject to transverse extrusion of concrete under axial load which results in the biaxial stress state of the steel tube. This causes a reduction in the normal constraint capacity which influences the friction on the interface. Due to the non-uniform pipe diameter, the variation was defined to be a macro-dimensional deviation by Virdi [32]. If concrete slipping causes movement to a smaller diameter section of steel tube, the constraint effect increases and friction is enhanced. Before slipping, the bond strength is mainly composed of the chemical cementing force and the mechanical interaction.

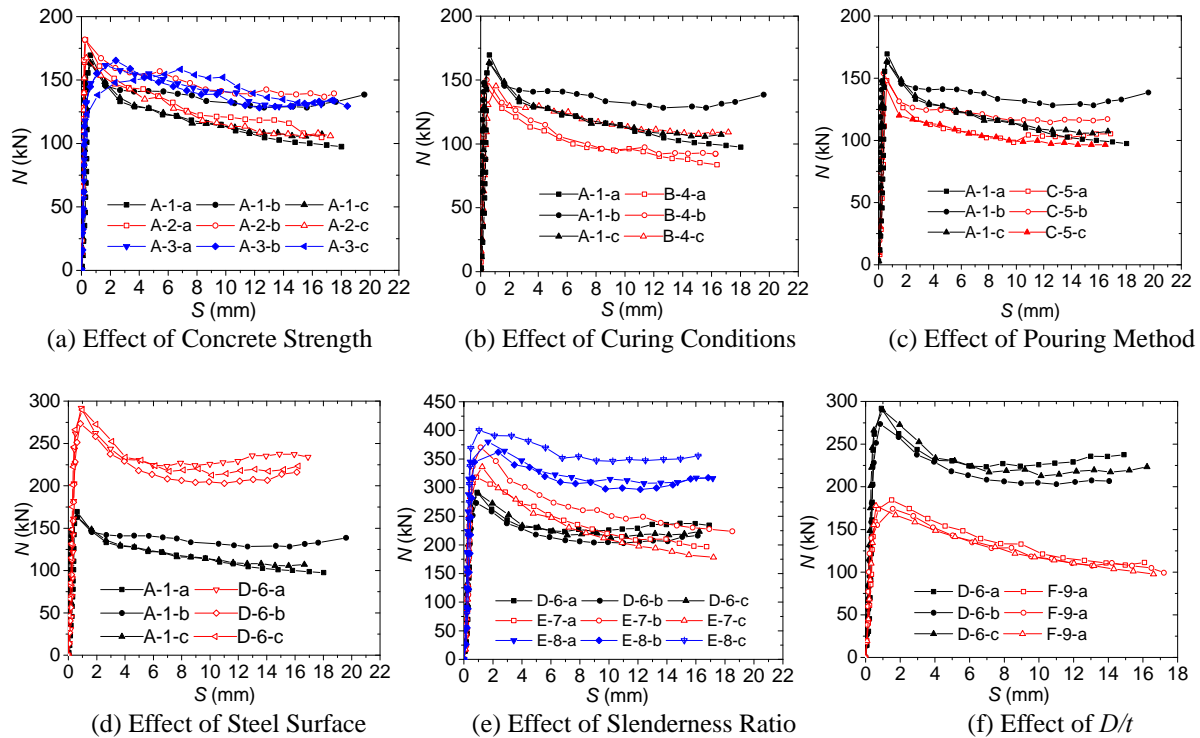


Figure 5. Load (N)-Slip (S) Curves: Push-out Tests

Figure 6 shows one typical bond-slip curve and different stages in the slipping process of a push-out test. At the beginning, the bonding stress is mainly provided by the chemical cementing force with no slip between concrete and steel (point A). As the load increased, a little slip occurred at the two ends of the specimens where the cementing force vanishes. Because the top end is loaded and the bottom end is unconstrained, the mechanical interaction force begins to work at the two ends (point B). Then, the slip at both ends increases and expands to the middle section. The cementing force exists only at the middle section where there is no relative slip. The bonding force of the other parts is mainly provided by the mechanical interaction force (point C). When the cementing force and mechanical interaction force reach the maximum value, the load reached failure (or ultimate) load N_u (point D), too. When the cementing force is broken completely, relative slip occurs over the whole interface between the steel tube and concrete core. The mechanical interaction also decreases upon large slip and the frictional force appears (point D). Then the mechanical interaction force is broken completely, and the slip increases quickly even as the load changes less (point F).

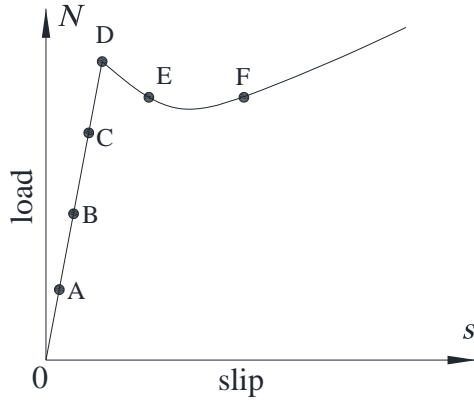


Figure 6. Bond-Slip Process

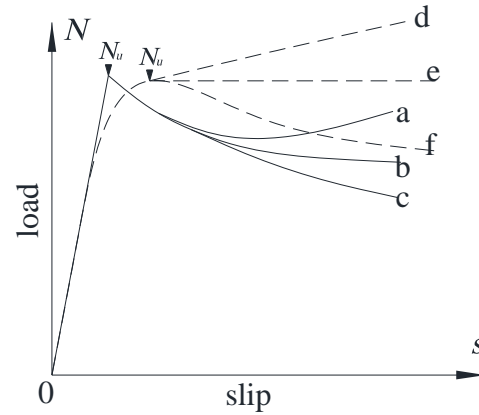


Figure 7. Classifications of Load-Slip Curves

Based on the test results in Figure 5, two classifications of load-slip curves can be seen: one has an obvious peak, the other doesn't, as shown in Figure 7. When there is no slip between the steel tube and the concrete, the bonding capacity consists of the cementing force and the mechanical interaction, which matches the friction force after slipping. If the sum of the cementing force and the mechanical interaction exceeds the initial friction force, the initial friction force cannot balance the bonding capacity before obvious slip occurs and the curves descend immediately with the appearance of a peak point. Otherwise, the curves ascend after obvious slip. However, the initial friction decreases during slippage because the friction reduces the roughness of the interface, which results in an inflection point, but not an obvious peak.

Based on the behavior after reaching the ultimate load, three types of curve are proposed (Figure 7). The macro-dimensional deviation causes an increase in the frictional force. If the macro-dimensional deviation is large, the increase in the friction is higher than the reduction in the initial friction, which causes the curve to have an ascending trend (lines a and d). Otherwise, the increase in friction is lower than the reduction therein, and the curve has a descending trend (lines c and f). In the situation intermediate to the aforementioned scenarios, the curve has an aclinic trend (lines b and e).

3.3 Effects of Main Factors on Average Strength

Table 2 shows the bond strength of specimens with different factors and Figure 5 shows the comparison of bonding process. Based on these two, the average bond strength of each group specimens is shown in Figure 8.

3.3.1 Effect of concrete strength

The concrete strength of groups A-1, A-2, and A-3 are 28.71 MPa, 30.71 MPa, and 37.38 MPa, respectively. The corresponding bond strengths are 1.43 MPa, 1.52 MPa, and 1.39 MPa, which show no obvious trend. The results indicate that the bond stress is independent of concrete strength. This is consistent with the studies of normal CFST tests by Viridi [32] and Liu *et al.* [33]. Shakir-Khalil [34] also proved that the data from normal CFST tests was scattered. However, Xue *et al.* [35], through a specimen test study, proposed that a higher concrete strength could increase the bond strength of normal CFSTs. The results showed that the bond strengths were 0.45MPa, 0.56MPa, 0.59MPa and 0.60MPa (the surface was treated by derusting machine) corresponding to concrete cube strengths of 41.9MPa, 53.1MPa, 77.8MPa and 83.7MPa. However, the increase was not obvious especially for the high strength concrete.

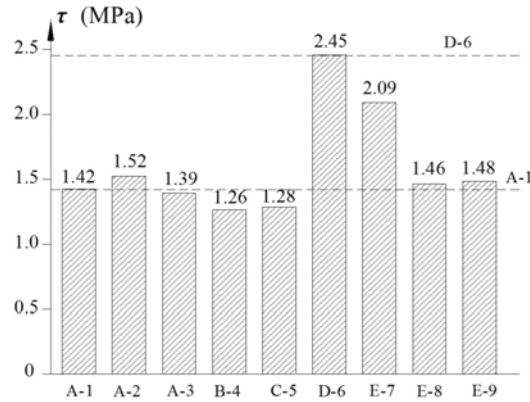


Figure 8. Comparison of Bond Strength

3.3.2 Effect of concrete curing condition

Comparison of specimens A-1 and B-4 shows the influence of concrete curing conditions on bond strength: group A-1 was cured under natural conditions while group B-4 was cured under sealed condition. As shown in Figure 8, bond strength under a natural curing condition was higher than that under sealed curing conditions, which matched normal CFSF data from Xue *et al.* [35]. Some researchers thought that the concrete shrinkage caused a tendency to separation between the concrete and steel and reduced the bond strength [33-35]. In fact, the concrete and steel only tended to separate, but did not do so completely. The tendency to separate causes tensile stress which is smaller than the cementing stress. When the load acts on the section, the transverse strain in the concrete produces a compressive stress in the steel, but some of the compressive stress is offset by the tensile stress caused by the tendency to separate.

3.3.3 Effect of concrete pouring method

Concrete in specimens A-1 and C-5 was vibrated by mechanical vibrator and manual, respectively. Figure 8 shows that the specimens vibrated mechanically have a higher bond strength than those compacted manually. The study of normal CFSTs by Viridi [32] also showed that adequate vibration could make the concrete denser and guaranteed that the steel tube and concrete would bond together to increase the bond strength. Otherwise, some clearance might remain between the two materials, which reduced the bond strength.

3.3.4 Effect of steel surface appearance

Specimens in group A-1, with their smooth steel surface, had a lower bond strength than specimens in D-6 with a rough steel surface (Figure 8). This is because a rough surface can increase the mechanical interaction force and the friction. The same results from tests on normal CFSTs were also proposed by Shakir-Khalil [34] and Xue *et al.* [35].

3.3.5 Effect of slenderness ratio

In order to avoid local buckling of steel, the slenderness ratio of the walls must satisfy the stipulated limiting value. Slenderness ratio can be expressed as $4L_0/D$ where L_0 is the interface length between the concrete and steel tube, and D is the external diameter of the steel tube. The slenderness ratios of specimens D-6, E-7, and E-8 were 12.28, 17.19, and 27.37, respectively. As shown in Figure 4 and Figure 5, specimens with a higher slenderness ratio sustained a higher

ultimate load but had a lower bond strength. The study of normal CFSTs by Virdi [32] and Liu *et al.* [33] showed the opposite trend with a minor increase in the slenderness ratio arrangement from 4 to 12. The results by Shakir-Khalil [34] showed that the slenderness ratio had no obvious influence on bond strength. Xue *et al.* [36] also found that the bond strength decreased with increasing slenderness ratio under an eccentric load which was similar to the results of these tests. Because the surface of groups D and E was rough, another three specimens were tested with smooth surface. The concrete strength was 31.35MPa. The bond strength were 1.56MPa, 1.57MPa and 1.21MPa corresponding to slenderness ratios of 12.28, 17.19 and 27.36. The results showed that the larger slenderness ratio had far smaller bond strength and the change of bond strength was not obvious when the slenderness ratio was small (less than 12). More detailed studies about the effects of slenderness ratio are needed.

3.3.6 Effect of diameter to thickness ratio

The diameter to thickness ratio reflects the strength of the steel tube to some extent, which can be expressed as D/t where D is the external diameter of the steel tube, and t is the thickness of the tube. The diameters to thickness ratio of specimens D-6 and F-9 were 28.5 and 45.6, respectively. The test results showed that the larger the diameter to thickness ratio, the lower the bond strength. Roeder *et al.* [12] also got the same results when studying normal CFSTs, but the results from normal CFSTs proposed by Virdi [32] indicated that the diameter-to-thickness ratio influenced bond strength less and the test results were scattered.

4. DISCUSSION OF REPEATED PUSH-OUT TEST RESULTS

Repeated push-out tests were conducted on four specimens (A-1-c, A-3-a, C-5-c and D-6-a). After the initial push-out test, the lightweight aggregate concrete slipped from the bottom of the steel tube to the upper end and the empty space changed from upper to bottom end. Then, take off the specimen from the loading system and reverse the two end of specimen to make the empty space at the upper end. A repeated loading process of initial push-out testing was conducted on the reversed specimen. The push-out test process had four load cycles in two directions containing the initial one, which was called the repeated push-out test here.

The load-slip curves of the repeated push-out tests are shown in Figure 9, where n is the number of cycles. Figure 9 shows that the ultimate load of $n = 1$ is the largest. For push-out at $n = 1$, the bond strength is provided by a cementing force and mechanical interaction. In other push-out tests, the cementing force is destroyed and the mechanical interaction is reduced by the previous slippage. The bond strength is mainly offered by the friction which is also reduced because of the smoother interface caused by slippage. Through the analysis of normal CFSTs, such a friction reduction was also proved by Xue *et al.* [35]. It also causes, in the same push-out direction as $n = 1, 3$ or $n = 2, 4$, the bond strength to decrease as the number of cycles increases. Generally, it is considered that the roughness of interface reduces more with increasing slip and cycling time. However, the test results showed that the bond strength at $n = 4$ was higher than that at $n = 3$.

After reaching the ultimate load, the load-slip curves for push-out in the same direction had similar trends: $n = 3$ tended to $n = 1$, and $n = 4$ tended to $n = 2$. The ultimate load for push-out corresponding to a larger number of cycles in the same direction was smaller. It was easier for the increase in friction caused by macro-dimensional deviation to balance the ultimate load. This resulted in a rising trend of the curves for $n = 3, 4$ compared to those of $n = 1, 2$, and caused the curves for push-out in the same direction to come together. However, these were not mentioned in the studies of normal CFST tests, but the tests result figures by Xue *et al.* also showed the similar conclusions [35].

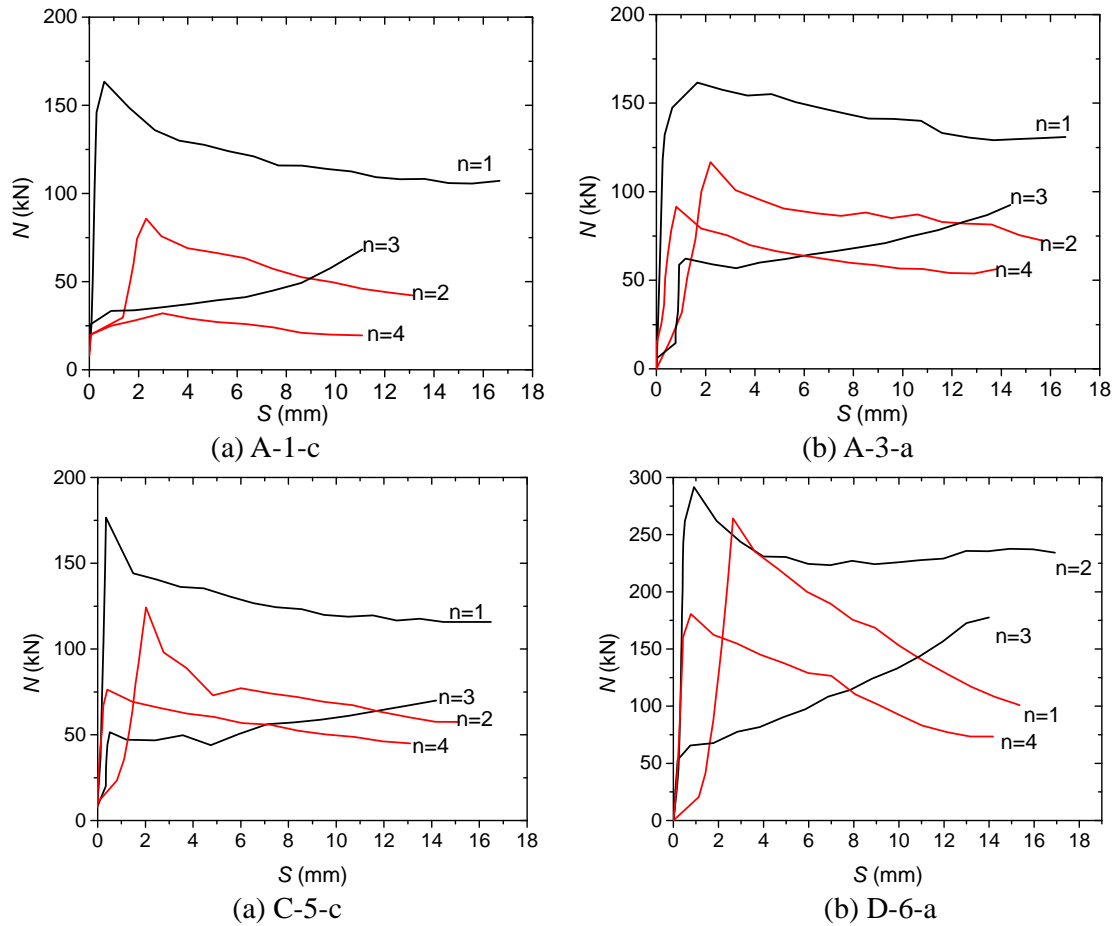


Figure 9. Load (N)-Slip (S) Curves: Repeated Push-out Test

5. BOND STRENGTH PREDICTION

Through the analysis of main factors on bond strength of LACFSTs, it can be concluded that the surface roughness, the slenderness ratio, and the diameter-to-thickness ratio are the main factors affecting behavior of the LACFST. The influence of concrete strength is not considered when calculating bond strength because of its smaller impact. Effects of concrete pouring and curing method on the bond strength cannot be ignored; but the influences of the two are not quantitatively considered due to the complexity of actual construction situations. Generally, the pouring and curing quality of concrete can be ensured according to the standard process of construction. In the process of a push-out test, the concrete is restrained by the steel tube, and the steel properties affect the bond strength. Some bond slip studies of normal CFSTs considered this by adopting a confinement coefficient and a steel area ratio [37], but the influence of steel area ratio and confinement coefficient are actually consistent when the effect of concrete strength is not considered. In practical engineering, the restraining effect of the steel tube on the concrete should be ensured because a low confinement coefficient causes local buckling. Meanwhile, slip occurs only with difficulty under conditions of obvious radial deformation of the steel tube caused by local buckling. The steel tube is required to deliver sufficient constraint to the concrete, otherwise it is not meaningful to discuss the interface bond slip. As shown in Figure 4, all of the specimens had no local buckling in the testing process. Based on the previous research into LACFSTs, a confinement coefficient larger than 1.0 was suggested to ensure the constraint effect [38]. Therefore,

the influence of steel properties was not considered in this discussion. In addition, the influence of other factors is considered by a safety coefficient.

With reference to the previous studies on normal CFSTs, a bond strength calculation formula was proposed according to the regression on the test results:

$$\tau = \gamma \times k \left[4.1625 - 0.2226 \left(\frac{L}{d} \right) - 0.0477 \left(\frac{D}{t} \right) \right] \quad (1)$$

Where, τ is the bond strength of an LACFST; γ is the safety coefficient; k is the influence coefficient for steel surface condition; l is the length of the interface; t is the thickness of the steel tube; d and D are the internal and external diameters of the steel tube, respectively. According to the suggestion arising from normal CFST studies, γ takes the value of 0.9 considering the errors in fabrication and unfavorable curing condition; k takes the value of 1.3 for a rusty surface without any de-rusting, 1.0 for a rusty surface with manual de-rusting, and 0.75 for rustless surfaces or rusty surfaces subjected to mechanical de-rusting [37].

The results from the use of Equation (1) are listed in Table 3 and compared to the test results. In the table, specimens B-4 and C-5 were not analyzed because the condition is not adopted in engineering practice. The average ratio of calculated bond strength to the test value was 0.973 with a standard deviation value of 0.033. The comparison shows that the results from Eq. 1 are accurate, and matched test data.

Table 3. Comparison of Test and Calculation Results

Specimen	Size (mm) $D \times t \times L$	L/d	D/t	γ	k	Bond strength (MPa)		τ_2 / τ_1
						Test(τ_1)	Calculation(τ_2)	
A-1	114×4×350	3.30	28.5	0.9	0.75	1.42	1.396	0.983
A-2	114×4×350	3.30	28.5	0.9	0.75	1.52	1.396	0.919
A-3	114×4×350	3.30	28.5	0.9	0.75	1.39	1.396	1.004
D-6	114×4×350	3.30	28.5	0.9	1.3	2.45	2.420	0.988
E-7	114×4×490	4.62	28.5	0.9	1.3	2.09	2.076	0.993
E-8	114×4×780	7.36	28.5	0.9	1.3	1.46	1.363	0.933
F-9	114×2.5×350	3.30	45.6	0.9	1.3	1.48	1.466	0.990
Average								0.973

6. CONCLUSIONS

The factors influencing bond strength were different from those found in studies of normal concrete-filled steel tubes. To clarify these reasons for this, a further study is needed. According to the test results and studies of the references, the following conclusions were obtained.

(1) The push-out tests on lightweight aggregate concrete-filled steel tubes gave two types of load-slip curves which either had obvious peaks or not. It depended on whether the friction after slip being smaller than the initial bond force or not. Each type of curve had three trends after ultimate load due to the degree of macro-dimensional deviation.

(2) According to these test, the bond strength was independent of the lightweight aggregate concrete strength. On the other hand, higher diameter-to-thickness ratios resulted in smaller bond strength. Moreover, a good quality of concrete vibration and curing could improve the bond strength.

(3) The repeated push-out test results showed that the ultimate load and bond strength corresponding to the first time push-out were the largest. In the same push-out direction, the ultimate load and bond strength decreased in time. After the ultimate load was conducted, the load-slip curves for push-out in the same direction were similar. These data were consistent with evidence from studies on normal concrete filled steel tubes.

(4) A calculation method of bond strength was proposed based on the test results. A comparison between test results and calculation results showed that the method was accurate when calculating the bond strength of lightweight aggregate concrete-filled steel tubes.

ACKNOWLEDGMENTS

The authors appreciate the support of The National Natural Science Fund of China (No.51208176), the Fundamental Research Funds for the Central Universities (2018B17414) and the Qing Lan Project. Besides, the first author would like to thank to Meijo University for the Invitation Fellowship Program.

REFERENCES

- [1] Chen, B.C. and Wang, T.L., "Overview of Concrete Filled Steel Tube Arch Bridges in China", Practice periodical on structural design and construction, 2009, Vol.14, No.2, pp. 70-80.
- [2] Xu, T., Xiang, T., Zhao, R., and Zhan, Y., "Nonlinear Finite Element Analysis of Circular Concrete-Filled Steel Tube Structures", Structural Engineering and Mechanics, 2010, Vol.35, No.3, pp.315-333.
- [3] Morino, S., and Tsuda, K., "Design and Construction of Concrete-Filled Steel Tube Column System in Japan", Earthquake Engineering and Engineering Seismology, 2002, Vol.4, No.1, pp. 51-73.
- [4] Han, L.H., Hou, C.C., and Wang, Q.L., "Behavior of Circular CFST Stub Columns under Sustained Load and Chloride Corrosion", Journal of Constructional Steel Research, 2014, Vol.103, pp.23-36.
- [5] Ge, H.B., Susantha, K.A.S., Satake, Y. and Usami T., "Seismic Demand Predictions of Concrete-filled Steel Box Columns", Engineering Structures, 2003, Vol.25, No.3, pp. 337-345.
- [6] Zhou, X., Yan, B., and Liu, J., "Behavior of Square Tubed Steel Reinforced-Concrete (SRC) Columns under Eccentric Compression", Thin-Walled Structures, 2015, Vol. 91, pp.129-138.
- [7] Assi, I.M., Qudeimat, E.M., and Hunaiti, Y.M., "Ultimate Moment Capacity of Foamed and Lightweight Aggregate Concrete-Filled Steel Tubes", Steel and Composite Structures, 2003, Vol.3, No.3, pp.199-212.
- [8] Fu, Z.Q., Ji, B.H., Lv, L., and Zhou, W.J., "Behavior of Lightweight Aggregate Concrete Filled Steel Tubular Slender Columns under Axial Compression", Advanced Steel Construction, 2011, Vol.7, No.2, pp.144-156.
- [9] Soheli, K.M.A., Liew, J.R., and Koh, C.G., "Numerical Modelling of Lightweight Steel-Concrete-Steel Sandwich Composite Beams Subjected to Impact", Thin-Walled Structures, 2015, Vol. 94, pp.135-146.
- [10] Mossahebi, N., Yakel, A., and Azizinamini, A., "Experimental Investigation of a Bridge Girder Made of Steel Tube Filled with Concrete", Journal of Constructional Steel Research, 2005, Vol.61, No.3, pp.371-386.

- [11] Dai, J.G., Tamon, U. and Yasuhiko, S., "Development of the Nonlinear Bond Stress–Slip Model of Fiber Reinforced Plastics Sheet–Concrete Interfaces with a Simple Method", *Journal of Composites for Construction*, 2005, Vol.9, No.1, pp.52-62.
- [12] Roeder, C.W., Cameron, B., and Brown, C.B., "Composite Action in Concrete Filled Tubes", *Journal of Structural Engineering*, 1999, Vol.125, No.5, pp.477-484.
- [13] Tao, Z., Song, T.Y., Uy, B., and Han, L.H., "Bond Behavior in Concrete-Filled Steel Tubes", *Journal of Constructional Steel Research*, 2016, Vol.120, pp.81-93.
- [14] Al-Mosawe, A., Al-Mahaidi, R., and Zhao, X.L., "Bond Behaviour between CFRP Laminates and Steel Members under Different Loading Rates", *Composite Structures*, 2016, Vol.148, pp.236-251.
- [15] Xie, T., and Ozbakkaloglu, T., "Behavior of Recycled Aggregate Concrete-Filled Basalt and Carbon FRP Tubes", *Construction and Building Materials*, 2016, Vol.105, pp.132-143..
- [16] Tahir, M.M., Shek, P.N., and Tan, C.S., "Push-off Tests on Pin-connected Shear Studs with Composite Steel–Concrete Beams", *Construction and Building Materials*, 2009, Vol. 23, No.9, pp. 3024-3033.
- [17] Chen, L., Dai, J., Jin, Q., Chen, L., and Liu, X., "Refining Bond–Slip Constitutive Relationship between Checkered Steel Tube and Concrete", *Construction and Building Materials*, 2015, Vol.79, pp.153-164.
- [18] Yan, J.B., Liew, J.R., Soheli, K.M.A. and Zhang, M.H., "Push-out Tests on J-hook Connectors in Steel–Concrete–Steel Sandwich Structure", *Materials and Structures*, 2014 , Vol.47, No.10, pp.1693-1714.
- [19] Chen, Y., Feng, R., Shao, Y., and Zhang, X., "Bond-slip behaviour of concrete-filled stainless steel circular hollow section tubes", *Journal of Constructional Steel Research*, 2017, Vol.130, pp. 248-263.
- [20] Abende, R., Ahmad, H. S., and Hunaiti, Y. M., "Experimental studies on the behavior of concrete-filled steel tubes incorporating crumb rubber", *Journal of Constructional Steel Research*, 2016, Vol. 122, pp. 251-260.
- [21] Aly, T., Elchalakani, M., Thayalan, P., and Patnaikuni, I., "Incremental collapse threshold for pushout resistance of circular concrete filled steel tubular columns", *Journal of Constructional Steel Research*, 2010, Vol. 66, No. 1, pp. 11-18.
- [22] Qu, X., Chen, Z., Nethercot, D. A., Gardner, L., and Theofanous, M., "Load-reversed push-out tests on rectangular cfst columns", *Journal of Constructional Steel Research*, 2013, Vol. 81, No. 3, pp. 35-43.
- [23] PetrusClotilda, Hamidhanizah, A., IbrahimAzmi, and Davylyn, N. J., "Bond strength in concrete filled built-up steel tube columns with tab stiffeners", *Canadian Journal of Civil Engineering*, 2011, Vol. 38, No. 6, pp. 627-637.
- [24] Nezamian, A., Almahaidi, R., and Grundy, P., "Bond strength of concrete plugs embedded in tubular steel piles under", *Canadian Journal of Civil Engineering*, 2006, Vol. 33, No. 2, pp. 111-125.
- [25] Xu, C., Huang, C., Jiang, D., and Song, Y., "Push-out test of pre-stressing concrete filled circular steel tube columns by means of expansive cement", *Construction & Building Materials*, 2009, Vol. 23, No. 1, pp. 491-497.
- [26] Mouli, M., and Khelafi, H., "Strength of short composite rectangular hollow section columns filled with lightweight aggregate concrete", *Engineering Structures*, 2007, Vol. 29, No. 8, pp. 1791-1797.
- [27] Eurocode 4. Design of composite steel and concrete structures. Part 1-1: General rules and rules for buildings, BSI. 2004.
- [28] AASHTO. "AASHTO-LRFD Bridge design guide specifications for GFRP-reinforced concrete bridge decks and traffic railings." American Association of State Highway and Transportation Officials, Washington, DC. 2009.

- [29] “Recommendations for design and construction of concrete filled steel tubular structure”, Tokyo: Architectural Institute of Japan. 1997.
- [30] CECS 28 : 2012, “Technical specification for concrete-filled steel tubular structures”, The Engineering Construction Association of China, 2012. (In Chinese)
- [31] GB/T228-2002, “Metallic Materials-Tensile Testing at Ambient Temperature”, The National Standard of China, 2002. (In Chinese)
- [32] Viridi, K. S., “Bond Strength in Concrete Filled Steel Tubes”, Int. Assoc. for Bridge & Structural Engineering, 1980, Vol.3, pp.125-139.
- [33] Liu, Y.J., Liu, J.P., and Chi, J.J., “Shear Bond Behaviors at Interface of Concrete-Filled Steel Tube”, Journal of Guangxi University (Natural Science Edition), 2010, Vol.35, No.1, pp. 17-23. (In Chinese)
- [34] Shakir-Khalil, H., “Pushout Strength of Concrete-Filled Steel Hollow Section Tubes”, The Structural Engineering, 1993, Vol.71, No.13, pp.230-233.
- [35] Xue, L.H., and Cai, S.H., “Bond Strength at the Interface of Concrete-Filled Steel Tubular Columns: part I”, Building Science, 1996, Vol.12, No.3, pp.22-8. (In Chinese)
- [36] Xue, L.H., and Cai, S.H., “The Influence of Load Eccentricity on Bond Strength at the Interface of Concrete-Filled Steel Tube Columns”, Building Science, 1997, Vol.13, No.2, pp.22-25. (In Chinese)
- [37] Xu, J.J., Chen ,Z.P., Xue, J.Y., and SU, Y.S., “Failure Mechanism of Interface Bond Behavior Between Circular Steel Tube and Recycled Aggregate Concrete by Push-out Test”, Journal of Building Structures, 2013, Vol.34, No.7, pp.148-157. (In Chinese)
- [38] Fu, Z.Q., Ji, B.H., Zhou, Y., and Wang, X.L., “An Experimental Behavior of Lightweight Aggregate Concrete Filled Steel Tubular Stub under Axial Compression”, In GeoHunan Int. Conf., 2011, pp.24-32.

FIRE RESISTANCE OF STEEL TUBULAR COLUMNS INFILLED WITH ULTRA-HIGH STRENGTH CONCRETE

X. Lyu^{1,2}, G.P. Shu^{1,2,*}, J.Y. Richard Liew³ and Er-F. Du^{1,2}

¹*School of Civil Engineering, Southeast University, Nanjing 210096, China*

²*Key Laboratory of C & PC Structures, Ministry of Education, Southeast University, Nanjing 210096, China*

**(Corresponding author: E-mail: sgp0818@vip.sina.com)*

³*Department of Civil and Environmental Engineering, National University of Singapore, E1A-07-03, 1 Engineering Drive 2, Singapore 117576, Singapore*

Received: 12 May 2017; Revised: 4 August 2017; Accepted: 25 November 2017

ABSTRACT: Ultra-high strength concrete filled steel tubular columns (UHSCFT) with compressive strength more than 100 MPa are an attractive option for high-rise buildings and several such applications have been seen in modern construction around the world. The compressive strength of ultra-high performance concrete/cement composite could reach as high as 180 N/mm². This paper investigates the fire resistance of externally protected ultra-high strength concrete filled tubular columns exposed to the standard ISO fire. Numerical analyses were carried out using a general finite element analysis software and the results were validated against the test results in terms of heat distribution and thermal-mechanical behavior. Comparison with the test results showed a reasonable agreement with finite element results in terms of temperature prediction and load displacement behavior during the fire. Finally, based on the validated finite element model, further numerical investigations were carried to study the effects of fire protection thickness, load ratio, the strengths of concrete and steel, steel contribution ratio, relative slenderness ratio and the steel section diameter on the fire resistance of ultra-high strength concrete filled tube columns.

Keywords: Buckling resistance, column filled tube, thermal analysis, finite element analysis, fire resistance, ultra-high strength concrete

DOI: 10.18057/IJASC.2018.14.3.8

1. INTRODUCTION

Steel tubular columns are commonly used in high-rise buildings because their load and fire resistance can be further enhanced by filling them with concrete (Lie and Chabot [1]; Tao et al. [2]; Zha et al. [3]). The main benefit of using concrete filled tubular columns is the increase of load bearing capacity without the need of additional formwork (Jamaluddin et al. [4]; Kang et al. [5]). The concrete core acts as heat sink to reduce the temperature of the steel tube when the composite column is subjected to fire (Xiao et al. [6]). Various types of concrete filling may be used in practice, including unreinforced concrete, steel bar reinforced concrete, and steel fiber reinforced concrete (Han et al. [7]; Fong et al. [8]; Xu et al. [9]). The infill concrete also enhances the steel tube's resistance to local buckling.

Studies on the fire resistance of steel tubular columns infilled with normal and high strength concrete have been carried out by several researchers (Wang and Young [10]; Yang et al. [11]; Liew and Xiong [12]; Li et al. [13]). Recent research focuses on the use of ultra-high strength concrete (UHSC) as infilling material to form concrete filled tubular members (CFTs) (Lee et al. [14]; Xiong and Liew [15]; Liew et al. [16]). Steel tubular members infilled with UHSC with compressive strength up to 180 N/mm² provide higher compression resistance and, therefore, smaller column size. Liew et al. [17 & 19] have investigated the behavior of such columns in both ambient temperature and fire situations.

Ultra-high strength concrete material is very brittle and has no post peak behavior after it is loaded beyond the maximum load. This is a serious drawback and limits its application in construction. However, when UHSC is used in concrete filled tubes, the confinement provided by the steel tube can improve the post-peak ductility of the ultra-high strength concrete depending on the steel contribution ratio as observed by Liew et al. [18] in the experimental studies.

This paper presents the nonlinear finite element analysis model to simulate the fire resistance of UHSC filled tubular columns exposed to the standard fire condition. The composite action between the steel and concrete has been considered in the numerical model. The column is subjected to axial compression followed by heating under standard ISO fire until failure. The analysis considers the influences of temperature on the strength and modulus of the UHSC material based on the test data from Xiong [19]. The accuracy of the numerical model is established by comparing the numerical results with test results. Finally, parametric studies are carried out to evaluate the effects of fire protection thickness, load ratio, strengths of concrete and steel, steel contribution ratio, column slenderness ratio and the steel section diameter on fire resistance of steel tubular columns infilled with UHSC. The findings are useful for the designer to derive cost-effective solutions in providing fire protection and determining the fire resistance performance of composite column.

2. TEMPERATURE CALCULATION OF CONCRETE FILLED TUBULAR MEMBERS

Experimental work on tubular beam-columns infilled with high strength and ultra-high strength concretes subjected to ISO standard fire have been carried out by Xiong [19]. The details of the test specimens are shown in Table 1. The test specimens for the analysis are taken from Xiong [Error! Bookmark not defined.]. All the columns are 3.81 m with 3.0 m long exposed to fire in the furnace, and the details are shown in Table 1 and Figures 1(a) & 1(b). The prediction of the temperature field in the ultra-high strength concrete filled tubular column is based on the fire temperature in the furnace.

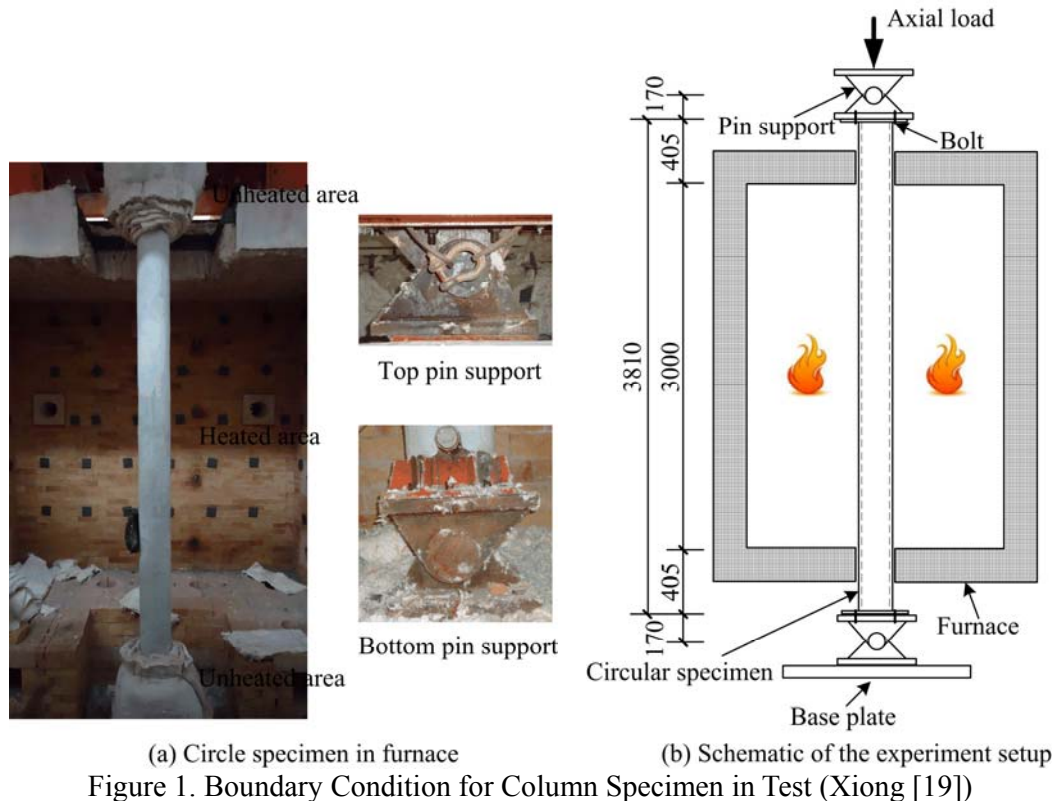
Table 1. Details of The UHSCFT Columns

Specimen	Diameter (D)× thickness (t_s) (mm × mm)	Steel yield strength f_y (MPa)	Steel Modulus of Elasticity E_a (GPa)	Concrete Cylinder Strength f_c (MPa)	t_p^* (mm)	δ^*	$\bar{\lambda}^*$
UCZ-1	219.1×16			161	5.9	0.50	1.01
UCZ-2	219.1×16	432	204	168	6.4	0.49	1.02
UCZ-3	219.1×16			164	8.1	0.49	1.02
UCZ-4	273×16	422	203	181	6.8	0.40	0.86
UCZ-5	273×10	418	201	180	8.6	0.28	0.94

*Notes: t_p is thickness of fire protection. $\delta = A_s f_y / (A_s f_y + A_c f_c)$ is the steel contribution ratio. $\bar{\lambda}$ is the relative slenderness.

The fire resistance of ultra-high strength concrete filled tubular (UHSCFT) column depends on the fire temperature to which the column is exposed, the temperature field in the column, the strength of the materials at elevated temperature and the member deformations during the fire exposure. Using the temperature-dependent thermal properties of the concrete and steel, the temperature history of the column can be obtained by solving the heat balance equation [20]. A two-dimensional nonlinear thermal analysis model for the UHSCFT column exposed to a fire on four sides is considered, with the assumption that no heat is flowing along the longitudinal axis [21-22]. The finite element simulations for both the heat transfer and structural analyses are conducted using the general finite element analysis package ABAQUS.

One of the main ingredients in making UHSC is bauxite aggregate which has better fire resistance than the siliceous aggregate as use in normal strength concrete (NSC). The residual strength and the strength reduction factor of UHSC are larger than those of NSC at elevated temperature. Furthermore, comparing UHSC with NSC, the strength reduction factor of UHSC is similar to NSC with calcareous aggregate, but higher than NSC with siliceous aggregate at temperature higher than 200°C. In other words, the strength and elastic modulus of UHSC are reduced less than those of NSC at elevated temperature. However, explosive spalling behavior of UHSC was observed when it was heated up to 500°C. But this can be prevented by adding polypropylene fibers 0.1% volume of concrete.



(a) Circle specimen in furnace (b) Schematic of the experiment setup
Figure 1. Boundary Condition for Column Specimen in Test (Xiong [19])

2.1 Thermal Properties of Ultra-High Strength Concrete (UHSC)

The thermal properties include the thermal conductivity, specific heat, thermal expansion, and the mass loss of the material at elevated temperatures. There are three material models of thermal properties which are often adopted for the heat transfer calculations. One is the Lie's thermal model, the second one is the AIJ code model, and the third one is the Eurocode model. In this paper, the thermal model is based on the Eurocode model [23-24] which considers the effects of water in the concrete on density and specific heat. Generally, the lower limit of thermal conductivity is used for normal strength concrete (NSC), while the upper limit is considered for high strength concrete (HSC) and ultra-high strength concrete (UHSC). The moisture content is assumed to be 3% for NSC and HSC, whereas it is ignored for UHSC.

2.2 Thermal Properties of Fire Protection Material

In the fire tests reported in Xiong [19], the fire protection material was a mixture of Portland cement (40%), perlite (25%), vermiculite (20%) and water (15%) by weight. The thermal properties

are assumed not to change with temperature. The thermal conductivity = $0.116 \text{ W/m}\cdot\text{K}$, specific heat = $1010 \text{ J/kg}\cdot\text{K}$ and density = 305 kg/m^3 are adopted based on the test data reported in Xiong [19].

2.3 Thermal Analysis of Specimens

The initial ambient temperature is set as 20°C . In the thermal analysis, 4-node shell element (DS4) is adopted to model the steel tube and 8-node brick element (DC3D8) for the concrete core and the fire protection with three layers along its thickness. The heat convection and radiation are considered as boundary conditions in the thermal analysis as shown in Figures 2a-c. The height of specimen exposed to fire is 3.0 m , while the height of specimen is 3.81 m . The composite column is subjected to uniform heating (close to an ISO standard fire) from the surrounding air in the furnace during the entire heating process.

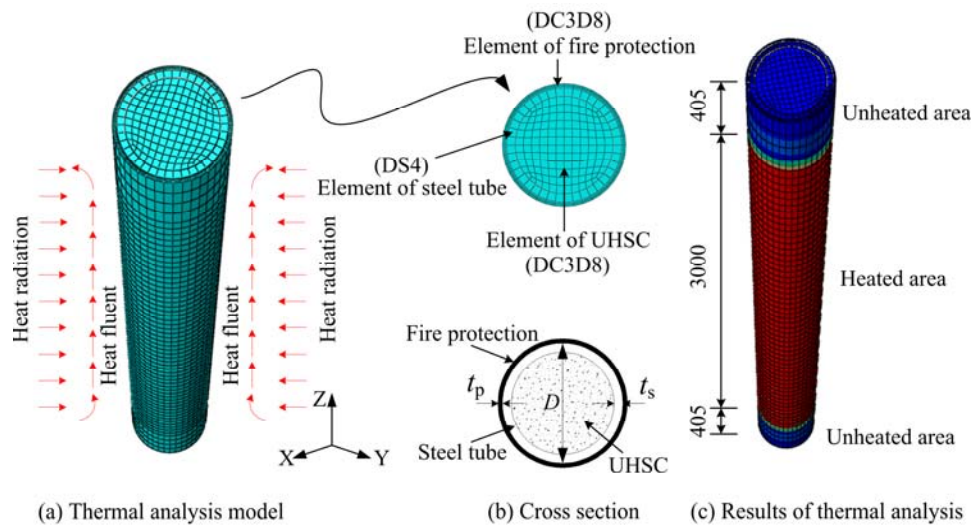


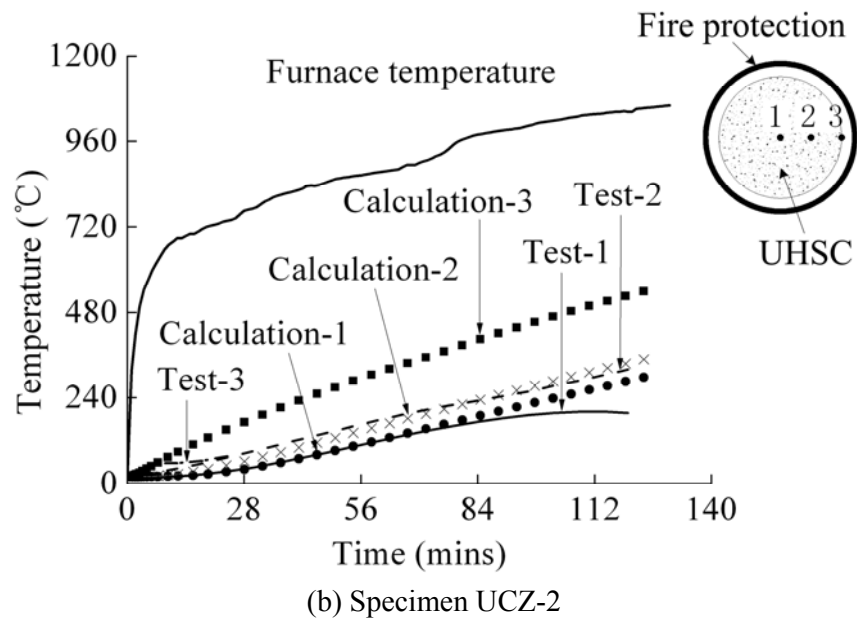
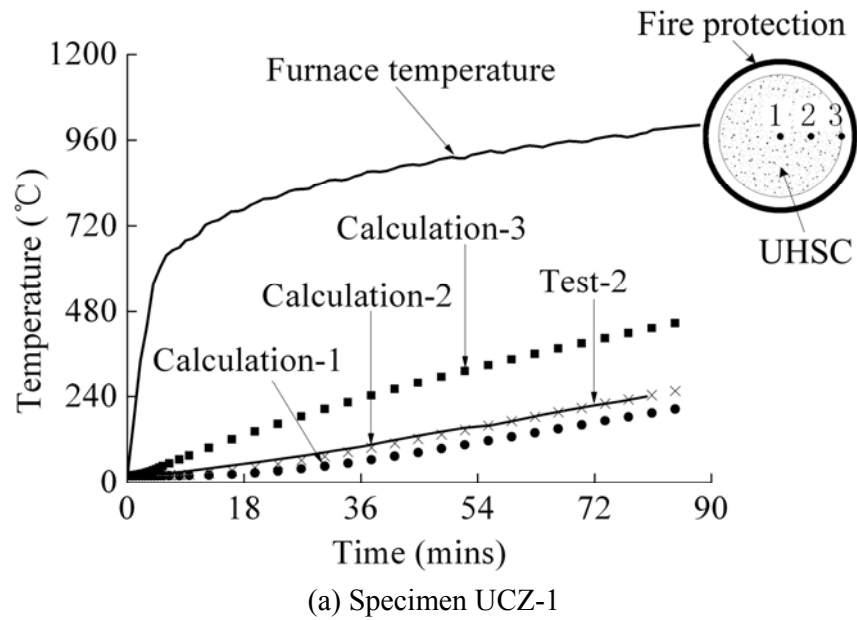
Figure 2. Boundary Conditions for Temperature Field and Calculation Results

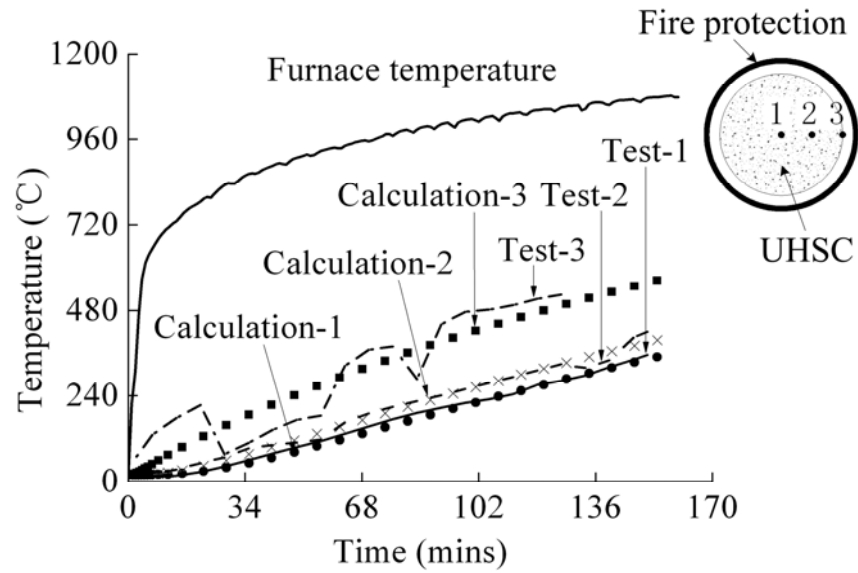
2.4 Comparison of Predicted Results with Tests

There are three measured points in the UHSCFT column. Point 1 is at the centre of column cross-section, point 2 is at the position of $r/2$ (r is radius of concrete core) and Point 3 is at the edge of the concrete core. The predicted temperatures based on the finite element analyses are compared with the measured temperatures from the tests, as shown in Figure 3. The furnace temperature was measured and plotted in Figures 3 (a)-(e).

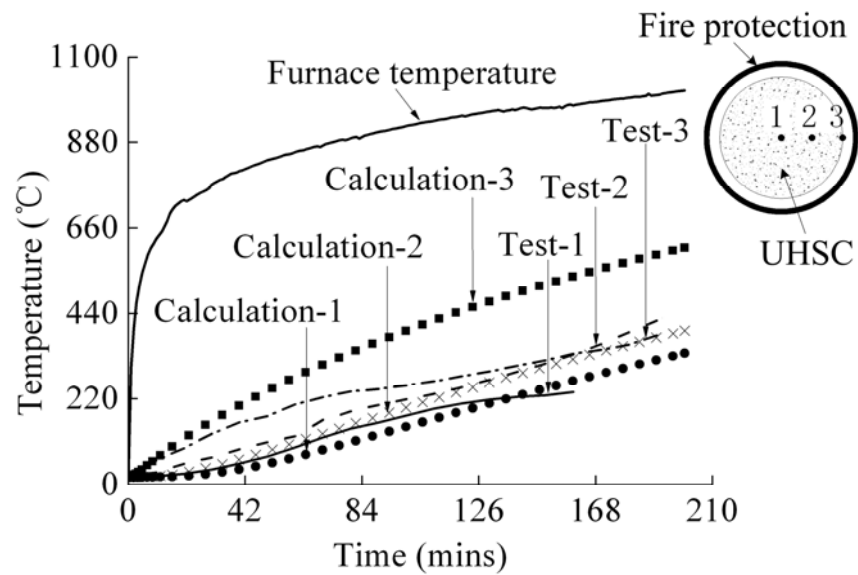
For specimen UCZ-1, the measured temperature at point 2 compared well with the predicted results. The mean error between the predicted temperature and measured temperature is less than 5%, what's more, with the temperature increasing, the value of the error becomes decreasing. The other two thermocouples at points 1 and 3 did not record any readings as they were damaged during the preparation of the test specimen. For specimen UCZ-2, the mean errors between the predicted temperature and measured temperature for points 1, 2 and 3 are less than 5%, although the error is a little big for point1 after exposing to fire 90 minutes. For specimens UCZ-3 and UCZ-5, the comparisons showed that the predicted temperatures were in reasonable agreement with the measured values. As shown in Figure 3c, the mean errors between the predicted temperature and measured temperature for points 1 and 2 are less than 4%, although the mean error is about 12% for point 3. For specimen UCZ-5, the mean errors between the predicted temperature and measured temperature for points 1 and 3 are less than 6%, although the mean error is about 15% for point 2.

The same reason was applied to the measure point 3 of UCZ-4, while the predicted temperature at points 1 and 2 are acceptable compared with the measured values.





(c) Specimen UCZ-3



(d) Specimen UCZ-4

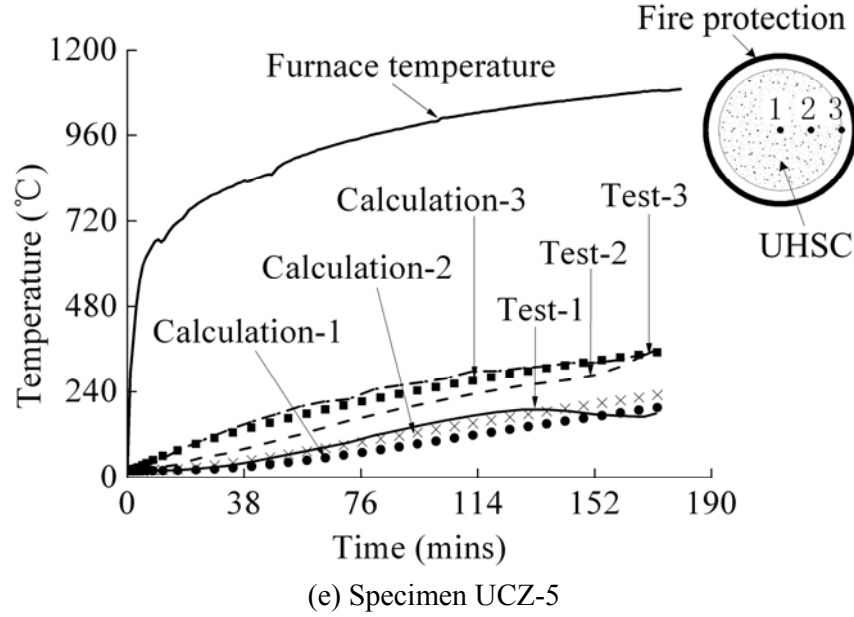


Figure 3. Comparison between the Predicted and Measured Temperatures for Specimens UCZ-1~5

3. MECHANICAL PROPERTIES AT ELEVATED TEMPERATURE

3.1 Ultra-High Strength Concrete (UHSC)

There is limited information on the mechanical properties of UHSC at elevated temperature. Xiong [19] conducted tests to evaluate the elastic modulus and compressive strength of the UHSC at elevated temperatures. In the tests, cylinder specimens with diameter = 100 mm and height = 200 mm were prepared. The specimens were heated in a furnace without pre-loading at a rate of 5°C/min until the target temperature was reached. Dosage of 0.1% polypropylene in volume was added into UHSC in case of spalling during heating. The target temperatures ranged between 100°C to 800°C at an increment of 100°C. Once the target temperature was reached, it was held for 4 hours to ensure that the temperature was uniformly distributed inside the test specimen. Finally, the specimen was subjected to compression until failure with displacement rate 0.4 mm/min during loading. A typical stress-strain relationship of UHSC at elevated for specimen UCZ-1 is shown in Figure 4. The reduction factors of the elastic modulus and compressive strength for specimens are shown in Tables 2 and 3, respectively. The test data were fitted into the stress-strain models in Eurocode 2 [23] as follow:

$$\sigma = \frac{3\varepsilon f_{c,\theta}}{\varepsilon_{c1,\theta} \left[2 + \left(\frac{\varepsilon}{\varepsilon_{c1,\theta}} \right)^3 \right]} \quad 0 \leq \varepsilon \leq \varepsilon_{cu1,\theta} \quad (1)$$

Where, $f_{c,\theta}$ is the compressive strength, $\varepsilon_{c1,\theta}$ is the strain corresponding to $f_{c,\theta}$, $\varepsilon_{cu1,\theta}$ is the strain for defining range of the descending branch.

Table 2. Reduction of Secant Modulus for UHSC at Elevated Temperature

Temperature (°C)	UCZ-1 (MPa)	UCZ-2 (MPa)	UCZ-3 (MPa)	UCZ-4 (MPa)	UCZ-5 (MPa)	Mean reduction
20	9.57×10^4	9.98×10^4	9.74×10^4	1.08×10^5	1.07×10^5	1.00
100	7.94×10^4	8.28×10^4	8.08×10^4	8.96×10^4	8.88×10^4	0.83
200	8.61×10^4	8.98×10^4	8.77×10^4	9.72×10^4	9.63×10^4	0.90
300	7.18×10^4	7.49×10^4	7.31×10^4	8.10×10^4	8.03×10^4	0.75
400	5.26×10^4	5.49×10^4	5.36×10^4	5.94×10^4	5.89×10^4	0.55
500	4.31×10^4	4.49×10^4	4.38×10^4	4.86×10^4	4.82×10^4	0.45
600	2.87×10^3	2.99×10^3	2.92×10^3	3.24×10^3	3.21×10^3	0.30
700	2.39×10^3	2.50×10^3	2.44×10^3	2.70×10^3	2.68×10^3	0.25
800	2.20×10^3	2.30×10^3	2.24×10^3	2.48×10^3	2.46×10^3	0.23

Notes: The data were obtained from Xiong's experiments.

Table 3. Reduction of Compressive Strength for UHSC at Elevated Temperature

Temperature (°C)	UCZ-1 (MPa)	UCZ-2 (MPa)	UCZ-3 (MPa)	UCZ-4 (MPa)	UCZ-5 (MPa)	Mean reduction
20	161	168	164	181	180	1.00
100	125	130	127	140	139	0.77
200	144	150	147	162	161	0.89
300	153	159	155	172	171	0.95
400	135	141	138	152	151	0.84
500	115	120	117	129	128	0.71
600	99	103	101	111	111	0.61
700	81	85	83	91	91	0.50
800	48	50	49	54	54	0.30

Notes: The data were obtained from Xiong's experiments.

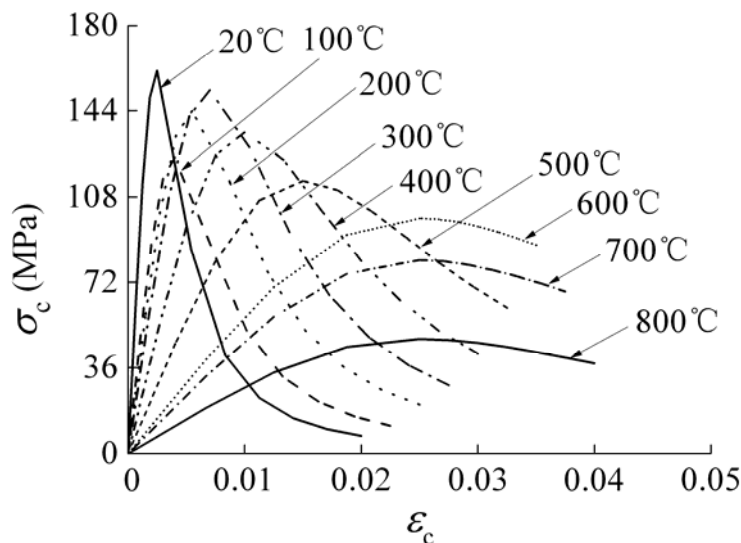


Figure 4. Stress-strain Relationship for UHSC of UCZ-1 at Various Temperatures

Spalling was not observed during heating of all specimens. As shown in Table 2, for the elastic modulus of UHSC at elevated temperature, an unusual deterioration and recovery were observed at the temperature range of 100°C~200°C. For compressive strength of UHSC at elevated temperature, an unusual deterioration was observed at the temperature 100°C, which was shown in Table 3.

However, with temperature increased range of 100°C~300°C, the strength was partly recovered. At 800°C, the strength was only about 30% of that at room temperature.

Seen from Figure 4, the peak stress decreases sharply at 100°C and recovery was observed at the temperature range of 100°C~300°C, which is the same as the compressive strength. The stress decreases sharply after the peak stress at temperature range of 20°C~300°C, but it decreases gently at temperature range of 400°C~800°C.

3.2 Steel

Eurocode 3 [25] provides the equations to describe the elastic modulus and effective strength of steel at elevated temperature. The reduction factors of elastic modulus, yield strength and the relationship of stress and strain at elevated temperature given in Eurocode 3:1-2 [25] are adopted for the numerical analysis.

4. FIRE RESISTANCE OF UHSCFT COLUMNS

4.1 Eurocode 4 Approach

According to the simplified method in Eurocode 4 [24], the plastic resistance of the concrete filled circular cross-section may be calculated as:

$$N_{pl,Rk} = A_a f_y + A_c f_{ck} \quad (2)$$

if $\bar{\lambda} > 0.5$. Otherwise, concrete confinement effect may be considered in calculating the cross section plastic resistance as:

$$N_{pl,Rk} = \eta_a A_a f_y + A_c f_{ck} (1 + \eta_c \frac{t_s}{d} \frac{f_y}{f_{ck}}) \quad (3)$$

Where A_a and A_c are cross-sectional areas of the steel section, concrete core respectively. η_a and η_c are the steel strength reduction and the concrete strength enhancement factor, respectively. f_y and f_{ck} are characteristic strengths of structural steel and concrete core respectively. t_s is the wall thickness of steel tube, d is the overall diameter of composite column.

To account for overall buckling of the column, the reduction factor χ is given in terms of the relative slenderness $\bar{\lambda}$ and the corresponding buckling curve as follow,

$$\chi = \left(\Phi + \sqrt{\Phi^2 - \bar{\lambda}^2} \right)^{-1} \leq 1.0 \quad (4)$$

where, $\Phi = 0.5[1 + \alpha(\bar{\lambda} - 0.2) + \bar{\lambda}^2]$ and

$$\bar{\lambda} = \sqrt{\frac{N_{pl,Rk}}{N_{cr}}} \quad (5)$$

α is an imperfection factor corresponding to the appropriate buckling curve. For concrete filled tubes, buckling curve “a” and $\alpha=0.21$ are adopted if the reinforcement ratio does not exceed 3%.

In the tests, there is no reinforcement in the UHSCFT columns, therefore $\alpha=0.21$ is adopted herein. For comparison with test results, $N_{pl,Rk}$ calculated from Eq. 2 or Eq. 3 should be based on characteristic strengths. $N_{cr}=\pi^2(EI)_{eff}/l_e^2$ is the Euler buckling load of the composite column, and $(EI)_{eff}=E_a I_a+0.6E_{cm}I_c$ is the effective flexural stiffness of the composite cross-section, where E_a is the modulus of elasticity of the structural steel and E_{cm} is the secant modulus of elasticity of concrete. I_s and I_c are the second moments of area of the structural steel section and the uncracked concrete section respectively.

The characteristic buckling resistance of composite column subject to compression is given as

$$N_{b,Rk} = \chi N_{pl,Rk} \quad (6)$$

4.2 Thermal-Mechanical Analysis

During the thermal stress analysis, the element mesh remains the same as the temperature field analysis without fire protection. But the element type is changed from heat transfer element to thermal mechanical element.

In the thermal-mechanical analysis, 8-node brick element (C3D8R) is adopted for the UHSC core and 4-node shell element (S4R) for steel tube. The finite element meshes for the column cross-section is shown in Figure 5a. The column is simply supported at both ends with the boundary conditions as shown in Figure 5a.

The observed failure mode of specimen UCZ-3 and the predicted failure mode from FEM are shown in Figures 5b-c. The temperatures, stresses and strains at the centre of each element are assumed to be representative of those of the entire element. Furthermore, it is assumed that the steel and the concrete had the same temperature, t , at the interface (Song et al. [26]; Wang et al. [27]). Mesh convergence studies have been performed to study the sensitivity of the mesh size on the predicted results. An optimized mesh size of 20 mm (length):20 mm (width):60 mm (depth) for the part of specimen inside furnace, 20 mm (length):20 mm (width):100 mm (depth) for the rest part of specimen outside furnace was selected to ensure that the predicted results are within 2% error.

The time-dependent thermal-mechanical analysis was performed using the ABAQUS, a general nonlinear finite element program. The column is assumed to have an initial bow imperfection approximating a half-sine curve of mid-height magnitude of $Length/1000$. This member imperfection has been adopted based on the first buckling mode shape of pin-ended column subject to axial compression.

The value of friction coefficient $\mu=0.2$ to 0.5 is assumed between the steel tube and concrete core [28]. Sensitivity study on the friction coefficient has been carried out based on specimen UCZ-3. The result is shown in Figure 6. According to the analysis results, the influence of friction coefficient on the fire resistance of composite column is insignificant when the value is between 0.3 and 0.5 . The use of $\mu=0.2$ causes convergence problem near the failure temperature. The use $\mu=0.3$ is most appropriate as the predicted displacement-time curve is closer to the test result. Finally, $\mu=0.3$ is selected for the friction coefficient in longitudinal direction. As for the friction coefficient in the tangential direction, this factor has little effect on the fire response of composite columns according to the previous research done in Espinos et al. [28] and thus $\mu=0.3$ is assumed. A "Hard" contact formulation is used in the transverse direction normal to the concrete core surface to capture the contact pressure between the steel and concrete surfaces when they are in contact and allow for separation when the two surfaces move in different directions.

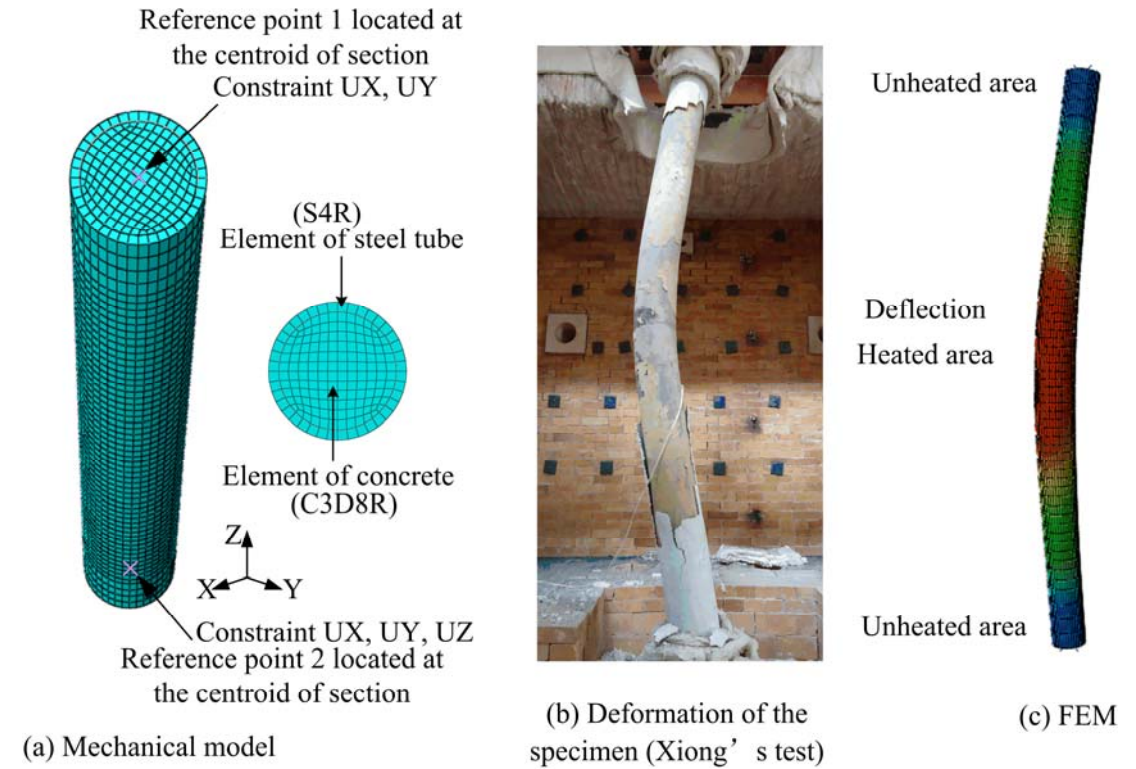


Figure 5. Boundary Conditions for Mechanical Models and Comparison of Experimental and Numerical Deformed Shapes after Fire Exposure for Specimen UCZ-3

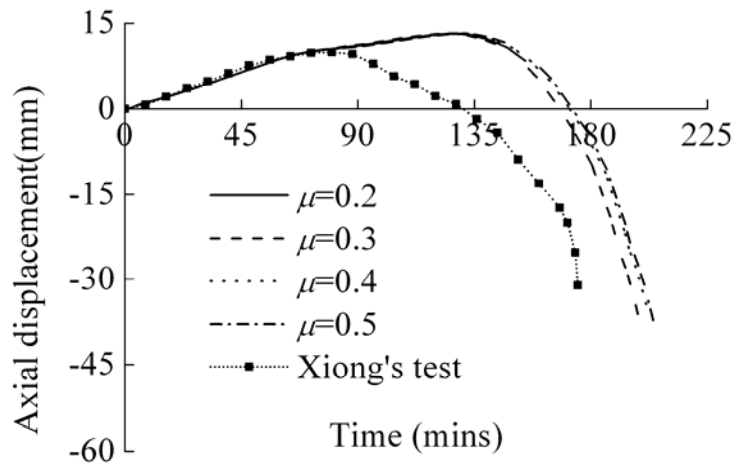
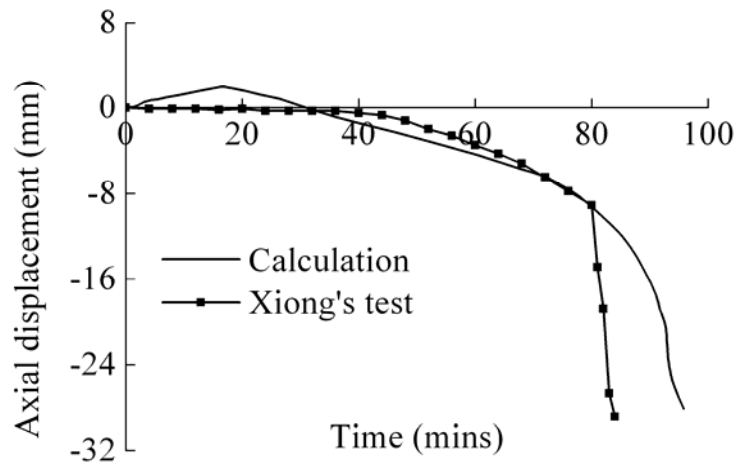


Figure 6. Comparison of Test and Predicted Results with Different Friction Coefficients

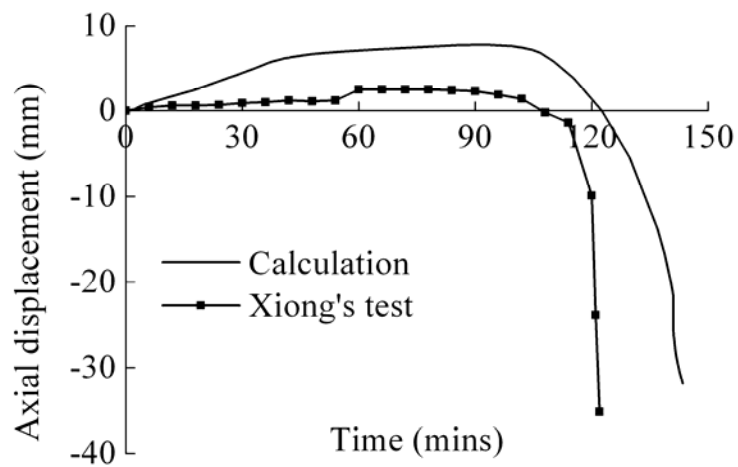
The period of time that a column can maintain the compressive load when subject to an ISO-834 Standard fire is determined [20]. For a column member subject to compression, failure occurs when either of the following two criteria is reached:

- (1) The axial deformation of the column reaches $0.01L$ mm, or
- (2) The axial deformation velocity exceeds $0.003L$ mm/min, where L is the fire exposed length of column in millimeter.

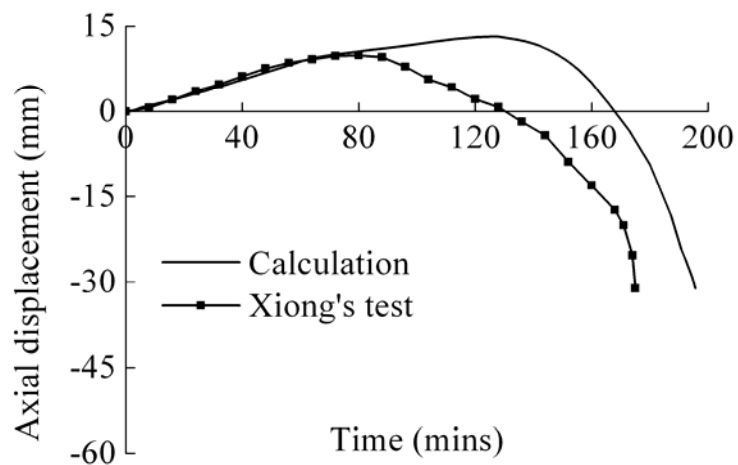
The results from the numerical analyses and tests are shown in Figure 7(a)-(e), and the comparisons are given in Table 4. The error of predicting the fire resistance of the concrete filled tubular columns, as compared to the test results, is within 15%. The error is considered to be reasonable and the numerical model will be used for parametric analyses in the subsequent sections.



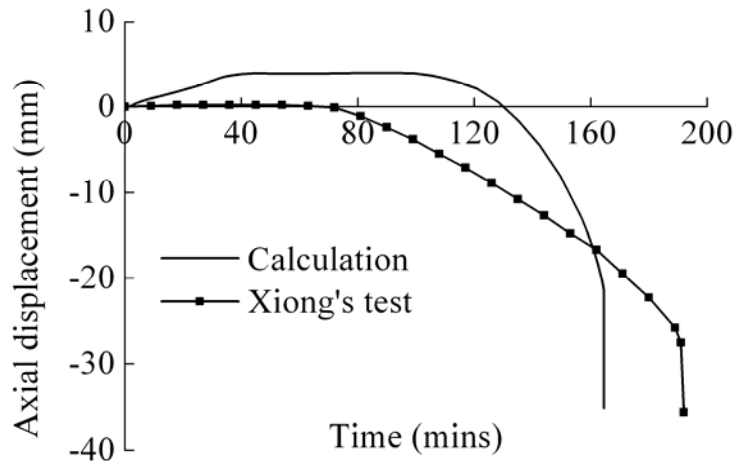
(a) Specimen UCZ-1



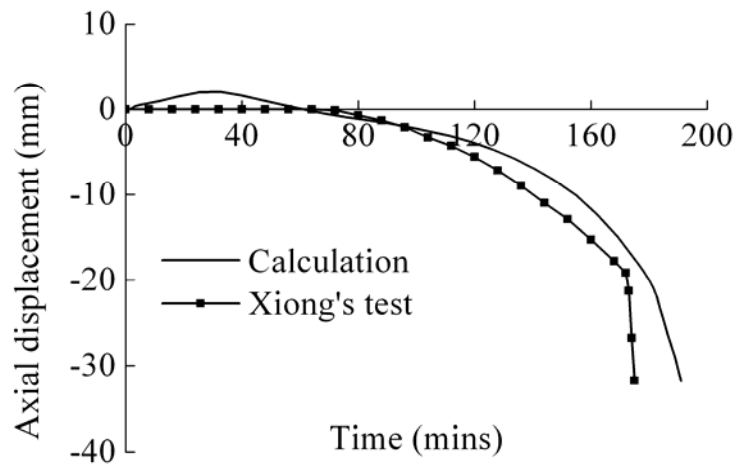
(b) Specimen UCZ-2



(c) Specimen UCZ-3



(d) Specimen UCZ-4



(e) Specimen UCZ-5

Figure 7. Comparison of Fire Resistance between the Calculation Results and Experimental Results (Xiong [19])

Table 4. Comparison of Fire Resistance Time between Predicted and Experimental Results

Specimen	t_p (mm)	β^*	FR*-Predicted (min)	FR*-Experiment (min)	Error (%)
UCZ-1	5.9	0.63	97	84	13
UCZ-2	6.4	0.59	140	122	15
UCZ-3	8.1	0.47	195	175	11
UCZ-4	6.8	0.53	165	191	-14
UCZ-5	8.6	0.56	191	175	9

Note: "FR" is the fire resistance time. " β " is load ratio.

5. PARAMETRIC STUDY ON FIRE RESISTANCE

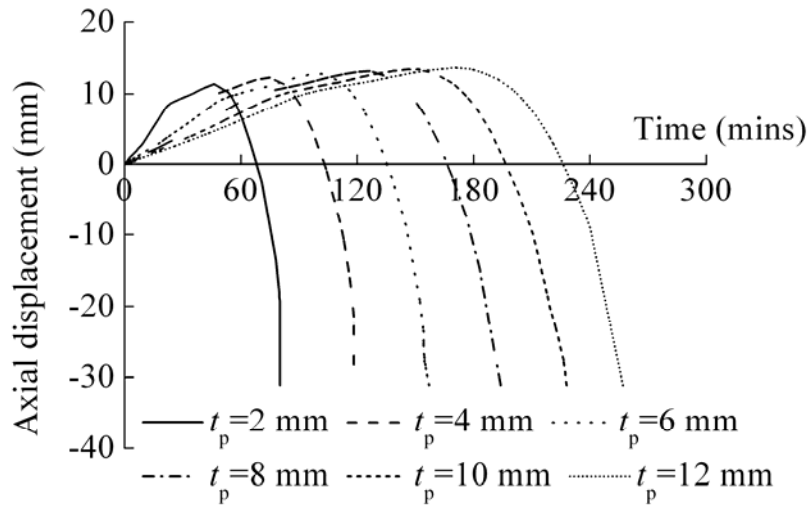
Parametric analysis is carried out on circular concrete filled tube section with diameter D and tube thickness t_s , length L , and is subjected to fire all round. The column is assumed to have an initial bow imperfection approximating a half-sine curve of mid-height magnitude of $L/1000$. The

column ends are assumed to be simply supported and it is subjected to axial compression. Same failure criteria as described in section 4 are assumed in calculating the fire resistance of the UHSCFT column. The load acting on the column is $0.5N_{b,Ek}$ in which $N_{b,Ek}$ is the characteristic buckling resistance of the member at ambient temperature based on Eurocode 4 [Error! Bookmark not defined.] prediction.

The parameters that influence the fire resistance of concrete filled tubes are studied using the finite element model established in Section 4. These parameters include fire protection thickness, load ratio β , strengths of the concrete and steel, relative slenderness ratio $\bar{\lambda}$ steel contribution ratio ($\delta = A_{afy}/(A_{afy} + A_{cf})$, where the A_a and A_c are the cross-sectional areas of steel tube and concrete core, respectively). The results are shown in Figs. 8-14.

5.1 Effect of Fire Protection Thickness

As shown in Figures 8(a) & (b), the thickness of fire protection has a great influence on the fire resistance of the composite column. The fire protection thickness, t_p , is varied from 2mm to 12mm, with the thickness of the steel tube t_s , steel contribution ratio δ and relative slenderness ratio $\bar{\lambda}$ unchanged. The relationship between the increase of fire protection and the fire resistance is almost linear and this information can be easily used for structural-fire design of concrete filled tube. In the beginning of heating, thermal axial expansion is more serious for columns with thinner fire protection. As the time of fire exposure is getting longer, the column deflects laterally and eventually leads to axial shortening until failure occurs with run-away deflection. Figure 8b shows the relationship between the fire protection thickness and the fire resistant time of the column. The increase of fire resistance time is about 18 minutes per unit thickness of fire protection in mm. The minimum fire protection thickness is about 5 mm to attain a 2-hour ISO standard fire rating.



(a)

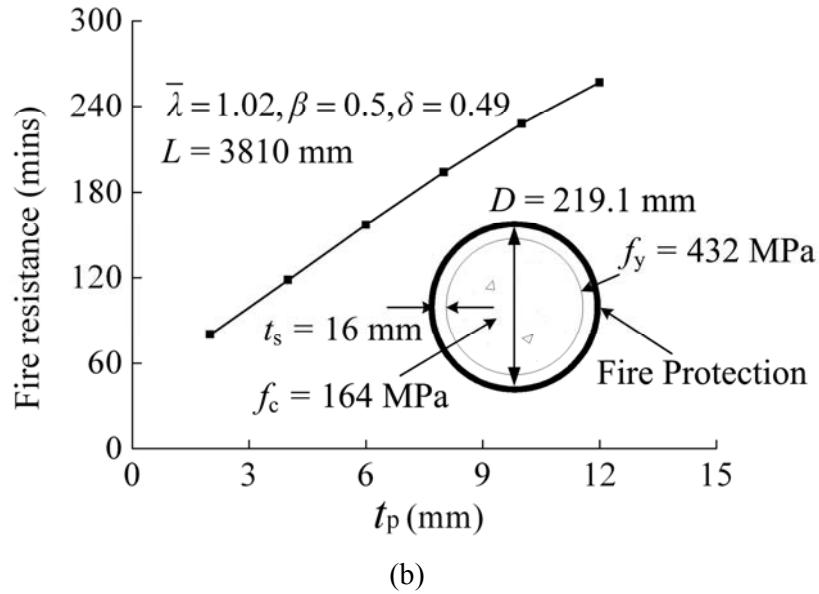
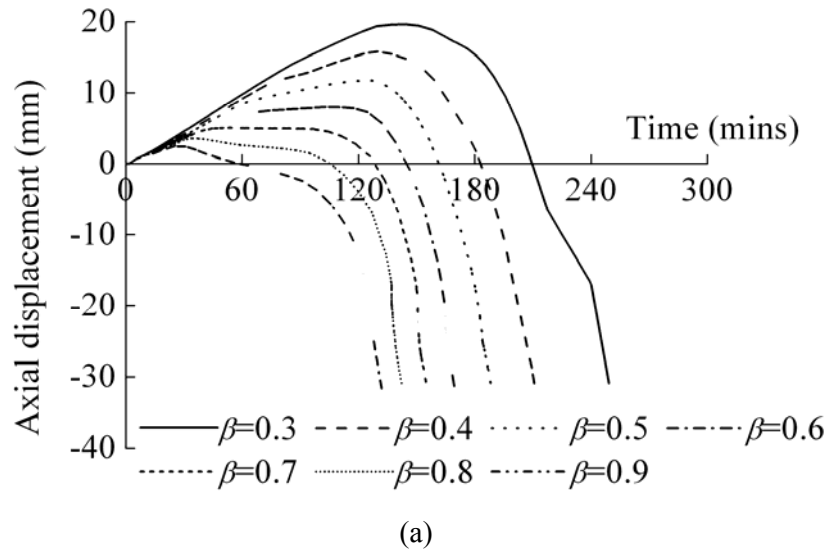


Figure 8. Relationship between Fire Protection Thickness (mm) and Fire Resistant Time (mins)

5.2 Effect of Load Ratio

Figure 9(a) shows the effects of load ratio on the fire resistance of the composite column, with the thickness of fire protection t_p , load ratio β , steel contribution ratio δ and relative slenderness ratio $\bar{\lambda}$ unchanged. Figure 9(b) shows that the relationship between the fire resistant time and load ratio is nonlinear. With the load ratio increasing, the fire resistance of the column decreases rapidly. It is obvious to see that the upward expansion is larger for columns subject to smaller load ratio. As expected, the fire resistance rating of the composite column decreased with an increase of applied load. For example, the fire resistance decreases 15% while the load ratio β changes from 0.3 to 0.4, but this trend becomes mild with the value of load ratio increasing. The fire resistance time decreases only 7% while the load ratio β varies from 0.8 to 0.9.



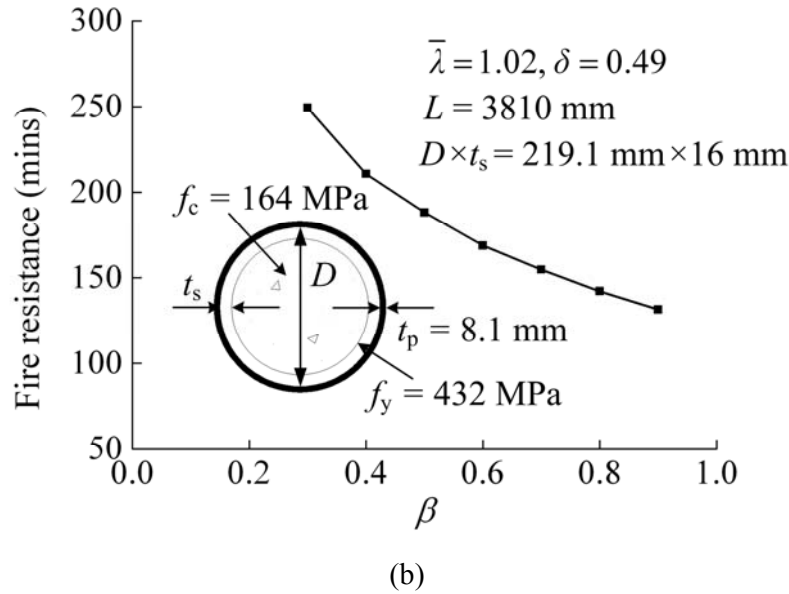
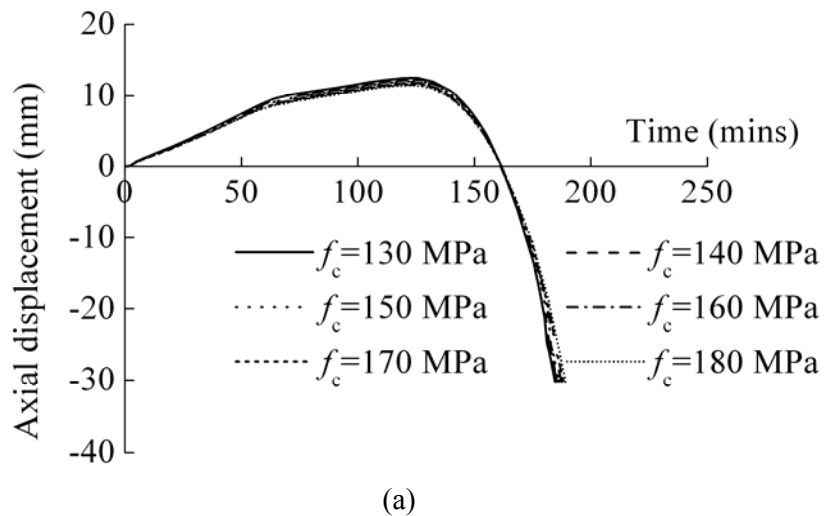


Figure 9. Relationship between Load Ratio and Fire Resistance Time (mins)

5.3 Effect of Concrete Strength

Figure 10(a) shows the effects of concrete strength on fire resistance of composite column, with the thickness of fire protection t_p , load ratio β and strength of steel f_y unchanged. Figure 10(b) plots the fire resistant time with respected to the concrete strength. It shows that the influence of concrete strength on the fire resistance of the composite column is insignificant. The fire resistance improves slightly and almost linearly with an increase of the concrete strength. For example, the fire resistance increases only 1%, while the concrete strength varies from $f_c=140\text{MPa}$ to $f_c=160\text{MPa}$, about 14% increment.



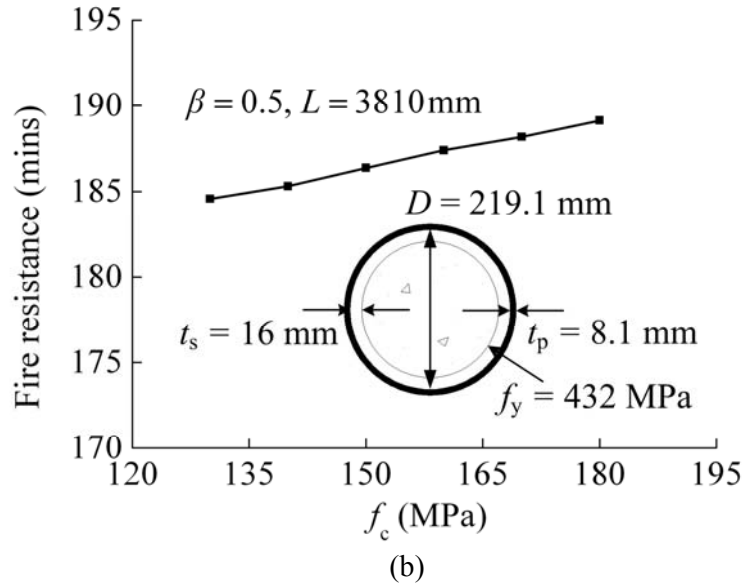
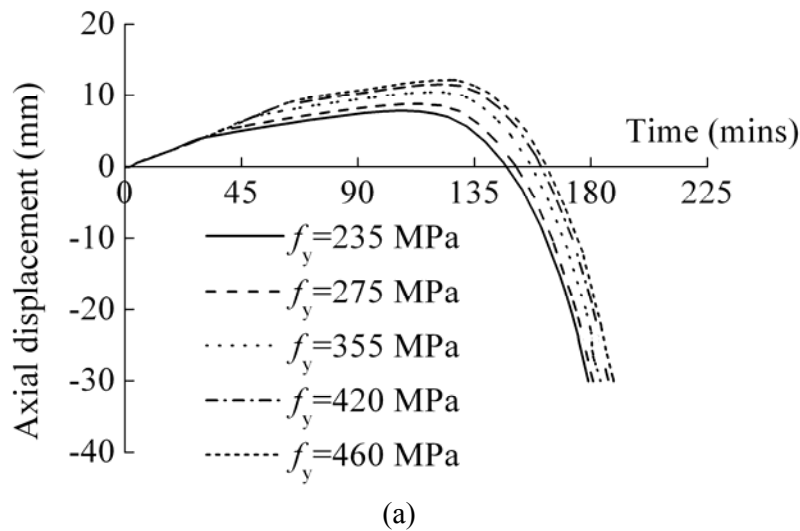


Figure 10. Relationship between Concrete Strength (MPa) and Fire Resistance Time (mins)

5.4 Effect of Steel Strength

Figure 11(a) shows the effects of steel strength on fire resistance of composite column, with the thickness of fire protection t_p , load ratio β and strength of concrete f_c unchanged. Figure 11(b) shows the fire resistant time with respected to the steel strength. It is observed that the steel strength has a moderate influence on the fire resistance of the composite column. The fire resistance improves slightly but linearly as the steel strength increases. For example, the fire resistance increases only 2%, while the concrete strength varies from $f_y=355$ MPa to $f_y=420$ MPa, about 18% increment.



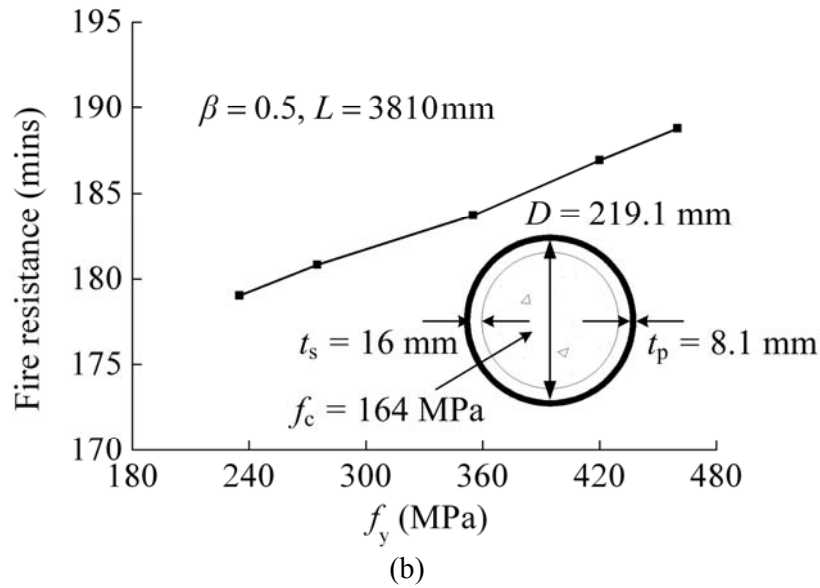
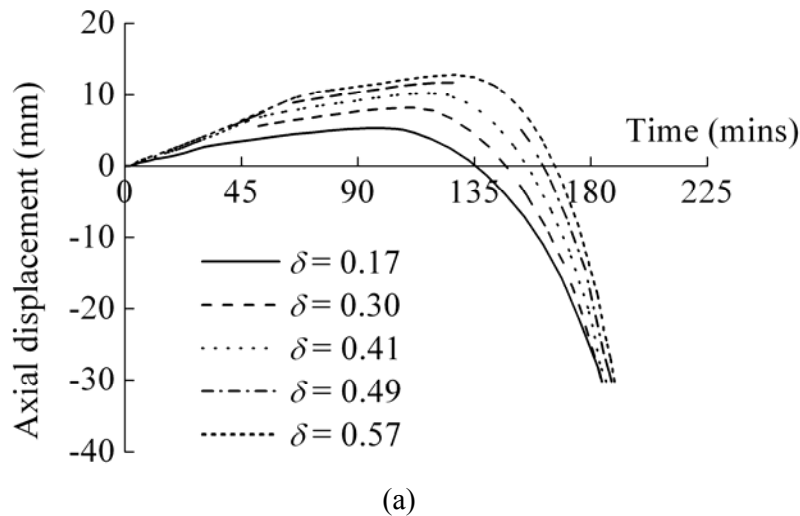


Figure 11. Relationship between Steel Strength (MPa) and Fire Resistance Time (mins)

5.5 Effect of Steel Contribution Ratio

The fire resistance of UHSCFT column increases somewhat with the increase of steel contribution ratio as shown in Figs. 12(a) & (b), with the thickness of fire protection t_p , load ratio β , strength of concrete f_c and strength of steel f_y unchanged. The fire resistance of the columns improves slightly with the increase of steel contribution ratio. With the steel ratio varied from 0.17 to 0.57, the fire resistance increases 5 minutes, in other words, only 3% increment.



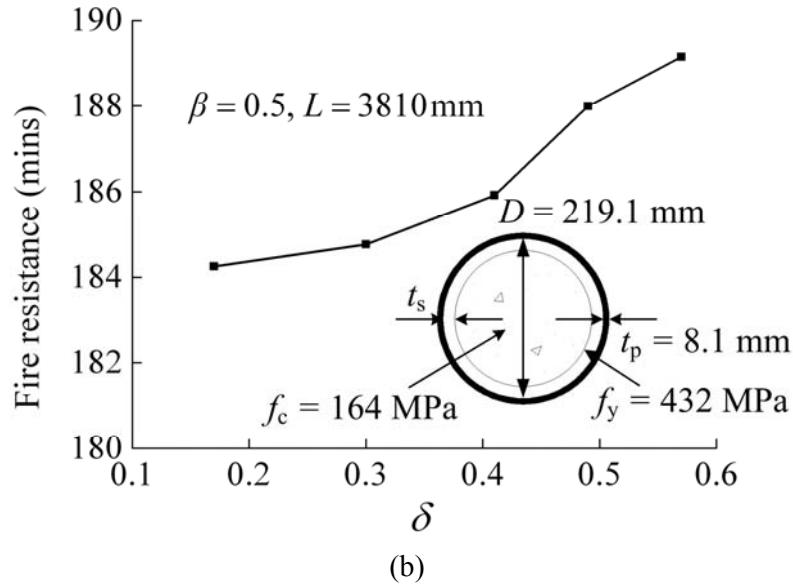
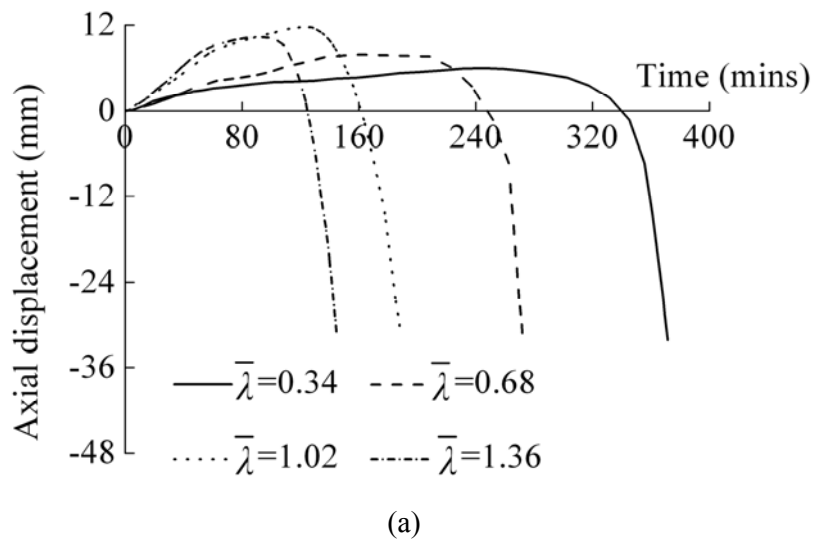


Figure 12. Relationship between Steel Contribution Ratio and Fire Resistance Time (mins)

5.6 Effect of Relative Slenderness Ratio

It is well known that the slenderness plays an important role in the buckling resistance of a column in compression. In order to study the effect of the column slenderness on fire resistance of UHSCFT column, the relative slenderness ratio $\bar{\lambda}$ varies from 0.34 to 1.36 by changing the column length L from 1270 mm to 5080 mm with an initial imperfection of $L/1000$. Figure 13 shows that the relative slenderness ratio has a significant influence on the fire resistance of composite column, with the thickness of fire protection t_p , load ratio β and steel contribution ratio δ unchanged. The fire resistance decreases significantly with the increase of the relative slenderness ratio. This can be attributed to larger second-order moment due to axial force acting on higher lateral deflection of the column with larger relative slenderness ratio.



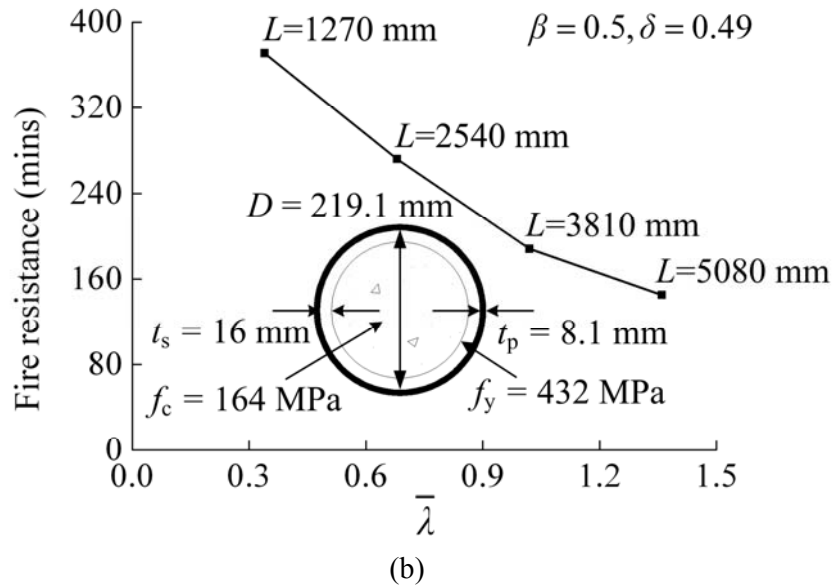
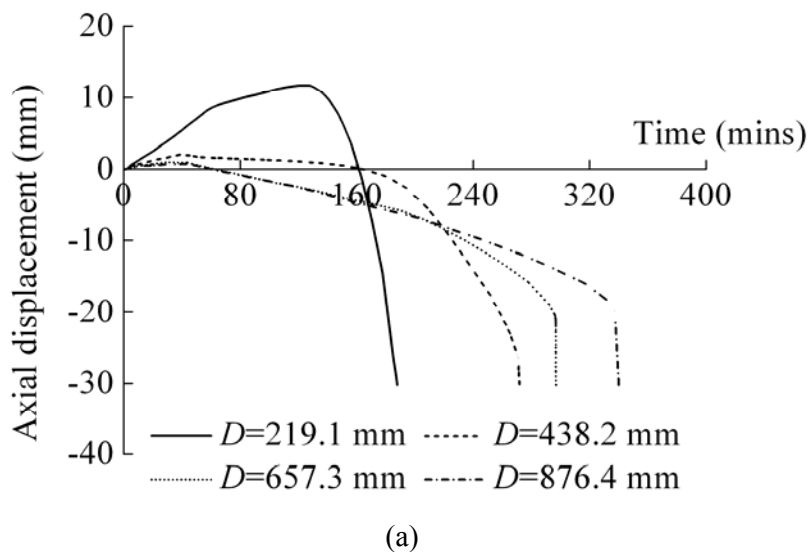


Figure 13. Relationship between Relative Slenderness Ratio and Fire Resistance Time (mins)

5.7 Effect of the Steel Section Diameter

The effects of outside diameter (D) of the composite column on the fire resistance is shown in Figure 14(a) & (b), with the thickness of fire protection t_p ($t_p=8.1$ mm), thickness of the steel tube t_s ($t_s=16$ mm), $\beta=0.5$ and $\bar{\lambda}=1.02$ of the column unchanged. The fire resistance improves obviously with the diameter increasing. This can be attributed to the longer time it takes the larger diameter column to reach temperatures at which it lost its strength so that the column can no longer support the applied load. The curves in this figure indicate that the column outside diameter, which is a measure for the column section size, has a very great influence on the fire resistance of the column. For example, with the steel section diameter varied from 219.1 mm to 438.2 mm, the fire resistance increases 84 minutes, in other words, 45% increment.



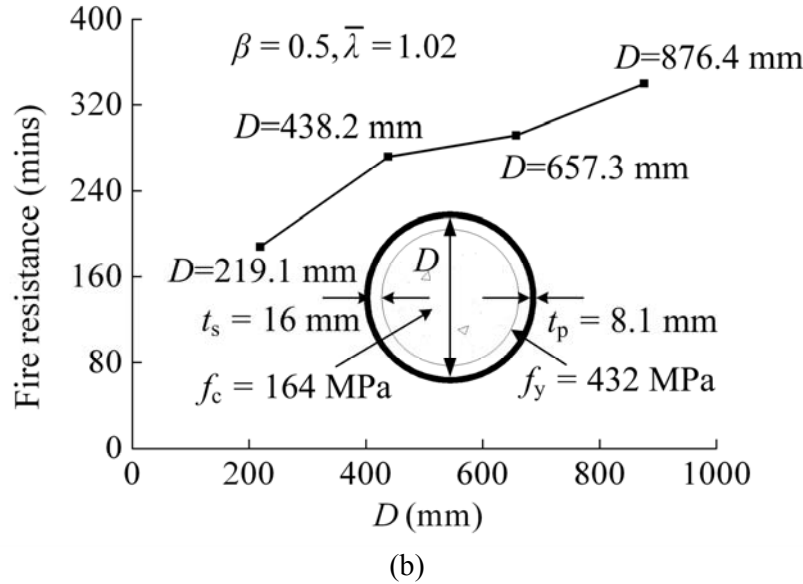


Figure 14. Relationship between Steel Section Diameter and Fire Resistance Time (mins)

Based on the analysis results, the thickness of protection, load ratio, relative slenderness ratio and the steel section diameter have significant effects on the fire resistance of UHSCFT columns subject to axial load. Whereas, the other parameters, such as the steel contribution ratio, the strength of concrete and steel have only moderate effects on the fire resistance of the columns.

6. CONCLUSION

This paper proposes a nonlinear finite element model to predict the temperature field and perform thermal-mechanical analysis of UHSCFT columns. The accuracy of the model has been established by comparing the predicted results with the fire test results. The established numerical model is then used to perform parametric analyses to investigate the load deformation behavior and fire resistance of steel tubular members infilled with ultra-high strength concrete.

By protecting the steel tube surface with a layer of low thermal conductivity material, UHSCFT columns can achieve adequate fire resistance, taking advantage of the heat capacity of the inner concrete core for to conduct heat away from the steel tube. The analyses show that the temperature of the steel tube and the ultra-high strength concrete core increased slowly with the increase of fire protection layer while the temperature of the furnace rose shapely close to ISO standard fire especially at the beginning of 10 minutes. The temperature distribution in the cross section, fire resistance and axial-load deformation of the UHSCFT columns calculated from the proposed numerical model were in reasonable agreement with the experimental results.

It was observed that the failure of UHSCFT columns occurred suddenly, showing brittle behavior. The fire resistance decreases significantly with the increase of the column relative slenderness ratio. The thickness of protection, load ratio, relative slenderness ratio and the diameter of steel section were found to have significant effects on the fire resistance of UHSCFT columns under axial compression. Whereas the steel contribution ratio, the strength of concrete, and strength of steel have only moderate effects on the fire resistance of the columns, if other parameters were kept the same.

The relationship between the increase of fire protection and the fire resistance is almost linear and this information provides useful guidance for structural-fire design of concrete filled tube. The effects of concrete strength and steel strength on fire resistance are nearly linear too, although this influence on fire resistance is limited. The curves in Figure 9 and Figure 13 roughly show that the fire resistance decreases more than quadratically with the relative slenderness ratio and load ratio. The effect of steel section diameter on fire resistance should be also considered as useful guidance for structural-fire design of concrete filled tube.

ACKNOWLEDGEMENTS

The research work is supported by the National Key Technology R&D Program of China during the 12th Five-Year Plan Period (No. 2012BAJ13B01). The financial support is highly appreciated.

REFERENCES

- [1] Lie, T.T. and Chabot, M., "Experimental Studies on the Fire Resistance of Hollow Steel Columns Filled with Plain Concrete", Internal Report No.611, Institute for Research in Construction, National Research Council of Canada, Ottawa, Canada, 1992
- [2] Tao, Z., Wang, Z.B., Han, L.H. and Uy, B., "Fire Performance of Concrete-Filled Steel Tubular Columns Strengthened by CFRP", *Steel and Composite Structures*, 2011, Vol. 11, No. 4, pp. 307-324.
- [3] Zha, X.X., Li, X.L., Wang, N. and Wan, C.Y., "Study on Axial Compression Bearing Capacity of Reinforced Concrete Filled Steel Tube Members", *Advanced Steel Construction*, 2016, Vol. 12, No. 2, pp. 94-108.
- [4] Jamaluddin, N., Lam, D., Dai, X.H. and Ye., J., "An Experimental Study on Elliptical Concrete Filled Columns under Axial Compression", *Journal of Constructional Steel Research*, 2013, Vol. 87, pp. 6-16.
- [5] Kang, W.H., Tao, Z. and Uy, B., "Design Strength of Concrete-Filled Steel Columns", *Advanced Steel Construction*, 2015, Vol. 11, No. 2, pp. 165-184.
- [6] Xiao, J.Z., Li, Z.W., Xie, Q.H. and Shen, L.M., "Effect of Strain Rate on Compressive Behaviour of High-Strength Concrete after Exposure to Elevated Temperatures", *Fire Safety Journal*, 2016, Vol. 83, pp. 25-37.
- [7] Han, L.H., Li, W. and Bjorhovde, R., "Developments and Advanced Applications of Concrete-Filled Steel Tubular (CFST) Structures: Members", *Journal of Construction Steel Research*, 2014, Vol.100, No.5, pp. 211-228.
- [8] Fong, M., Chan, S.L. and Uy, B., "Advanced Design for Trusses of Steel and Concrete-Filled Tubular Sections", *Engineering Structures*, 2011, Vol. 33, No. 12, pp.3162-3171.
- [9] Xu, Y., Fu, Y., Zhang, Y. and Zhao, X., "Fire Resistance of Crisscross Concrete Filled Steel Tube Core Columns in The Different Axial Compression", *Advanced Materials Research*, 2011, Vol. 163-167, pp. 157-160.
- [10] Wang, K. and Young, B., "Fire Resistance of Concrete-Filled High Strength Steel Tubular Columns", *Thin-Walled Structures*, 2013, Vol. 71, pp. 46-56.
- [11] Yang, H., Liu, F.Q. and Gardner, L., "Post-Fire Behaviour of Slender Reinforced Concrete Columns Confined by Circular Steel Tubes", *Thin-Walled Structures*, 2015, Vol. 87, pp. 12-29.
- [12] Liew, J.Y.R. and Xiong, M.X., "Design Guide for Concrete Filled Tubular Members with High Strength Materials to Eurocode 4", Research Publishing Services, 2015, ISBN-13: 978-981-09-3267-1; ISBN-10: 981-09-3267-7. 32-37.

- [13] Li, G.C., Yang, Z.J., Lang, Y. and Fang, C., "Behavior of High Strength Concrete Filled Square Steel Tubular Columns with Inner CFRP Circular Tube Under Bi-Axial Eccentric Loading", *Advanced Steel Construction*, 2013, Vol. 9, No. 3, pp. 231-246.
- [14] Lee, J.H., Sohn, Y.S., and Lee, S.H., "Fire Resistance of Hybrid Fibre-Reinforced, Ultrahigh-Strength Concrete Columns with Compressive Strength from 120 to 200 MPa", *Magazine of Concrete Research*, 2012, Vol. 64, No. 6, pp. 539–550.
- [15] Xiong, M.X. and Liew, J.Y.R., "Spalling Behavior and Residual Resistance of Fibre Reinforced Ultra-High Performance Concrete after Elevated Temperatures", *Materiales de Construcción*, 2015, Vol. 65, No.320, pp. 1-10.
- [16] Liew J.Y.R, Xiong, M.X. and Xiong, D.X, "Design of Concrete Filled Tubular Beam-Columns with High Strength Steel and Concrete", *Structures*, 2016, Vol 8, Part 2, pp. 213–226.
- [17] Liew, J.Y.R., Xiong, M.X. and Xiong, D.X., "Design of High Strength Concrete Filled Tubular Columns for Tall Buildings", *International Journal of High-Rise Buildings*, 2014, Vol. 3, No. 3, pp. 1-7.
- [18] Liew, J.Y.R., Xiong M.X. and Tran C.T., "Design Guide for Concrete Filled Tubular Members with High Strength Materials – An Extension of Eurocode 4 Method to C90/105 Concrete and S550 Steel", *Building and Construction Authority of Singapore*, 2015, pp. 23-40, 69-72.
- [19] Xiong, M.X., "Fire Resistance of Ultra-High Strength Concrete Filled Steel Tubular Columns", PhD Dissertation, 2013, National University of Singapore, Singapore.
- [20] ISO-834-1, "Fire-Resistance Tests-Elements of Building Construction Part1: General Requirements", *International Standard ISO-834*, Geneva, 1999.
- [21] Yu, M., Zha, X. X., Ye, J. Q. and Li, Y., "Fire Responses and Resistance of Concrete-Filled Steel Tubular Frame Structures", *International Journal of Structural Stability and Dynamics*, 2010, Vol. 10, No. 2, pp. 253-271.
- [22] Dai, X.H. and Lam, D., "Shape Effect on the Behaviour of Axially Loaded Concrete Filled Steel Tubular Stub Columns at Elevated Temperature", *Journal of Constructional Steel Research*, 2012, Vol. 73, pp. 117-127.
- [23] ECS, Eurocode 2, "Design of Concrete Structures-Part 1-2, General Rules-Structural Fire Design", EN 1992-1-2, European Committee for Standardization, 2004.
- [24] ECS, Eurocode 4, "Design of Composite Steel and Concrete Structures-Part 1-2, General Rules-Structural Fire Design", EN 1994-1-2, European Committee for Standardization, 2005.
- [25] ECS, Eurocode 3, "Design of Steel Structures-Part 1-2, General Rules-Structural Fire Design", EN 1993-1-2, European Committee for Standardization, 2005.
- [26] Song, T. Y., Han, L. H. and Uy, B., "Performance of CFST Column to Steel Beam Joints Subjected to Simulated Fire Including The Cooling Phase", *Journal of Constructional Steel Research*, 2010, Vol. 66, pp. 591-604.
- [27] Wang, R.L., Zhang, C. and Li, G.Q., "Simple Approach for Performance-Based Fire Safety Design of Circular CFT Columns in Large Enclosure", *Advanced Steel Construction*, 2016, Vol. 12, No. 1, pp. 32-43.
- [28] Espinos, A., Romero, M.L. and Hospitaler, A., "Advanced Model for Predicting The Fire Response of Concrete Filled Tubular Columns", *Journal of Constructional Steel Research*, 2010, Vol. 66, No. 8-9, pp. 1030-1046.

EXPERIMENTAL STUDY OF MECHANICAL BEHAVIOUR OF ANGLES IN TRANSMISSION TOWERS UNDER FREEZING TEMPERATURE

L.Q. An ¹, W.Q. Jiang ¹, Y.P. Liu ^{2,*}, Q. Shi ³, Y.D. Wang ¹ and S.X. Liu ¹

¹ *Department of Mechanical Engineering, North China Electric Power University, Baoding, Hebei, China*

² *Department of Civil and Environmental Engineering, The Hong Kong Polytechnic University, Hong Kong, China*

³ *Electric Power Economic Research Institute of Eastern Inner Mongolia electric power Co., Ltd., Hohhot, China*

**(Corresponding author: E-mail: ceypliu@polyu.edu.hk)*

Received: 12 May 2017; Revised: 4 August 2017; Accepted: 25 November 2017

ABSTRACT: Compared with the lower-grade steel members, the application of steel angles made of Q420 greatly reduces the self-weight of lattice transmission tower and further leads to the saving of foundation cost. However, unlike the conventional transmission towers, the strength and brittleness of the towers using higher-grade steel are more sensitive to freezing temperature, especially in cold regions. It is noted that the studies on transmission line tower at cold region are limited in literature. In this paper, a series of tests such as Charpy impact test, uniaxial tensile test and tensile notch test were carried out at low temperatures to investigate the mechanical properties and toughness of steel angles made of Q235B, Q345B and Q420C as well as welded joints using Q420C. The results show that the toughness of steel angles decreases with the lowering temperature while the strength increases with the decreasing temperature. The heat affected zone in welded joints is more susceptible to fracture than the parent material. A strength reduction method is proposed for the design of transmission tower in cold regions with rich experimental data provided. The influence of stress concentration at low temperatures was also investigated for fracture resistant design.

Keywords: Steel angle, low temperature, transmission tower, toughness, notch sensitivity

DOI: 10.18057/IJASC.2018.14.3.9

1. INTRODUCTION

Steel materials of strength above 400 MPa become widely used in transmission line engineering due to its light weight and high loading capacity. More importantly, the high strength steel can avoid the largely use of compound sections in the design of transmission towers subjected to heavy loads, which not only brings a more reliable load transfer mechanism but also simplifies the fabrication work. Also, structural engineers may face problems when using the direct analysis to design transmission tower as the initial member imperfection of compound sections has not been given in the design codes such as AISC-LRFD [1] and EC3 [2]. The direct analysis method is a powerful and reliable tool which can well predict the structural behavior of transmission tower considering joint performance [3-4]. Generally speaking, the application of high strength steel can improve the safety and structural performance of transmission engineering with a reduction in fabrication and construction cost.

It should be pointed out that the mechanical properties and toughness of the high-strength steel may be quite different from that of normal steel, due to the different rolling process, crystal phases and chemical components. It is reported that the elongation decreases commonly with the increasing of steel strength, which indicates the lower plastic deformation capacity and ultimate-to-yield strength ratio for higher grade steel as the temperature decreases [5-8]. Obviously, the transmission tower

made of higher grade steel has higher load-carrying capacity than that made of normal steel. According to the theory of fracture mechanics, the higher strength steel is more sensitive to defect and therefore increases the risk of brittle fracture at low temperature [9-12]. This concern leads to the limited use of higher strength steels such as Q420 and Q460 in transmission towers especially in the low temperature area.

In the past decades, considerable number of steel structures collapsed in cold regions due to brittle fracture. It is reported that the number of tower collapsed at low temperature environment in China has increased several dozen times from 1988 to 2013. It seems that the use of higher strength steel causes severe brittle problems in cold regions of China. For all steel grades, the Chinese structural steel is classified into A, B, C and D. There is no requirement of Charpy impact test for Class A while the temperature of Charpy impact test is 20°C, 0°C and -20°C for Class B, C and D respectively. In Chinese market, the steel angles for transmission towers are generally made of Class B and C. Thus, there is an urgent need to verify the performance of steel angles at temperatures lower than -20°C for routine design or evaluation of existing tower in cold regions.

For UHV (Ultra High Voltage) and EHV (Extra High Voltage) transmission towers, their main legs usually consist of multiple angles which are connected by bolts for easy fabrication and transportation. In the process of drilling bolt hole, the commonly used method is punching process, which easily causes microcrack and crack source around the wall of hole. The microcrack will be quickly expanded when the temperature of steel angle is below the ductile-brittle transition temperature. This leads to the failure of bolted joints and further the collapse of the transmission tower.

A typical transmission tower contains four main legs which are the key members to transfer the external loads to the foundation. The brittle failure of main angles at low temperature will lead to the collapse of the tower and further endanger the safe and stable operation of the whole power system. Thus, there is an urgent need of experimental study of the mechanical properties, fracture toughness and notch sensitivity of steel angles used in transmission tower at low temperature. It is of great importance to the design and construction of UHV (Ultra High Voltage) and EHV (Extra High Voltage) transmission lines in cold regions. In this paper, a series of tests such as Charpy impact test, uniaxial tensile test and tensile notch test were carried out at low temperatures to investigate the mechanical properties and toughness of steel angles made of Q235B, Q345B and Q420C as well as welded joints using Q420C. From this study, the strength reduction method and some recommendations is proposed for the design of transmission tower in cold regions.

2. SETUP OF EXPERIMENTAL TESTS

In this paper, totally 31 transmission lines (500 kV and above) which are in operation or under construction at the regions of China with annual average temperature below 0°C are investigated. Among them, there are 24, 1 and 6 towers for 500 kV, 660 kV and 750 kV lines respectively. For the minimum temperature in the design stage, there are 9, 17 and 5 towers designed for -40°C, -35°C and -30°C respectively. These transmission lines are mainly made of steel angles except one named Qingyun-Jixi 500 kV double circuit which used Q345B steel tubes. Six line towers (two 500 kV lines, one 660 kV line and three 750 kV lines) are used Q420B and Q420C steel angles while the other towers are made of Q235B and Q345B steel angles.

Experimental study is the effective approach to investigate the mechanical behaviour of engineering structures [13-15]. To evaluate the actual performance of the towers mentioned above, a series of tests such as Charpy impact test, uniaxial tensile test and uniaxial tensile test with notch were carried out at low temperatures to investigate the mechanical properties and toughness of steel angles made

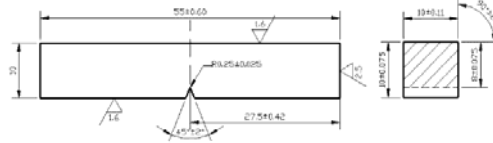
of Q235B, Q345B and Q420C. The welded joints using Q420C steel plate were also studied with consideration of different thicknesses to minimize the influence of these parameters due to randomness.

2.1 Low Temperature Impact Toughness Test

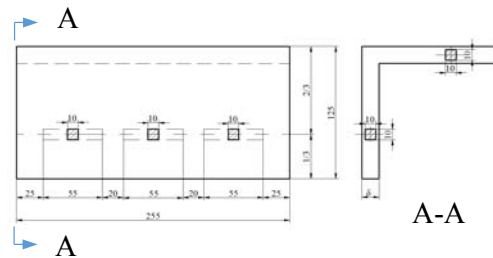
Various factors such as material processing, accuracy of testing machine, swing and frame fit, test temperature control and location of sample may lead to large discrepancy of the impact test results. Therefore, the number of test samples is generally not less than three.

The Q235B and Q345B steel materials are commonly used in transmission lines. In this paper, four groups of Charpy impact tests in terms of steel grade and member/joint were performed at specified temperature from 100°C to -60°C according to the standard GB/T 229-2007 [16]. The interval is 10°C for temperature from 0°C to 100°C while 5°C is used from -60°C to -5°C.

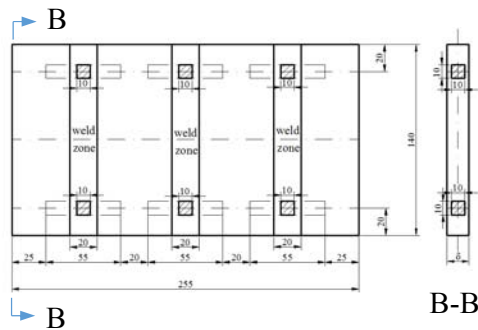
The locations and dimensions of the specimens (as seen in Figure 1a) of Q235B and Q345B steel angles for Charpy impact test are determined in accordance with the standard GB/T 229-2007 [16]. The specimens were sampled from the steel angle named L140×12 with the location shown in Figure 1b.



(a) Geometry of Impact Test Specimen



(b) Sampling of Steel Angle



(c) Sampling of Welded Joints

Figure 1. Sampling and Geometry of Impact Test Specimens

Similarly, the preparation of test specimens of Q420C for Charpy impact test is shown in Figure 1 in accordance with the standard GB/T 229-2007 [16]. The test specimens of Q420C were sampled from the steel angle named L125×12, L140×14 and L160×16 with plate thickness of 12 mm, 14 mm and 16 mm respectively. The Q420C welded joints were sampled from welding plates considering thickness of 12 mm, 14 mm and 16 mm. Three identical samples were made for each specified model and thickness and therefore, there are nine impact test specimens accounting for three different plate thicknesses. The tests were performed at each specified temperature points (i.e. 20, -20, -45, -60°C) according to the standard GB/T 229-2007 [16].

The impact tests are shown and listed in Table 1. In summary, the samples for Charpy impact test have accounted for the influence of steel grade, member/weld joint, plate thickness and temperature change.

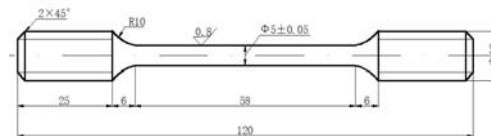
Table 1. Impact Test List

Steel grade	Type	Temperature range $T/^\circ\text{C}$	Temperature points n_T	Number of samples n_S
Q235B	Steel angle	100~0	10	10×4
		-5~-60	12	12×4
Q345B	Steel angle	100~0	10	10×4
		-5~-60	12	12×4
Q420C	Steel angle	20,-20,-45,-60	4	4×3×3
Q420C	Welded joint	20,-20,-45,-60	4	4×3×3

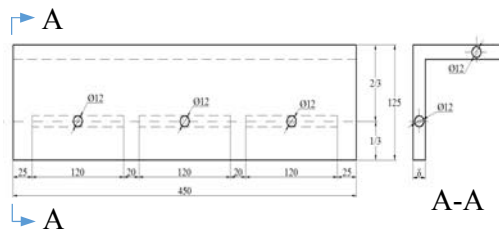
2.1 Low Temperature Tensile Tests

The locations and dimensions of the specimens (as seen in Figure 2a) of Q235B and Q345B steel angles for low temperature tensile test are determined in accordance with the standard GB/T 13239-2006 [17]. The specimens were sampled from the steel angle named L140×12 with the location shown in Figure 2b.

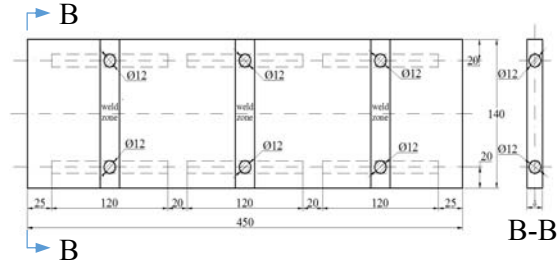
Five tensile test specimens were performed at each specified temperature from 20°C to -50°C (i.e. 20, 0, -10, -20, -30, -40, -50°C) according to the standard GB/T 13239-2006 [17].



(a) Specimen for Low Temperature Tensile Test



(b) Sampling of Steel Angle



(c) Sampling of Welded Joints

Figure 2. Sampling and Geometry of Tensile Test Specimens

Additionally, mechanical properties of Q420C high-strength steel and its welded joint were determined by smooth tensile test specimens as shown in Figure 2c, which were machined in accordance with the standard GB/T 13239-2006 [17]. Respectively, smooth tensile test specimens of Q420C high-strength steel were sampled from the steel angle named L125×12, L140×14 and L160×16 (marked as 12 mm, 14 mm and 16 mm), and its welded joints were sampled from welding plates with thickness of 12 mm, 14 mm and 16 mm respectively. Make three identical samples from each specified model and thickness. Then nine replicated tensile test specimens were performed at each specified temperature points (i.e. 20, -10, -20, -45°C) according to the standard GB/T 13239-2006 [17]. The smooth tensile test list is shown in Table 2.

Table 2. Smooth Tensile Test List

Steel grade	Type	Temperature points $T/^{\circ}\text{C}$	Number of samples ($n_T \times n_S$)
Q235B	Steel angle	20~-50	7×5
Q345B	Steel angle	20~-50	7×5
Q420C	Steel angle	20,-10,-20,-45	4×9
Q420C	Welded joint	20,-10,-20,-45	4×9

2.2 Notch Sensitivity Tests

The specimens of Q235B and Q345B for notch sensitivity tensile test were sampled from the steel angle named L140×12. The geometry of the test specimens made of Q235B and Q345B steel angles for notch tensile test is shown in Figure 3. They were prepared in accordance with the standard HB 5214-1996 [18]. The locations and dimensions of the specimens of Q235B and Q345B steel angles for notch tensile test can be seen in Figure 2b.

There were five tensile test specimens performed at each specified temperature from 20°C to -50°C (i.e. 20, 0, -10, -20, -30, -40, -50°C) according to the standard HB 5214-1996 [18]. The notch tensile tests are listed in Table 3.

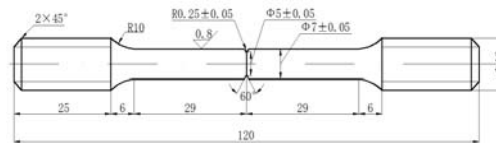


Figure 3. Geometry of Notch Tensile Test Specimens

Table 3. Notch Tensile Test List

Steels	Temperature points $T/^{\circ}\text{C}$	Number of samples ($n_T \times n_S$)
Q235B	20~-50	7×5
Q345B	20~-50	7×5

2.3 Experimental Equipment

As shown in Figure 4a, the machine for testing material properties at low temperature is SANS-50KN. The compressor is used for refrigeration and its lowest operating temperature is -90°C . The pendulum impact testing machine with maximum impact energy of 300J was adopted in the impact tests, as seen in Figure 5b. The cooling medium is alcohol and its lowest operating temperature is -60°C . These machines are suitable for large quantities of low temperature tests because of high speed and high precision of temperature control. Figure 5a shows a part of the specimens after impact test while Figure 5b demonstrates several specimens after tensile test.

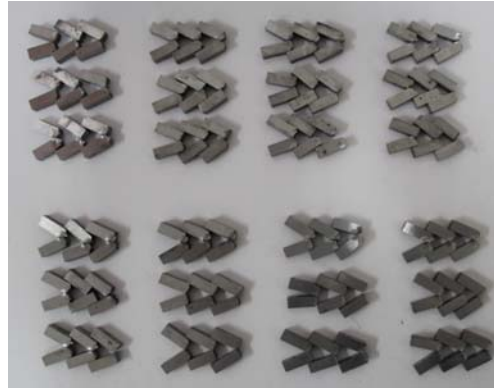


(a) The Tensile Testing Machine



(b) The Pendulum Impact Testing Machine

Figure 4. Material Properties Testing Machines



(a) Specimens after impact test



(b) Specimens after Tensile Test

Figure 5. Specimens after Experimental Test

3. TEST RESULTS AND DISCUSSION

3.1 Low Temperature Impact Test

In structural engineering, the Charpy impact energy A_{KV} is widely employed as material toughness measurement in design as it partially reflects the fracture resistant ability of steel [19].

The Charpy impact tests of Q235B and Q345B were performed at 22 specified temperature points from 100°C to -60°C and the corresponding Charpy impact energy A_{KV} are listed in Table 4. Similarly, the Charpy impact tests of Q420C steel angles and the butt weld joints were performed at each specified temperature points (i.e., 20, 0, -20, -60°C) with the Charpy impact energy A_{KV} presented in Table 5.

In this paper, the relationship between the impact energy A_{KV} and temperature is regressed by Boltzmann function in Eq. 1 which is widely used for great dispersion of experimental data. Large quantities of experimental researches have shown that the Boltzmann function can well establish the correlation between impact energy and temperature [19], because it leads to minimal residuals with clear physical meanings of all parameters.

$$y = \frac{A_1 - A_2}{1 + e^{(t - t_0)/\Delta t}} + A_2 \quad (1)$$

Table 4. Charpy Impact Energy A_{kV} (J) of Q235B and Q345B Steel Angles

Q235B	T/°C	100	80	70	60	50	40	30	20	10	0	-5
		153	119	151	112	121	148	129	171	182	56	36
	A_{kV}/J	119	129	156	161	120	130	158	168	187	46	25
		167	145	117	152	152	138	143	184	89	60	26
		112	116	154	143	112	138	160	174	165	42	29
		T/°C	-10	-15	-20	-25	-30	-35	-40	-45	-50	-55
	23		17	12	8	4	8	5	6	6	3	3
	A_{kV}/J	14	14	11	9	9	7	8	4	7	3	4
		15	17	17	9	5	5	4	5	4	4	4
		17	16	10	10	7	5	5	5	4	5	3
	Q345B	T/°C	100	80	70	60	50	40	30	20	10	0
112			122	152	175	155	169	93	153	106	62	85
A_{kV}/J		161	132	151	173	150	175	169	141	131	56	58
		185	164	174	113	125	163	164	153	103	54	60
		149	131	159	154	161	169	159	152	114	57	68
		T/°C	-10	-15	-20	-25	-30	-35	-40	-45	-50	-55
49			40	22	39	15	27	10	8	10	8	7
A_{kV}/J		45	41	24	29	35	10	12	7	7	5	5
		45	55	35	25	12	16	11	9	6	6	5
		46	33	22	30	16	7	11	8	8	7	6

Table 5. Charpy Impact Energy A_{kV} (J) of Q420C Steel Angles and Welded Joints

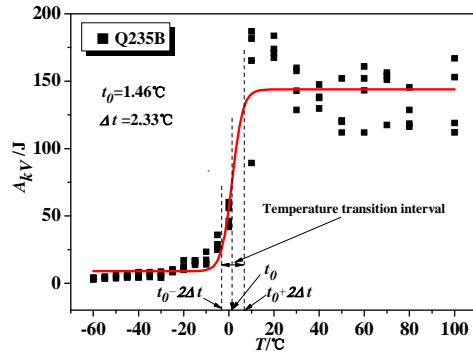
Steel grade/Type		Q420C/Steel angle				Q420C/Welded joint			
$T/^{\circ}\text{C}$		20	-20	-45	-60	20	-20	-45	-60
A_{kV}/J		92	105	40	22	158	46	33	7
		91	103	31	20	122	63	30	12
		143	101	36	15	163	52	25	13
		171	122	76	38	172	63	39	16
		177	140	57	60	152	39	26	19
		176	149	69	58	131	71	21	25
		153	131	83	22	126	58	35	29
		176	124	82	18	111	73	36	28
		176	115	39	61	154	57	48	27

In Eq. 1, y is the value of impact energy; t represents the temperature variable; A_1 and A_2 are the Charpy impact energy values of the lower and upper shelf respectively; t_0 is the transition temperature of ductile to brittle; Δt is the temperature transition interval, which reflects the ductile-brittle transition rate. The parameters A_1 , A_2 , t_0 and Δt are determined by curve-fitting technique with test data. The smaller of Δt , the narrower of the temperature range across the transition temperature region, and the material is easier from ductile to brittle.

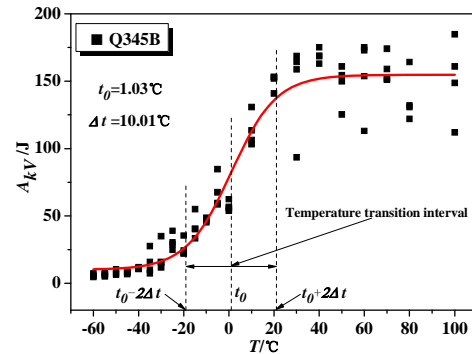
The Charpy impact test results of Q235B, Q345B and Q420C steel angles as well as Q420C welded joints at low temperature and the curves obtained by fitting Boltzmann function are plotted in Figure 6.

Table 6. Parameters in Boltzmann Function by Curve-fitting

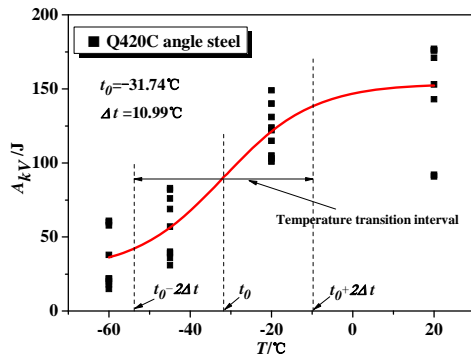
Steel grade	Type	The lower shelf A_1/J	The upper shelf A_2/J	Brittle-ductile transition temperature $t_0/^\circ\text{C}$	temperature transition interval $\Delta t/^\circ\text{C}$
Q235B	Steel angle	8.93	143.93	1.46	2.33
Q345B	Steel angle	10.02	154.75	1.03	10.01
Q420C	Steel angle	27.27	153.44	-31.74	10.99
Q420C	Welded joint	19.56	143.22	-12.69	10.22



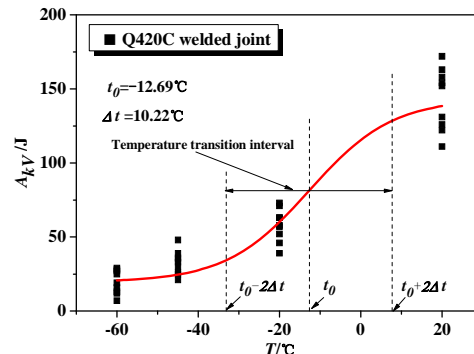
(a) Q235B Steel Angle



(b) Q345B Steel Angle



(c) Q420C Steel Angle



(d) Q420C Welded Joint

Figure 6. Low Temperature Impact Test Results

As shown in Figure 6, the impact energy of four kinds of materials decreases with the decrease of temperature starting at 20°C. The impact energy reduces rapidly with the decrease of temperature until reaching a certain temperature. The fitting results such as A_1 , A_2 , t_0 and Δt in Boltzmann function are listed in Table 6.

It is clearly shown in Figures 6a and 6b that the curve of the temperature transition interval of Q235B is more rapid than Q345B, which indicates that Q235B more likely becomes brittle at low temperature. From Table 6, it is also found that t_0 of Q345B steel angle is 0.44°C which is lower than Q235B; Δt of Q345B steel angle is 7.67°C which is higher than Q235B. Therefore, the ability to resist low temperature and cold brittleness of Q345B is higher than Q235B.

As shown in Table 6, the ductile-brittle transition temperature of Q235B, Q345B and Q420C steel angles are 1.46°C, 1.03°C and -31.74°C respectively. The ductile-brittle transition temperature of Q420C steel angles is about -33°C lower than Q235B and Q345B steel angle. Thus, the ability of Q420C steel angles to resist low temperature and cold brittleness is better than Q235B and Q345B steel angles.

The ductile-brittle transition temperature of Q420C steel angles and welded joints are -31.74°C and -12.69°C respectively. Clearly, the ability of Q420C welded joints to resist low temperature and cold brittleness is much lower than its parent material.

From the above, Q420C steel angles are recommended in the region at low temperature, but the use of Q420C welded joints should be minimized.

3.2 Low Temperature Tensile Tests

In the design of lattice transmission tower, the mechanical properties of angle steel such as yield strength σ_s and ultimate tensile strength σ_b as well as the ultimate-to-yield strength ratio are vital for the determination of load resistance of steel member.

The mechanical properties of Q235B and Q345B steel angles at 7 specified temperature points from 20°C to -50°C are presented. The values of yield strength σ_s and ultimate tensile strength σ_b as well as the ultimate-to-yield strength ratio for five tested specimens under seven temperature points are listed in Table 7. Similarly, the mechanical properties of steel angles and butt welded joints made of Q420C were performed at several specified temperature points (i.e. 20, 0, -20, -45°C). The values of yield strength σ_s and ultimate tensile strength σ_b as well as the ultimate-to-yield strength ratios for the nine tested specimens under four temperature points are listed in Table 8.

Extensive theoretical and experimental researches indicated that, in the temperature range from -70°C to 20°C, the variations of yield strength and ultimate tensile strength with temperature can be expressed by Eqs. 2 to 4 as follows [20],

$$\sigma_s = \sigma'_s e^{q_s(T'-T)} \quad (2)$$

$$\sigma_b = \sigma'_b e^{q_b T'-T)} \quad (3)$$

$$k = q_b/q_s \quad (4)$$

where σ_s , σ'_s and σ_b , σ'_b are the yield strength and ultimate tensile strength at temperature T and T' respectively; q_s and q_b are the temperature sensitive factors of yield strength and ultimate tensile strength respectively; k is the ratio of q_b and q_s .

In addition, the yield-to-ultimate strength ratio of angle steel with considering temperature can be derived from the Eqs. 2 and 3.

$$\frac{\sigma_s}{\sigma_b} = \frac{\sigma'_s}{\sigma'_b} e^{(q_s - q_b)(T'-T)} \quad (5)$$

Table 7. Mechanical Properties of Q235B and Q345B Steel Angles from Tensile Test

Steel grade	Property	T/°C						
		20	0	-10	-20	-30	-40	-50
Q235B	σ_b /MPa	418	406	452	460	473	488	491
		422	442	465	501	485	477	508
		402	443	474	516	461	500	512
		396	436	500	456	476	482	501
		368	450	501	461	467	486	483
	Mean	401.20	435.40	478.40	478.80	472.40	486.60	499.00
	σ_s /MPa	243	242	302	315	315	330	358
		298	288	279	396	337	337	369
		236	277	348	402	314	353	375
		224	311	394	295	292	358	374
		206	298	405	281	292	329	324
	Mean	241.40	283.20	345.60	337.80	310.00	341.40	360.00
	σ_b/σ_s	1.66	1.54	1.38	1.42	1.52	1.43	1.39
Q345B	σ_b /MPa	548	560	570	575	600	601	612
		549	569	576	588	573	609	612
		550	562	568	578	591	618	606
		543	560	578	577	589	605	608
		539	557	568	580	588	624	610
	Mean	545.80	561.60	572.00	579.60	588.20	611.40	609.60
	σ_s /MPa	348	344	386	371	437	408	397
		426	416	423	443	386	458	403
		407	348	378	379	391	437	390
		346	346	423	376	390	434	409
		361	377	362	382	385	468	407
	Mean	377.60	366.20	394.40	390.20	397.80	441.00	401.20
	σ_b/σ_s	1.45	1.53	1.45	1.49	1.48	1.39	1.52

The temperature sensitivity coefficients q_s and q_b and the ratio k in Eqs. 2 to 4 for Q235B, Q345B and Q420C steel angles as well as Q420C welded joints at six temperature points from 0°C to -50°C are determined from tests and listed in Table 9.

The mechanical properties such as yield strength σ_s and ultimate tensile strength σ_b of Q235B and Q345B steel angles at seven temperature points from -20°C to -50°C, and the average value curve of test results and their prediction curves from these equations are shown in Figure 7 and Figure 8. The mechanical property indices of Q420C angle steel and its welded joint test results at four temperature points (i.e. 20, 0, -20, -45°C) and their prediction curves of test results are shown in Figure 9.

As shown in Table 9, the temperature sensitivity coefficients q_s and q_b of Q235B and Q345B are all positive. According to Eqs. 2 and 3, the positive temperature sensitivity coefficients indicates that the yield strength σ_s and ultimate tensile strength σ_b of Q235B and Q345B angle steel are increased with decreasing of temperature. It also can be seen in Table 9 that, the parameter k of Q235B is less than 1 while the parameter k of Q345B is greater than 1. It means that for Q235B angle steel at low temperature the increment of σ_b is smaller than σ_s , while the increment of σ_b is larger than σ_s for Q345B angle steel.

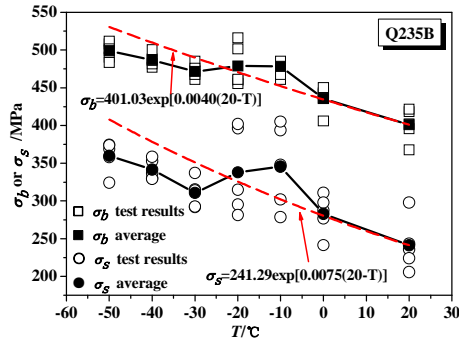
Table 8. Mechanical Properties of Q420C Steel Angles and Butt Welded Joints

Property	Q420C/Steel angle				Q420C/Welded joint			
T/°C	20	-10	-20	-45	20	-10	-20	-45
σ_b /MPa	654	671	690	699	557	541	587	584
	660	680	683	698	557	574	581	585
	657	677	693	702	553	528	573	550
	572	612	610	606	514	514	539	561
	571	594	604	598	510	526	530	546
	572	591	607	603	510	546	537	511
	620	640	641	663	600	575	636	643
	622	646	648	664	601	611	611	630
	613	639	646	665	585	564	611	646
Mean	615.67	638.89	646.89	655.33	554.11	553.22	578.33	584.00
σ_s /MPa	460	479	543	517	450	457	486	446
	474	496	519	522	444	443	471	460
	485	491	521	531	429	423	450	486
	413	441	496	445	412	433	452	468
	427	442	479	425	415	449	455	470
	448	447	469	432	398	397	440	451
	487	487	486	521	449	437	472	500
	477	492	503	505	455	446	464	484
	467	475	499	510	454	432	474	475
Mean	459.78	472.22	501.67	489.78	434.00	435.22	462.67	471.11
σ_b/σ_s	1.34	1.35	1.29	1.34	1.28	1.27	1.25	1.24

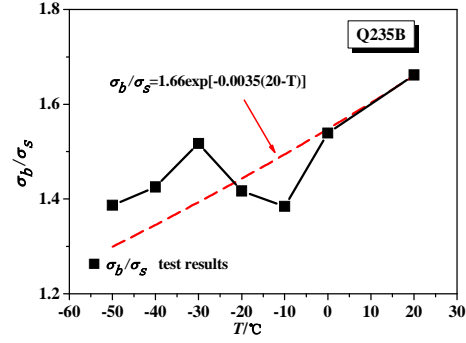
Table 9. Temperature Sensitivity Coefficients

Steel grade/Type	T/°C	$q_s/(10^{-3} \cdot ^\circ\text{C}^{-1})$ Mean	$q_b/(10^{-3} \cdot ^\circ\text{C}^{-1})$ Mean	k	
Q235B/ Steel angle	0	7.98	4.09	4.00	0.53
	-10	11.96	5.87		
	-20	8.40	4.42		
	-30	5.00	3.27		
	-40	5.78	3.22		
	-50	5.71	3.12		
Q345B/ Steel angle	0	-1.53	1.43	1.58	1.81
	-10	1.45	1.56		
	-20	0.82	1.50		
	-30	1.04	1.50		
	-40	2.59	1.89		
	-50	0.87	1.58		
Q420C/ Steel angle	-10	0.89	1.23	1.14	0.85
	-20	2.18	1.24		
	-45	0.97	0.96		
Q420C/ Welded joint	-10	0.09	-0.05	0.61	0.62
	-20	1.60	1.07		
	-45	1.26	0.81		

As shown in Table 9, the temperature sensitivity coefficients q_s and q_b of Q420C steel angles and its welded joint are also all positive, which indicate that the yield strength σ_s and ultimate tensile strength σ_b of Q420C angle steel and its welded joint are also increased with decreasing of temperature. The parameter k of Q420C steel angles and its welded joint at low temperature are all less than 1, which indicate that the increment of σ_b is smaller than σ_s .

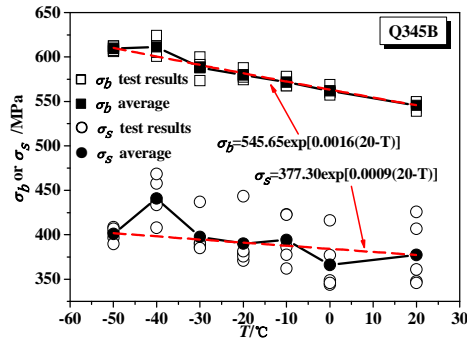


(a) Ultimate and Yield Tensile Strength

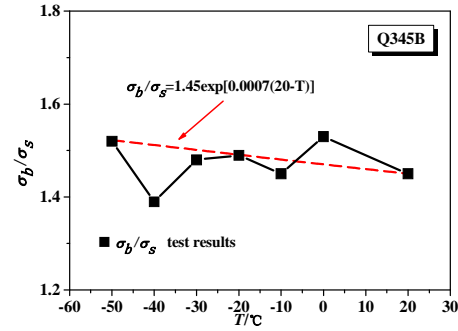


(b) Ultimate-to-yield Strength Ratio

Figure 7. Mechanical Property Indices of Q235B Steel Angles

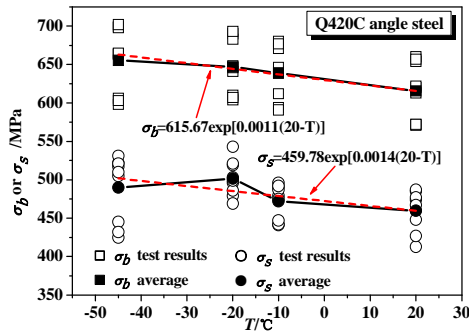


(a) Ultimate and Yield Tensile Strength

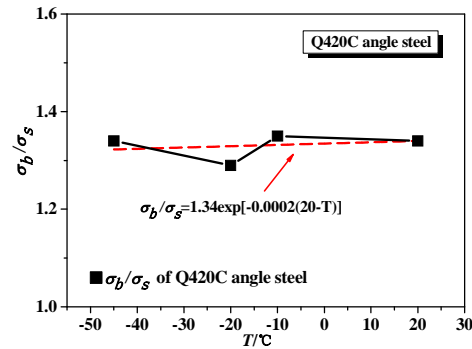


(b) Ultimate-to-yield Strength Ratio

Figure 8. Mechanical Property Indices of Q345B Steel Angles

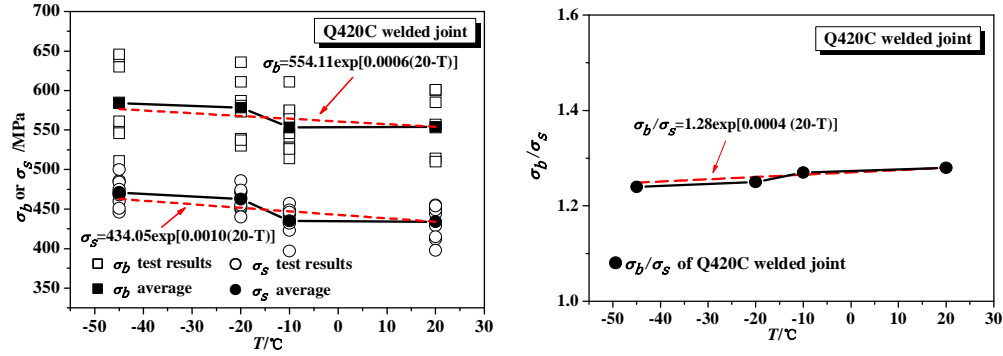


(a) Ultimate and Yield Tensile Strength



(b) Ultimate-to-yield Strength Ratio

Figure 9. Mechanical Property Indices of Q420C Steel Angles



(a) Ultimate and Yield Tensile Strength (b) Ultimate-to-yield Strength Ratio

Figure 10. Mechanical Property Indices of Q420C Weld Joints

Figure 7 shows the mechanical property indices of Q235B steel angles from -50°C to 20°C including yield strength, ultimate tensile strength and ultimate-to-yield strength ratio as well as its prediction curves based on Eqs. 2 to 3. The yield strength σ_s and ultimate tensile strength σ_b of Q235B steel angle are increased from 241.40 MPa and 401.20 MPa to 360.00 MPa and 499.00 MPa respectively (see Figure 7a). It is clear that the yield strength and ultimate tensile strength are increased with increasing temperature. As shown in Figure 7b, the ultimate-to-yield ratios σ_b/σ_s of Q235B steel angle is dramatically decreased from 1.66 to 1.39 as the temperature decreased from 20°C to -50°C , which indicates the brittleness increased and plasticity decreased at low temperature.

Figure 8 shows the mechanical property indices as well as its prediction curves of Q345B steel angles from -50°C to 20°C . It can be seen in Figure 8a that, the yield strength and ultimate tensile strength are increased from 377.60 MPa and 545.80 MPa to 401.20 MPa and 609.60 MPa respectively. However, as shown in Figure 8b, the ultimate-to-yield ratios are changed and different from Q235B (see Figure 7b), which are varied between 1.45 and 1.53, and slightly increased with decreasing of temperature.

Figure 9 shows the mechanical property indices as well as its prediction curves of Q420C steel angles from -45°C to 20°C . As shown in Figure 9a, when the temperature decreases from 20°C to -45°C , the yield strength and ultimate tensile strength of Q420C steel angle are increased from 459.78 MPa and 615.67 MPa to 489.78 MPa and 655.33 MPa respectively. It can be seen in Figure 9b, the ultimate-to-yield ratios of Q420C steel angles are varied between 1.29 and 1.35, which is also different from Q235B.

Figure 10 shows the mechanical property indices as well as its prediction curves of Q420B weld joints from -45°C to 20°C . As shown in Figure 10a, with the temperature decreases from 20°C to -45°C , the yield strength and the ultimate tensile strength of Q420C welded joints are increased from 434.05 MPa and 554.10 MPa to 471.11 MPa and 655.33 MPa respectively. It can be seen in Figure 10b, the ultimate-to-yield ratios of Q420C welded joints are varied between 1.24 and 1.27.

As shown in Figures 7a, 8a and 9a, the yield strength and tensile strength of Q235B, Q345B and Q420C steel angles are all increased with the decrease of temperature. However, the temperature has more influence on the yield strength and tensile strength of Q235B steel angles than the Q345B and Q420C steel angles as the slop of the Q235B curves is greater than the others. It can be concluded that the influence of low temperature on yield strength and tensile strength will decrease with the increase of steel grade.

As shown in Figures 9a and 10a, the influence of low temperature on the yield strength and tensile strength of Q420C steel angles and its weld joints is quite similar. Taking yield strength for example, the yield strength of Q420C steel angles and its weld joints is slightly increased from 459.78 MPa and 434.05 MPa to 489.78 MPa and 471.11 MPa respectively with the temperature decreasing from 20°C to -45°C.

Figures 7b, 8b, 9b and 10b show the ultimate-to-yield ratio versus temperature curves of Q235B, Q345B and Q420C steel angles and Q420C weld joints. It can be seen from the figures, the influence of temperature on the ultimate-to-yield ratio is quite different. The ultimate-to-yield ratio of Q235B steel angle is dramatically decreased from 1.66 to 1.39, while Q345B and Q420C steel angles are varied between 1.45 and 1.53, 1.29 and 1.35 respectively. Hence, it is clear that the low temperature will dramatically increase the yield strength, tensile strength and brittleness of Q235B steel angles and decrease plasticity; but the low temperature has less influence on Q345B and Q420C steel angles and Q420C weld joints.

3.3 Notch Sensitivity Tests

The appearance of microcrack around bolt hole will affect the mechanical performance of steel angles at low temperature. In practice, steel members with notch become brittle under three-dimensional stress state and strain concentration occurs which is called the notch sensitivity. To evaluate the notch sensitivity of steel angles at low temperature, the notch sensitivity factor and the stress concentration coefficient of notch specimens are expressed in Eqs. 6 to 7 as follows [21,22],

$$q_t = \sigma_b / \sigma_{bH} \quad (6)$$

$$K_t = \sigma_{bH} / \sigma_s \quad (7)$$

where σ_b is the ultimate tensile strength of the smooth specimen, σ_{bH} is the ultimate tensile strength of specimen with notch, σ_s is the yield stress as the appearance of non-proportional elongation of smooth specimens. It can be seen from the equations, the notch sensitivity factor is defined as the ratio of σ_b and σ_{bH} , the stress concentration coefficient is the ratio of σ_{bH} and σ_s . Thus, the smaller of q_t and K_t , the smaller influence of notch.

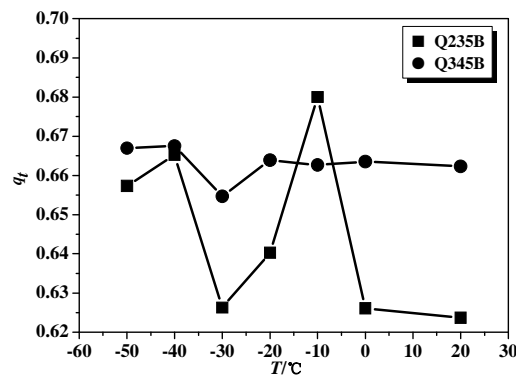


Figure 11. Notch Sensitivity Factors

The tensile tests of Q235B and Q345B steel angles were performed at seven specified temperature points from 20°C to -50°C. The values of ultimate tensile strength σ_b for 5 test specimens with 7 specified temperature points are listed in Table 11. According to the yield stress σ_s and ultimate tensile strength of the smooth specimen σ_b listed in Table 7, the notch sensitivity factor q_t and the

stress concentration coefficient K_t are calculated and listed in Table 10. Figure 11 shows the notch sensitivity factor versus temperature curves.

Table 10. Notch Tensile Test Results of Q235B and Q345B Steel Angles

Steel grade	Property	T/°C						
		20	0	-10	-20	-30	-40	-50
Q235B	Ultimate tensile strength	623	716	660	701	772	742	765
		636	651	695	720	739	705	748
		685	732	709	810	780	714	786
		638	715	728	770	720	781	749
		632	663	680	738	753	717	747
	σ_{bH}/MPa	642.8	695.4	694.4	747.8	752.8	731.8	759.0
	q_t	0.62	0.63	0.68	0.64	0.63	0.66	0.66
	K_t	2.66	2.46	2.01	2.21	2.43	2.14	2.11
Q345B	Ultimate tensile strength	823	836	863	878	917	947	916
		880	881	882	872	884	912	915
		813	846	864	880	906	939	912
		792	827	855	870	889	892	902
		812	843	851	867	896	889	925
	σ_{bH}/MPa	824.0	846.6	863.0	873.4	898.4	915.8	914.0
	q_t	0.66	0.66	0.66	0.66	0.65	0.67	0.67
	K_t	2.18	2.31	2.19	2.24	2.26	2.08	2.28

As shown in Figure 11, the notch sensitivity factor q_t of Q345B, which is changed between 0.65 and 0.67, is slightly increased with the decrease of temperature. Therefore, the temperature has little effect on the notch sensitive coefficient of Q345B steel angles. However, it is clear that the gap sensitive coefficient of Q235B steel angles, which is varied between 0.62 and 0.68, is much more sensitive to the decrease of temperature. Hence, it can be concluded that the sensitivity of the gap will increase with the increasing of steel grade of angel section. In other words, it should be taken more care on the use of high steel grade angle members at low temperature.

As shown in Table 10, the stress concentration coefficient K_t for Q235B steel angle varies between 2.01 and 2.66 while the range of K_t is from 2.08 to 2.31 for Q345B. It indicates that there is no clear increasing or decreasing tendency on the stress concentration of the two kinds of steel angles at low temperature. Thus, the effect of low temperature on K_t is insignificant. In practice, it is recommended that the stress concentration coefficient K_t of steel angles is taken as 3 to prevent the occurrence of brittle fault due to the possible existence of the notch at low temperature.

4. CONCLUSIONS

The application of higher strength steel such as Q420 can improve the safety and structural performance of transmission engineering with a reduction in fabrication and construction cost. However, the mechanical properties and toughness of the higher grade steel are different from that of commonly used steel such as Q235 and Q345, due to the different rolling process, crystal phases and chemical components especially under low temperature. The lack of support by experimental tests limits the use of Q420 and Q460 in transmission towers at the low temperature area. This paper fills the gap by carrying out a series of tests such as Charpy impact test, uniaxial tensile test and tensile notch test at low temperatures to investigate the mechanical properties and toughness of steel

angles made of Q235B, Q345B and Q420C as well as welded joints using Q420C. Several useful conclusions are made for design purpose and presented as follows:

- 1) The impact energy of steel materials decreases with the decreasing of temperature starting from 20°C. The ductile-brittle transition temperature of Q235B, Q345B and Q420C steel angles and Q420C welded joints are 1.47°C, 1.03°C, -31.74°C and -12.69°C, respectively. The ability to resist low temperature and cold brittleness of Q420C steel angles are better than Q235B and Q345B steel angles. Q420C steel angles are preferred in the cold region, but the welded joints of Q420C should be avoided.
- 2) The tensile strength σ_b and yield strength σ_s of Q235B, Q345B and Q420C steel angles and Q420C welded joints are increased with the decreasing of temperature. Also, the increment of σ_b at low temperature is smaller than σ_s for Q235B and Q420C steel angles and Q420C welded joints; but the increment of σ_b is greater than σ_s for Q345B steel angles. Welding process will significantly reduce the performance of Q420C steel angle and therefore, the welded joints of Q420C steel should be avoided at low temperature conditions.
- 3) In low temperature region, the design load resistance of steel angles can be calculated by the design strength specified in national design code with the reduction factor obtained from experimental test. The strength reduction factor of Q235B, Q345B and Q420C steel angles and Q420C welded joints are recommended as 0.90, 0.90, 0.75 and 0.70 respectively.
- 4) The effect of low temperature on stress concentration due to microcrack is insignificant. The stress concentration coefficient K_t of Q235B and Q345B steel angles is recommended as 3 for connection design of transmission tower. The notch sensitivity factor q_t of Q345B is larger than Q235B and therefore, it should take more care on the rolling process and fabrication works on the members made of higher steel grade such as Q420.

ACKNOWLEDGMENT

The authors acknowledge the financial support provided by the Natural Science Foundation of China (51408221), the Natural Science Foundation of Hebei Province of China (E2015502016), the Fundamental Research Funds for the Central Universities of China (2014ZD36). The third author is grateful to the financial supports by Innovation and Technology Fund of the Hong Kong SAR Government for the project “Development of an energy absorbing device for flexible rock-fall barriers (ITS/059/16FP)”.

REFERENCES

- [1] AISC-LRFD. Specification for Structural Steel Buildings. AISC, Inc, One East Wacker Driver, Suite 700, Chicago, Illinois 60601-1802, 2010.
- [2] Eurocode3. EN 1993-1-1: Design of Steel Structures - General Rules and Rules for Buildings, European Committee for Standardization. 2005.
- [3] Jiang, W. Q., Wang, Z. Q. and McClure, G., et al., “Accurate Modeling of Joint Effects in Lattice Transmission Towers”, *Engineering Structures*, 2011, Vol. 33, No. 5, pp. 1817-1827.
- [4] Jiang, W. Q., Liu, Y. P. and Chan, S. L., et al., “Direct Analysis of An Ultrahigh-voltage Lattice Transmission Tower Considering Joint Effects”, *Journal of Structural Engineering*, 2017, Vol. 143, No. 5, pp. 4017009.
- [5] Wang, Y. Q., Liu, X. Y. and Hu, Z. W., et al., “Experimental Study on Mechanical Properties

- and Fracture Toughness of Structural Thick Plate and Its Butt Weld along Thickness and at Low Temperatures”, *Fatigue & Fracture of Engineering Materials & Structures*, 2013, Vol. 36, No. 12, pp. 1258-1273.
- [6] Xu, Y., “Research on the Bearing Capacity of High-strength Steel Tubular H-Joints in High-Voltage Transmission Lines”, *Applied Mechanics & Materials*, 2014, Vol. 513-517, pp. 4123-4126.
 - [7] Wang, Y. Q., Liu X. Y. and Lin Y., et al., “Experimental Study on Fracture Toughness of High-Strength Structural Steel and Its Butt Weld”, *Advanced Steel Construction*, 2015, Vol. 11, No. 4, pp. 440-451.
 - [8] Jing, H., Huo L. and Zhang Y., et al., “Effect of Yield Ratio on Fracture Toughness for High Strength Steel”, *Acta Metallurgica Sinica*, 1996, Vol. 32, No. 3, pp. 265-268.
 - [9] Barsom, J. M. and Rolfe, S.T., “Fracture and Fatigue Control in Structures : Applications of Fracture Mechanics”, 1987, No. 5, pp. 83.
 - [10] Toribio, J., “A Fracture Criterion for High-strength Steel Notched Bars”, *Engineering Fracture Mechanics*, 1997, Vol. 57, No. 4, pp. 391-404.
 - [11] Rogers, C. A. And Hancock, G. J., “Fracture Toughness of G550 Sheet Steels Subjected to Tension”, *Journal of Constructional Steel Research*, 2001, Vol. 57, No. 1, pp. 71-89.
 - [12] Yang, F. Y., Li, X. B. and Chen, X., et al., “Study on Low Temperature Service Capabilities and Application of Power Transmission Tower Steel”, *Proceedings of the CSEE*, 2013, Vol. 33, No. 1, pp. 117-122. (in Chinese)
 - [13] Yu, Z.X., QIAO, Y.K. and ZHAO, L., et.al. “A Simple Analytical Method for Evaluation of Flexible Rockfall Barrier Part 1: Working Mechanism and Analytical Solution”, *Advanced Steel Construction*.2018, Vol. 14, No. 2, pp.115-141.
 - [14] Yu, Z.X., QIAO, Y.K. and ZHAO, L., et.al. “A Simple Analytical Method for Evaluation of Flexible Rockfall Barrier Part 2: Application and Full-scale Test”, *Advanced Steel Construction*. 2018, Vol. 14, No. 2, pp.142-165.
 - [15] Wang, F.Y., Xu, Y.L. and Zhan, S. “Concurrent Multi-scale Modeling of a Transmission Tower Structure and Its Experimental Verification”, *Advanced Steel Construction*. 2017, Vol.3 No.3 pp.258-272.
 - [16] “GB/T2009-2007 Metallic Materials-Charpy Pendulum Impact Test Method”, Beijing: China Standards Press, 2008. (in Chinese)
 - [17] “GB/T 13239-2006 Metallic Materials-Tensile Testing at Low Temperature”, Beijing: China Standards Press, 2006. (in Chinese)
 - [18] HB 5214-1996 Normal Temperature Metal Notch Tensile Test Method”, Beijing: China Standards Press, 1996. (in Chinese)
 - [19] Wang, Y. Q., Liu, X. Y. and Hu, Z. W., et al., “Experimental Study on Mechanical Properties and Toughness of q460c High-strength Steel and its Butt Welded Joint at Low Temperature”, *Fatigue & Fracture of Engineering Materials & Structures*, 2014, Vol. 3, No. 14, pp. 456-469.
 - [20] Wang, Y. Q., Zhou, H. and Shi, Y. J., et al., “Mechanical Properties and Fracture Toughness of Rail Steels and Thermite Welds at Low Temperature”, *International Journal of Minerals, Metallurgy and Materials*, 2012, Vol. 19, No. 5, pp. 409-420.
 - [21] Može, P., Beg, D. and Lopatič, J., “Net Cross-section Design Resistance and Local Ductility of Elements made of High Strength Steel”, *Journal of Constructional Steel Research*, 2007, Vol. 63, No. 11, pp. 1431-1441.
 - [22] Cai, Y. and Young, B., “Structural Behavior of Cold-formed Stainless Steel Bolted Connections”, *Thin-Walled Structures*, 2012, Vol. 83, pp. 147-156.

A NEW NUMERICAL MODELLING APPROACH FOR FLEXIBLE ROCKFALL PROTECTION BARRIERS BASED ON FAILURE MODES

X. Qi¹, Z.X. Yu^{2*}, L. Zhao³, H. Xu⁴ and S.C. Zhao⁵

¹ *Lecturer, School of Civil Engineering, Southwest Jiaotong University, Chengdu, China
State Key Laboratory of Geohazard Prevention and Geoenvironment Protection,
Chengdu University of Technology, Chengdu, China*

² *Associate Professor, School of Civil Engineering, Southwest Jiaotong University, Chengdu, China*

³ *Researcher Fellow, Department of Civil and Environmental Engineering,
The Hong Kong Polytechnic University, Hong Kong, China*

⁴ *Lecturer, School of Civil Engineering, Southwest Jiaotong University, Chengdu, China*

⁵ *Professor, School of Civil Engineering, Southwest Jiaotong University, Chengdu, China*

**(Corresponding author: E-mail: yzxzrq@home.swjtu.edu.cn)*

Received: 15 August 2017; Revised: 3 September 2017; Accepted: 18 November 2017

ABSTRACT: To study the mechanical behaviour of the flexible rockfall protection barriers under impact load, four full-scale impact tests involving protection capacities of 750 kJ and 2000 kJ were conducted, including two successful and two failed tests. The experimental results show that the system has three working stages. Among these three stages, the second and the third stages play significant roles in both absorbing the impact energy and ensuring the system performance reasonable. Based on the observed failure modes in the tests, the key factors leading to the breakdown of the system are investigated. A new numerical modelling approach is established, which is able not only to predict the capacity of the flexible protection barrier subjected to the rockfall impact but also to accurately simulate the main failure modes such as buckling of the steel post and breakage of the rope. The experimental results are employed to assess and verify the calculation model, and the numerical responses of the system are in good agreement with the test data. Furthermore, a flexible rockfall protection barrier with a capacity of 5000 kJ is designed by using the numerical procedure as an effective tool, shown by a full-scale impact test.

Keywords: Rockfall protection barrier, full-scale testing, finite element model, dynamic response, failure mode

DOI: 10.18057/IJASC.2018.14.3.10

1. INTRODUCTION

One of the most common protection measures for falling rock disasters is a flexible rockfall protection barrier, which mainly consists of a steel wire-ring net, support ropes, uphill ropes, energy dissipating devices and posts, as shown in Figure 1. In comparison to typical rigid protection structures, such as a rigid fence and an earth dam, the barrier structure consumes more impact energy owing to its flexibility, relying on the tension-compression balance among different components. Currently, flexible rockfall protection barriers have been widely used and have proved to be effective [1,2].

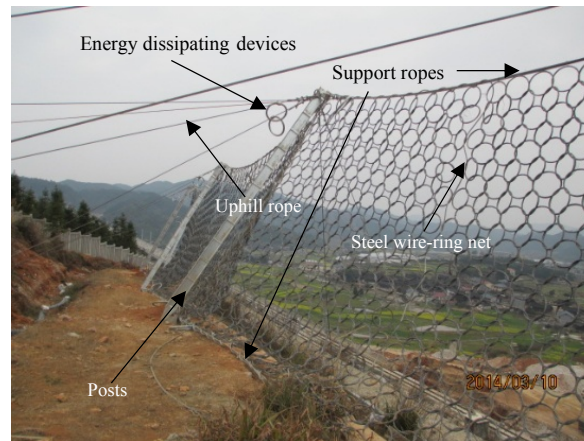


Figure 1. Composition of a Flexible Rockfall Protection Barrier

Previously, most research and experimental tests essentially focused on the static behaviour of the individual components of the protective barrier, such as interception nets and energy dissipating devices. Castro-Fresno et al. [3] studied the mechanical properties of a net with different configurations using tensile, slip and shear tests in concentrated and uniform load modes. Díaz et al. [4] investigated the energy-consuming characteristics of spring-type energy dissipator. Castanon-Jano et al. [5] summarized the composition and energy dissipating principle of the different energy dissipators used in the rockfall interception system and evaluated the energy dissipating capacity. Muhunthan et al. [6] researched the bolt forms of flexible rockfall protection barriers. Arndt et al. [7] studied the influence of the boundary constraint on the mechanical properties of the net. Without the design perspective of the structural level, the flexible protective barrier system is only a combination of those components. However, with the increased protection energy of commercial products, to date, the maximum energy level has reached 8000 kJ, and the performance of the entire system has been considered. To determine the system parameters and verify the structural configuration, many full-scale impact tests were conducted at artificial [8] and natural [9,10] rockfall test sites, so the entire impact process and protection capacity were intuitively observed. In *Guideline for European Technical Approval of Falling Rock Protection Kits (ETAG 27)* [11], the flexible rockfall protection barrier was, for the first time, regarded as an integrated structure rather than assembled components, which means that the loading mechanism and the failure mode should be treated as an internal interaction in the structural design. Moreover, the full-scale impact test, in addition to devices for recording the experimental data, became obligatory for final safety verification as well as more expensive. Yu et al. [12, 13] proposed a simple analytical method for fast evaluation of the performance of the flexible rockfall barrier system and established the equation for prediction of large deformation of flexible rockfall barrier system. Xu et al. [14] proposed an energy allocation based design approach for quickly determining the specification, size and amount of components of a flexible rockfall protection barrier structure, which based on a reliable numerical modelling validated by several experimental tests that include both component tests and full-scale impact tests.

To save costs, numerical models were developed to improve the design efficiency as well as avoid the risk of failing on-site impact tests. To propose the design method of protective barriers, the relationship between the key parameters, such as impact elongation, braking time, energy dissipation and internal forces, were obtained based on finite element [15] and discrete element [16] approaches, and the model was verified by comparison with the test results. Gentilini et al. [9,17,18] equated the ring into a quadrilateral and a triangle, ignoring the bending of the net unit, modelled the components in the system by truss elements, and established an overall 3D calculation model of flexible rockfall protection barriers. Escallón et al. [19] established the calculation units of the

interception net based on a reverse formula and genetic algorithm. Although the existing models are able to simulate the entire impact process of flexible protection barriers, most models only present good working performance for successful interception. In other words, few of models involve failure simulation or failure pattern prediction, so the effective guidance for the design and optimization of the structure cannot be provided.

In this paper, two failed full-scale impact tests that involve protection capacities of 750 kJ and 2000 kJ as well as two corresponding successful tests are presented. Three working stages of the system during the successful interception impact process are defined, and the damage mechanism of the structure is analysed. Then, a numerical approach that can predict the failure modes, verified by the experimental results, is developed for design of the barrier structural design. The details of the full-scale tests are introduced in Section 2, as well as the description of the failure mechanism and mode of the flexible protection barriers. The methods of modelling each component and boundary constraints in the numerical simulation are shown in Section 3. In Section 4, the comparison between the test and the simulation results are employed to validate the proposed numerical model. Finally, a high-performance flexible rockfall barrier with a capacity of 5000 kJ is designed by numerical procedure, and both the experimental and the predicted results are presented in Section 5.

2. FULL-SCALED ROCKFALL TEST

2.1 Test Set Up

The rockfall impact test shown in Figure 2 refers to the representative standard *ETAG 27*. The test site, located in Xinjin County (Sichuan, China) includes the reaction wall, the cantilever crane and the testing equipment.

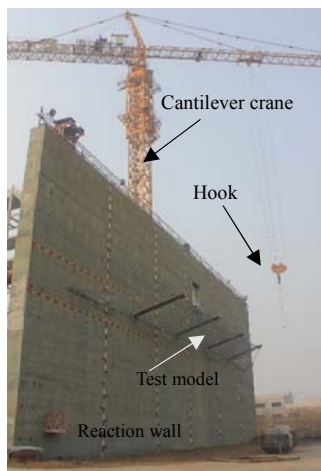


Figure 2. Overall View of the Test Site

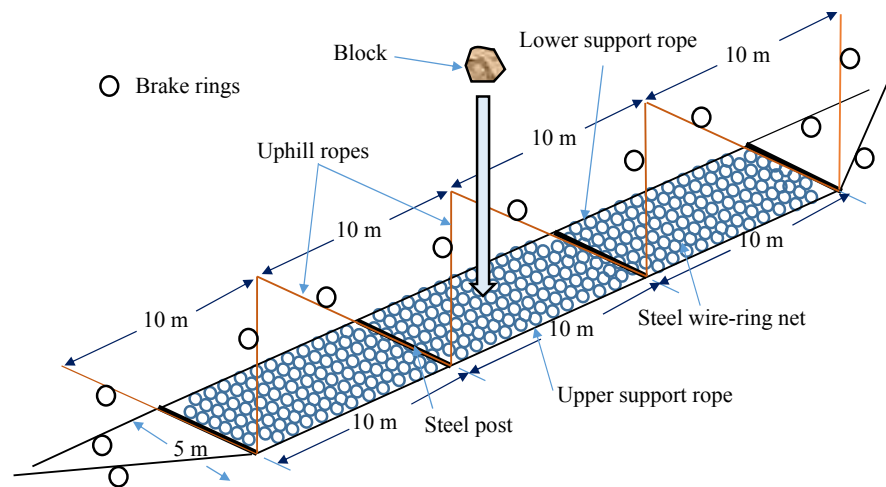


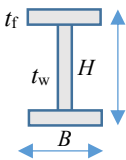
Figure 3. Test System Composition

To study the failure modes of the barrier system, two failed experiments (RXI-750-1 and RXI-2000-1) are selected, and after some improvements, the corresponding successful experiments (RXI-750-2 and RXI-2000-2) are also presented. Furthermore, a 5000 kJ impact test was carried out to verify the correctness of the proposed numerical approach in prediction and design.

The layout of the test models is shown in Figure 3. Each test model has three functional modules

and four steel posts with a height of 5 m. The horizontal spacing between the posts is 10 m. The post feet are fixed on the RC reaction wall by a pin hinge that provides rotational freedom in the vertical plane, and the post caps are connected to the uphill rope. All of the posts and the net are set horizontally, subjected to the impact load of a free-falling block. A high-speed camera is used to record the entire impact process, as well as the deformation of the brake rings. Load cells with a frequency of 10000 Hz are used to measure the tensile force of uphill ropes and support ropes.

Table 1. Main Parameters of the Experimental Models

	RXI-750-1	RXI-750-2	RXI-2000-1	RXI-2000-2	RXI-5000
Steel wire-ring net	R7/3/300	R7/3/300	R12/3/300	R12/3/300	R19/3/300
Uphill ropes	1Φ16	1Φ16	1Φ22	2Φ22	2Φ22
Support ropes	2Φ18	2Φ18	2Φ18	2Φ22	2Φ24
Post <div>  </div>	$H=200$ mm $B=100$ mm $t_w=7$ mm $t_f=11$ mm	$H=175$ mm $B=175$ mm $t_w=7$ mm $t_f=11$ mm	$H=200$ mm $B=200$ mm $t_w=8$ mm $t_f=12$ mm	$H=200$ mm $B=200$ mm $t_w=8$ mm $t_f=12$ mm	$H=300$ mm $B=300$ mm $t_w=10$ mm $t_f=15$ mm
Number of brake rings in support rope	24	24	22	22	32
Number of brake rings in uphill ropes	16	16	32	24	72
Block(mass/height)	5 t/15 m	5 t/15 m	6.5 t/32 m	6.5 t/32 m	15.6 t/32 m
Results	Failed	Successful	Failed	Successful	Successful
Note	Steel posts bulked		Upper support rope broke		

The configuration details are given in Table 1. It can be seen that as the protection capacity grows, the component sizes and amount of brake rings become larger, while all the brake rings used in the test are GS-8002 type [20]. With respect to RXI-750-1, the steel posts with wider flanges are adopted in RXI-750-2, and the difference between RXI-2000-1 and RXI-2000-2 is the number of brake rings on the uphill ropes.

2.2 Three-Stage Mechanical Behaviour

According to the full-scale impact test results recorded by the high-speed camera and the load cells, the braking time of the block lasts 0.25~0.5 s, which is mainly related to the system configuration. As the braking time increases, the impact force decreases. By analysing the high-speed photography, it is found that the impact force and deformation of the system are characterized by similar three-stage behaviour in the two successful tests (RXI-750-2, RXI-2000-2), revealing an entire working mechanism of the intercepting process (Figure 4).

In the first stage, the initial equilibrium state of the system, in which the barrier structure is only subjected to its own gravity, is converted into the tight state, as shown in Figure 4a. The deformation of the system in this stage that mainly caused by bending deformation of steel wire-rings and slipping of the net along the support ropes. This accounts for 30-40% of the total impact elongation, while most of the material in the system remains within the elastic state. Until the end of this stage, all the break rings have not yet been activated.

In the second stage, as the elongation of the system along the impact direction increases, the tensile forces of the support ropes become greater, leading to activations of most of the dissipators on the support ropes. With the shrinkage towards the middle module, the steel wire-ring net slides along the support ropes, forming a funnel shape as illustrated in Figure 4b. During this process, the energy dissipated by the system mainly consists of the sliding friction work and the plastic deformation of the brake rings.

In the third stage, an additional elongation of the system is supplied by the activation of the dissipator on the uphill ropes, as shown in Figure 4c. Then, the block continues to move downwards, even as the strokes of the brake rings are moved, until the maximum elongation is reached, when the total kinetic energy of the block has transferred into the internal energy of the barrier structure completely. At the end of this stage, the impact area of the wire-ring net has significant plastic deformations, including plastic bending and stretching. In addition, with respect to the original position, both middle posts swing down, and the displacements depend on the elongations of the brake rings on the uphill ropes.

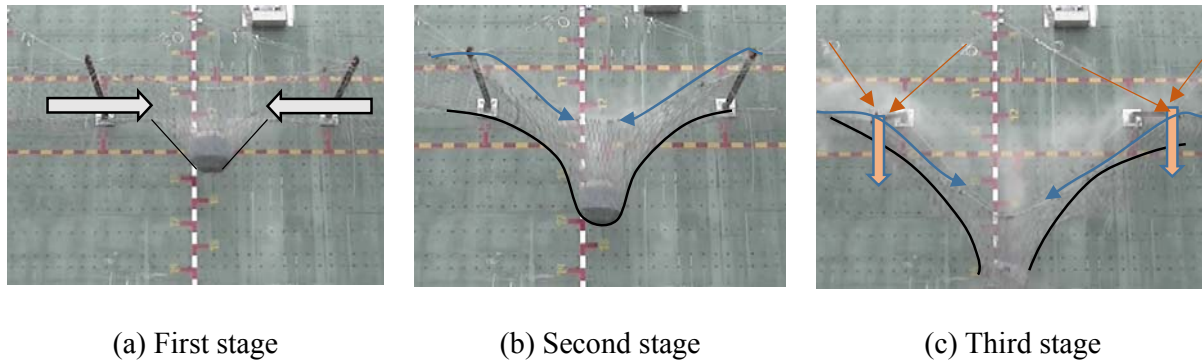


Figure 4. Deformation Characteristics of the Barrier Structure at Three Different Stages

2.3 Damage Mechanism and Failure Modes of the System

In the two failed experiments, buckling of the posts occurred in the model RXI-750-1, and the upper support rope broke in model RXI-2000-1. Using high-speed photography, it can be seen that both tests present a complete first stage; however, the force transferring characteristics of different experimental models are very discrepant in the second and third stages.

The model RXI-750-1 was damaged at the end of stage 2. From Figure 5a, C-type semi-wavy buckling of the steel posts occurred before it should have rotated around the horizontal axis of the fixed end in the vertical plane. The model RXI-750-2 showed the complete three-stage mechanical behaviour, while the brake rings on the support and uphill ropes fully worked. The system remained intact after the test, as shown in Figure 5b.

At the end of the second stage, the brake rings on the support ropes in model RXI-2000-1 were stretched relatively completely. Since the brake rings on the uphill ropes were not activated due to the overlarge activation force, the system could not enter into the third stage, resulting in breakage of the support ropes and destruction of the system, as shown in Figure 5c. As seen from Figure 5d, with respect to model RXI-2000-1, the less number of brake rings led to an adequate activation force, enabling the system to enter into the third stage. Then, the dissipators on both of the support ropes and the uphill ropes ran the full stroke to intercept the block successfully, indicating the satisfying integral working performance of the barrier system.

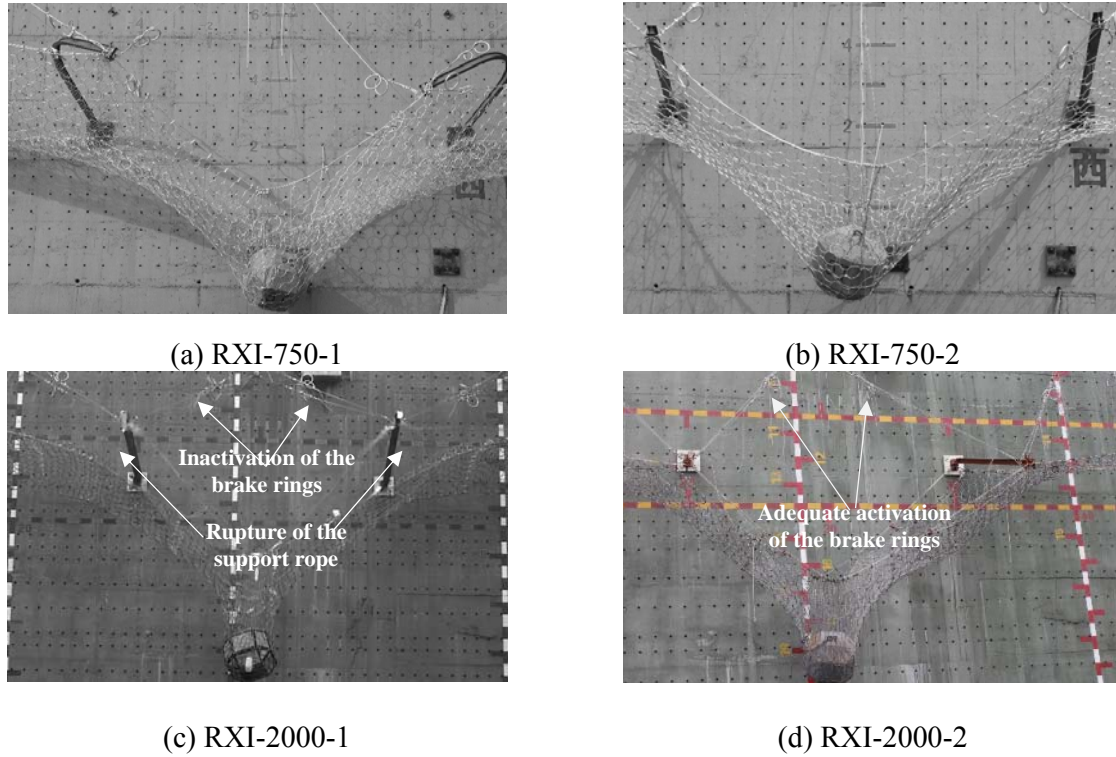


Figure 5. Test Results of Different Configurations for Model RXI-750 and RXI-2000

According to the analysis of the force transferring characteristics of the system, the elongations of the upper and lower support ropes greatly influence the deformability of the barrier structure. In particular, the upper support rope plays a very important role in activating the second and the third stages, since the post caps were directly connected with the uphill ropes to support it.

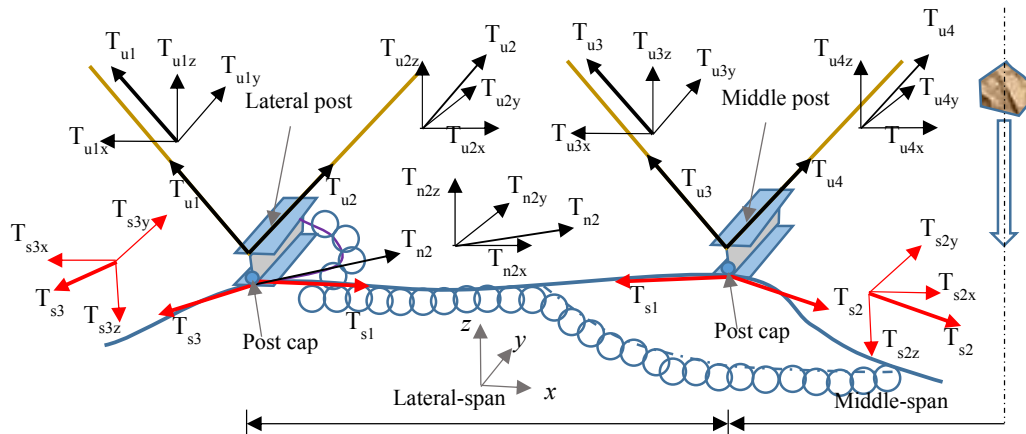


Figure 6. Force Transferring Mechanism among the Upper Support Rope, the Post Caps and the Uphill Ropes

Figure 6 depicts the internal forces of the upper support rope and the uphill ropes as well as their three components in the global coordinate system. The tensile forces of the upper support ropes in the lateral-span and middle-span are T_{s1} and T_{s2} , respectively. In the second stage, when the upper support rope slides towards the middle span, each post cap subjected to loadings from the upper support rope and the uphill ropes tends to swing to the opposite direction along which the support

rope slides. Simultaneously, the vertical component T_{s2z} of the upper support rope in the middle-span, acting on the post cap, is totally borne by the uphill ropes. As the elongation of the system increases at this stage, the impact force between the block and the wire-ring net keeps increasing, and the internal forces of the upper support rope and the vertical load T_{s2z} act on the post caps. Once the tensile force of the uphill ropes reaches a threshold equal to the activation force of the dissipators, the posts will swing down depending on the elongations of the brake ring on the uphill ropes, signifying that the system enters into the third stage.

The planar hinges at the post feet enable the posts to rotate freely in the vertical plane. While in the horizontal plane, the rotation is restricted finitely, which means that the posts can swing towards both lateral sides freely within a small range, as depicted in Figure. 7. Hence, in the first stage and the majority of the second stage, the posts are only subjected to axial loading due to the boundary conditions and the small magnitude of the interaction forces between the post caps and the support ropes. However, once the rotation of the post in the vertical plane is beyond the limitation, an additional bending moment will act on the post suddenly so that the uniaxial compression state of the post will be converted to the compound loading state that includes uniaxial compression and a bending moment about the weak axis. The post is prone to buckling damage as the load increases, similar to the failure mode of model RXI-750-1.

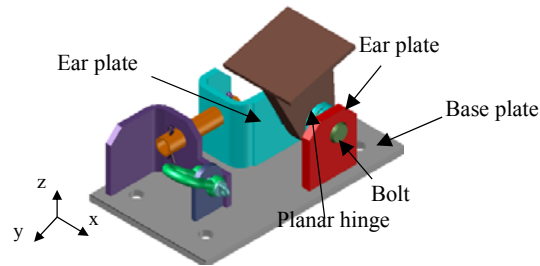


Figure 7. Configuration of the Base Plate of the Post

Therefore, in the third stage, a large portion of the kinetic energy of the block is consumed in terms of plastic strain energy and sliding friction of the dissipators on the uphill ropes. On the other hand, if the brake rings on the uphill ropes are not activated, the kinetic energy needs to be dissipated by the increasing impact force acting along the direction of deformation of the system. Thus, the tensile forces of the support ropes and the wire-ring net continue to increase so that the support ropes and the net would be broken. Hence, the activation of the dissipators on the uphill ropes relieves, to some extent, the burden of the high tensile forces of the support ropes and the wire net. The posts continue to be subjected to uniaxial loading without large transverse forces, avoiding buckling damage. Although it is shown from the experiments that the working states of the upper and lower support ropes are similar to each other, due to the different spatial locations related to the posts, the demand of elongation for the lower support ropes is greater than that for the upper support ropes, resulting in fuller strokes of the dissipators on the lower support rope. Meanwhile, the tensile force of the lower support ropes is also greater than that of the upper ropes.

Accordingly, failure modes of the flexible barrier structure can be generally classified as the following three types:

- 1) Collapse of the system caused by the buckling failure of the steel posts, in most cases featured by C-type semi-wavy buckling
- 2) Breakage of the uphill ropes and support ropes
- 3) Breakage of the steel wire-ring net

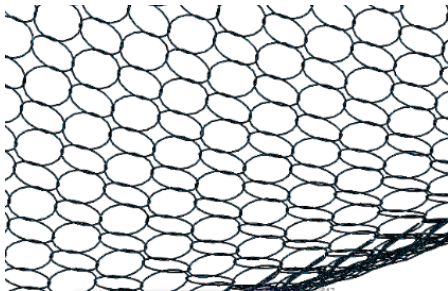
3. NUMERICAL SIMULATION APPROACH

According to the working process and potential failure modes studied from the tests, difficulties caused by highly nonlinear problems must be overcome for simulating the dynamic response of the flexible barrier structure. To establish an accurate numerical method, except the impact contact relationship and the elastoplastic material properties, various other key features should also be considered. These include the large deformation of the net, the sliding relationships among the components, the constraints of the steel post feet, the conversion process from axial pressure instability to bending instability of the steel posts, and the failure criteria of the components. Then, a three-dimensional finite element model that can predict the impact results and failure modes is developed and presented to provide effective guidance for optimizing and designing the flexible barrier structure.

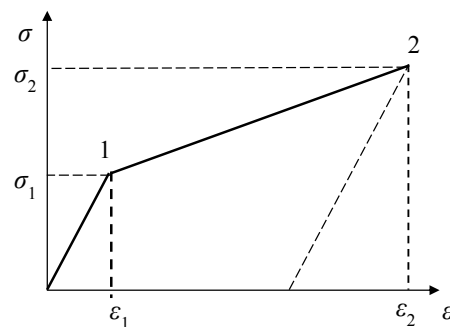
3.1 Main Bearing Components

1) The wire-ring net is modelled as an interlocking collection of rings, and each ring connects to four other rings using the automatic contact algorithm (Figure 8a). Each ring is composed of super-strength steel wires with a diameter of 3 mm and yield strength of 1.770 GPa. The beam element and a piecewise elastoplastic material model is used, while the behaviour of the elements is described by both the cross-sectional area and the uniaxial stress-strain relationship (Figure 8b). σ and ε represent the effective stress and effective strain, respectively. According to the material test results, $\sigma_1=1.2$ GPa, $\sigma_2=1.77$ GPa, $\varepsilon_1=0.002$ and $\varepsilon_2=0.05$.

2) It is difficult to accurately simulate the geometrical non-linearity that particularly refers to the sliding behaviour between the net and the ropes. In this paper, the segments of the support ropes that can slide along the post caps are modelled by means of the sliding cable elements (Figure 8c), which act as pulley systems. Each sliding cable element contains three dominant nodes, which are node 1, node 2 and node 3, as depicted in Fig. 8d. The intermediate node (node 1) coincides with the post end node, and the sliding distance of the support rope depends on the location of the two lateral points (node 2 and node 3). Even though the spatial positions of the support ropes change during the impact process of the system, the positive distance (Δ_{1-2}) along the axial direction of the sliding cable element is always equal to the negative distance (Δ_{1-3}) to coordinate the elongation of the support ropes. However, a friction coefficient equal to 0.15 is set between the support rope and the post cap so that the tensile force of the support rope is also influenced by the sliding friction as the rope slides along the post cap. Sufficient length, mainly relying on the maximum stroke of the dissipators, should be reserved for the sliding cable element in case the sliding distance is beyond the length of the sliding cable element. The final positions of the dominant points of the sliding cable element (node 1, 2 and 3) are determined by the rotation of the posts and the extension of the break rings, since the coordinates of node 1 are always duplicated with that of the post ends.



(a) Wire-ring net



(b) Constitutive laws for steel of the wire-ring

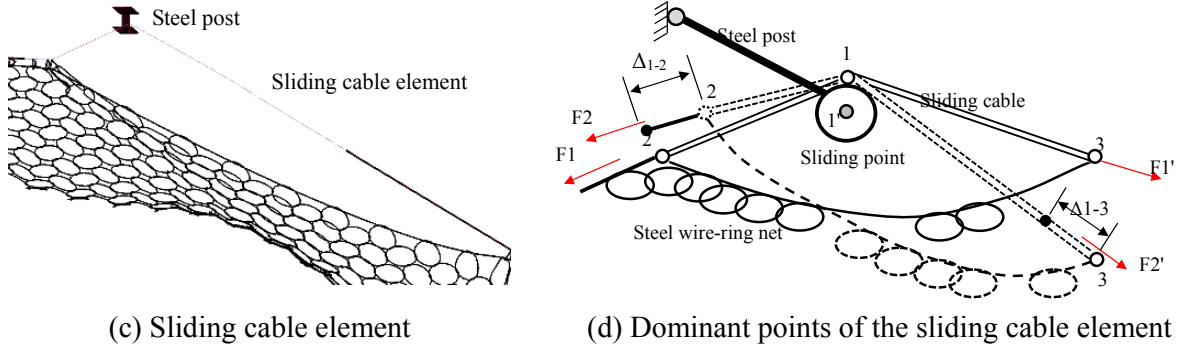


Figure 8. Elements Adopted for the Wire-ring Net and Sliding Segments of the Support Ropes

3) Nonlinear springs are employed in this paper as dissipators. Based on a group of quasi-static brake rings tests (Figure 9a), the force-displacement relationship is defined, and the key parameters are determined, as shown in Figure 9b. F_1 represents the activation force of the brake ring. L represents the maximum elongation of the brake ring, $L \approx \pi d$. L_e denotes the breakout elongation of the brake ring, and according to the test results (Figure 9) and statistical analysis, $L_e \approx L/50$. L_1 is the simplified sliding length of the brake ring; $L_1 \approx L/5$, $L_2 \approx 4L/5$, and $k_1 \approx F_1 / L_1 \approx \mu_s F_n / L_1$, and μ_s is the friction factor between the preload sleeve and the brake ring.

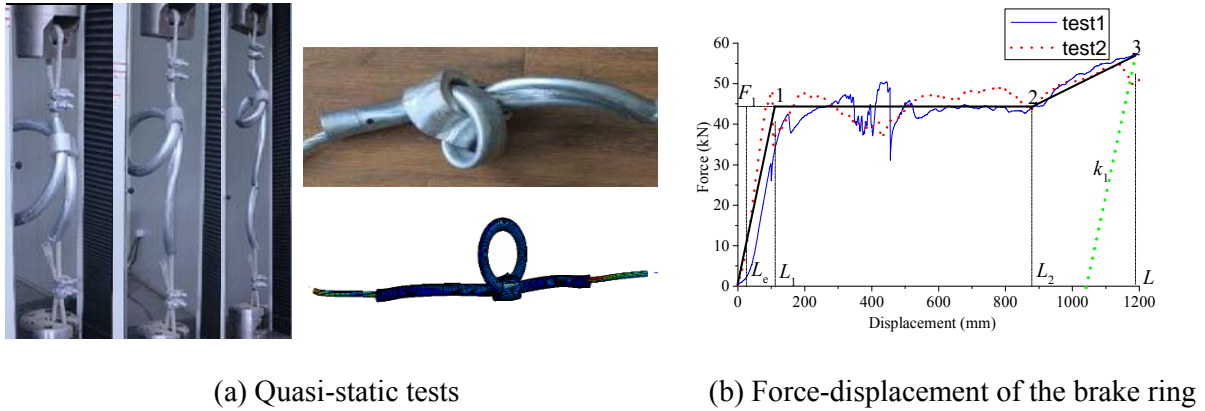


Figure 9. Numerical Model of the Brake Rings Based on Experimental Tests

3.2 Boundary Constraints

The automatic contact technique governed by the symmetric penalty function method is applied to the numerical model. In particular, a dynamic friction coefficient equal to 0.2 is set between the block and the wire-ring net, among the wire-rings. As depicted in Figure 10a, the support rope is connected to the wire-ring net via shackles, which are modelled as rigid elements. The guided-cable relationship [18] is employed between the shackles and the support rope so the shackles can slide along the rope during the impact process.

An ideal hinge joint is used at the post foot for free rotation in the vertical plane, while a nonlinear rotational spring is set for behaviour of the post in the horizontal plane. The relationship between bending moment M and rotational angle θ is illustrated in Figure 10b, in which $\theta_1 = 15^\circ$ and $k_1 = \min\{k_{\theta c}, k_{\theta p}\}$. $k_{\theta c}$ and $k_{\theta p}$ are the bending stiffness of the posts and pin hinge lugs, respectively, in the horizontal plane. $k_{\theta c}$ is determined by the actual cross-section dimensions of the post, $k_{\theta p}$ depends on the configuration of the post foot, mainly influenced by the dimensions of the pin and the pin-hole, as well as the distance between the ear plates (Figure 7), and the value can be obtained by the numerical simulation from a 3D FE model.

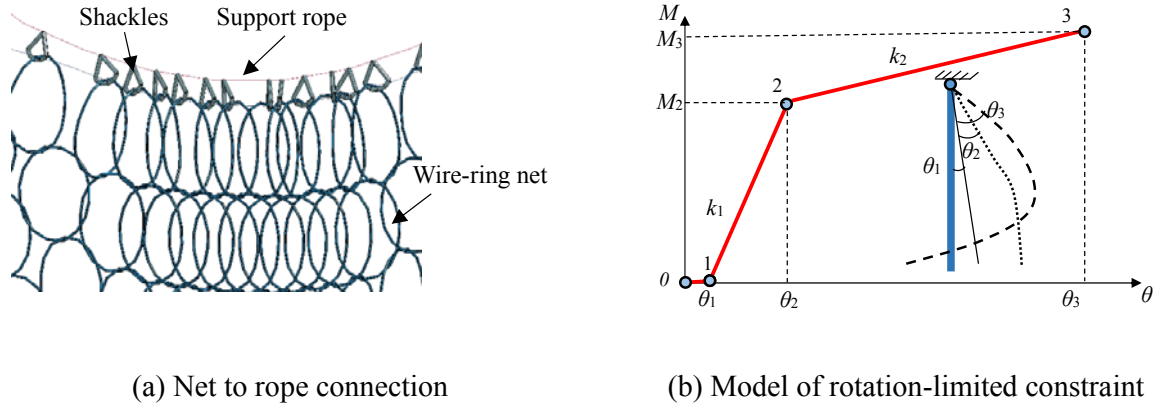


Figure 10. Typical Boundary Conditions

3.3 Dynamic Algorithm Method

An explicit dynamic algorithm is employed to calculate the entire collision process between the block and the net. To ensure the accuracy of the simulation, the scale factor for the Rayleigh time-step is set to 0.9. For lightening the computational burden, the block is initially positioned above the wire-ring net with a small gap, and an initial velocity is defined according to the impact energy level. The calculation is terminated at the end of the first rebound after impact. Furthermore, the stress of the model is initialized only under the gravity before impact. It is noted that, to preliminarily assess the results, the balance among the global internal energy, kinetic energy and hourglass energy must be taken into account to verify the stability of the energy state of the entire system.

4. ANALYSIS OF THE CALCULATION RESULTS

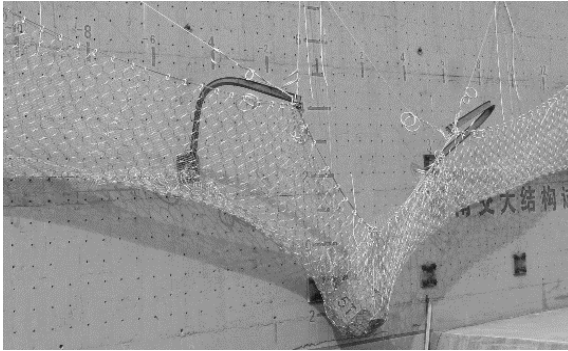
Based on the aforementioned numerical approaches, 4 models were simulated using the commercial LS-DYNA software program (notations referred to in Section 2).

The numerical simulations reproduced the features observed in each working stage of the tests, including the sliding of the support ropes, the deformation of the brake rings, the rotation of steel posts, and the similar failure modes.

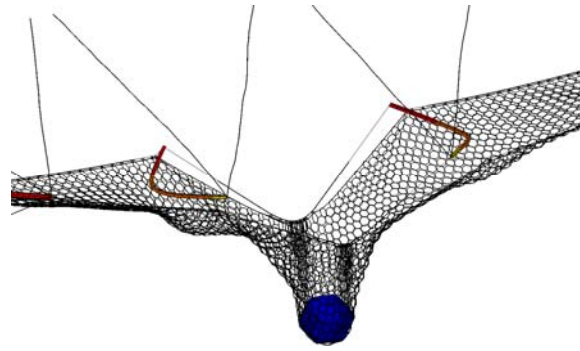
For the test model RXI-750-1, a system collapse occurred, as seen in Figures 11a and 11b. There are two reasons leading to this failure mode. First, the brake rings mounted on the longitudinal upper support ropes between the lateral post and the middle post were jammed at the post cap along which the ropes were sliding, resulting in the increase of lateral force and bending moment of the posts. Second, under great axial compression, it is much easier for damage to occur about the weak axis plane of the post with an H-type cross section than about the strong axis plane. Compared with model RXI-750-1, wider flange plates were adopted in model RXI-750-2. Through calculation, even if the brake rings are jammed at the post caps, requirements can be met by the increased bending stiffness about the weak axis plane of the post. Therefore, the result of model RX-750-2 was consistent with the expectation that the abovementioned failure mode is avoided, as seen in Figures 11c and 11d.

With regard to model RXI-2000-1, considering the impact energy is large enough, to ensure the support ropes slide smoothly through the post caps, all the brake rings on the support ropes were mounted symmetrically at both outer sides of the lateral posts rather than between the posts.

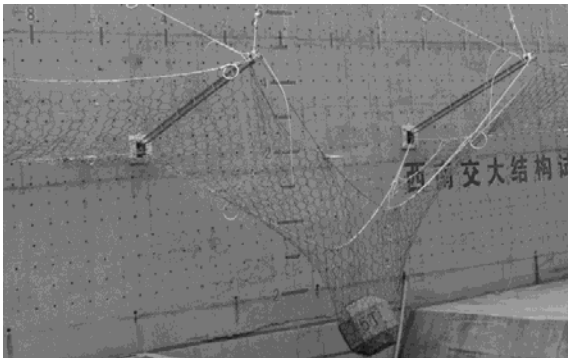
However, the upper support rope in model RXI-2000-1 was broken during the test, as depicted in Figure 11e. These results occur because the third working stage explained in Figure 4c was not activated, so the great impact of the internal forces was unexpectedly borne in the net and the support ropes. This impact mainly occurred because the four brake rings are mounted on each uphill rope in terms of a parallel connection, leading to an excessively large activation force. As shown in Figure 11f, the numerical simulation also represented the phenomenon that the activation force of the brake rings on the uphill ropes is too large, so they fail to participate in the system work. Therefore, in model RXI-2000-2, only two brake rings are mounted on each uphill rope, as illustrated in Figures 11g and 11h. The final result shows that the improved system has successfully intercepted the rock without damage.



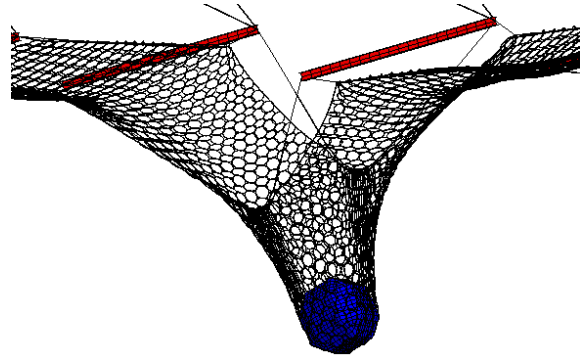
(a) Test result of model RXI-750-1



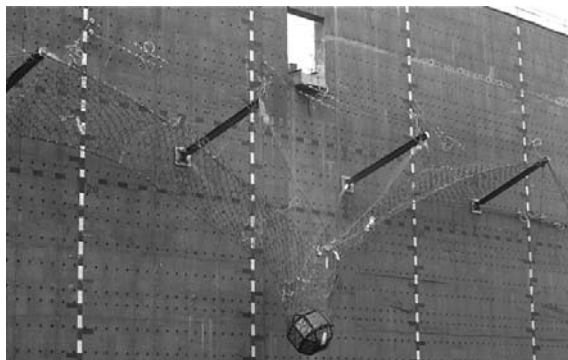
(b) Simulation result of RXI-750-1



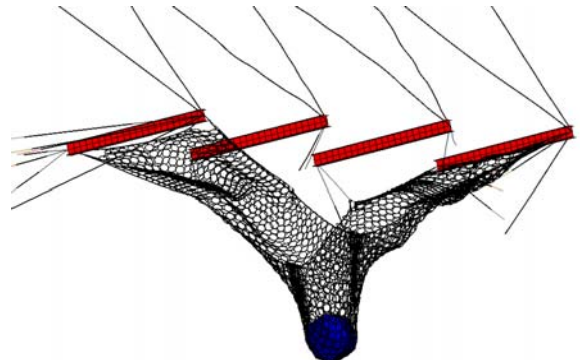
(c) Test result of model RXI-750-2



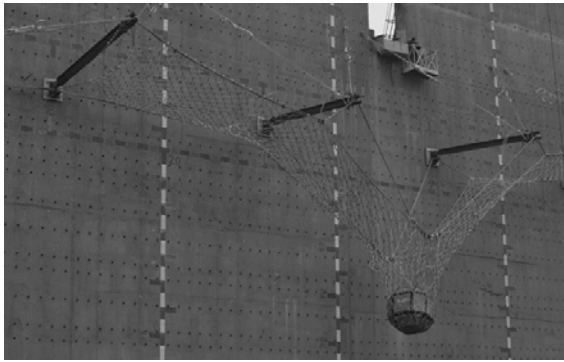
(d) Simulation result of RXI-750-2



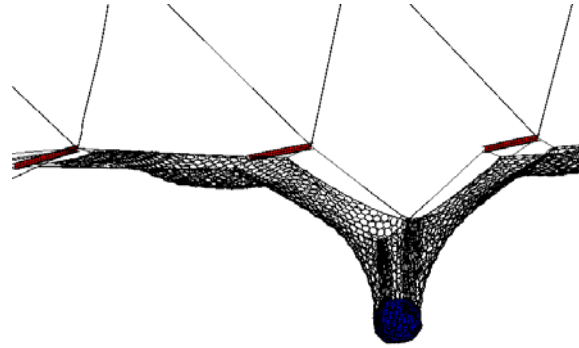
(e) Test result of model RXI-2000-1



(f) Simulation result of RXI-2000-1



(g) Test result of model RXI-2000-2



(h) Simulation result of RXI-2000-2

Figure 11. Experimental Results and Numerical Simulation Results

The tensile forces in different ropes of model RXI-750-2 and RXI-2000-2 from tests and simulations are given in Figure 12, which shows coincidences between experimental and numerical time-history curves. Also from Figure 12 it is clear that the tensile force of the support rope is obviously greater than that of the uphill rope.

Figure 13 plots the time-history curves of impact forces from the simulations, which captures the main features of the test data. In particular, the mechanical behaviour characterized by three different stages can be reflected in the numerical results. According to the European guidelines [11] some key indexes of the deformation, such as the elongation along the impact direction and the residual height after the test (the minimum distance between the lower and the upper rope), are very important parameters to evaluate the barrier performance. As given in Table 2, the maximum deviation of the vertical elongation and the residual protective height between tests and simulations are 5% and 16%, respectively. Such deviation can be caused by many reasons, of which the most important include the slightly eccentric impact in the tests, measurement errors, as well as the inevitable differences between the experimental and numerical models, such as the complicated connecting measures modelled by the simplified joints or elements.

Table 2. Comparison of Key Deformation Indexes between Tests and Simulations

		Models	Results (m)	Deviation
Vertical maximum impact deformation	RXI-750-2	Test	5.6	4%
		Simulation	5.8	
	RXI-2000-2	Test	7.0	5%
		Simulation	7.36	
Residual height after the test	RXI-750-2	Test	2.4	16%
		Simulation	2.8	
	RXI-2000-2	Test	3.4	5%
		Simulation	3.6	

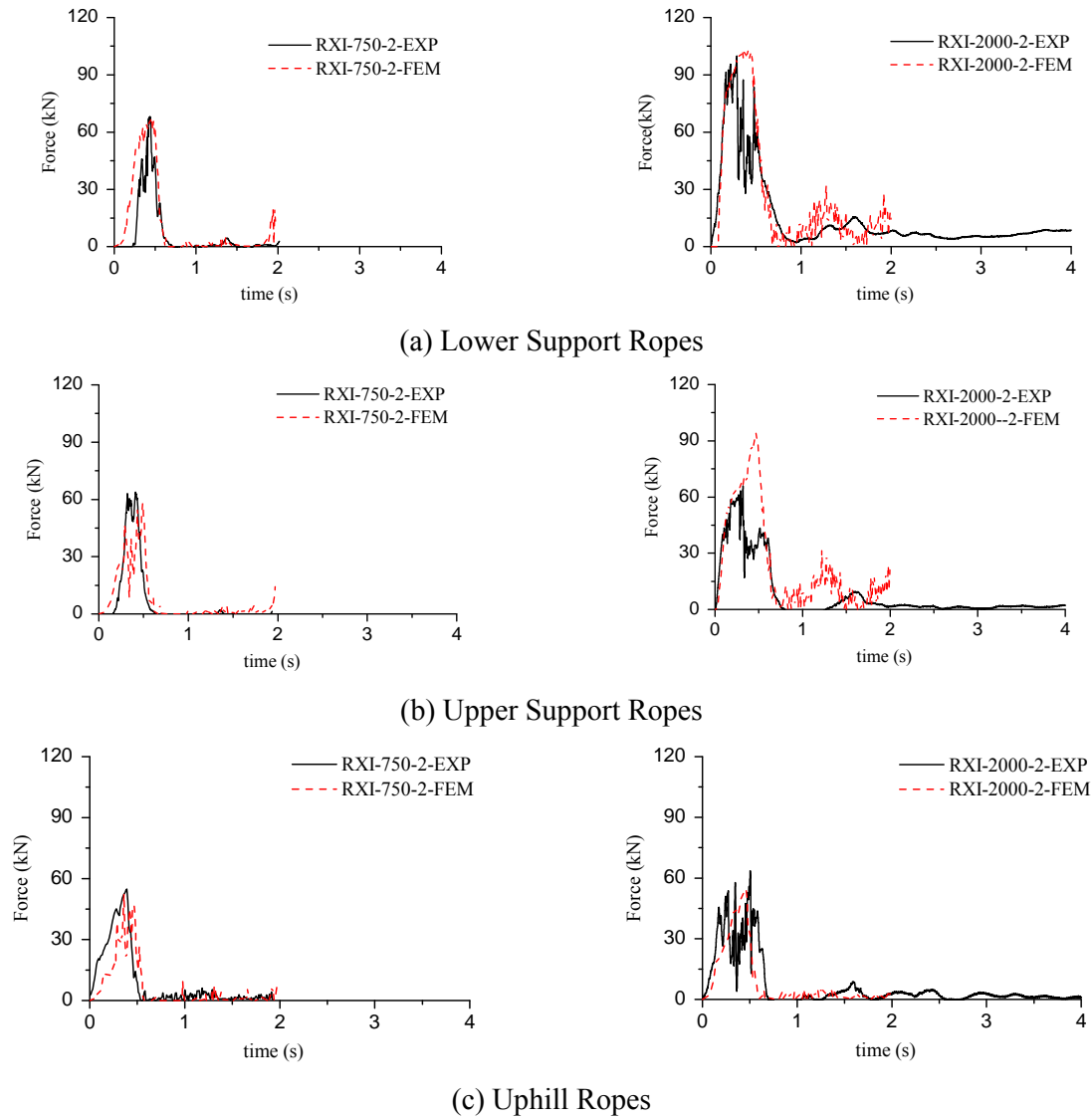


Figure 12. Time-history Curves of Tensile Forces

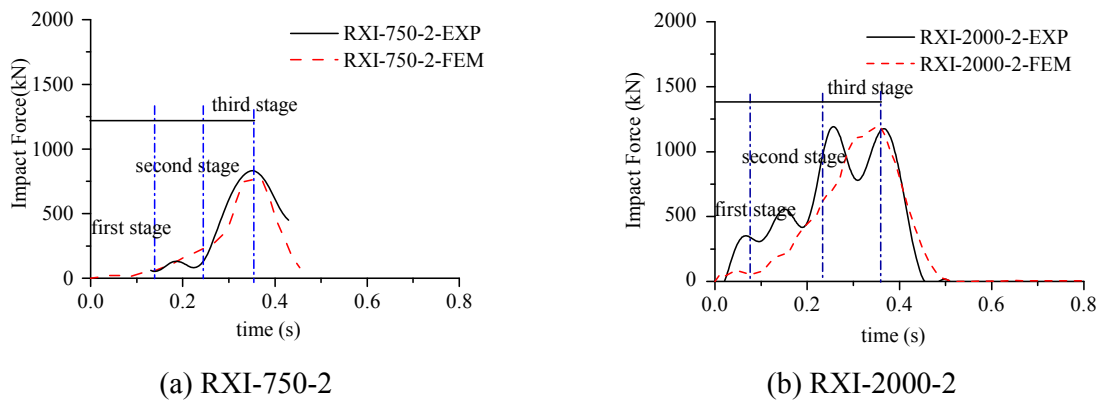


Figure 13. Comparison of the Time-history Curves of the Impact Forces between Experimental and Numerical results for models

5. UTILIZATION OF THE MODEL FOR DESIGN

Based on the above numerical strategy, a new type of high-performance flexible protective barrier was constructed. The main parameters of components in the system are shown in Table 1. Verified by the design procedure based on the numerical simulation, model RXI-5000 can successfully intercept the block with impact energy of 5000 kJ. According to the impact process simulation, the wire-ring net was immediately thrust downward at the beginning of impact, leading to the elongation of the support ropes owing to the activation of the brake rings mounted on the support ropes. The interaction between the posts and the support ropes grew when the support ropes slipped along the posts. Then, the steel posts transferred the forces to the uphill ropes, and the brake rings on the uphill rope were activated, which supplied displacement for the steel posts. The simulation result indicated that all components of the barrier, especially the wire-ring net, and the brake rings on the support ropes and uphill ropes worked fully during the entire impact process.

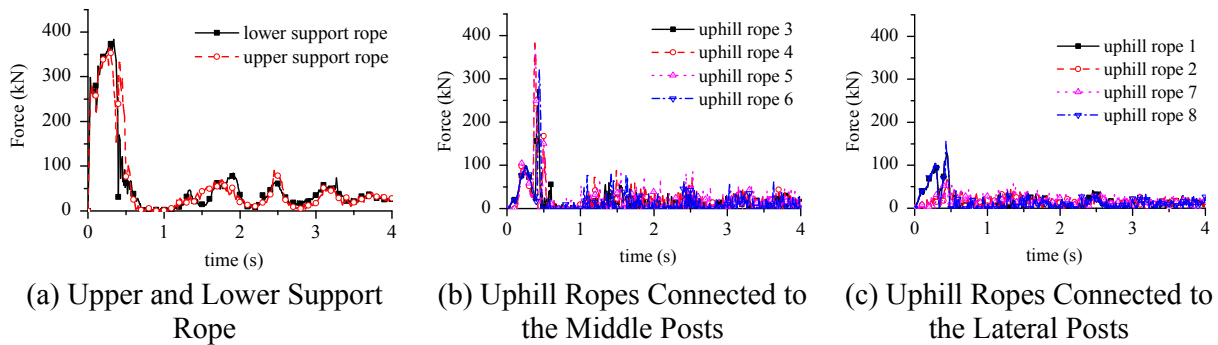


Figure 14. Tensile Forces of Ropes of model RXI-5000

After checking the internal forces of each component to guarantee the necessary safety reserve coefficients, a full-scale test of RXI-5000 was conducted. In particular, the tensile forces in the ropes of model RXI-5000 from the numerical simulation are obtained, as shown in Figure 14. The peak forces of the upper and lower support ropes shown in Fig. 14a are much greater than those of models RXI-750 and RXI-2000. The greatest peak force of the uphill ropes connected to the middle posts (Fig. 14b) is as large as the force of the support ropes that nearly reaches 400 kN. Relatively, the peak forces of the uphill ropes connected to the lateral posts are much lower, as depicted in Fig. 14c.

Figure 15 depicts the comparison of the impact process of model RXI-500 between the test (the first column) and the numerical simulation (the second column), including the moments of initial contact ($t=0.05$ s), the sway of the steel posts ($t=0.22$ s), the maximum displacement during impact ($t=0.44$ s), and the final state after the first rebound ($t=0.60$ s). The results show that the numerical simulation of the entire process is in a good agreement with the test results. Furthermore, the time-history curves of the impact force and the displacement of the block predicted via the simulation are compared with the test results in Figure 16. The good match between the simulation and the test results indicates that the new system has the capacity for protecting against the block with an impact energy of 5000 kJ and again proves the three-stage behaviour for successful rock interception.

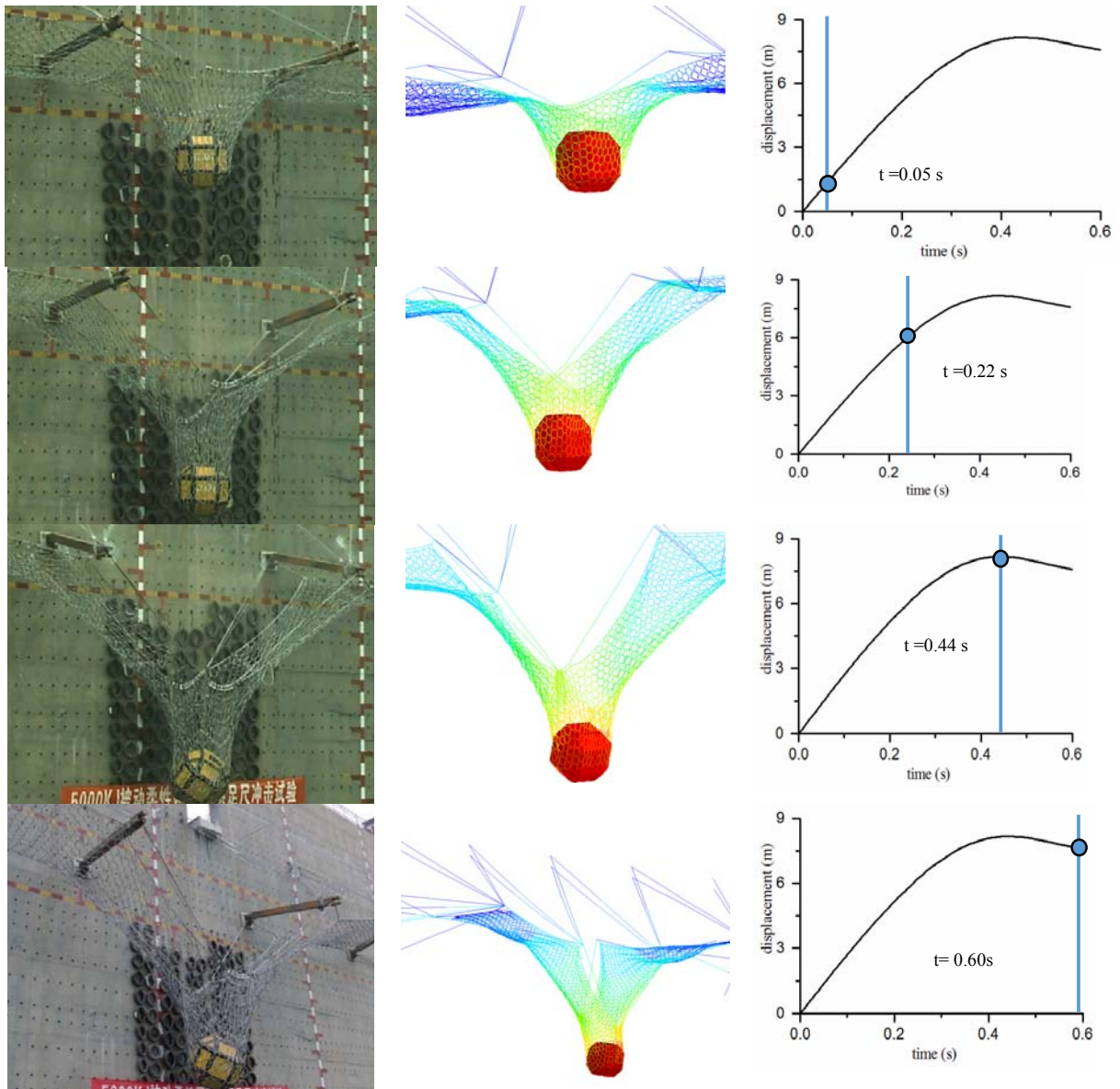


Figure 15. Test Result and Simulation Prediction of the Entire Impact Process of Model RXI-5000

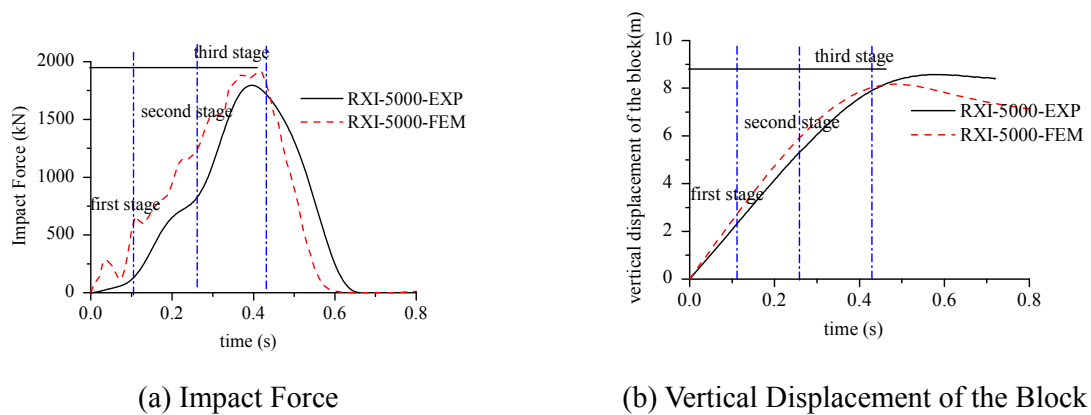


Figure 16. Comparison of Time-history Curves between Simulation and Test

6. CONCLUSIONS

1) According to two groups of full-scale tests, the load-transferring mechanism and failure modes of the flexible rockfall protective barrier are revealed. An effective and successful interception of the flexible rockfall protective barrier structure consists of three mechanical stages, which are classified with key moments when the specific components are loaded or activated. Hence, the protection capacity of the structure is determined not only by the capacity of each component but also by the rational assortment and allocation of each part, which can realize the three-stage behaviour.

2) A numerical approach for the flexible barrier structure is presented, which has been validated by comparison with the experimental results. The proposed simulation method can reappear in the three-stage mechanical behaviour, as well as be reproduced in the different failure modes in the actual structures. Therefore, the numerical model can be used as an efficient tool for design and optimization, owing to its good performance in predicting the response of the barrier structure under impact loads.

3) A high-performance flexible barrier structure with protection capacity of 5000 kJ has been numerically designed and experimentally tested. The sufficient safety reserve coefficients are necessary in the design. Furthermore, to enable each part of the system to work fully and for actions to transfer smoothly among all components, these are the most essential issues to be addressed.

ACKNOWLEDGMENT

The work of this study was supported by the National Natural Science Foundation of China [Grant No. 51408498, 51678504], Department of Science and Technology of Sichuan Province [Grant No. 2018JY0029], the foundation of State Key Laboratory of Geohazard Prevention and Geoenvironment Protection [Grant No. SKLGP2016K013] and the Fundamental Research Funds for the Central Universities [Grant No. 2682017CX006].

REFERENCES

- [1] Gottardi, G., Govoni, L. and Mentani, A., "The Effectiveness of Protection Systems Toward Rockfall Risk Mitigation", 2011 Bundesanstalt für Wasserbau. Vogt, Schuppener, Straub & Bräu, 2011, pp. 157-164.
- [2] Has, B., Hanaoka, M., Nozawa, E., Momose, A. and Sasaki, K., "Behavior and Mechanism of Earthquake-Induced Landslides within Pre-Existing Landslide Topography: the Case of the 2004 Mid-Niigata Prefecture Earthquake, Japan", Disaster Mitigation of Debris Flows, Slope Failures and Landslides, Japan, Interpraeven, 2006, pp. 35-46.
- [3] Castro-Fresno, D., Diaz, J.J.D.C., López, L.A. and Nieto, P.J.G., "Evaluation of the Resistant Capacity of Cable Nets using the Finite Element Method and Experimental Validation", Engineering Geology, 2008, Vol. 100, No. 1, pp. 1-10.
- [4] Díaz, J.J.D.C., Nieto, P.J.G., Castro-Fresno, D. and Rodríguez-Hernández, J., "Nonlinear Explicit Analysis and Study of the Behaviour of a New Ring-type Brake Energy Dissipator by FEM and Experimental Comparison", Applied Mathematics and Computation, 2010, Vol. 216, No. 5, pp. 1571-1582.

- [5] Castanon-Jano, L., Blanco-Fernandez, E., Castro-Fresno, D. and Ballester-Muñoz, F., “Energy Dissipating Devices in Falling Rock Protection Barriers”, *Rock Mechanics and Rock Engineering*, 2016, Vol. 50, No. 3, pp. 603-619.
- [6] Muhunthan, B. and Radhakrishnan H., “Finite Element Analysis of Hybrid Barrier for Rock Fall Slope Protection”, Final Report, Department of Civil and Environmental Engineering, Washington State University, 2007.
- [7] Arndt, B., Ortiz, T. and Turner, A.K., “Colorado’s Full-Scale Field Testing of Rockfall Attenuator Systems”, *Transportation Research E-Circular*, 2009.
- [8] Peila, D., Pelizza, S. and Sassudelli, F., “Evaluation of Behaviour of Rockfall Restraining Nets by Full Scale Tests”, *Rock Mechanics & Rock Engineering*, 1998, Vol. 31, No. 1, pp.1-24.
- [9] Gentilini, C., Govoni, L., Miranda, S.D., Gottardi, G. and Ubertini, F., “Three-dimensional Numerical Modelling of Falling Rock Protection Barriers”, *Computers and Geotechnics*, 2012, Vol. 44, No. 44, pp. 58-72.
- [10] Gottardi, G. and Govoni, L., “Full-scale Modelling of Falling Rock Protection Barriers”, *Rock Mechanics and Rock Engineering*, 2010, Vol. 43, No. 3, pp. 261-274.
- [11] European Organisation for Technical Approvals, “Guideline for European Technical Approval of Falling Rock Protection Kits (ETAG 027)”, Brussels, February, 2012.
- [12] Yu Z.X., Qiao Y.K., Zhao L., et.al. A simple analytical method for evaluation of flexible rockfall barrier part 1: working mechanism and analytical solution [J]. *Advanced Steel Construction*, 2018, Vol. 14, No. , pp. 115-141.
- [13] Yu Z.X., Qiao Y.K., Zhao L., et.al. A simple analytical method for evaluation of flexible rockfall barrier part 2: application and full-scale test [J]. *Advanced Steel Construction*, 2018, Vol. 14, No. , pp. 142-165.
- [14] Xu H., Gentilini G., Yu Z.X., et.al. An energy allocation based design approach for flexible rockfall protection barriers[J]. *Engineering Structures*. 2018, Vol. 173, pp. 831-852.
- [15] Grassl, H., Bartelt, P., Ammann, W.J. and Roth, A., “Behavior, Design and Reliability of Highly Flexible Rockfall Protection Systems for Highways”, *Proc. 53rd Highway Geology Symposium*, California, 2002.
- [16] Nicot, F., Cambou B. and Mazzoleni G., “Design of Rockfall Restraining Nets from a Discrete Element Modelling”, *Rock Mechanics and Rock Engineering*, 2001, Vol. 34, No. 2, pp. 99-118.
- [17] Gentilini, C., Ubertini, F., Govoni, L., Gottardi, G. and Miranda, S.D., “Modelling of Falling Rock Protection Barriers”, *International Journal of Physical Modelling in Geotechnics*, 2011, Vol. 11, No. 4, pp. 126-137.
- [18] Gentilini, C., Gottardi, G., Govoni, L., Mentani, A. and Ubertini, F., “Design of Falling Rock Protection Barriers using Numerical Models”, *Engineering Structures*, 2013, Vol. 50, No. 3, pp. 96-106.
- [19] Escallón, J.P., Wendeler, C., Chatzi, E. and Bartelt, P., “Parameter Identification of Rockfall Protection Barrier Components through an Inverse Formulation”, *Engineering Structures*, 2014, Vol. 77, pp. 1-16.
- [20] TB/T 3089—2004, “The Flexible Safety Net for Protection of Slope along the Line”, China Railway Publishing House, Beijing, 2004. (in Chinese)

AXIAL RESIDUAL CAPACITY OF CIRCULAR CONCRETE-FILLED STEEL TUBE STUB COLUMNS CONSIDERING LOCAL BUCKLING

C. Yang ¹, Z.X. Yu ^{1,2,3,*}, Y.P. Sun ^{1,3,4}, L. Zhao ⁵ and H. Zhao ⁶

¹ School of Civil Engineering, Southwest Jiaotong University, Chengdu, China

² National Engineering Laboratory for prevention and control of geological disasters in land transportation, Chengdu, China

³ China-Japan Resilient and Sustainable Concrete Structure Research Center, Chengdu, China

⁴ Department of Architecture, Graduate School of Engineering, Kobe University, Kobe, Japan

⁵ Department of Civil and Environmental Engineering, The Hong Kong Polytechnic University, Hong Kong, China

⁶ State Key Laboratory of Geohazard Prevention and Geoenvironment Protection, Chengdu University of Technology, Chengdu, China

*(Corresponding author: E-mail: yzxzrq@swjtu.edu.cn)

Received: 19 June 2017; Revised: 2 September 2017; Accepted: 17 November 2017

ABSTRACT: This paper proposes a superposition method considering local buckling to estimate the residual capacity of circular concrete-filled steel tube stub columns (CFSTs) under axial compression based on substantial experimental data, consisting of 3 recently conducted tests as well as 150 test results from available literature. The proposed approach accounts for the influence of local buckling of the steel tube on confining effect, by introducing a coefficient to reduce the compressive strength of concrete in the post-buckling stage. Three specimens, including a bare steel stub column with circular hollow section (CHS), a CHS with concrete restraint and a CFSTs, were tested to investigate the contribution of concrete on the local buckling. Further, the mechanical model of steel tube was established and the design equations for residual bearing capacity of the tube were derived. The nominal load-shortening curves of the concrete core are extracted from 150 collected experimental curves of the CFSTs, with different parameters such as diameter-to-thickness (D/t) ratio, yield strength f_{sy} and concrete strength f_{cp} . The variation of the stiffness degradation in the curves indicates that the effect of local buckling on both ductility and residual compressive strength of the concrete core are correlated with the section type of the steel tube. The residual compressive strength decreases exponentially with the increase of the generalized outer diameter-to-thickness ratio.

Keywords: CFST, stub column, circular section, axial residual capacity, superposition method, local buckling

DOI: 10.18057/IJASC.2018.14.3.11

1. INTRODUCTION

With the increasing of natural disasters occurred during the past decades [1-3], the study on the analysis and design of engineering structures not only focus on the normal structural service condition, but also on the ultimate capacity [4-7] and the post-buckling stages to improve the anti-collapse performance of structures and members, especially the load-bearing columns [8-10].

In view of the outstanding compressive resistance and ductility, CFSTs have been widely used as load-bearing columns in high-rise buildings. Generally, a portion of compressive load will be borne by the steel tube, which results in the reduction of confining effect and induces local buckling. Consequently, the ductility and composite effects of CFSTs will be significantly influenced, which finally affect the residual bearing capacity of the CFSTs.

For the ultimate bearing capacity, the CFSTs is generally considered as a unified element or a composite element, corresponding to unified method and superposition method, respectively.

However, in the post-buckling stage, the entire cross-section of the CFST no longer satisfies the plane section assumption, and many mechanical behaviours, such as passive confinement and local buckling, would be significant in the process of the interaction, which means that the working mechanism of the CFST depends on the cooperativity of the steel tube and concrete rather than consistency. Therefore, it is better to regard the CFST as a composite element.

Besides, the composite response of CFSTs in compression is complicated due to the local buckling of the steel tube. On one side, the residual strength and deformation of the steel tubes are strongly related to the buckling strain [11], but the local buckling mode will be influenced by the concrete restraint. On the other side, because the Poisson's ratio of steel tube is higher than that of concrete in elastic range, compared with the steel tube confined concrete stub column (STCCs), the compressive stress in the steel tube of the CFST leads to the development of the confining stress in a lagging manner throughout the load history. For thin-walled CFSTs and the CFSTs with high strength concrete, the passive confinement often appears after the local buckling of steel tubes [12-14]. Many researches showed that the CFST with high strength concrete exhibits a steep degradation of stiffness in the early post-buckling stage [14-16], which means that the confinement from the steel tube cannot continue to effectively keep a well compressive strength of the concrete core. In summary, the mechanical model of the confined concrete of STCCs is not suitable for the concrete core of CFST.

The composite element theory has been adopted by Eurocode 4 and many researchers [18, 36] to estimate the confining effect before buckling of steel tube. The theory estimates the axial capacity of CFST column by combining the axial capacities of steel tube and concrete. However, most of the studies do not pay attention to the residual capacity of CFST column in the post-buckling stage, but it is valuable in the study of structural anti-collapse design. Compared with long column, the confining effect of short column before the buckling of steel tube can be neglected, when buckling occurs, the lateral deformation of steel tube will strengthen the confining effect, the residual capacity of CFST short column will be enhanced significantly, and the compressive capacity of the steel tube will decrease due to the buckling effect. Therefore, the confining effect and the degeneration of the axial capacity of the steel tube affect the residual capacity of CFST short column, which leads to the result that estimation of the residual capacity becomes very complicated, and it is necessary to take into account the influence of the non-linear factors when using the superposition method.

The CFSTs studied in this paper requires the entire cross section loaded, but only relying on the concentric compressive tests of CFST, the mechanical curves of the concrete core and the steel tube are difficult to measure respectively, and the effect of lateral restraint on local buckling of the steel tube is also not easy to clarify. Therefore, the paper carried out three axially compressive experimental tests of short columns, including a bare CHS, a CHS with concrete restraint, and a CFST, with the similar material parameters and the same size. The mechanical model of the steel tube was proposed based on the analysis of the measured data.

Furthermore, based on 150 experimental load-shortening curves from the previous CFST tests, the unified various ductile characteristics of the concrete cores in CFSTs were clearly exhibited with the consideration of the local buckling of steel tube. The work can predict the residual bearing capacity of CFSTs in a simple way.

Based on the above analysis, the calculation expressions of axial residual capacity of CFSTs considering local buckling were derived by superposition method, using a coefficient to reduce the compressive strength of concrete in the post-buckling stage.

2. MECHANICAL MODEL OF STEEL TUBE

The mechanical behaviour of the steel tube in CFST is affected by the concrete core, the influence of which is mainly reflected in the local buckling. Experimental researches on the thin-walled CFSTs have shown that the pattern of local buckling of the steel tubes is an outwards buckle instead of wrinkled buckle [17-18]. O'Shea and Bridge [14] pointed out that the local buckling affects the strength of the steel tube in CFSTs. Some Japanese researchers [18] considered the axial stress-strain relationship of the steel tube in CFST as an elastic-perfectly plastic model as shown in Figure 1. Obviously, the model ignores the local buckling, which causes the decrease in axial bearing capacity of the steel tube. Wang and Zhang [19] proposed a steel tube model including a descending portion depending on the steel ratio, yield strength of the steel tube and unconfined compressive strength of the concrete core. However, their model only focuses on the yielding of the steel tube. Overall, the effective contribution of the concrete core on the mechanical model of the steel tube in CFST is still a difficult problem.

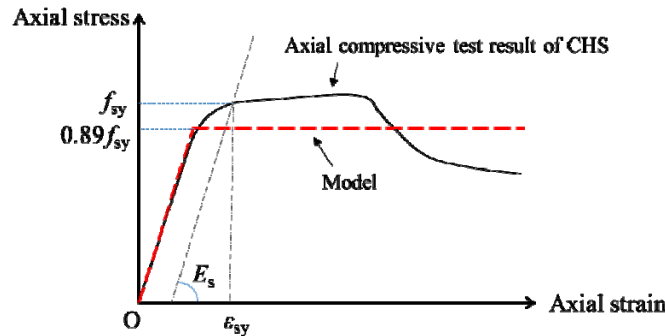


Figure 1. Axial Stress-strain Model of the Steel Tube in CFST

O'Shea and Bridge [20] conducted a series of experimental studies on CHS stub columns, with D/t ratio ranging from 55 to 220. These studies included axially compressive tests of CHSs with and without internal restraint.

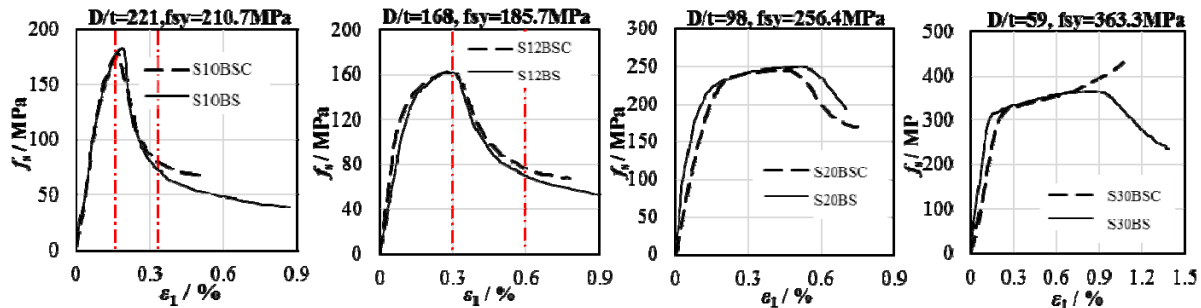


Figure 2. Results of CHSs with and without Internal Restraint under Axial Compression

All the complete experimental curves of the CHSs, as shown in Figure 2, exhibit a similar process in the ascending portion, regardless of whether concrete filled the tubes or not. Moreover, except the column labelled S30BSC exhibiting strain hardening in the post-ultimate stage because the filled concrete was touched by the loading platen as stated in the original, the developments of degradation stiffness in the other comparative curves are nearly in perfect agreement within the range of twice ϵ_{sm} . The stiffness appears to be improved for strain beyond $2\epsilon_{sm}$, probably because the concrete shares some axial load gradually, as in the case of the last column.

Johansson and Gylltoft [17] carried out a set of axially compressive tests of a CHS without any restraint and a thick-walled CFST loading the steel tube firstly. According to the comparison of the experimental results between the two types of the columns as shown in Figure 3, a little difference of the structural compressive stress-strain relationships was also exhibited prior to the compression of the concrete in CFST.

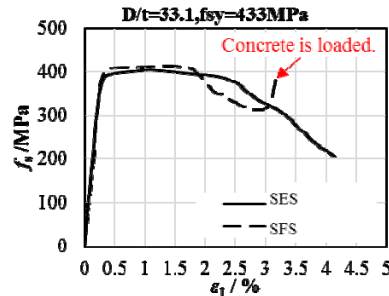


Figure 3. Results of a CHS and a CFST Test under Axial Compression from Reference [17]

The experimental curves using the solid lines in Figure 2 and Figure 3 are from the bare CHSs. According to the experimental results of the above comparative tests, one interesting conclusion can be drawn: the concrete filled in the CHS has little effect on the local buckling strength and deformation for the CHSs under axial compression. However, it is still a problem that the effect of concrete dilatation on the steel tube in CFSTs when considering the concrete to withstand the axial load. Therefore, the paper designed three experimental specimens to study the restraint effect from the concrete core to the steel tube of CFSTs.

2.1 Setup and Results of the Tests

Three short specimens were tested under concentric axial loading. As shown in Figure 4, the first column was a bare CHS labelled CHS-125; the second was a CHS partially filled in concrete labelled CHS-125-C; and the third was a CFST labelled CFT-125-C30. To obtain a reliable load-axial shortening curve in the post-buckling stage, about 100 mm in the specimen CHS-125-C was left unfilled. The axial displacements of the specimens were recorded by the linear variable differential transducers (LVDTs) in four directions. To study the interaction between the core and the steel tube, nine vertical and nine horizontal electrical strain gauges, arranged 120° apart, were attached at three heights of each specimen. All the tests were carried out with a 10 MN electro-hydraulic servo pressure testing machine.

The outer diameter (D) and thickness (t) of the steel tubes for all the specimens were 376 mm and 3.04 mm respectively, and the length (L) was 3.0 times of D . The yield strength of the steel tubes was 305.3 MPa. The unconfined compressive strength of the concrete core in the CFST was about 39.6 MPa.

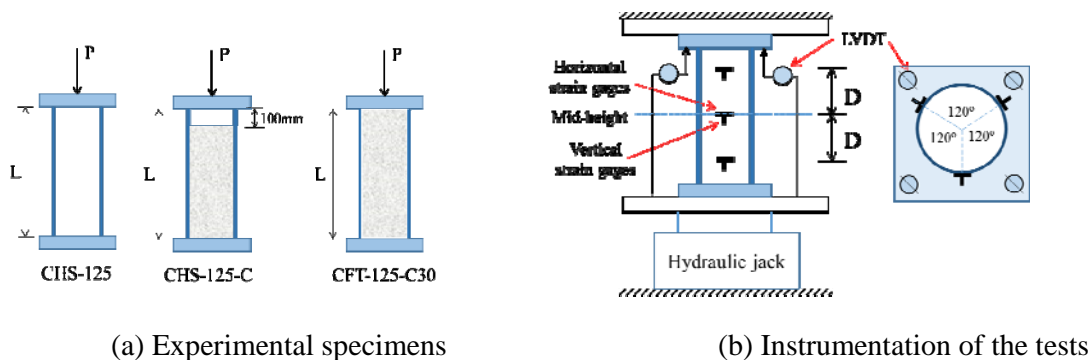


Figure 4. Design of the Tests

The structural behaviours of the three specimens are represented in Figure 5. When the load reaches a peak, the wrinkled buckles of CHS-125 distributed at a distance of one diameter from the middle height. CHS-125-C occurred an outwards buckle in the unfilled region at the shortening strain of 0.0018, and then the peak load arrived when the shortening strain was 0.0022. At the 0.002 of the shortening strain when the specimen was still in the elastic stage, an outwards buckle appeared near the upper end of the CFT-125-C30, and the peak load of the CFST was at the shortening strain of 0.0063. The load-axial shortening responses between the CHS-125 and CHS-125-C are similar as the experimental curves shown in Figure 5.

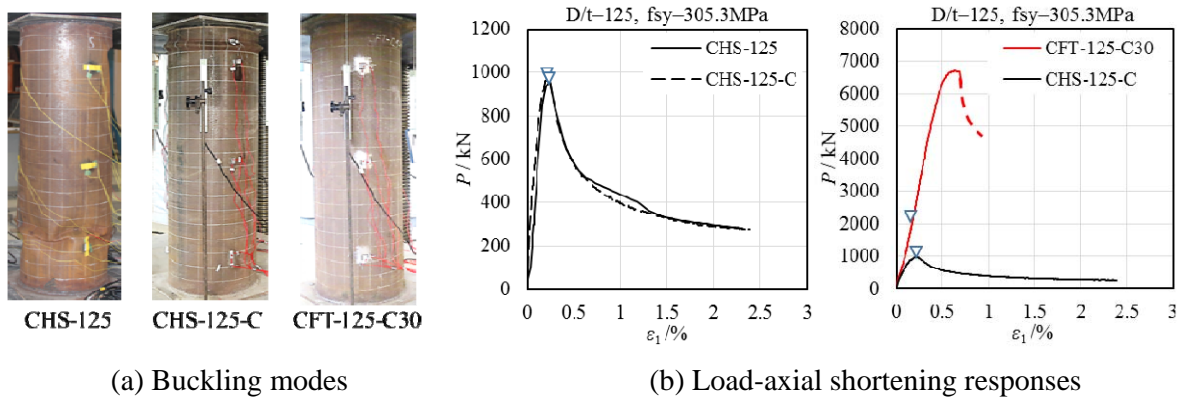


Figure 5. Structural Behaviours of the Three Specimens

Based on the information from the strain gauges, the development of the material properties of the three specimens are drawn in Figure 6 and Figure 7. Figure 6 shows the horizontal and vertical strain in mid-height for the two CHSs and the CFST. Both of the principal strains have a similar development before the tube buckle. Comparing the descending portion between the CHS-125 and the CHS-125-C, the unloading behaviour caused by the local buckling in CHS-125-C has not been significantly displayed, since the vertical strain of the CHS-125-C shows a gentle decline. Because the concrete filled in the CHS-125-C is not loaded, the only reason to explain the phenomenon is that the bond between the concrete and the inner wall of the steel tube preventing the stress unloading.

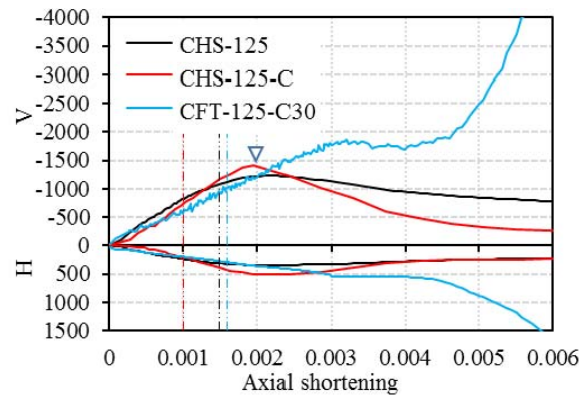


Figure 6. Principal Strains of the Three Specimens at Mid-height

However, for the CFT-125-C30, the principal strains for the steel tube exhibit a steep increase in the non-local buckling region after the axial shortening strain reaches 0.004. Based on Figure 7, the farther away from the buckling, the more obvious the rapid development trend of the principal strains became. The above phenomenon clear implied that the dilatation of the concrete core leads to the growth of the horizontal strain for the steel tube, which was accompanied by a further compression in the vertical direction. On the other side, the analysis of the measured results showed

that the steel tube of CFT-125-C30 yielded before the local buckling. As shown in Figure 7, the three dotted lines represent the different starting position of the steel yield at corresponding heights of the specimen.

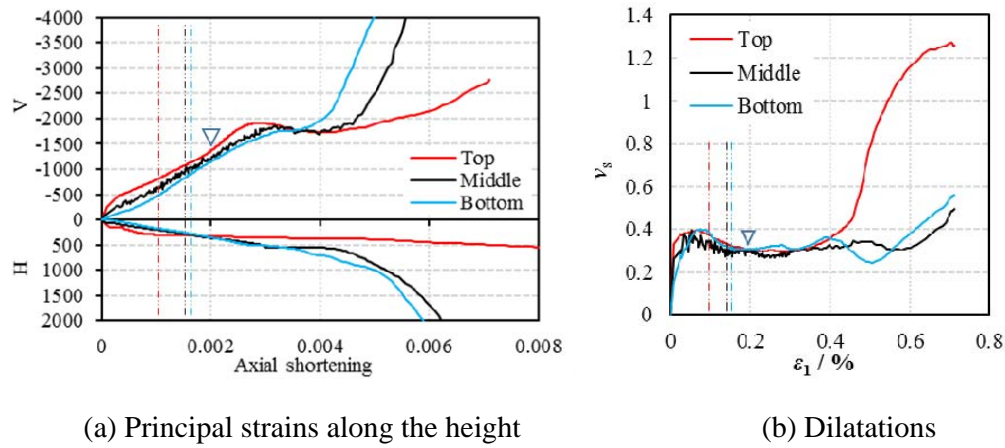


Figure 7. Development of Material Properties of the Steel Tube in CFT-125-C30

In summary, the interaction between the steel tube and the concrete core in CFT-125-C30 determines the development of the steel strength, and the passive confinement from the steel tube to the concrete core has displayed since the local buckling.

2.2 Compressive Stress-Strain Relationship

Based on the above experimental results, Table 1 lists the peak stress f_{sm} of the steel tubes and the corresponding the peak stress ε_{sm} , except that the ε_{sm} of CFT-125-C30 corresponds to the buckling. All the deviations of f_{sm} between the CHSs with and without the internal restraint are very small, and have no regularity with the D/t ratio increasing. The most of deviation of ε_{sm} for the CHSs and CFSTs are within 20%, and the scattering results from the instability of plastic flow of the material as the steel yields.

Table 1. The Peak Stress and Peak Strain of the Steel Tubes

Group	Name	D/t	$f_{sm}(\text{MPa})$	$\varepsilon_{sm}(\%)$	Deviation ratio of f_{sm}	Deviation ratio of ε_{sm}
1	SES	33.1	404.5	1.08		
	SFS	33.1	414.0	1.48	2.35%	37.04%
2	B30BS	58.5	371.4	0.85		
	B30BSC	58.5	363.5	0.69	-2.13%	-18.82%
3	S20BS	98	248.1	0.52		
	S20BSC	98	244.8	0.42	-1.33%	-19.23%
4	CHS-125	114.6	249.7	0.24		
	CHS-125-C	114.6	253.6	0.22	1.56%	-8.33%
	CFT-125-C30	114.6		0.20*		-16.7%
5	S12BS	168	162.7	0.29		
	S12BSC	168	163.0	0.29	0.18%	0.00%
6	S10BS	220.9	181.8	0.19		
	S10BSC	220.9	178.0	0.17	-2.09%	-10.53%

Note: The value with * represents the local buckling stress of the steel tube in CFT-125-C30.

From the above analysis process of the principal strains of the steel tubes, the compressive stress-axial strain relationship of the CHSs with or without the internal restraint is not affected by the buckling modes. Depended on the dilatation of the steel tube, the concrete core of the CFST promotes the utilization of the material strength in the stress distribution of the cross-section, which implies that the interaction between the steel tube and the concrete core mainly affect the passive confinement in the post-buckling stage rather than the axial stress of the steel tube.

In summary, the paper uses the complete compressive stress-strain relationship of the CHSs to analysis the mechanical behaviour of the steel tube in CFSTs.

Yang [11] proposed a single parameter model of a complete compressive stress-strain curve for CHSs, given by Eq. 1, and introduced a simple calculation method to obtain the continuous strength f_{sm} of CHS in compression, given by Eq. 2, which has the same acceptable accuracy and a wide application range as the result from Eq. 1. Both of these equations are based on regression analysis of 48 available experimental data on columns.

$$f_s = \begin{cases} E_s \varepsilon_s \left(Q + \frac{1-Q}{\left(1 + |\varepsilon_s / \varepsilon_{ch}|^6\right)^{1/6}} \right) & \varepsilon_s \leq \varepsilon_{sm} \\ \frac{A}{\varepsilon_s + B} & \varepsilon_s > \varepsilon_{sm} \end{cases} \quad (1a)$$

$$\varepsilon_{sm} = \frac{f_{sy}}{E_s} \cdot \frac{0.25}{\alpha^{1.3}} \quad (1b)$$

$$Q = 0.03(\varepsilon_{sm} \%)^{-0.63} \quad (1c)$$

$$\varepsilon_{ch} = \frac{Sf_{sy} - QE_s \varepsilon_{cm}}{(1-Q)E_s} \quad (1d)$$

$$f_{sm} = S \cdot f_{sy} = \frac{1}{0.82 + 1.22\alpha} \cdot f_{sy} \quad (2)$$

$$\alpha = \frac{D}{t} \frac{f_{sy}}{E_s} \quad (3)$$

In the above equations, α is the generalized outer diameter-to-thickness ratio. Q and ε_{sh} represent the second stiffness and the characteristic strain in the ascending portion. A and B governing the descending portion can be solved from a system of linear equations after the determination of the peak coordinates (ε_{sm}, f_{sm}) and the residual stress $f_{s,res}$.

The residual stress $f_{s,res}$ of CHSs is highly correlated with the peak stress ε_{sm} , as described below, corresponding to the axial residual strain ε_{res} of 0.04, where the decline of steel tubes in the compressive stress becomes sufficiently gentle, based on the available experimental data, as mentioned in reference [11].

$$f_{s,res} = R \cdot f_{sy} = (0.12 + 0.23\varepsilon_{sm} \%) \cdot f_{sy} \leq f_{sy} \quad (4)$$

Note that ε_{sm} in the civil engineering structures is usually not less than 0.2%, except for certain non-compact sections with large D/t ratio well exceeding the specified upper limit corresponding to local buckling. This information indicates that the concrete core in CFSTs should receive certain confinement before severe damage occurs.

2.3 Principal Stresses

Based on the research of the experimental tests, the steel tube of the CFT-125-C30 yielded prior to the local buckling. The result was also verified by many available tests including [12-14, 21]. It is useful to confirm the plane stress state of the steel tube in CFSTs, and to study the interaction between steel tubes and concrete cores in the post-buckling stage.

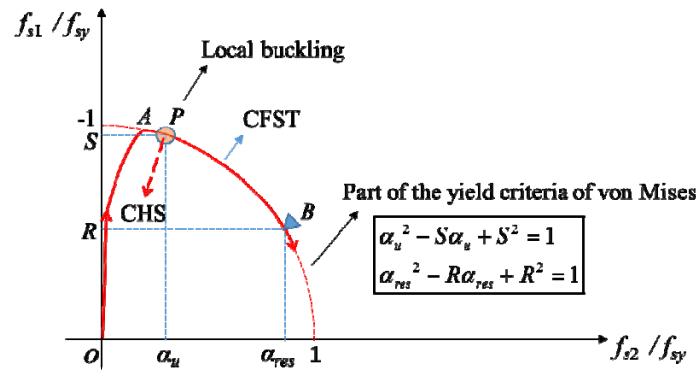


Figure 8. Development of the Plane Stress State of the Steel Tube

The process of principal stresses for steel tubes of CFSTs is shown in Figure 8. Due to the concrete dilatation, the principal stresses for the overall CFST can be further developed after local buckling of the steel tube. The plane stress state is assumed to obey the yield criteria of von Mises.

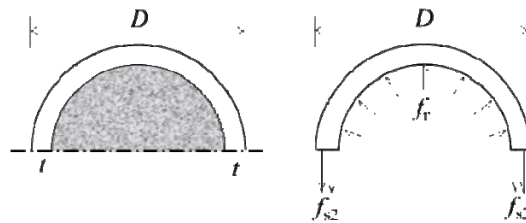


Figure 9. Equilibrium Relationship between the Horizontal Stress f_{s2} and the Confining Stress f_r

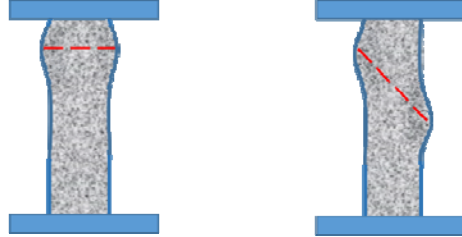
Finally, the confining stress f_r of the steel tube can be obtained based on the equilibrium relationship in the cross-section, as shown in Figure 9, and the function is:

$$f_r = \frac{2t}{D-2t} f_{s2} \quad (5)$$

Relying on the mechanical model in the vertical direction, the load-axial shortening curve for the concrete core should be extracted from the experimental structural curve of the CFST. And the compressive strength of the concrete core in the post-buckling stage can be obtained based on the confining stress f_r , which is used to research the residual bearing capacity of the CFSTs.

3. ANALYTICAL INVESTIGATION OF CONCRETE

Brittle-ductile transition behaviour of the concrete core in CFSTs depends on both the D/t ratio of steel tube and f_{cp} . In general, the CFSTs have two typical failure modes [22], as shown in Figure 10. To investigate the reliable compressive capacity of the concrete core of the CFST in the post-buckling, the confining effect is systematically studied depending on the key influencing factors, such as the section type of the steel tube and the concrete strength f_c as well as the local buckling.



(a) Splitting failure

(b) Shear and sliding failure

Figure 10. Two Typical Failure Modes of CFSTs under Compression

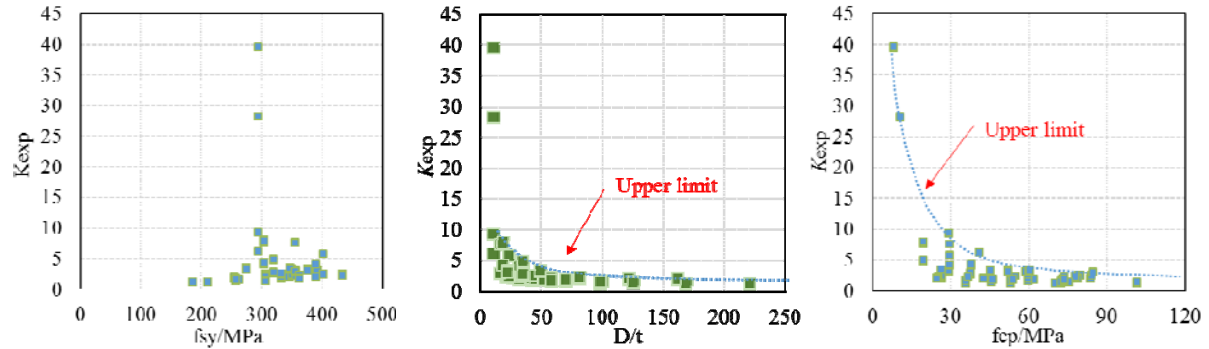
3.1 Influencing Factors of Confinement without Considering the Local Buckling

It is meaningful to determine the confinement effect by studying the influence of the potential factors. To avoid the influence of local buckling in CFSTs, the steel tube confined concrete columns (STCCs) are selected as research objects. To this, 85 experimental data sets of STCCs in compression were collected from the references [17, 21, 23-30], with a wide range of structural factors: D/t ratio ranges from 10.1 to 220.9, f_{sy} ranges from 185.7 to 433 MPa, and f_{cp} ranges from 8.0 to 101.5 MPa. The key data of several typical STCCs are shown in Table 2, where f_{cp} is the compressive strength of the same size concrete cylinders without confinement.

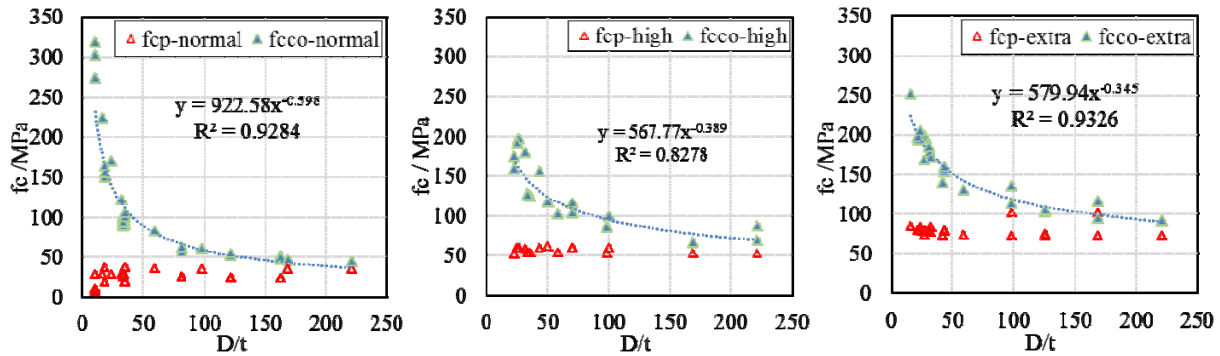
Table 2. Dimensions and Properties of STCCs in the Tests from Literature

$D(\text{mm})$	D/t	f_{sy} (MPa)	f_{cp} (MPa)	$N_{u,\text{exp}}$ (kN)	$f_{cc0,\text{exp}}$ (MPa)	K_{exp}	Ref.
159	33.1	433	54.6	2220	126.7	2.32	[17]
166	33.2	274.6	29.1	1888	98.8	3.39	[21]
121	10.1	294.2	41.0	1873	253.6	6.18	
121	10.1	294.2	8.0	2354	318.7	39.64	
150	50.0	254	61.8	1910	117.3	1.9	[23]
210	70.0	254	59.7	3390	103.8	1.74	
200	100.0	263	59.9	3000	99.5	1.66	
133.3	26.6	351	73.5	2004	167.9	2.28	[24]
158.9	31.0	356.3	59.0	3108	179.2	3.04	[25]
152.4	48.8	347	45.2	2456	146.5	3.24	[26]
159	31.8	390	29.3	2120	121.6	4.15	[27]
101.8	34.6	319.5	37.6	724.2	100.3	2.67	[28]
101.8	17.9	304.8	19.4	961.4	149.9	7.71	
190	220.9	210.7	35.9	1240	44.6	1.24	[29]
165	58.5	363.3	46.1	1759	88.2	1.91	
190	220.9	210.7	70.1	2433	87.4	1.25	
190	168.1	185.7	53.0	1862	67.3	1.27	
190	125.0	306.1	75.3	2870	104.6	1.39	
114.3	22.0	376.3	52.2	1483	175.0	3.35	[30]

In Table 2, the strength enhancement factor K_{exp} is the ratio of $f_{cc0,exp}$ to f_{cp} , where $f_{cc0,exp}$ is the ultimate compressive strength of the confined concrete defined as the ratio of the measured peak load $N_{u,exp}$ to initial pressure area of concrete A_c . Undoubtedly, the value of K_{exp} reflects the highest level of confinement provided by the steel tube to the concrete. Figure 11a shows the relationships of K_{exp} and three primary experimental variables of STCCs. Although f_{sy} is observed to be almost irrelevant to K_{exp} , the confinement from the steel tube diminishes with the increasing of the D/t ratio, the upper limit of K_{exp} decreases with the increasing of D/t ratio in a power function when the D/t ratio is more than 20, as shown in the second panel of Figure 11a. A similar analysis result in regard to f_{cp} is also reflected in the third panel of Figure 11a.



(a) Relationships between K_{exp} and the Primary Experimental Variables of STCCs



(b) Influence of D/t ratio to f_c

Figure 11. Influence of the Primary Variables for Confinement

Figure 11b reveals the more specific influence relationships among D/t ratios and different strength ranges of f_{cp} . The relationship between D/t ratio and $f_{cc0,exp}$ exhibits a clear power function with a high correlation coefficient, which is better than the D/t ratio and K_{exp} . Two conclusions can be obtained from Figure 11b that the enhancement of concrete strength in STCCs is (1) obvious for the specimens unless the D/t ratio is greater than 100 and (2) becoming worse with the increasing of f_{cp} .

3.2 Influence of Local Buckling on the Confining Effect

To gain a unified various ductile characteristics of the concrete core with different failure modes, 150 experimental load-shortening curves from the previous tests of the CFSTs are collected, as shown in Table 3. Based on the complete compressive mechanical model of the steel tube, the nominal load-axial shortening curves of the concrete core should be extracted from the experimental curves of the CFSTs, which have considered the effect of the local buckling.

Table 3. Summary of the available Test Specimens for CFSTs

D (mm)	D/t	α	f_{sy} (MPa)	f_{cp} (MPa)	Ref.
108~133	18.1~125	0.038~0.799	232~429	83.4~97.2	[13]
108~450	15.2~220.9	0.061~0.202	283~834	21.8~88	[18]
152~273	15.2~36.9	0.0445~0.0523	274.6~377	9.7~75.1	[21]
152.4	48.8	0.0897	347	55.1	[26]
114~115	22.9~30.5	0.0408~0.0511	343~365	26.4~98.4	[31]
114.3	34.1	0.0476	287.3	32.5~104.9	[32]
152.4	92.4	0.1216	270	73	[33]
120~180	79.5~120.8	0.0666~0.1911	222.7	18.3~36.4	[34]
114.3	19.4~41.7	0.0335~0.0478	235~355	56.2~107.2	[35]
114~167	20.4~53.9	0.0305~0.0808	300	45.6~62.4	[36]
112.6	19.5~38.9	0.0286~0.0684	360	21.4~29.7	[37]
100~250	25.4~133.7	0.0449~0.098	282~482.5	47.2~80.2	[15,38,39]
153~203	51~67.7	0.0792~0.1051	318.3~380	29.8~63.3	[40]
149~219	19.9~165	0.0425~0.1492	338~438	32.9~74	[16,41]
110	36.7	0.0712	398	44.8~52	[42]
133~168	24.5~50.4	0.0439~0.0871	325.3~392.0	34.3~71.6	[43]
182~309	63.5~94	0.0445~0.0523	312.8~362.5	46.8~50.5	[44]
100~450	15.2~220.9	0.0304~0.202	185.7~834	9.7~107.2	Range

Because the initial mechanical parameters of the steel tube were comprehensively considered by α . According to the classification provided in EC3 [45] and AISC [46], the cross-section types of the steel tube are divided into six parts based on the α , as shown in Figure 12. Depending on α and f_{cp} , the unified various ductile characteristics of the concrete core in the post-buckling stage are shown in Table 4.

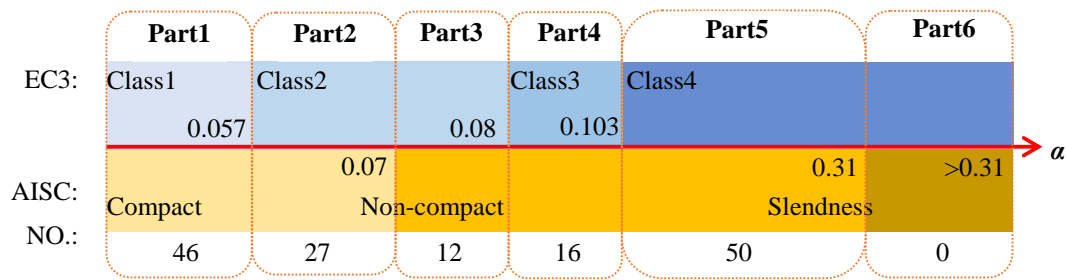


Figure 12. Classification and Limiting Value for the Steel Tubes

In Table 4, ductility and failure types of various CFST sections with increasing f_{cp} are shown in different colours. The label “A” represents splitting failure of the concrete core, and the label “B” represents shear and sliding failure. The lightest background colour reflects an unlimited growth trend of the strength of the concrete core. The middle colour shows a considerable compressive strength for the concrete core but with obvious damages. The deepest colour means the serious damages of concrete core, the confining effect on which is weak, and the residual capacity of CFSTs is not available.

Table 4. Ductility and Failure Modes of the Concrete Core of CFSTs in the Post-buckling Stage

α	f_{cp}	$\leq 30\text{MPa}$	30~40MPa	40~50MPa	50~60MPa	>60MPa
Part 1: Class1&Compact		A	B	B	B	B
Part 2: Class2&Compact		A	B	B	B	B
Part 3: Class2&Non-Compact		A	B	B	B	B
Part 4: Class3&Non-Compact		B	B	B	B	B
Part 5: Class4&Non-Compact		B	B	B	B	B

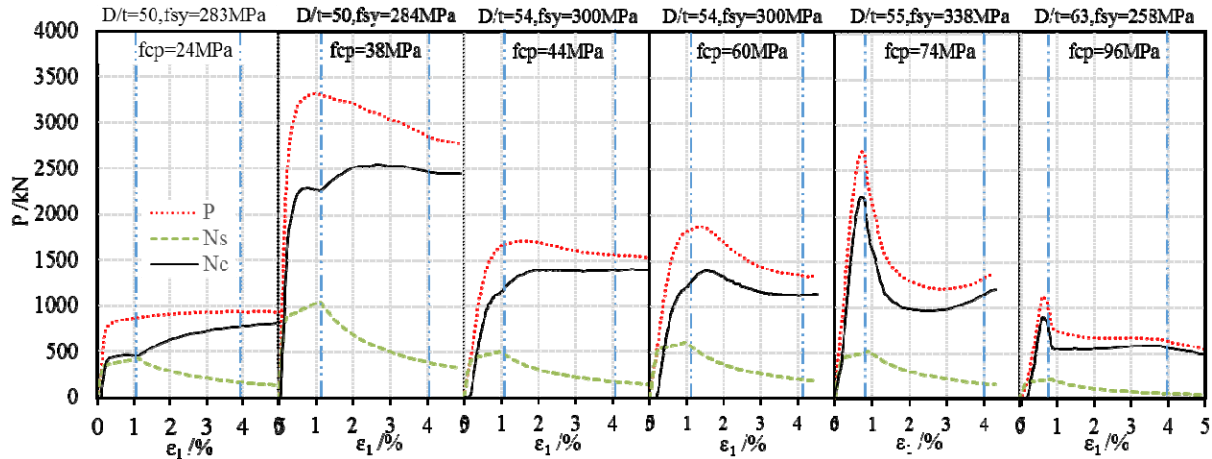


Figure 13. Nominal Performance Curves of the Concrete Core

To provide a clearer variation trend of the concrete ductility, Figure 13 lists a series of nominal performance curves of the concrete core filled in the steel tubes with similar mechanical parameters in black. In Figure 13, the experimental curves of load P and overall axial shortening strain ε_1 are shown in red. The bearing capacity N_s in the green curves are calculated by the following Eq. 9, in which the f_{s1} is based on Eq. 1 to Eq. 3. And the nominal bearing capacity of concrete N_c is the remaining strength by subtracting the N_s from the axial load P .

$$N_s = A_s f_{s1} \quad (9)$$

where A_s is the initial area of the steel tube in CFSTs, f_{s1} is the compressive stress of the steel tube.

In summary, the effect of local buckling on the development of concrete compressive strength in the post-buckling stage is clearly reflected. Because of the differences in the dilatation of different strength concrete, a further improvement of the concrete strength is exhibited due to the local buckling if the steel tube is filled in medium and low strength. The improved effect becomes weaker with the increasing unconfined strength of the concrete core.

4. RESIDUAL BEARING CAPACITY OF CFST

4.1 Superposition Method

Based on the study on confining effect, when the axial shortening strain reaches 0.04, the confining stress would be stable, which means that the axial bearing capabilities of the steel tube and the

concrete core are stable as well. Therefore, the residual bearing capacity N_{res} of the CFSTs can be estimated by the superposition of the two axial bearing capabilities. The paper determines N_{res} by the superposition method, and the equation is:

$$N_{res} = N_{s,res} + N_{c,res} = A_s f_{s,res} + \eta A_c f_{cc,res} \quad (10)$$

Where $f_{cc,res}$ represents the confined compressive strength of the concrete core by steel tube. The simplified equation is proposed as follows.

$$f_{cc,res} = K_{cal} \cdot f_{cp} = f_{cp} + 4.1 f_{r,res} \quad (11)$$

Where $f_{r,res}$ is the confining stress when of the axial shortening stain is 0.04. Based on the Eq. 5 and von Mises yield criterion shown in Figure 8, $f_{r,res}$ is calculated as follows.

$$f_{r,res} = \frac{2t}{D-2t} \alpha_{res} f_{sy} \quad (12a)$$

$$\alpha_{res}^2 - R \alpha_{res} + R^2 = 1 \quad (12b)$$

The Eq. 11 is based on the work proposed by Richart [47], which is used to calculate the ultimate compressive strength of the confined concrete. Due to the inevitable damage of the concrete core for most of the CFSTs in the post-buckling stage, a strength reduction factor η is introduced in the superposition method. Based on the nominal $N_{c,res}$ collected from the nominal concrete performance curves of the available CFST tests as shown in Table 3. The nominal η can be calculated by $N_{c,res}/(A_c f_{cc,res})$.

According to the Table 4 and the Figure 11, considering the high correlation between the ductility and the compressive strength of the concrete core, the influencing factor α is the best parameter to obtain a reasonable η . As the Figure 14 shows, a power function relation exists between the upper limit of η and α , as shown in Eq. 13.

$$\eta = 0.25 \alpha^{-0.5} \quad (13)$$

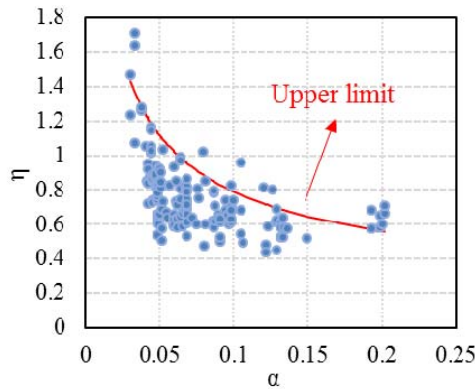


Figure 14. Relationship between η and α

4.2 Verification of the Proposed Method

According to the various ductile behaviours of the concrete core shown in Table 4, when the concrete strength f_{cp} does not exceed 40 MPa, the residual capacity of the CFST is outstanding due to the superior ductility. When f_{cp} exceeds 40 MPa, the residual capacity reduces rapidly with the decreasing of α . This paper discusses the accuracy of the residual capacity of the CFSTs with the best ductility, as shown in Figure 15. The post-buckling behavior of the concrete core in the CFSTs studied in Figure 15 corresponds to the lightest background in Table 4.

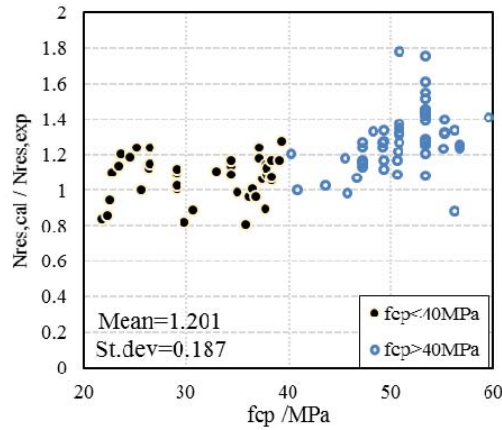


Figure 15. Comparisons between the Calculated and Measured Residual Capacity of CFSTs with the Best Strength Enhancement of the Concrete Core

Generally, the deviation of the ratio of $N_{res,cal}$ to $N_{res,exp}$ mainly concentrated in the range of 0.8 to 1.4. The average value is 1.201 and the standard deviation is 0.187. The estimate is more accurate and stable when f_{cp} does not exceed 40 MPa, which is consistent with the ductile characteristics of the CFSTs.

Figure 16 shows all the ratios of $N_{res,cal}$ to $N_{res,exp}$ considering the influencing factors of α and f_{cp} . Obviously and also not surprising, the deviation of $N_{res,cal}$ to $N_{res,exp}$ is also most accurate and stable when f_{cp} does not exceed 40 MPa. On the other side, for the CFST with poor ductility, a scattering of $N_{res,cal} / N_{res,exp}$ is observed. The main reasons of the scattering are from the value of η and measured residual capability $N_{res,exp}$, maybe because some of the collected CFSTs were tested by load control, which greatly affects the accuracy in the post-ultimate stage.

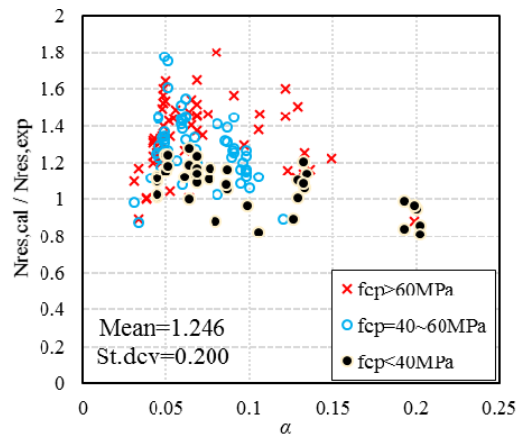


Figure 16. Comparisons between the Calculated and Measured Values of the Residual Capacity for all selected CFSTs

5. CONCLUSIONS

In this paper, the post-buckling behaviour of CFSTs was studied in detail, and the residual capacity of CFSTs was predicted by a superposition method considering the local buckling of steel tube. In summary, the following conclusions can be drawn:

(1) Comparing to the experimental test results, the superposition method can well predict the residual capacity of the CFSTs with normal strength concrete and the thick-walled CFSTs with high strength concrete. However, the accuracy is relative low for the thin-walled CFSTs with high strength concrete.

(2) The local buckling of the steel tube may influence the compressive strength of the concrete core in the post-buckling stage. A further improvement of the concrete strength is exhibited due to the local buckling if the steel tube is filled in medium and low strength concrete. The benefit effect becomes weaker with the increasing of the strength of the concrete core. The effect of the concrete core on the steel tube is the local buckling mode, and the mechanical behaviours of steel tubes in CFSTs under axial compression are similar to that of CHSs.

ACKNOWLEDGMENT

The authors are grateful for the financial support by the National Key Research and Development Program of China (Grant No. 2016YFC0802205), the National Natural Science Foundation of China (Grant No. 51678504) and Department of Science and Technology of Sichuan Province (Grant No. 2018JY0029).

REFERENCES

- [1] Yu, Z.X., Qiao, Y.K., Zhao, L., Xu, H., Zhao S.C. and Liu, Y.P., "A Simple Analytical Method for Evaluation of Flexible Rockfall Barrier Part 1: Working Mechanism and Analytical Solution", *Advanced Steel Construction*, 2018, Vol. 14, pp. 115-141.
- [2] Xu, H., Gentilini, C., Yu, Z.X., Qi, X. and Zhao, S.C., "An Energy Allocation Based Design Approach for Flexible Rockfall Protection Barrier", *Engineering Structures*, 2018, Vol. 173, pp. 831-852.
- [3] Zhou, F.L., Cui, H.C., Shigetaka, A.B.E., Lv, X.L., Sun, Y.P., et al., "Inspection Report of the Disaster of the East Japan Earthquake by Sino-Japanese Joint Mission", *Building Structure*, 2012, Vol. 42, pp. 1-20. (in Chinese)
- [4] Liu, S.W., Liu, Y.P. and Chan, S.L., "Advanced Analysis of Hybrid Steel and Concrete Frames Part 1: Cross-section Analysis Technique and Second-order Analysis", *Journal of Constructional Steel Research*, 2012, Vol. 70, pp. 326-336.
- [5] Liu, S.W., Liu, Y.P. and Chan, S.L., "Advanced Analysis of Hybrid Steel and Concrete Frames Part 2: Refined Plastic Hinge and Advanced Analysis", *Journal of Constructional Steel Research*, 2012, Vol. 70, pp. 337-349.
- [6] Yu, Z.X., Qiao, Y.K., Zhao, L., Xu, H., Zhao, S.C. and Liu, Y.P., "A Simple Analytical Method for Evaluation of Flexible Rockfall Barrier Part 2: Application and Full-scale Test", *Advanced Steel Construction*, 2018, Vol. 14, pp. 142-165.
- [7] Xu, H., Gentilini, C., Yu, Z.X., Wu, H. and Zhao, S.C., "A Unified Model for the Seismic Analysis of Brick Masonry Structures", *Construction and Building Materials*, 2018. Vol. 184, pp. 733-751.

- [8] Chen, W.F. and Ross, D.A., "Test of Fabricated Tubular Columns", American Society of Civil Engineers, 1977, Vol. 103, pp. 619-634.
- [9] Liu, S.W., Chan, T.M., Chan, S.L., et al. "Direct Analysis of High-strength Concrete-filled-tubular Columns with Circular & Octagonal Sections", Journal of Constructional Steel Research, 2017, Vol. 129, pp. 301-314.
- [10] Zhao, H., Sun, Y.P., Takeuchi, T. and Zhao, S.C., "Comprehensive Stress-strain Model of Square Steel Tube Stub Columns under Compression", Engineering structures, Vol.131, pp. 503-512.
- [11] Yang, C., Zhao, H., Sun, Y.P. and Zhao, S.C., "Compressive Stress-strain Model of Cold-formed Circular Hollow Section Stub Columns Considering Local Buckling". Thin-walled Structures, 2017, Vol. 120, pp. 495-505.
- [12] Cao, B.Z., Zhang, Y.C., Wang, Q.P., et al. "Mechanical Behavior of Circular Concrete Filled Thin-walled Steel Tube Stub Columns", Journal of Harbin Institute of Technology, 2005, Vol. 37, No. 8, pp. 141-144. (in Chinese)
- [13] Tan, K.F., Pu, X.C. and Cai, S.H., "Study on the Mechanical Properties of Steel Extra-high Strength Concrete Encased in Steel Tubes", Journal of Building Structures, 1999, Vol. 20, No.1, pp. 10-15. (in Chinese)
- [14] O'Shea, M.D. and Bridge, R.Q., "Tests on Thin-walled Concrete-filled Steel Tubes", Twelfth International Specially Conference on Cold-formed Steel Structures, St. Louis, Missouri, U.S.A., 1994, pp. 399-419.
- [15] Han, L.H., Yao, G.H. and Zhao, X.L., "Tests and Calculations for Hollow Structural Steel (HSS) Stub Columns Filled with Self-consolidating Concrete (SCC)", Journal of Constructional Steel Research, 2005, Vol. 61, No. 9, pp. 1241-1269.
- [16] Yu, Z.W., Ding, F.X. and Lin, S., "Researches on Behavior of High-Performance Concrete Filled Tubular Steel Short Columns", Journal of Building Structures, 2002, Vol. 23, No. 2, pp. 41-47. (in Chinese)
- [17] Johansson, M. and Gylltoft, K., "Mechanical Behavior of Circular Steel-Concrete Composite stub columns", Journal of Structural Engineering, 2002, Vol. 128, No. 8, pp. 1073-1081.
- [18] Sakino, K., Nakahara, H. and Morino, S., et al., "Behavior of Centrally Loaded Concrete-filled Steel Tube Short Columns", Journal of Structural Engineering, ASCE, 2004, Vol. 130, No.2, pp.180-188.
- [19] Wang Y.Y. and Zhang, S.M., "Research on Basic Behavior of High-strength Concrete-filled Steel Tubular Short Columns under Axial Compressive Loading", Journal of Harbin Institute of Technology, 2005, Vol. 37, pp.100-103. (in Chinese)
- [20] O'Shea, M.D. and Bridge, R.Q., "Local Buckling of Thin-walled Circular Steel Sections with or Without Internal Restraint", Journal of Constructional Steel Research, 1997, Vol. 41, No.2/3, pp. 137-157.
- [21] Cai, S.H. and Jiao, Z.S., "Behavior and Ultimate Strength of Short Concrete-filled Steel Tubular Columns", Journal of Building Structures, 1984, Vol. 5, No. 6, pp. 13-29.(in Chinese)
- [22] Fujimoto, T., Mukai, A. and Nishiyama, I., et al., "Axial Compression Behavior of Concrete Filled Steel Tubular Stub Columns using High Strength Materials". Journal of Structural & Construction Engineering, AIJ, 1997, Vol. 62, No. 498, pp. 161-168. (in Japanese)
- [23] Zhou, X.H., Liu, J.P. and Zhang, S.M., "Behavior of Circular Tubed Reinforced Concrete Stub Columns under Axial Compression", Engineering Mechanics, 2009, Vol. 26, No. 11, pp. 53-59.
- [24] Zhang, S.M., Liu, J.P., Ma, L. and Xing, T., "Axial Compression Test and Analysis of Circular Tube Confined HSC Stub Columns", China Civil Engineering Journal, 2007, Vol. 40, No.3, pp. 24-31, 68. (in Chinese)
- [25] Wang, Y.Y. and Zhang, S.M., "Influencing Factor Analysis on Failure Modes of Concrete-filled Steel Tubular Stub Columns Subjected to Axial Compression", Journal of Harbin Institute of Technology, 2005, Vol. 37, No. 8, pp. 133-136. (in Chinese)

- [26] Fam, A., Frank, S.Q. and Rizkalla, S., "Concrete-filled Steel Tubes Subjected to Axial Compression and Lateral Cyclic Loads", *Journal of Structural Engineering*, 2004, Vol. 130, No. 4, pp. 631-640.
- [27] Johansson, M., "The Efficiency of Passive Confinement in CFT Columns", *Steel and Composite Structures*, 2002, Vol. 2, No. 5, pp. 379-396.
- [28] Sakino, K., Tomii, M. and Watanabe, K., "Sustaining Load Capacity of Plain Concrete Stub Columns Confined by Circular Steel Tubes", *Proceedings of the International Specialty Conference on Concrete-filled Steel Tubular Structures*, ASCCS, Harbin, China, pp. 112-118.
- [29] O'Shea, M.D. and Bridge, R.Q., "Test on Circular Thin-walled Steel Tubes Filled with Medium and High Strength Concrete", *Department of Civil Engineering Research Report No. R755*, Sydney, 1997.
- [30] Orito, Y., Sato, Y. and Tanaka, N. and Watanabe, Y., "Study on Unbonded Steel Tube Concrete Structures", *Composite Construction in Steel & Concrete*, ASCE, 2010, pp. 786-804.
- [31] Ellobody, E., Young, B. and Lam, D., "Behavior of Normal and High Strength Concrete-filled Compact Steel Tube Circular Stub Columns", *Journal of Constructional Steel Research*, 2006, Vol. 62, No. 7, pp. 706-715.
- [32] Oliverira, W.L.A.D., Nardin, S.D., Ana Lúcia H. de Cresce El Debs, et al., "Influence of Concrete Strength and Length/ Diameter on the Axial Capacity of CFT Columns", *Journal of Constructional Steel Research*, 2009, Vol. 65, No. 12, pp. 2103-2110.
- [33] Prion, H.G.L. and Boehme, J., "Beam-column Behavior of Steel Tubes Filled with High Strength Concrete", *Canadian Journal of Civil Engineering*, 1994, Vol. 21, No. 2, pp. 207-218.
- [34] Cao, B.Z., Zhang, Y.C., Wang, Q.P., et al, "Mechanical Behavior of Circular Concrete Filled Thin-walled Steel Tube Stub Columns", *Journal of Harbin Institute of Technology*, 2005, Vol. 37, pp. 141-144. (in Chinese)
- [35] Ekmekyapar, T. and Al-Eliwi B.J.M., "Experimental Behaviour of Circular Concrete Filled Steel Tube Columns and Design Specifications", *Thin-walled Structures*, 2016, Vol. 105, pp. 220-230.
- [36] Abed, F., Alhamaydeh, M. and Abdalla, S., "Experimental and Numerical Investigations of the Compressive Behavior of Concrete Filled Steel Tubes (CFSTs)", *Journal of Constructional Steel Research*, Vol. 80, No. 1, pp. 429-439.
- [37] Gupta, P.K., Sarda, S.M. and Kumar, M.S., "Experimental and Computational Study of Concrete Filled Steel Tubular Columns under Axial Loads", *Journal of Constructional Steel Research*, 2007, Vol. 63, No. 2, pp. 182-193.
- [38] Han, L.H. and Yao, G.H., "Experimental Behaviour of Thin-walled Hollow Structural Steel (HSS) Columns Filled with Self-consolidating Concrete (SCC)", *Thin-walled Structures*, 2004, Vol. 42, No. 9, pp. 1357-1377.
- [39] Han, L.H., Tao, Z. and Wang, W.D., "Advanced Composite and Mixed Structures-Testing, Theory and Design Approach", *China Science Publishing & Media Ltd*, 2009. (in Chinese)
- [40] He, F., Zhou, X.H., and Tang, C.H., "Experimental Research on the Bearing Behavior of High-strength-concrete-filled Steel Tube under Axial Compression", *Engineering Mechanics*, 2000, Vol. 17, No. 4, pp. 61-66. (in Chinese)
- [41] Yu, Z.W., Ding, F.X. and Cai, C.S., "Experimental Behavior of Circular Concrete-filled Steel Tube Stub Columns", *Journal of Constructional Steel Research*, 2007, Vol. 63, No. 2, pp. 165-174.
- [42] Ke, X.J., Chen, Z.P., Ying, W.D., et al., "Experimental Study on the Axial Compression Performance of High-strength Concrete Filled Steel Tube Columns", *Building Structure*, 2014, Vol. 44, No. 16, pp. 46-49, 76. (in Chinese)

- [43] Zhang, S.M. and Wang, Y.Y., "Failure Modes of Short Columns of High-strength Concrete-filled Steel Tubes", China Civil Engineering Journal, 2004, Vol. 37, No. 9, pp. 1-10. (in Chinese)
- [44] Tian, Y., "Experimental Research on Size Effect of Concrete-filled Steel Tubular Stub Columns under Axial Compressive Load", M.A. Thesis, Harbin Institute of Technology, 2014. (in Chinese)
- [45] Eurocode 3, "Design of Steel Structures. Part 1-1: General Rules and Rules for Buildings", CEN, Bruxelles, 2005.
- [46] American Institute of Steel Construction (AISC), "Specification for Structural Steel Buildings", Chicago, 2010.
- [47] Richart, F.E., Brandtzen, A. and Brown, R.L., "A Study of the Failure of Concrete under Combined Compressive Stresses", Bulletin 185, University of Illinois Engineering Experimental Station, 1928, Vol. 26, No. 12.



SECOND ANNOUNCEMENT AND CALL FOR PAPERS

NINTH INTERNATIONAL CONFERENCE ON ADVANCES IN STEEL STRUCTURES (ICASS 2018)

5-7 December 2018 - Hong Kong, China

Jointly organised by

The Hong Kong Institute of Steel Construction
&
Department of Civil and Environmental Engineering
The Hong Kong Polytechnic University

This will be the ninth in the international conference series on Advances in Steel Structures, with the first, second, third and sixth of the conferences series held in Hong Kong, fourth in Shanghai, fifth in Singapore, seventh in Nanjing and eighth in Portugal. As with the eight previous successful conferences, this conference is intended to provide a forum for researchers and professionals to discuss and disseminate recent advances in analysis, behaviour, design and construction of steel, aluminium and composite steel-concrete structures.

Those wishing to participate in the conference are invited to submit short 200-400 word abstracts for papers related to the general topics of the conference, which are: Aluminium and Glass Structures, Analysis Method, Cold-Formed Steel, Composite Construction, Connections, Design, Experiment, Expert Systems, Fatigue and Fracture, Frames, Offshore Platforms, Performance-based Structural Design, Prefabricated Construction, Scaffolding, Seismic-resistant Structures, Stability Design, Steel, Steel Structures, Structural Health Monitoring, Structural Optimisation, Structural Stability and Sustainability. Selected papers will also be published in the International Journal of Advances in Steel Construction which carries a mission of technology transfer and is widely circulated among the engineering and building professionals.

Please use the template to prepare an abstract and send it to ICASS2018@outlook.com. Abstracts and papers will be peer-reviewed by the Scientific Committee.



INTERNATIONAL SCIENTIFIC COMMITTEE

F.G. Albermani (Australia)	D.A. Nethercot (UK)
R. Beale (UK)	J.G. Nie (China)
F.S.K. Bijlaard (Netherlands)	J.A. Packer (Canada)
R. Bjorhovde (USA)	J.L. Peng (Taiwan)
M.A. Bradford (Australia)	X.D. Qian (Singapore)
D. Camotim (Portugal)	K. Rasmussen (Australia)
J.M. Castro (Portugal)	J. Ricles (USA)
T.H.T. Chan (Australia)	J.M. Rotter (UK)
W.F. Chen (USA)	R. Sause (USA)
Y.Y. Chen (China)	P. Schaumann (Germany)
S.P. Chiew (Singapore)	N.E. Shanmugam (Singapore)
Y.S. Choo (Singapore)	Y.J. Shi (China)
G.G. Deierlein (USA)	G. Shi (China)
S.L. Dong (China)	G.P. Shu (China)
D. Dubina (Romania)	X.P. Shu (China)
L. Gardner (UK)	L.S.da Silva (Portugal)
H.B. Ge (Japan)	N. Silvestre (Portugal)
Y. Goto (Japan)	G.S. Tong (China)
Y.L. Guo (China)	N.S. Trahair (Australia)
L.H. Han (China)	K.C. Tsai (Taiwan)
G.J. Hancock (Australia)	C.M. Uang (USA)
T. Helwig (USA)	B. Uy (Australia)
S. Herion (Germany)	M. Veljkovic (Netherlands)
B.A. Izzuddin (UK)	P.C.G. da S. Vellasco (Brazil)
J.P. Jaspart (Belgium)	A. Wadee (UK)
S.A. Jayachandran (India)	F. Wald (Czech)
T.L. Karavasilis (UK)	A. Walicka (Poland)
S.E. Kim (Korea)	E. Walicki (Poland)
S. Kitipornchai (Australia)	L.J. Wang (China)
K. Kwok (Australia)	W. Wang (China)
D. Lam (UK)	Y.C. Wang (UK)
S.S. Law (China)	C.M. Wang (Australia)
W. Li (China)	D. White (USA)
G.Q. Li (China)	E. Yamaguchi (Japan)
J.Y.R. Liew (Singapore)	Y.B. Yang (China)
D. Lignos (Switzerland)	Q.R. Yue (China)
L.R.O. de Lima (Brazil)	R. Zandonini (Italy)
T.H. Lip (Australia)	X.L. Zhao (Australia)
E.M. Lui (USA)	X.H. Zhou (China)
Y.L. Mo (USA)	R.D. Ziemian (USA)

IMPORTANT DATES

First call for paper:	1 January 2018
Abstract submission deadline:	1 March 2018
Notification of abstract acceptance:	1 April 2018
Full paper submission:	1 June 2018
Notification of full paper acceptance:	1 August 2018
Early bird registration:	on or before 1 September 2018
Announcement of programme:	1 October 2018

REGISTRATION FEE

The conference registration fee is US\$750 (Early bird registration before 1st September 2018)/US\$850, which covers conference proceedings, conference banquet, lunches and refreshments.

OFFICIAL LANGUAGE

English will be the official language of the Conference for both oral and written presentations.

PROCEEDINGS

The proceedings of the conference will be published by the Hong Kong Institute of Steel Construction.

ORGANISING COMMITTEE

Siu-Lai Chan (Chair)	Tak-Ming Chan (Co-Chair)	Songye Zhu (Co-Chair)
Yaopeng Liu	Siwei Liu	

LOCAL SCIENTIFIC COMMITTEE

Francis.T.K. Au	Goman.W.M. Ho	Y.Q. Ni	A.S. Usmani
C.M. Chan	Eddie S.S. Lam	S.J. Pan	Y. Xia
W.T. Chan	Paul H.F. Lam	Derek K.L. So	Jackie Yau
Edward S.C. Chan	C.K. Lau	Andrew K.W. So	Ben Young
W.K. Chow	Andy Lee	Ray K.L. Su	W.K. Dominic Yu
Reuben Chu	Y.S. Liu	J.G. Teng	S.W. Yuen
J.G. Dai	S.H. Lo	Ben Tse	Z.H. Zhou

SUPPORTING INSTITUTIONS



SUPPORTING JOURNAL



ORGANIZING PARTNER



For further information, please contact:

Carol Deng - Conference Secretary

E-mail: icass2018@outlook.com

Address: International Journal of Advanced Steel Construction,
CEE, The Hong Kong Polytechnic University, Hong Kong, China.



CONFERENCE WEBSITE:

<http://www.icass2018.com>

SCIENTIFIC COMMITTEE

Chairman: František Wald

Scientific secretary: Michal Jandera

G.A. Altay (Turkey)	R. Landolfo (Italy)
I. Balaz (Slovakia)	N. Lopes (Portugal)
C. Baniatopoulos (Greece)	R. Leon (USA)
A. Bureau (France)	J.R. Liew (Singapore)
E.M. Batista (Brazil)	J. Loughlan (UK)
R. Beale (UK)	J. Macháček (Czech Republic)
R. Bjorhovde (USA)	M. Mahendran (Australia)
M.A. Bradford (Australia)	F. Mazzolani (Italy)
B. Brune (Germany)	E. Mirambell (Spain)
L. Calado (Portugal)	D. Nethercot (UK)
D. Camotim (Portugal)	J. Packer (Canada)
S.L. Chan (Hong Kong, China)	J. Paik (South Korea)
T.M. Chan (Hong Kong, China)	S. Pajunen (Finland)
R. Casciaro (Italy)	N. Rangelov (Bulgaria)
K.F. Chung (Hong Kong, China)	K.J.R. Rasmussen (Australia)
C. Chiorean (Romania)	E. Real (Spain)
M. D'Aniello (Italy)	B. Rossi (Belgium)
H. Degée (Belgium)	F. Roure (Spain)
J.-F. Démonceau (Belgium)	R. Sause (USA)
F. Dinu (Romania)	B.W. Schafer (USA)
D. Dubina (Romania)	L.S. Silva (Portugal)
L. Dunai (Hungary)	N. Silvestre (Portugal)
S. Easterling (USA)	H. Snijder (Netherlands)
A. Elghazouli (UK)	R. Stroetmann (Germany)
M. Fontana (Switzerland)	J.G. Teng (Hong Kong, China)
D. Frangopol (USA)	V. Ungureanu (Romania)
L. Gardner (UK)	H. Unterweger (Austria)
M. Garlock (USA)	B. Uy (Australia)
G. Garcea (Italy)	I. Vayas (Greece)
P. Gonçalves (Brazil)	P. Vellasco (Brazil)
F. Guarracino (Italy)	P. Vila Real (Portugal)
J. Hajjar (USA)	A. Wada (Japan)
G.J. Hancock (Australia)	N. Yardimci (Turkey)
M. Hjiiaj (France)	B. Young (Hong Kong, China)
B. Izzuddin (UK)	R. Zandonini (Italy)
Z. Kolakowski (Poland)	B. Zhao (France)
M. Kotelko (Poland)	R. Ziemian (USA)
U. Kuhlman (Germany)	A. Zingoni (South Africa)
D. Lam (UK)	Y.B. Yang (Taiwan, China)

ORGANISING COMMITTEE

K. Cábová
J. Dolejš
M. Eliášová
M. Jandera
J. Macháček

P. Ryjáček
Z. Sokol
M. Šorf
F. Wald
B. Židlický

COLLOQUIUM CONTACT

sdss2019.cz
info@sdss2019.cz



The International Colloquium on Stability and Ductility of Steel Structures

Prague 2019
11-13 September



FACULTY OF CIVIL
ENGINEERING
CTU IN PRAGUE

INTRODUCTION

The series of International Colloquia on Stability and Ductility of Steel Structures have been supported by the Structural Stability Research Council (SSRC) for more than forty years and its objective is to present the progress in theoretical, numerical and experimental research in the field of stability and ductility of steel and steel-concrete composite structures. Special emphasis is laid on new concepts and procedures concerning the analysis and design of steel structures and on the background, development and application of rules and recommendations either appearing in recently published Codes or Specifications or about to be included in their upcoming versions.

This International Colloquium series started in 1972 in Paris and its subsequent editions took place in different cities with the last five being held in: Timisoara, Romania (1999), Budapest, Hungary (2002), Lisbon, Portugal (2006), Rio de Janeiro, Brazil (2010) and Timisoara, Romania (2016).

The 2019 edition of SDSS is organized by the Czech Technical University in Prague. The university held the second edition of the Eurosteel conference in 1999 and first three editions of Applications of Structural Fire Engineering (ASFE) conference (2009, 2011 and 2013).

It is our pleasure to invite you to Prague again for the International Colloquium SDSS at the beginning of September 2019.

František Wald
Michal Jandera



DATE AND VENUE

11-13 September 2019

Czech Republic - Prague

Czech Technical University in Prague

Faculty of Civil Engineering

Thákurova 7, 166 29 Prague 6

KEY DATES

Call for abstracts and submission opening: **01.06.2018**

Abstract submission deadline: **31.10.2018**

Acceptance of abstracts and call for papers: **15.12.2018**

Submission of full papers: **15.02.2019**

Acceptance of papers: **01.05.2019**

Submission of final papers and registration: **15.05.2019**

SDSS 2019 opening: **11.09.2019**

REGISTRATION FEE

	Early bird registration by 1 June 2019	Standard registration after 1 June 2019
Conference participant regular	€ 500	€ 580
Conference participant student	€ 400	€ 450
Accompanying person	€ 120	€ 150
Kutná Hora trip after the closing session	€ 95	

No more than two papers can be presented by one registered participant. The conference participant fee covers an electronic copy of the Proceedings, admission to the technical sessions, lunches, coffee breaks, welcome reception and banquet dinner. The student registration fee applies to students of up to 35 years of age.

Welcome reception and conference banquet are included in the fee for accompanying persons.

The sightseeing trip to Kutná Hora can be purchased separately on request and will be organised for 10 participants as minimum. It is planned for the afternoon of the last day of the conference after the Closing Session.

ABSTRACT SUBMISSION

Abstract should be submitted to the e-mail address **michal.jandera@sdss2019.cz** by 31st October 2018. The abstract should summarise the content of the paper clearly and highlight its contribution to the current scope of knowledge and research.

PROCEEDINGS

The papers accepted by the SDSS 2019 Scientific Committee and presented at the colloquium will be published in electronic Proceedings distributed to the participants at registration and covered by SCOPUS.

MAIN TOPICS OF THE COLLOQUIUM

- Advanced structural analysis
- Bridges and footbridges
- Cold-formed members
- Connections
- Cyclic and blast loading
- Damage repair and assessment of steel structures
- Design codes and standards
- Dynamic behaviour and analysis
- Fatigue and fracture mechanics
- Fire engineering
- Frames
- High strength & stainless steel
- Innovative structural designs and applications
- Lightweight aluminium structures
- Lightweight fibre reinforced plastic composite structures
- Member behaviour: tension, compression, beams, beam-columns
- Off-shore structures
- Plate, shell and space structures
- Reliability and safety
- Robustness
- Seismic-resistant structures
- Stability of glass and hybrid structures
- Steel-concrete composite members and structures
- Thin-walled constructions
- Trusses, towers and masts
- Tubular constructions

**ORDER
FORM**

ISSN 1816-112X

**Advanced Steel Construction,
an international journal**Indexed by the Science Citation Index Expanded,
Materials Science Citation Index and ISI Alerting Services**From:****To:** Secretariat, Advanced Steel Construction, an international journal
Fax: (852) 2334-6389

I/ We would like to enter a subscription to the *International Journal of Advanced Steel Construction (IJASC)* published by The Hong Kong Institute of Steel Construction.

Please complete the form and send to:

International Journal of Advanced Steel Construction
c/o Department of Civil and Environmental Engineering
The Hong Kong Polytechnic University
Hung Hom, Kowloon, Hong Kong

Fax: (852) 2334-6389 Email: ceslchan@polyu.edu.hkPublished by : The Hong Kong Institute of Steel Construction
Website: <http://www.hkisc.org/>**Please tick the appropriate box**

- ☐ Please enter my hard-copy subscription (**4 issues per year**).
☐ Please send me a complimentary copy of the *Advanced Steel Construction, an International Journal (IJASC)*.

Please tick the appropriate box(es)

	<u>Print</u>	<u>On-line is free</u>
Personal	<input type="checkbox"/> US\$ 125	
Institutional	<input type="checkbox"/> US\$ 280	

Total Amount US\$ _____

Methods of payment ☐ Please invoice me
(please tick the appropriate box(es)) ☐ Cheque enclosed for US\$ _____ payable to
Hong Kong Institute of Steel Construction Limited
(No personal cheque accepted)

Ship to

Name (Prof./ Dr./ Mr./ Ms.) _____
Address _____

City/ State/ Postal Code _____
Country _____
Email _____ Fax _____